The synthesis and luminescence properties of new platinum and iridium complexes

BONNEAU, MICKAELE

The Synthesis and Luminescence Properties of New Platinum and Iridium Complexes

Mickaële Bonneau

A thesis submitted in partial fulfilment of the requirements for the degree of Ph.D.

Department of Chemistry

December 2014

Abstract

In the field of the development of new transition metal complexes as phosphorescent dopants for organic light emitting devices (OLEDs) or bio-imaging agents, new iridium(III), platinum(II), and palladium(II) complexes were synthesized and their luminescence properties studied.

The arylation of *fac*-Ir(thpy)$_3$ complexes (where thpy = N^C-cyclometallated 2-thienylpyridine) with various chromophores such as pyrene or naphthalimide was carried out using palladium-catalysed C–H activation (an approach of "chemistry on the complex"). A second series of iridium complexes, Ir(Me-ppy)$_2$(tta) functionalized with the same type of fluorophores *via* the tta unit, were synthesized and their photophysical properties studied (ppy = 2-phenylpyridine; tta = thenoyltrifluoroacetone).

To increase the rigidity of the square planar geometry associated with cyclometallated platinum(II) and palladium(II) complexes, we have introduced new tetradentate ligands of the coordination type C^N^N^C. Their photophysical studies have shown that all synthesized platinum complexes are phosphorescent at room temperature with quantum yields from 0.12 to 0.78. Furthermore, unusual phosphorescence at room temperature of some palladium complexes has been observed.

The synthesis of new iridium complexes of the type $[Ir(ppy)_2(N^N)]^{n+}$ (where n= 1 or 0) is also reported, where N^N = 1-isoquinolinebenzimidazole, 2-quinolinebenzimidazole, 3-isoquinolinebenzimidazole or 2,2'-bisbenzimidazole. According to the protonation state of the azole nitrogen atoms, the charge of the iridium complex is modified. The cationic (N-protonated) and neutral (non-protonated) forms of the iridium complexes were obtained using two different synthetic methods. The introduction of isoquinolyl units leads to a red-shift in the emission compared to the previously studied pyridyl analogue $[Ir(ppy)_2(pbz)]^{n+}$ (pbz = 2-pyridylbenzimidazole). Furthermore, the photophysical properties are dependent on the isomeric form and on the protonation state. In the case of the 2,2'-bisbenzimidazole ligand, *three* different forms may be anticipated in principle, namely a cationic (di-protonation), a neutral (mono-protonation) and an anionic form (no protonation). To date, the first two have been isolated and

studied. A pH titration showed the presence of a third form of the iridium complex at pH ≥ 10.5, tentatively ascribed to the anionic form.

Finally, new iridium(III) and platinum(II) complexes bearing phosphine-based P^N or sulfur-based S^S ligands, respectively, were synthesized and their photophysical properties studied.

DECLARATION

The research described herein was undertaken at the Department of Chemistry at Durham University between December 2011 and December 2014. All of the work is my own, except where specifically stated otherwise. No part of it has previously been submitted for a degree at this or any other university.

STATEMENT OF COPYRIGHT

Aknowlegements

Firstly, my most sincere thanks go to my supervisors, Dr Gareth Williams and Dr Véronique Guerchais for all the support, guidance and encouragement given throughout my PhD studies.

I also acknowledge the Department of Chemistry, University of Durham, University of Rennes 1 and the CNRS, for the financial support to undertake this research.

I would like to thank the members of the jury for agreeing to review my work and have moved to Durham: Dr. Philip Dyer from Durham University, Dr. Valery Kozhevnikov from Northumbria University and Dr. Claude Lapinte from University of Rennes 1.

I am grateful to Dr. Henri Doucet and Dr. Kassem Beydoun for the catalysis, Dr. Juan A. Aguilar Malavia, Dr. Alan Kenwright and Catherine Heffernan for NMR spectroscopy; Dr. Peter Stokes, Dr. David Parker and Dr Jackie A. Mosely for mass spectrometry; Dr. Dmitry S. Yufit for X-ray crystal structures; and to everyone else from the glassblowers to those who provide tea.

I would also like to thank all members of the Guerchais' group and Williams' group, past and present:
In Rennes: Muriel Escadeillas, Dr. Moussa Zaarour, Dr. Julien Boixel, Dr. Paul Savel, Dr. Yves-Marie Hervault, He Xiaoyan, Claus Hierlinger, Pramila Selvanathan, Dr. Andrea Mulas and Dr. Dang Tung Thanh.
In Durham: Dr. Victoria Whittle, Dr. Gemma Freeman and your lovely Disney's songs, Raminder and your special dishes (tin can) and all of the 4th year project students: Adam (and the thermometer), Joe, Esmee, Ruth and Marius. Thank you for your friendship, your help and making the lab such a fun place to work – it has been a pleasure to work with you all.

Finally I would like to thank my family and friends for all the support and encouragement they have given. In particular, I would like to thank my parents my sister and Maxime, who have been brilliant throughout, and always knew how to make me smile.

Abbreviations

Å	Angstrom (10^{-10} m)
acac	acetylacetonate
AlQ_3	tris(8-Hydroxyquinolate)aluminium
2-ap	2-aminopyridine
4-ap	4-aminopyridine
Ar	Aryl ring
ASAP	Atmospheric Solids Analysis Probe
bbz	2,2'-bis(benzimidazole)
Bodipy	boron-dipyrromethene
bpy	2,2'-bipyridine
BSA	Bovine Serum Albumin
C^N	Ligands that bind through a cyclometa1ated ring and a central pyridine ring
CV	Cyclic Voltammetry
Cys	Cystein
Dap	diaminopyridine
dbbpy	4,4’-di-*tert*-butyl-2,2’-bipyridine
DFT	Density Functional Theory
DCM	dichloromethane
4,5-dfppy	4,5-difluorophenylpyridine
4,6-dfppy	4,6-difluorophenylpyridine
DMAc	dimethylacetamide
DMF	dimethylformamide
DMSO	dimethylsulfoxide
DNA	deoxyribonucleic acid
DNBS	2,4-dinitro-benzenesulfonyl
Dap	diaminopyridine
Dpm	Dipivaloylmethane
Dpp	2,9-diphenyl-1,10-phenanthroline

dppf	[1,1′-Bis(diphenylphosphino)ferrocene]dichloropalladium(II)
Egcv	Electrochemical band gap
Egopt	Optical band gap
EPA	Diethyl ether: isopropane: ethanol (2:2:1 v/v)
eq	equivalent
ES^+	Positive ion electrospray ionisation
ET	Electron transfer
Et	Ethyl
ε	Extinction coefficient (L mol^{-1} cm^{-1})
fac	facial
Fc	Ferrocene
FLIM	Fluorescence Lifetime Imaging Microscopy
HeLa	An adherent cultured cell line derived from human cervical carcinoma cells
Hcy	Homocystein
HOMO	Highest occupied molecular orbital
HRMS	High Resolution Mass Spectroscopy
Hz	Hertz
IC	Internal Conversion
ILCT	Intraligand charge transfer
ISC	Intersystem crossing
ITO	Indium tin oxide
k_{nr}	Rate constant of non-radiative decay
k_r	Rate constant of radiative decay
λ_{abs}	Absorption wavelength
λ_{em}	Emission wavelength
λ_{exc}	Excitation wavelength
λ_{max}	Wavelength at which an absorption/emission band maximum occurs
LC	Ligand centered
LUMO	Lowest unoccupied molecular orbital
MALDI	Matrix assited laser desorption ionisation
Me	Methyl

MeCN	Acetonitrile
mer	meridional
MLCT	Metal-to-ligand charge transfer
MMLCT	Meta-metal-to-ligand charge transfer
MS	Mass spectrometry
NIR	Near Infrared
nm	nanometer
NMR	Nuclear magnetic resonance
N^N	Ligands that bind through two central azolic ring
N^N^C	Ligands that bind through a cyclometa1ating rings and two central pyridine ring
N^N^N^N	A tetradentate ligand coordinating via four nitrogens
OLED	Organic light emitting device/ diode
ORTEP	Oak Ridge thermal ellipsoid plot
Ox	Oxidation
Pbz	pyridylbenzimidazole
P^C	Ligands that bind through a cyclometa1ating rings and a phosphine
PET	photoinduced electron transfer
pH	Hydrogen potential
pKa	Logarithmic measure of the acid dissociation constant
P^N	Ligands that bind through a pyridine ring and a phosphine
P^P	Ligands that bind through two phosphine
PPA	Polyphosphoric acid
ppm	Parts per million
ppy	2-phenylpyridine
p-tpy	2-(p-tolyl)pyridine
py	pyridine
φ	Quantum yield
q	quinolinolato
red	reduction
Rf	Retention function
RNA	Ribonucleic acid

RT	Room temperature
SCE	Saturated Calomel Electrode
sh	shoulder
S_n	nth excited singlet state
S_0	Singlet ground state
SOC	Spin Orbit Coupling
S^S	Ligands that bind through two sulfur
τ	Lifetime
^{t}Bu	*tert*-butyl
tdt	toluene-3,4-dithiolate
TFA	Trifluoroacetic acid
THF	Tetrahydrofuran
thpy	2-(2-thienyl)pyridine
T.M.	Transition Metal
TTA	thienyltrifluoroacetonate
UV	Ultraviolet

TABLE OF CONTENT

ABSTRACT..... i
DECLARATION.....iii
AKNOWLEDGEMENTS.....iv
ABBREVIATIONS.....v

CHAPTER ONE: Introduction

1. Introduction to luminescence..... 2
   1.1. Definition..... 2
   1.2. Absorption..... 2
   1.3. Emission..... 3
   1.4. Orbital transitions..... 6
2. Heavy-Metal complexes..... 7
   2.1. Luminescence Tuning..... 9
      2.1.1. Effect of cyclometallation..... 9
      2.1.2. Modulation of the HOMO-LUMO gap by functionalization..... 10
      2.1.3. Effect of symmetry..... 11
   2.2. Applications..... 12
      2.2.1. OLEDs..... 12
      2.2.2. Bio-imaging and bio-sensors..... 14
3. Objectives:..... 19
4. References..... 20

CHAPTER TWO: Thienyl Arylated Iridium *bis*- and *tris*-cyclometallated Ir(C^N-Ar)$_3$ and Ir (Me ppy)$_2$(tta-Ar) Complexes

1. Arylated *facial tris*-cyclometallated thienylpyridine iridium complexes *fac*-Ir(thpy-Ar)$_3$26
   1.1. Synthesis of the precursor complex *fac*-Ir(thpy)$_3$..... 26
      1.1.1. Classical method, first example of complex *fac*-Ir(thpy)$_3$..... 26
      1.1.2. Synthesis of the complex *fac*-Ir(thpy)$_3$ using alternative methods..... 26

1.2. Photophysical properties of complex *fac*-Ir(thpy)$_3$, 1 28
1.3. Synthesis and photophysical properties of functionalized *fac*-Ir(thpy)$_3$ complexes . 29
1.3.1. Functionalization on the proligand 29
1.3.2. Functionalization using "*Catalysis-on-the-complex*" 31
1.3.3. Palladium-catalyzed arylation/C-H bond activation 33
1.3.4. Synthesis of *mono*-, *bis*- and *tris*- benzonitrile *fac*-Ir(thpy)$_3$ derivatives 34
1.4. Photophysical characterization of arylated *fac*-Ir(thpy-Ar)$_3$ complexes 35
1.5. Iridium complexes functionalized with polycyclic-aromatic dyes 37
1.5.1. Neutral iridium complexes 37
1.5.2. Cationic iridium complexes 38
1.5.3. Iridium complexes incorporating cyclometalated aromatic dyes 40
2. Results and discussion 42
2.1. Synthesis of the bromoaryl derivatives 43
2.2. Pd-Catalyzed arylation of 2-methylthiophene 44
2.3. Catalytic arylation of the complex *fac*-Ir(thpy)$_3$ 45
2.3.1. Synthesis 45
2.3.2. Photophysical studies 48
2.4. Catalytic arylation of the complex Ir(Meppy)$_2$(tta) 52
2.4.1. Synthesis 53
2.4.2. Photophysical properties of arylated thiopheneketones th-Ar and their Ir(III) complexes. 54
3. Concluding Remarks 59
4. References 61

CHAPTER THREE: Heavy-Metal Complexes Containing Tetradentate Ligands

1. Introduction 65
1.1. Cyclometallated platinum complexes of a bidentate ligands 65
1.2. Cyclometallated platinum complexes with terdentate ligands 66
1.3. Tetradentate cyclometallated platinum complexes 68
1.3.1. Platinum complexes of "pseudocyclometallated" tetradentate Schiff-base ligands.... 68

1.3.2. Cyclometallated platinum complexes 71
1.4. Tetradentate palladium complexes 79
1.5. Objectives 81
2. Synthesis and characterization of tetradentate heavy-metal complexes 83
2.1. N^N^N^N Tetradentate Heavy-Metal Complexes 83
2.1.1. Background 83
2.1.2. Synthesis 84
2.1.3. Characterization 86
2.2. C^N^N^C Tetradentate Platinum Complexes 90
2.2.1. Synthesis of the tetradentate ligands 90
2.2.2. Synthesis of platinum complexes 93
2.2.3. Characterization of Platinum complexes 97
2.3. Synthesis and Characterization of Palladium Complexes 114
2.3.1. Synthesis of the tetradentate palladium complexes 115
2.3.2. Characterization of the Pd(II) complexes 116
2.4. C^N^N^C Gold, Mercury and Iridium Complexes 125
2.4.1. Mercuric complex 125
2.4.2. Gold Complex 126
3. Concluding Remarks 127
4. References 129

CHAPTER FOUR: pH Sensitive Heavy-Metal Complexes

1. Introduction 135
1.1. Sensors for amino acids and sugar molecules 136
1.2. DNA / RNA sensors 137
1.3. Cation sensors 138
1.4. Intracellular pH sensors 139
1.5. Objectives 142
2. Synthesis and characterizations 144
2.1. Preparation of the ligands/proligands 144

2.1.1. Benzimidazole derivatives 144
2.1.2. *Bis*-benzimidazole derivatives 144
2.2. Preparation of the complexes 145
2.2.1. Neutral complexes 145
2.2.2. Cationic complexes 146
2.3. Characterizations 147
2.3.1. NMR spectroscopy 147
2.3.2. Crystal structures 149
2.3.3. DFT calculations 151
2.3.4. Electrochemistry 154
2.4. Photophysical studies 159
2.4.1. Absorption in dichloromethane 159
2.4.1.1. Quinolyl and isoquinolyl iridium complexes 159
2.4.2. *bis*-benzimidazole iridium complexes 161
2.4.3. Emission studies in degassed DCM at 298 K 162
2.4.3.1. Neutral (iso)-quinolyl iridium complexes 162
2.4.3.2. Cationic (iso)-quinolyl iridium complexes 163
2.4.3.3. Comparison between $Ir(ppy)_2L^{10}$ and $[Ir(ppy)_2(L^{10}H)]PF_6$ 164
2.4.3.4. Emission of the *bis*-benzimidazole iridium deriatives 164
2.4.4. Emission in EPA solution at 77 K 167
2.5. pH dependence of optical properties 170
2.5.1. $Ir(ppy)_2L^{10}$ and $[Ir(ppy)_2(L^{10}H)]PF_6$ 170
2.5.2. $Ir(ppy)_2L^{11}$ and $[Ir(ppy)_2(L^{11}H)]PF_6$ 172
2.5.3. $Ir(ppy)_2L^{12}$ and $[Ir(ppy)_2(L^{12}H)]PF_6$ 174
2.5.4. $[Ir(ppy)_2(L^{14}H_2)]PF_6$, $Ir(ppy)_2(L^{14}H)$ and $[Ir(ppy)_2(L^{14})]Na$ 175
3. Concluding Remarks 178
4. References 180

CHAPTER FIVE: Iridium and Platinum Complexes Containing Sulfur-based or Phosphine-based Ligands

1. Introduction 185

2. Heteroleptic iridium(III) and platinum(II) complexes bearing sulfur-based ligands..... 187
2.1. Synthesis..... 187
2.1.1. Ligand Synthesis..... 187
2.1.2. Synthesis of metal complexes of the SPNPS ligand..... 187
2.1.2.1. Iridium complex..... 188
2.1.2.2. Platinum complexes..... 188
2.2. Characterisation..... 189
2.2.1. NMR spectroscopy..... 189
2.2.2. Crystallography..... 191
2.2.3. Electrochemistry..... 193
2.2.4. Photophysics..... 193
3. Heteroleptic iridium(III) complexes bearing phosphine-based ligands..... 195
3.1. Electrochemistry..... 196
3.2. Photophysics..... 196
3.2.1. Absorption..... 196
3.2.2. Emission..... 197
4. Concluding Remarks..... 199
5. References..... 200

CHAPTER SIX: Experimental Methods

1. Materials and Methods..... 205
2. Characterization Techniques..... 205
3. Photophysical Characterizations..... 206
4. Electrochemical Measurements..... 208
5. General Procedures..... 208
5.1. General Procedures for Chapter Three..... 208
5.1.1. Synthesis of Tetradentate Ligands..... 208
5.1.2. Synthesis of tetradentate complexes..... 209
5.2. General Procedures for Chapter Four..... 209
5.2.1. Ligands Synthesis..... 209
5.2.2. Complexes Synthesis..... 210

6. Experimental Details for Chapter Two 210
7. Experimental details for Chapter Three 222
8. Experimental details for Chapter Four 240
9. Experimental details for Chapter Five 249
10. References 252

APPENDIX

A.1 Crystallographic Data.....253
A.2 Publications.....276

CHAPTER ONE:

INTRODUCTION

1. Introduction to luminescence

1.1. Definition

The word *luminescence* refers to the emission of light by materials other than that which occurs through the process of incandescence (where the energy source is heat). Depending on the origin of the excitation energy, luminescence can be sub-divided into different categories, for example, chemiluminescence when the energy comes from a chemical reaction, electroluminescence when emission arises as a result of the application of an electric field, and photoluminescence when the energy source is light (usually of higher energy than that emitted).[1]

1.2. Absorption

When a molecule absorbs a photon of suitable wavelength, an electron is promoted from its ground state S_0 to a higher energy orbital, producing a singlet excited electronic state S_n. This process is very fast, in the range of less than a femtosecond, a timescale over which the nuclei are effectively stationary. Thus, the Born-Oppenheimer approximation is valid because the nuclei remain fixed during the much faster electronic transition - transitions are therefore vertical in a typical diagram of potential energy surfaces, wherein the *x* axis refers to nuclear coordinates. (**Figure 1**) [2]

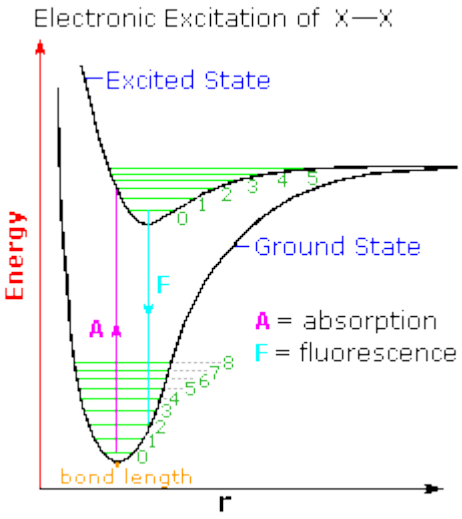

Figure 1. Diagram showing potential energy surfaces of ground and excited states of a molecule as a function of some one-dimensional nuclear coordinate r (*e.g.* a bond length)

The energy absorbed is defined by the difference between the energy of the ground state and the excited state. This energy of absorption is calculated by the Planck's relation:[3]

$$E = h\nu$$

h is the Planck's constant and ν is the frequency of the photon. In the absorption of light, the intensities of the incident light (I_0) and transmitted light (I) at a specific wavelength λ are related by the Beer-Lambert law:[4]

$$A(\lambda) = \log I_0/I$$

We define absorbance A(λ) as the capacity of the sample to absorb light. The absorbance is directly proportional to the the molar concentration, *c*, and the path length through the sample, *l*, as shown by the Beer-Lambert equation:

$$A(\lambda) = \varepsilon.l.c$$

The proportionality constant in this equation, ε, is the extinction coefficient, the capacity of a molecule to absorb a specific wavelength. Extinction coefficients are related to the nature of the transition. In fact, if the transition is forbidden by the principles of quantum mechanics, the extinction coefficient results to be small (e.g. < 10^2 dm^3 mol^{-1} cm^{-1}). On the other hand, if the transition is allowed, the extinction coefficient is larger (10^4–10^6 dm^3 mol^{-1} cm^{-1}). Selection rules have generally been used for predicting the nature of the electronic transitions. According to the spin selection rule, an allowed transition could only occur between two states of the same spin multiplicity (ΔS= 0).[5] However, this rule could be relaxed by a heavy atom effect that leads to a high spin-orbit coupling due to the fast moving electrons around a highly positively-charged nucleus. Spin-orbit coupling results from the interaction of the electron magnetic moments with the magnetic field generated by their own orbital motion. This effect is most prominently observed in molecules containing heavy atom(s) such as 2nd and 3rd row transition metal ion(s).

1.3. Emission

When a molecule absorbs a photon, the molecule is promoted to an excited state named S_n from its fundamental state S_0 (**Figure 2**). According to Kasha's rule the excited molecule undergoes rapid relaxation *via* a non-radiative pathway to the lowest singlet excited state S_1, a process which is normally much faster than radiative emission from higher S_n states.[6] From this populated excited state S_1, the relaxation to the fundamental ground state can occur through different pathways (**Figure 2**). Non-radiative decay is defined by transfer of the excess of energy into vibrational, rotational or translational energy, either within the

same molecule or between other molecules or solvent in the local environment. Radiative decay corresponds to the emission of a photon of energy corresponding to the difference between the energies of S_1 and S_0. This phenomenon is called fluorescence. This process does not involve a change in spin multiplicity, as the spins of the electrons in the two singly occupied molecular orbitals of the excited state are anti-parallel, as in the ground state. The fluorescence happens at lower frequencies compared to the excitation radiation because the emissive transition takes place after some energy is dispersed to the environment as vibrational energy. On the other hand, the energy can be transferred to a triplet excited state T_1 through intersystem crossing (ISC) under the influence of spin-orbit coupling (SOC), and then goes back to the ground state S_0.[3] ISC occurs when the energy curve of the singlet and triplet excited states cross each other, therefore conversion from ↑↓ to ↑↑ of the electronic spins is possible and the molecule enters an excited triplet state.[7]

The corresponding radiative transition back to the ground state, which is called phosphorescence, involves a change of spin.[8] Because it is a spin-forbidden transition, phosphorescence is characterized by a longer lifetime; for organic molecules, it is typically in the millisecond to seconds range.[9] In this case, non-radiative processes are usually much faster than phosphorescence at room temperature, and so phosphorescence is not usually observed at room temperature from organic molecules in solution. In transition metal complexes, luminescence is accelerated by the strong spin-orbit coupling of the metal atoms that promotes the triplet-to-singlet transition by introducing a mixed character of singlet and triplet states.[2] In small radius metal complexes, ISC is generally much faster than either fluorescence or the S_1 to S_0 non-radiative transition, which means that only phosphorescence is observed at room temperature.[10]

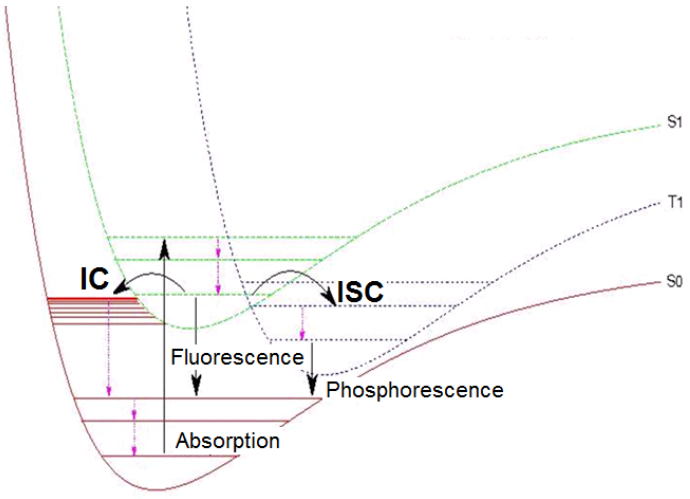

Figure 2. Jablonski diagram showing the first excited singlet and triplet states, S_1 and T_1, the ground state S_0, and the processes that can occur between them.

The Stokes shift is the difference (in wavelength or frequency units) between positions of the band maxima of the absorption and emission spectra of the same electronic transition (**Figure 3**). In the case of phosphorescence, the difference between absorption and emission is larger than for fluorescence, because it includes the S_1-T_1 gap, absorption being normally to the singlet state. Indeed, although often used, the term Stokes shift is perhaps erroneous in such cases, because the states to which absorption occurs and from emission occurs are not the same. [11]

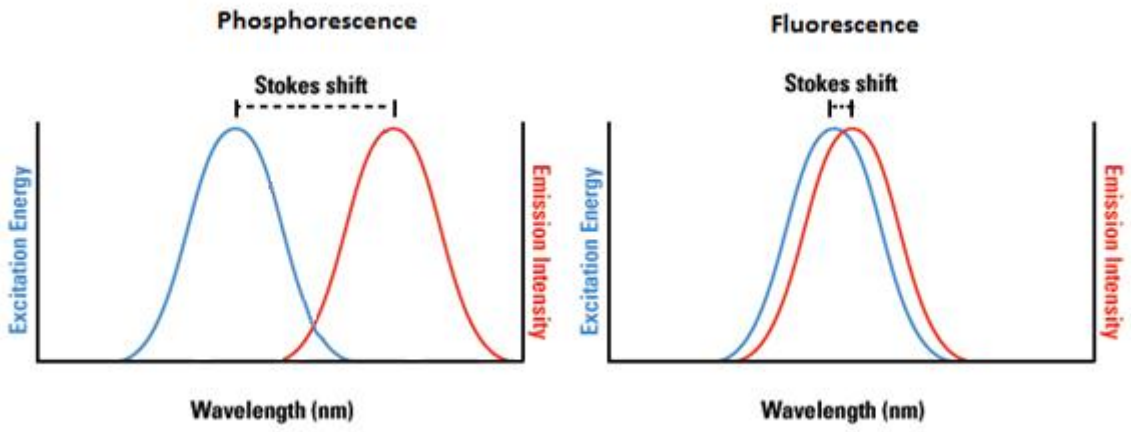

Figure 3. Representation of Stokes shift principle for a phosphorescence and a fluorescence effect

The luminescence lifetime τ refers to the timescale of the luminescence observation. For luminescence that decays mono-exponentially with time:

$$I_t = I_0 \exp(-kt)$$

the lifetime is defined as the reciprocal of the experimentally observed first-order rate constant of decay, *k*. Here, I_t is the intensity at a given time *t* after pulsed excitation, and I_0 is the intensity at *t*=0. The magnitude of *k* (and hence of τ) is determined by the radiative decay constant (k_r) and non-radiative decay constant (k_{nr}) of the molecule from its excited state S_1 or T_1, as follows:

$$\tau = 1/ (k_r + k_{nr})$$

The emission efficiency is defined by the luminescence quantum yield, which is the number of photons that are emitted relative to the number absorbed by the system (Figure).[12,13]

$$\phi = \text{number of emitted photons / number of absorbed photons}$$

For an excited state formed with unitary efficiency, the quantum yield is determined by the radiative (k_r) and non-radiative (k_{nr}) rate constants through the following relationship:[20,21]

$$\phi = k_r / (k_r + k_{nr}) = k_r\tau$$

Quantum yields of metal complexes are generally highest in the green region: they fall off towards the blue because of the energetic proximity of higher-lying deactivating states and towards the red because of increased vibrational deactivation.

1.4. Orbital Transitions

Molecular orbitals (MOs) include several atomic orbitals and can be described as being of predominantly metal or ligand character, depending upon which atomic orbitals have the most similar energy to the MO of interest (**Figure 4**).[14,15,16] When radiation is absorbed, an electronic transition between two molecular orbitals occurs and the resulting excited state can be characterized approximately by the molecular orbitals involved.[17] The assignment of the various bands that appear in the absorption spectra of transition metal complexes is often a very difficult task to solve because the absorption spectra reflect the complexity of the electronic structure of the molecule. Charge transfer (CT) involves displacement of the electronic charge from the ligands to the metal or *vice versa* and can be itself of a number of types.

In metal complexes, charge-transfer transitions are classified according to the direction of movement of charge in the excited state compared to the ground state (**Figure 4**).[18,19] For example, metal-to-ligand charge transfer (MLCT) is defined as the promotion of an electron from a d orbital of the metal to a π^* orbital of the ligand.[20] Ligand-to-metal charge transfer (LMCT) refers to an electronic transition from an orbital of the ligand to an orbital of the metal.[21] The promotion of an electron between two orbitals both localized on the ligand such as π-π^* transitions can be define as LC, ligand-centered or intraligand transitions.[22,23] Furthermore, metal, centered transitions (MC) may be observed in which the participating MOs are localized predominantly on the metal centre and involve electron promotion between two orbitals of the metal.[24,25]

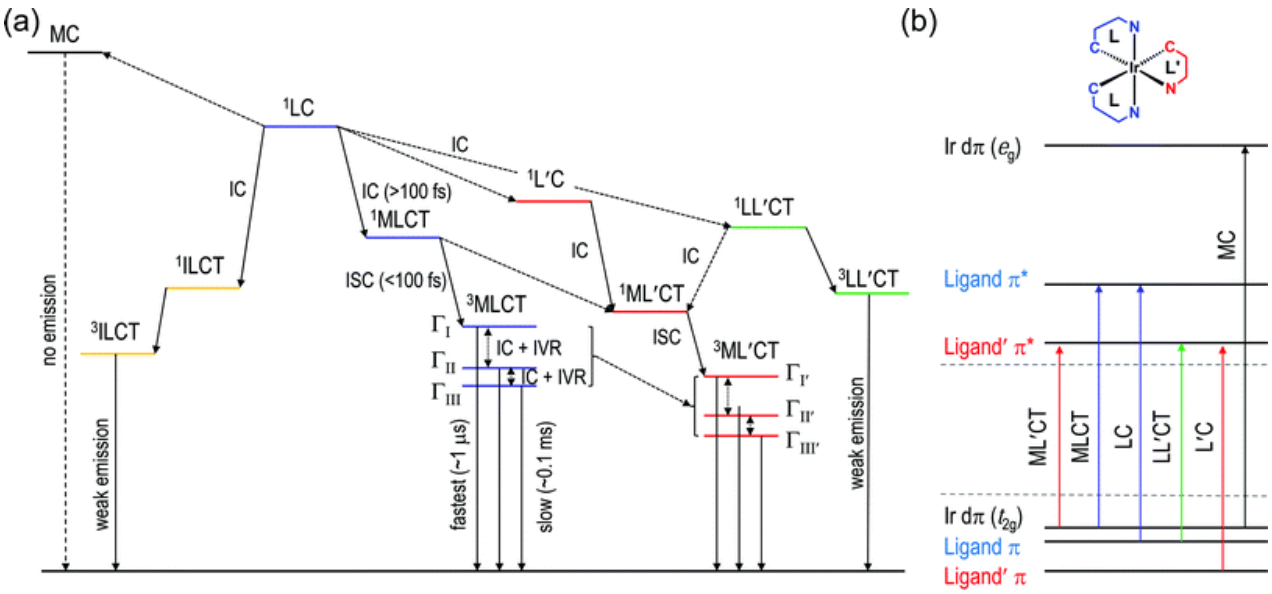

Figure 4. Representation of electronic transitions for an iridium d^6 complex (right) [26]

2. Heavy-Metal Complexes

Aside from metalloporphyrins, the first luminescent heavy-metal complex to be discovered was $[Ru(bpy)_3]^{2+}$, reported by Paris and Brandt in 1959 (bpy = 2,2'-bipyridine).[27] Its emission was attributed to an ^{3}MLCT transition from the d orbital of the metal centre to the π* of the 2,2´-bipyridine ligand (**Figure 5**).

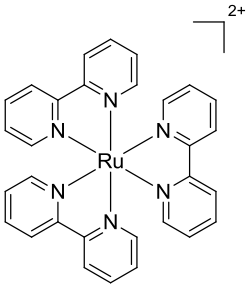

Figure 5. Structure of $[Ru(bpy)_3]^{2+}$

The complex $[Ru(bpy)_3]^{2+}$ has been one of the most extensively studied heavy-metal complexes, and has been applied as a sensor for O_2, as a photosensitizer or photocatalyst, for example.[28,29,30] However, its poor solubility in organic solvents, due to the dicationic charge, is a limitation for some applications. Other d^6 metal ions can be used to prepare phosphorescent complexes, for instance, iridium(III) and rhodium(III) from group 9 of the periodic table, osmium(II), and rhenium(I) (**Figure 6**).

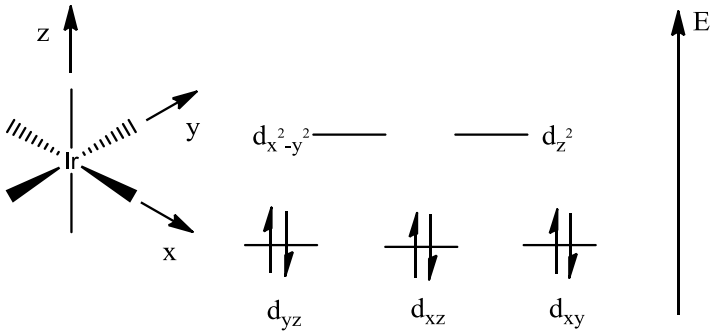

Figure 6. Representation of frontier molecular orbitals of a d^6 iridium complex

Just as d^6 complexes are generally *pseudo*-octahedral, d^8 complexes tend to be square-planar, particularly those from the 2nd and 3rd row transition metal series where the ligand field is strong, such as Pt(II), Pd(II), Ir(I) and Au(III) (**Figure 7**). This geometry involves three stabilized d orbitals, namely d_{xz}, d_{yz} and d_{z2}, one slightly destabilized, d_{xy}, and the final $d_{x^2-y^2}$ very strongly destabilized, hence accounting for the predominance of this geometry for d^8 ions.

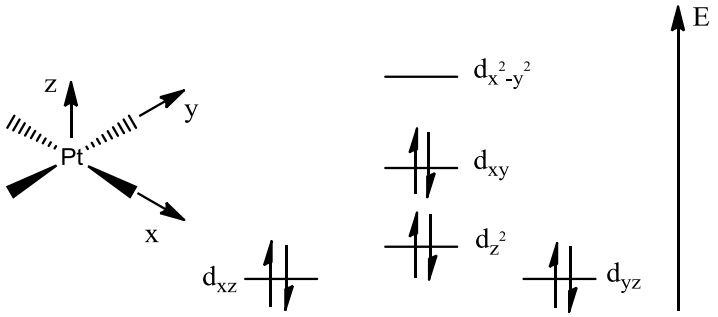

Figure 7. Representation of frontier molecular orbitals of an octahedral (low spin) d^8 platinum(II) complex

The population of the anti-bonding $d_{x^2-y^2}$ orbital by absorption of light involves an increase of the metal-ligand bond lengths and hence a deformation of the molecule in its excited state. The introduction of conjugated or electron-rich ligands, such as those incorporating aromatic rings, leads to new transitions: ligand-centered (π–π* or n-π*), MLCT and/or LMCT. Often, the energy of these excited states is lower than the lowest d-d excited state. However a higher-lying, but thermally accessible d-d excited state can quench the luminescence of the complexes. The emission properties are then closely related to the energetic gap (ΔE) between the d-d state and the other excited states (*e.g.* LC or MLCT). In fact, cyclometallated ligands like phenylpyridine (ppy) typically ensure a large ΔE thanks to the C–M bond (strong σ-donor) working synergistically with the M–N bond (strong π-acceptor) to generate a very strong ligand field.

2.1. Luminescence tuning of heavy-metal complexes

2.1.1. Effect of cyclometallation

Martin *et al.* reported the first synthesis of $[Ir(bpy)_3]^{3+}$in 1958 (**Figure 8**). The reaction between K_3IrCl_6 and bpy at 272 °C gave the final product in 20 minutes.[31] At 77K, $[Ir(bpy)_3]^{3+}$ has highly structured ligand-centered emission at λ_{em} = 440 nm and a lifetime of τ = 80 μs.[32] In degassed acetonitrile at 293 K, however, the lifetime is much shorter, τ = 1.2 μs, with a quantum yield of ϕ = 0.025 (**Table 1**)**.** This is indicative of an emissive state that is primarily ligand-centred with a relatively small element of MLCT character, unlike $[Ru(bpy)_3]^{2+}$, which exhibits emission from an MLCT excited state. [33]

Orthometallated $Ir(ppy)_3$ was first synthesised by Watts *et al.* in 1985 (**Figure 8**).[34] The reaction between 2,2'-phenylpyridine (ppy) and $IrCl_3.H_2O$ led to the formation of a dimer, which reacted again with 2-phenylpyridine to give the final product. The cyclometallated carbons induce a strong ligand field, which increases the energy of the metal-centred d-d* states and so attenuates their potentially deactivating ability.[35,36,37] In degassed DCM at 298 K, $Ir(ppy)_3$ shows an emission maximum at λ_{em} = 510 nm, red-shifted compared to $[Ir(bpy)_3]^{3+}$, and a luminescence lifetime, τ = 1.9 μs, with a quantum yield originally measured to be ϕ = 0.40 (**Table 1**).[38] More recent works suggests that this value was substantially underestimated, and latest work reports a value of 0.97.[39] The strong donor effect due to the cyclometallation of the phenyl ring involves a red-shift of the emission wavelength compared to $[Ir(bpy)_3]^{3+}$. The much higher quantum yield is attributed to more efficient participation of the metal in the excited state (*i.e.* MLCT rather than π-π*), which is necessary to ensure a high k_r value through relaxation of the spin-selection rule.[40]

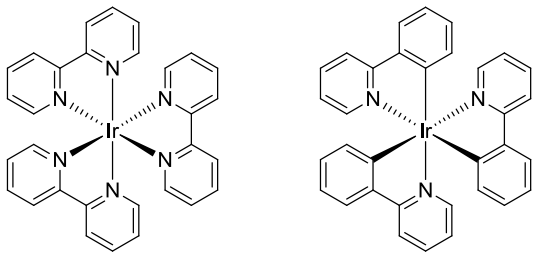

Figure 8. Representation of **$[Ir(bpy)_3]^{3+}$** and ***fac*-$Ir(ppy)_3$**

The complex Ir(dpyx)(dppy) is identified as the *bis*-tridentate isomer of the archetypal $Ir(ppy)_3$ (**Figure 9**). The comparison of these two systems showed that the *bis*-tridentate system displays a set of strong absorption bands in the visible region around λ_{abs} = 500 nm

characteristic of MLCT transitions, but they emit at significantly lower energy than *fac*- and *mer*-Ir(ppy)$_3$. This stabilisation is reasonable in that a lowering in energy of the acceptor ligand π* orbitals (LUMO) would be expected upon increased delocalization across the three aromatic rings of the N^C^N ligand. Furthermore, it has been shown that in iridium(III) complexes containing terdentate cyclometallating ligands, low-energy emission is achieved in cases of more extended π systems.[41,42,43]

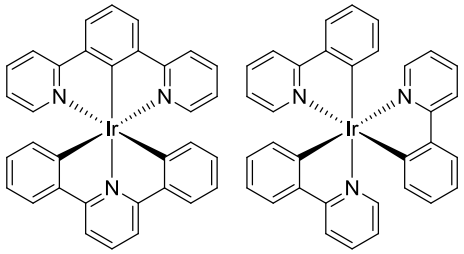

Figure 9. Representation of Ir(dpyx)(dppy) and *fac*-Ir(ppy)$_3$

Table 1. Photophysical data for [Ir(bpy)$_3$]$^{3+}$, Ir(dpyx)(dppy) and *fac*-Ir(ppy)$_3$ in degassed DCM solution at 298K [36,37,38]

	λ_{em} / nm	Φ_{PL}	τ / μs	k_r / 10^5 s^{-1}	k_{nr} / 10^5 s^{-1}
[Ir(bpy)$_3$]$^{3+}$	440	0.025	1.2	0.21	8.1
Ir(dpyx)(dppy)	585	0.21	3.8	0.55	2.1
fac-Ir(ppy)$_3$	510	0.40	1.9	2.1	3.2

2.1.2. Modulation of the HOMO-LUMO gap by functionalization

Chemical modification of the chromophoric cyclometallating ligand enables tuning of the emitting properties in a manner that can be readily understood in terms of the influence of electron-donating and -withdrawing substituents on the energies of the frontier orbitals. In fact, the level of the HOMO and / or the LUMO states can be modulated by introducing electron-rich or electron-deficient ligands (**Figure 10**). As an example, *fac*-Ir(ppy)$_3$ displays an emission maximum of λ_{em} = 508 nm in 2-MeTHF, but for the derivative incorporating two fluorine atoms in the phenyl ring (positions 4 and 6), λ_{em} = 466 nm. The F atoms destabilize the level of the HOMO and thus increase the HOMO-LUMO energy gap. In contrast, the introduction of an electron-rich aryl unit will increase the energy of HOMO level, thus reducing the gap. For example, the emission of *fac*-Ir(thpy)$_3$ is red-shifted compared to *fac*-Ir(ppy)$_3$: λ_{em} = 545 nm in DCM.[43,44,45]

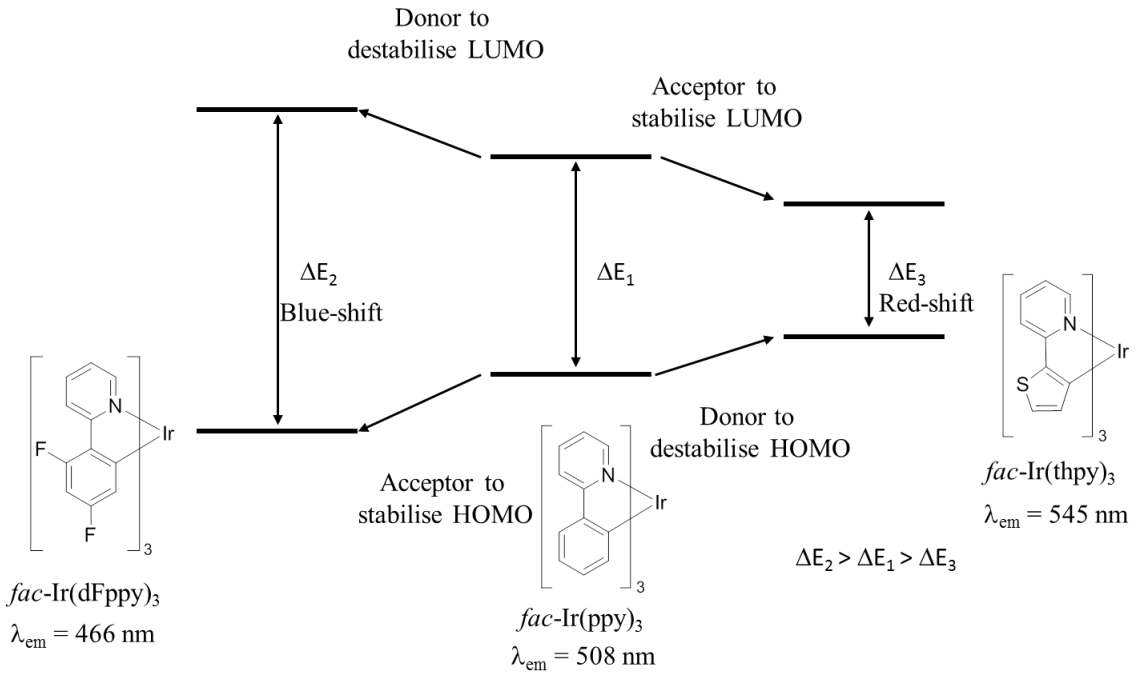

Figure 10. Modulation of the HOMO / LUMO level by functionalization of the C^N ligand.[43,44,45]

2.1.3. Effect of Symmetry

The photophysical properties of a complex depend on the metal, the ligand, its geometry and also its symmetry. For example, facial and meridional isomers may have different properties. In the case of a *tris*-phenylpyridine complex, the *fac* isomer is that in which the three pyridyl rings lie on one face of the octahedron (and the metallated carbons necessarily therefore on the other), whereas in the *mer*, they lie on a meridian.

The meridional isomers of *tris*-cyclometallated metal complexes exhibit photophysical characteristics different from those of their facial analogues.[44,44,45] For example, the emission in *mer*-Ir(tpy)$_3$ occurs as a single intense band at 550 nm whereas *fac*-Ir(tpy)$_3$ shows an emission at 510 nm (**Table 2**). Relative to their facial isomers, *mer*-iridium complexes are easier to oxidize and show a broader red-shifted emission.[45] The broad emission spectra are indicative of a large geometric distortion in the excited state. This may include an increase in length of the already long mutually *trans* Ir–C bonds, consistent with the observation of photolytic cleavage of one of these bonds and subsequent isomerisation to the facial isomer.[43] At room temperature, the *mer*-isomers of the phenylpyridyl derivatives also have much lower luminescent quantum yields and shorter emission decay lifetimes than their facial counterparts. The poor luminescence efficiency is attributed to the high non-radiative decay rates associated with the occurrence of the photoisomerisation process.[46] To conclude, facial

complexes are more studied in the literature because of their better luminescence properties and higher photochemical and thermal stabilities compared to the meridional complexes.

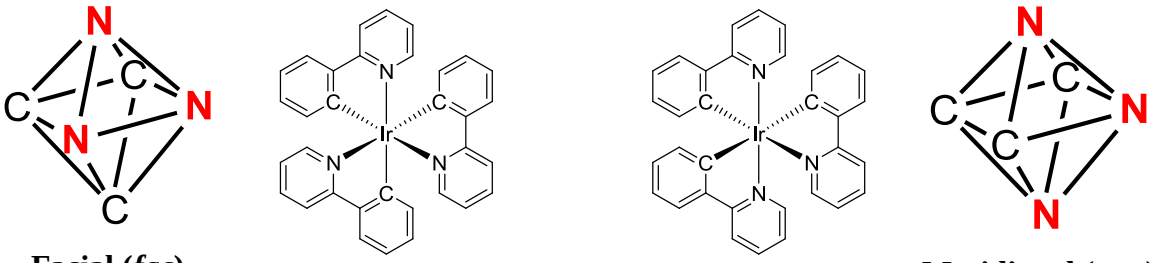

Figure 11. Representation of *fac*-Ir(ppy)$_3$ (left) and *mer*-Ir(ppy)$_3$

Table 2. Photophysical data of facial and meridional Ir(ppy)$_3$, Ir(tpy)$_3$ and Ir(4,6dfppy) in degassed DCM solution at 298K [43,44,45]

	λ_{em} / nm		Φ_{PL}		τ / μs		k_r / 10^5 s^{-1}		k_{nr} / 10^5 s^{-1}	
	fac-	*mer*-	*fac*-	*mer*-	*fac*-	*mer*-	*fac*	*mer*-	*fac*-	*mer*-
Ir(ppy)$_3$	510	512	0.40	0.036	1.9	0.15	2.1	2.4	3.2	64
Ir(tpy)$_3$	510	550	0.50	0.051	2.0	0.26	2.5	2.0	2.5	36
Ir(4,6dfppy)	468	482	0.43	0.053	1.6	0.21	2.7	2.5	3.6	45

2.2. Applications

2.2.1. OLEDs

One of the main applications of phosphorescent complexes is as emitters for organic light-emitting diodes (OLEDs). In order to be usefully applied in OLEDs, heavy-metal complexes must show good phototophysical and thermal stabilities, a high phosphorescence quantum efficiency, relatively short phosphorescence lifetimes, and the potential for facile colour tuning through ligand structure control. The first example of OLEDs operating at practicable voltages was reported by Tang and VanSlyke in 1987.[47] In 1998, Baldo *et al.* and Ma *et al.* independently reported the use of phosphorescent transition metal complexes in the emissive layer of OLEDs.[48,49] A typical OLED device with multilayer structure is depicted in **Figure 12**.[50] The device is composed of layers of organic materials stacked between an anode, such as indium tin oxide (ITO), and a metallic cathode, such as Al/LiF or Ag/Mg/Ag. The devices are typically comprised of the following layers:

(1) Electron-transporting layer (HTL), such as *tris*(8-hydroxyquinolate) aluminum (Alq_3).

(2) Emissive layer (EML), in which an emissive dopant is doped into the host material. The singlet and triplet levels of the host should be higher than those of the dopant in order to prevent undesired reverse energy transfer from the dopant to the host and to confine the triplet excitons in the emissive layer. In this regard, carbazole compounds, such as *N*,*N*'-dicarbazolyl-4-4'-biphenyl (CBP), are commonly used as host materials.

(3) Exciton blocking layer, such as 2,9-dimethyl-4,7-diphenyl-1,10-phenanthroline (BCP), which confines excitons within the organic emissive layer for improving the electroluminescence quantum efficiency.

(4) Hole-transporting layer (HTL), such as *N*,*N*'-*bis*(naphthalene-1-yl)-*N*,*N*'-bis(phenyl)-benzidine (NBP).

Devices that incorporate phosphorescent – as opposed to fluorescent – dopants show a great increase in the performance in terms of efficiency.[51,52] The formation ratio of singlet and triplet states in electroluminescence is 1:3. Fluorescence is the emission of a photon from a singlet excited state. In contrast, phosphorescence involves radiative relaxation from triplet states. Then phosphorescent OLED internal efficiency can, in principle, be increased as high as 100% whereas fluorescent OLEDS can only reach 25%.

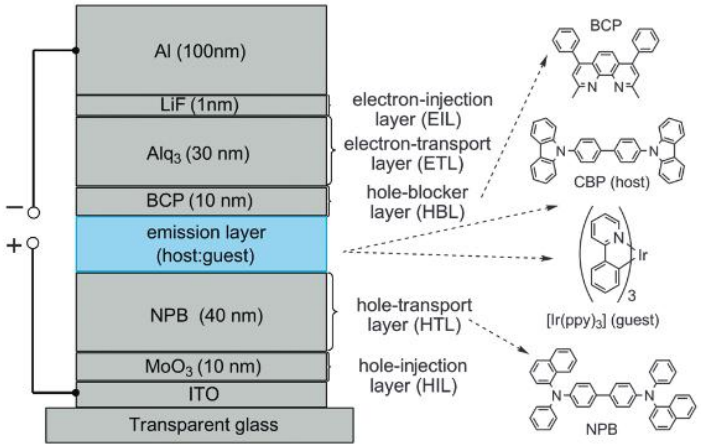

Figure 12. Schematic of a multilayer OLED including a hole injection/transport layer (HIL/HTL), an emissive layer (host/guest), a hole blocker layer (HBL) and finally transporter/injection layers (ETL/EIL)[51]

Iridium complexes of cyclometallated arylpyridine ligands have attracted a great deal of interest as OLED phophors, for example, $Ir(ppy)_3$, $Ir(dFppy)_2(pic)$, and $Ir(piq)_2(acac)$ as green, blue, and red emitters, respectively (ppyH = 2-phenylpyridine, F_2ppyH = 2-(2,4-

difluorophenyl)pyridine; piqH = 1 phenylisoquinoline; picH = picolinic acid; acacH = 2,4-pentanedione).[53,54,55,56,57]

2.2.2. Bio-imaging and bio-sensors

Heavy metal-complexes have interesting behaviour for application in bio-imaging. Compared to fluorescent organic molecules, which have a luminescence lifetime on the nanosecond scale, heavy-metal complexes show phosphorescence emission with a lifetime in the range of microseconds. This long lifetime allows an easy discrimination of phosphorescence from the fluorescent background of the cell or tissue sample on the basis of the timescale.

Organic or biological dyes (*e.g.* green fluorescent protein, GFP) are mostly used in confocal microscopy at present, but there are still disadvantages such as a short fluorescence lifetime, self-quenching effects, high photobleaching rate, and strong pH dependence in some cases.[58] Lanthanide(III) complexes show a long luminescence lifetime (μs to milliseconds) in the visible (*e.g.* Eu and Tb) or NIR (*e.g.* Yb, Nd) regions of the spectrum.[59] However, free lanthanides are highly toxic, and so suitable complexes must show a high stability with respect to metal ion dissociation, which demands the use of macrocyclic or highly polydentate ligands. Direct excitation of many lanthanide ions is problematic due to low ε values, and instead an additional chromophore must be incorporated into the complex to absorb and subsequently transfer energy to the lanthanide.

In order to be usefully applied in life sciences, luminescent heavy-metal complexes require certain attributes such as good stability and solubility in water, good photophysical properties and a low toxicity in cells. In the field of bio-imaging, a large Stokes shift has two-fold importance: to prevent self-quenching (*i.e.* the re-absorption of emitted light by neighbouring fluorophores), and to distinguish the emission of the fluorophore from autofluorescence (*i.e.* emission from endogenous fluorophores such as DNA, NADPH, aromatic amino acids), which, while itself useful in imaging, can interfere with desired fluorophore emission. Typically, autofluorescence Stokes shifts are small (tens of nm) and large Stokes shift fluorophores allow autofluorescence to be filtered out without losing signal intensity. Due to their MLCT transition, inorganic complexes show large Stokes shifts (as discussed earlier subject to the caveat about the strict definition of Stokes shift), and are thus potentially very attractive probes for bio-imaging.

Heavy-metal complexes show good photophysical properties in degassed solution, with notable quantum yields and lifetimes in the range of μs.[60,61] In the presence of oxygen, quantum yields and lifetimes can decrease by a factor of 60 compared to the values in degassed solutions.[62] This phenomenon occurs by an efficient energy transfer from the triplet excited stated of the molecule T_1 to the triplet ground state of the oxygen. The luminescence of the complex is quenched and a singlet state oxygen($^1\Delta_g$) is formed.(**Figure 13**).[63] Oxygen concentration is then quantified according to the changes in the luminescence intensity and in the lifetime of the complex.[64]

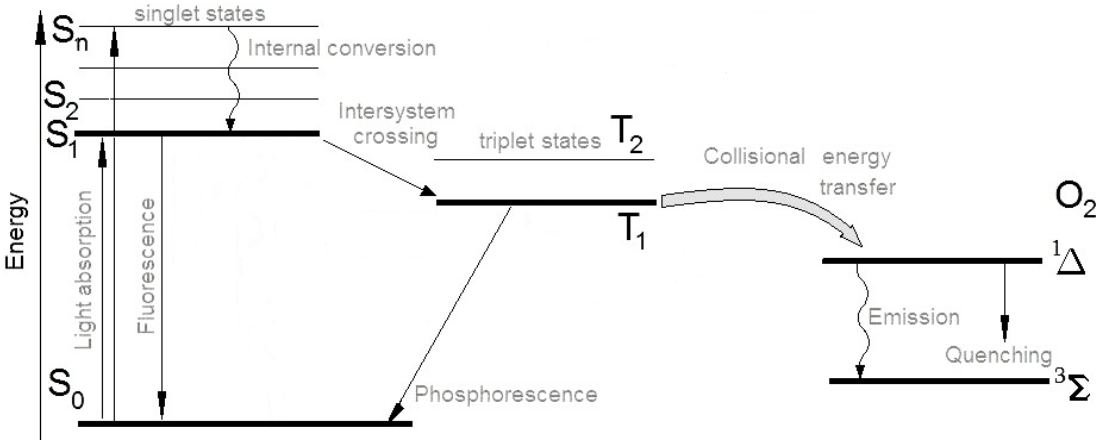

Figure 13. Effect of the triplet oxygen on the emission

Tobita *et al*. developed a small-molecule oxygen sensor (C343-Pro4-BTP) that uses coumarin 343 as an oxygen-insensitive fluorophore and the iridium complex BTP as an oxygen-sensitive phosphor (**Figure 14**).[65] The blue fluorescence of the coumarin is insensitive to O_2, having a short lifetime, whereas the red phosphorescence of the Ir(III) complex is quenched by O_2, as it has a long excited state lifetime. The ratio of the fluorescence to the phosphorescence of the C343-Pro4-BTP showed a quantitative dependence on the oxygen concentrations in a DMPC membrane as well as in solution. Oxygen quenching experiments on C343-Pro4-BTP in HeLa cells demonstrated the potential of the molecular probe for quantitative mapping of local oxygen levels in living cells and tissues.

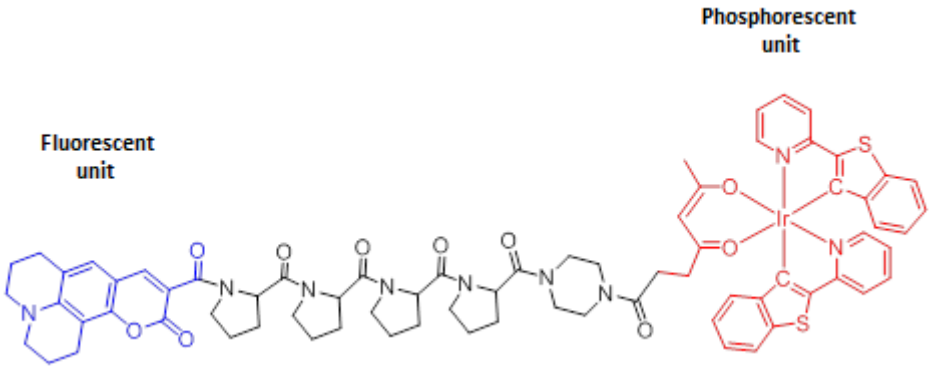

Figure 14. Iridium complex bearing a coumarin unit used for imaging O_2 in cells [62]

A chemosensor is generally defined as a combination of two units: a receptor unit and a signaling unit.[66,67] The receptor unit can selectively bind the analytes. The signaling units can record the interaction between receptors and analytes by modification of the luminescence properties. Phosphorescent heavy-metal complexes can act as signaling units, emitting light that is modulated in response to the analyte-binding process.

To date, several approaches have been reported for linking the receptor to the phosphorescent signaling unit. One approach involves linking the receptor to the ligand of a complex through a spacer (**Figure 15**). It is defined as ‘‘receptor–σ-signaling unit approachs’’ which involves switchable phosphorescent chemosensors.[62,63]

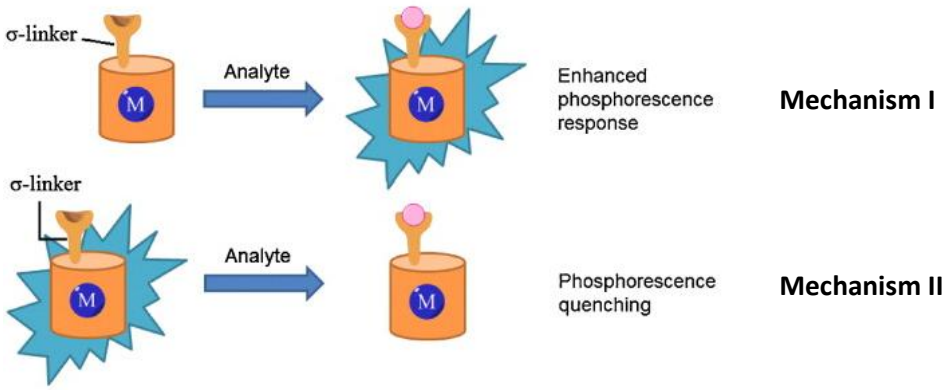

Figure 15. ‘‘receptor–σ-signaling unit approach to the analyte’’ [63]

Furthermore, the receptor can be conjugated to a ligand without a spacer. This approach is called the ‘‘receptor–conjugated signaling unit approach’’ (**Figure 16**). By comparison with ‘‘receptor–conjugated signaling unit approach’’, phosphorescence can be modulated by its intensity and also by its emission wavelength. To date many ratiometric phosphorescent chemosensors have been developed by this route. Finally, an irreversible

chemical reaction between a heavy-metal complex and analytes is possible. This approach is called ‘‘chemodosimeter approach’’. Ratiometric phosphorescence probes could be easily developed by this approach.

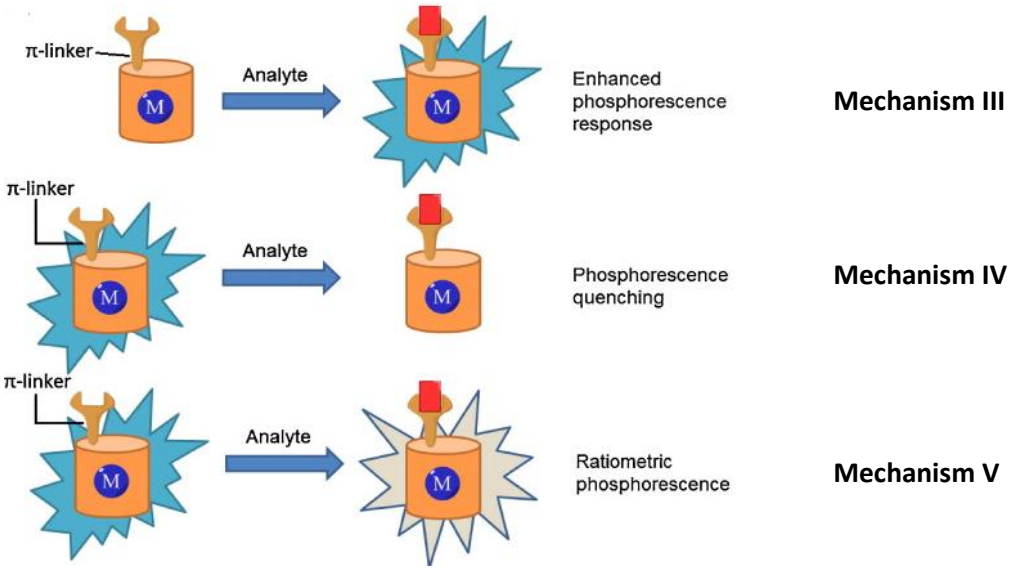

Figure 16. “receptor–conjugated signaling unit approach’’ [62]

Secondly, the excited state properties of phosphorescent heavy-metal complexes are very rich and different excited states can lead to different emission properties. If the receptor is connected to the ligand by a spacer, or if a specific recognition site is incorporated into the ligand, the interaction of the receptor with the analyte will perturb the energy levels of the excited states. This will induce interconversion among the different charge-transfer states, thereby producing a change in phosphorescent signal and realizing the detection (mechanism II). This mechanism II of phosphorescent chemosensors is usually achieved by the ‘‘receptor–conjugated signaling unit approach’’ for linking receptor and signaling unit. The third kind of mechanism is based on fluorescence resonance energy transfer (**FRET**) (mechanism III), which is dependent on a change in the energy transfer between energy donor and acceptor after binding with analyte.

For the d^8 and d^{10} heavy-metal complexes, there exists intermolecular metal–metal interactions (such as Pt···Pt and Au···Au), which can significantly influence the excited state properties of complexes, such as the formation of ^{3}MMLCT or ^{3}LMMCT excited states.[68] If the binding of complexes with analytes influences the metal-metal interaction, the emission properties can be changed. Utilizing this mechanism (mechanism IV), some novel

phosphorescent chemosensors can be designed. The phosphorescent emission of heavy-metal complexes is sensitive to the local environment. If binding of heavy-metal complexes with analyte changes local surroundings and leads to a change in phosphorescent emission, the detection can be realized (mechanism V). This mechanism is often utilized to design phosphorescent probes for biomolecules.

In 2012, Lee *et al.* synthesized and studied a new iridium complex bearing a 4-(dimesitylboryl)benzoate as chemosensor.[69] At room temperature, the complex emits a weak emission at λ_{max} = 615 nm. The quenching of the luminescence of the complex was attributed to a photoinduced electron transfer (PET). By addition of fluorine, the phosphorescence of the iridium complex turns "on" as the emission intensity increases by a factor of 10. The binding of receptor with analyte (F^-) can inhibit the PET and restore the emission. Other examples showing the opposite effect (the addition of analyte inducing PET and quenching the emission of the complex) have already been developed. The ''receptors-signaling unit approach'' for linking receptor and signaling unit is usually used for designing PET-based phosphorescent chemosensors.

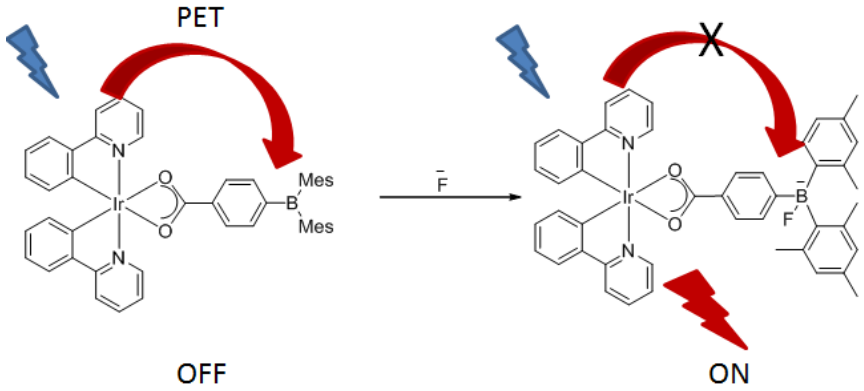

Figure 17. Representation of an OFF /ON Iridium complex[66]

In 2014, Wong *et al.* synthesized and studied an iridium complex bearing a *tris*-(2-pyridylmethyl)amine ligand as a Zn^{2+} receptor.[70] The interaction between the Zn^{2+} ion and the iridium complex will modify the emission properties of the complex. In fact, the free iridium complex emits blue light (λ_{em}= 495 nm), whereas the binding of a metal ion will produce a green light at around λ_{em} = 555 nm. Zn^{2+} ions involve a suppression of the photoinduced electron transfer by binding the complex.

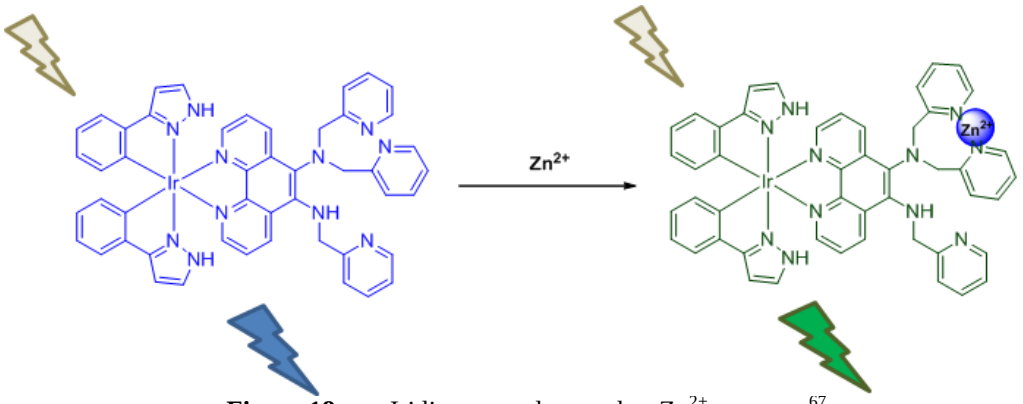

Figure 18. Iridium complex used as Zn^{2+} receptor [67]

3. Thesis objectives:

The objectives of this PhD were to synthesize new luminescent heavy-metal complexes for applications in OLEDs or bio-imaging. The manuscript is composed of four chapters, with a bibliographic section for each chapter.

Chapter 2 will describe the synthesis of new *tris*-cyclometallated and *bis*-cyclometallated iridium complexes incorporating more extended chromophoric units. The synthesis was performed by functionalization of thiophene-containing iridium complexes by a palladium-catalyzed C–H activation on the cyclometallated thienyl ring. This project was done in collaboration with Dr. Henri Doucet (University of Rennes 1). The absorption and emission properties of the resulting complexes were studied to observe the influence of the chromophore on the properties.

In order to obtain better emitters, new rigid heavy-metal complexes with tetradentate ligands will then be described in Chapter 3. The synthesis of tetradentate platinum(II) complexes incorporating a C^N^N^C ligand will be first developed and their photophysical properties studied. An investigation of luminescent tetradentate palladium complexes and a brief exploration into gold complexes with the same ligands will then be discussed.

Chapter 4 will be devoted to the synthesis and the study of new iridium(III) complexes incorporating (iso)-quinolylbenzimidazole and 2,2´-bisbenzimidazole ligands. Owing to the presence of azole rings, the excited-state propertie of these compounds are pH-sensitive, which may render them of potential interest in future sensory applications.

Finally, Chapter 5 presents the synthesis and the photophysical studies of new cyclometallated iridium(III) and platinum(II) complexes bearing new ancillary ligands, including those with phosphorus or sulfur ligating atoms in place of the nitrogen or oxygen atoms more commonly used in other studies to date.

4. References

[1] J. Michl, *Top. Curr. Chem.*, 1974, **46**, Photochemistry.

[2] P. W. Atkins, "*Physical Chemistry*", Fifth Edition, Oxford University Press.

[3] G. Gerhard, *Entropy*, 2010, **12**, 1975.

[4] G. B. Porter, *Intr. to Inorg. Photochem.*, 1983, **60**, 785.

[5] D. C. Harris, M. D. Bertolucci, *Symmetry and Spectroscopy*., 1978, Oxford University Press.

[6] M. Kasha, *Discuss. Faraday Soc.*, 1950, **9**, 14.

[7] M. L. Muro, A. A. Rachford, X. Wang, F. N. Castellano, *Top. Organomet. Chem.*, 2010, **29**, 159.

[8] J. R. Lakowicz, "*Principles of Fluoresence Spectroscopy*", Plenum Press, 1999.

[9] P. Borrell, "*Photochemistry: A Primer*", Edward Arnold Ltd., London, 1973.

[10] A. Gilbert, J. Baggot, "*Essentials of Molecular Photochemistry*", Blackwell Scientific Publications, Oxford, 1991.

[11] J. R. Lakowicz, *Principles of Fluorescence Spectroscopy*, 1983, Plenum Press, New York.

[12] B. Valeur, M. Berberan-Santos, "*Molecular Fluorescence: Principles and Applications*", 2012, Wiley-VCH.

[13] R. J. Lakowicz, "*Principles of Fluorescence Spectroscopy*", Kluwer Academic, Plenum Publishers, 1999.

[14] G. A. Crosby, R. J. Watts, D. H. Carstens, *Science*, 1970, **170**, 1195.

[15] V. Balzani, F. Bolletta, M. T. Gandolfi, M. Maestri, *Top. Curr. Chem.*, 1978, **75**, 1.

[16] M. K. De Armond, C. M. Carlin, *Coord. Chem. Rev.*, 1981, **36**, 325.

[17] V. Balzani, A. Juris, M. Venturi, S. Campagna, S. Serroni, *Chem. Rev.*, 1996, **96**, 759.

[18] T. J. Meyer, *Pure Appl. Chem.*, 1990, **62**, 1003.

[19] W. E. Jones, S. M. Baxter, G. F. Strouse, T. J. Meyer, *J. Am. Chem. Soc.*, 1993, **115**, 7363.

[20] S. Lamansky, P. Djurovich, D. Murphy, F. Abdel-Razzaq, H. E. Lee, C. Adachi, P. E. Burrows, S. R. Forrest, M. E. Thompson, *J. Am. Chem. Soc.*, 2001, **123**, 4304.

[21] C. K. Li, X. X. Lu, K. M. C. Wong, C. L. Chan, N. Zhu, V. W. W. Yam, *Inorg. Chem*., 2004, **43**, 7421.

[22] M. Polson, M. Ravaglia, S. Fracasso, M. Garavelli, F. Scandola, *Inorg. Chem.*, 2005, **44**, 1282.

[23] Y. You and S. Y. Park, *J. Am. Chem. Soc*., 2005, **127**, 12438

[24] M. Z. Hoffmann, *Ed. Inorg. Photchem.*, State of the Art. J. Chem. Educ. 1983, **60**, 784.

[25] A. W. Adamson, *Properties of Excited States*, 1983, **60**, 797.

[26] Y. You, W. Nam, *Chem. Soc. Rev.*, 2012, **41**, 7061-7084.

[27] J. P. Paris, W. W. Brandt, *J. Am. Chem. Soc.*, 1959, **81**, 5001.

[28] D. P. Rillema, D. S. Jones, H. A. Levey, *Chem. Commun.*, 1979, 849.

[29] A. Juris, V. Balzani, F. Barigelletti, S. Campagna, P. Besler, A. Von Zelewsky, *Coord. Chem. Rev.*, 1988, **84**, 85.

[30] V. Balzani, A. Credi, M. Venturi, *Molecular Devices and Machines*, A Journey into the Nanoworld, Wiley-VCH, Weinheim, 2003.

[31] B. Martin, G. M. Waind, *J. Chem. Soc*, 1958, 4284.

[32] C. M. Flynn and J. N. Demas, *J. Am. Chem. Soc,* 1974, **96**, 1959.

[33] J. L. Kahl, K. W. Hanck, K. DeArmond, *J. Am. Chem. Soc,* 1991, **113**, 3984.

[34] K. A. King, P. J. Spellane, R. J. Watts, *J. Am. Chem. Soc.*, 1985, **107**, 1431.

[35] W. Sotoyama, T. Satoh, H. Sato, A. Matsuura, N. Sawatari, *J. Phys. Chem. A*, 2005, **109**, 9760.

[36] S. W. Lai, M. C. W. Chan, Y. Wang, H. W. Lam, S. M. Peng, C. M. Che, *J. Organometallic Chem.*, 2001, **133**, 617-618.

[37] J. A. G. Williams, A. Beeby, E. S. Davies, J. A. Weinstein, C. Wilson, *Inorg. Chem.*, 2003, **42**, 8609.

[38] A. B. Tamayo, B. D. Alleyne, P. I. Djurovich, S. Lamansky, I. Tsyba, N. N. Ho, R. Bau, M. E. Thompson, *J. Am. Chem. Soc.*, 2003, **125**, 7377.

[39] T. Sajoto, P. I. Djurovich, A. B. Tamayo, J. Oxgaard, W. A. Goddard III, M. E. Thompson, *J. Am. Chem. Soc.*, 2009, **131**, 9813-9822.

[40] H. Yersin, D. Donges; *Top. Curr. Chem.*, **2001**, *214*, 81.

[41] T. Yutaka, S. Obara, S. Oawa, K. Nozaki, N. Ikeda, T. Ohno, Y. Ishii, K. Sakai, M. Haga, *Inorg. Chem.*, 2005, **44**, 4737.

[42] M. Polson, S. Fracasso, V. Bertolasi, M. Ravaglia, F. Scandola, *Inorg. Chem.*, 2004, **43**, 1950.

[43] A. J. Wilkinson, A. E. Goeta, C. E. Foster, J. A. G. Williams, *Inorg. Chem.*, 2004, **43**, 6513.

[44] T. Karatsu, E. Itoh, S. Yagai, A. Kitamura, *Chem. Phys. Lett.*, 2006, **424**, 353-357.

[45] A. B. Tamayo, B. D. Alleyne, P. I. Djurovich, S. Lamansky, I. Tsyba, N. N. Ho, R. Bau, M. E. Thompson, *J. Am. Chem. Soc.*, 2003, **125**, 7377.

[46] T. Karatsu, T. Nakamura, S. Yagai, A. Kitamura, K. Yamaguchi, Y. Matsushima, T. Iwata, Y. Hori, T. Hagiwara, *Chem. Lett.*, 2003, **32**, 886.

[47] C. W. Tang, S. A. VanSlyke, *Appl. Phys. Lett.*, 1987, **51**, 913.

[48] M. A. aldo, D. F. O' rien, Y. You, A. Shoustikov, S. Sibley, M. E. Thompson, S. R. Forrest, *Nature*, 1998, **395**, 151.

[49] Y. Ma, H. Zhang, J. Shen, C.-M. Che, *Syn. Met.*, 1998, **94**, 245.

[50] H. Yersin, *Top. Curr. Chem.*, 2004, **241**, 1.

[51] H. Yersin, in Highly Efficient OLEDs with Phosphorescent Materials, ed. H. Yersin, Wiley-VCH Verlag GmbH & Co. KgaA, Weinheim, Germany, 2008.

[52] M. A. Baldo, D. F. O'Brien, Y. You, A. Shoustikov, S. Sibley, M. E. Thompson, S. R. Forrest, Nature, 1998, **395**, 151-154.

[53] S. Lamansky, P. Djurovich, D. Murphy, F. Abdel-Razzaq, R. Kwong, I. Tsyba, M. Bortz, B. Mui, R. Bau, M. E. Thompson, *Inorg. Chem.*, 2001, **40**, 1704.

[54] M. Cocchi, D. Virgili, V. Fattori, D. L. Rochester, J. A. G. Williams, *Adv. Funct. Mater.*, 2007, **17**, 285.

[55] J. Kalinowski, M. Cocchi, D. Virgili, V. Fattori, J. A. G. Williams, *Chem. Phys. Lett.*, 2006, **432**, 110.

[56] C. Adachi, M. A. Baldo, M. E. Thompson, S. R. Forrest, *J Appl. Phys.*, 2001, **90**, 5048.

[57] W. Sotoyama, T. Satoh, N. Sawatari, H. Inoue, *Appl. Phys. Lett.*, 2005, **86**, 153505.

[58] (a) R. P. Haugland, *The Handbook*, A Guide to Fluorescent Probes and Labeling Technologies, Molecular Probes Inc., Eugene, Oregon, 10th edn, 2005, 397.
(b) H. Kobayashi, M. Ogawa, R. Alford, P. L. Choyke, Y. Urano, *Chem. Rev.*, 2010, **110**, 2620.
(c) R. P. Haughland, *Handbook of fluorescent probes and research chemicals*, Molecular Probes Inc., Eugene, OR, 9th edn, 1996.
(d) R. Y. Tsien, *Angew. Chem., Int. Ed.*, 2009, **48**, 5612.

[59] (a) J. C. G. Bünzli, *Chem. Rev.*, 2010, **110**, 2729.
(b) S. V. Eliseevaa, J. C. G. Bünzli, *Chem. Soc. Rev.*, 2010, **39**, 189.
(c) C. P. Montgomery, B. S. Murray, E. J. New, R. Pal, D. Parker, Acc. Chem. Res., 2009, **42**, 925.
(d) J. N. Elizabeth, P. David, G. S. David, W. W. James, *Curr. Opin. Chem. Biol.*, 2010, **14**, 238.
(e) E. G. Moore, A. P. S. Samuel, K. N. Raymond, *Acc. Chem. Res.*, 2009, **42**, 542.

[60] S. Obara, M. Itabashi, S. Tamaki, Y. Tanabe, Y. Ishili, K. Nozaki, M. Haga, *Inorg. Chem.*, 2006, **45**, 8907.

[61] C. S. K. Mak, A. Hayer, S. I. Pascu, S. E. Watkins, A. B. Holmes, A. Kçhler, R. H. Friend, *Chem. Commun.*, 2005, 4708.

[62] J. H. Burroughes, D. D. C. Bradley, A. R. Brown, R. N. Marks, K. Mackay, R. H. Friend, P. L. Burns, A. B. Holmes, *Nature*, 1990, **347**, 539.

[63] M. S. Lowry, S. Bernhard, *Chem. Eur. J.*, 2006, **12**, 7970.

[64] M. C. De Rosa, P J. Mosher, C. E. B. Evans, R. J. Crutchley, *Macromol. Symp.*, 2003, **196**, 235.

[65] T. Yoshihara, Y. Yamaguchi, M. Hosaka, T. Takeuchi, S. Tobita, *Angew. Chem. Int. Ed.*, 2012, **51**, 4148-4151.

[66] Q. Zhao, F. Li, C. Huang, *Chem. Soc. Rev.*, 2010, **39**, 3007.

[67] Q. Zhao, C. Huang, F. Li, *Chem. Soc. Rev.*, 2011, **40**, 2508-2524.

[68] V. W. W. Yam, E. C. C. Cheng, *Chem. Soc. Rev.*, 2008, **37**, 1806.

[69] R. S. Vadavi, H. Kim, K. M. Lee, T. Kim, J. Lee, Y. S. Lee, M. H.Lee, *Organometallics*, 2012, **31**, 31-34.

[70] D.-L. Ma, H.-Z. He, H.-J. Zhong, S. Lin, D. S.-H. Chan, L. Wang, S. M.-Y. Lee, C.-H. Leung, C.-Y. Wong, *ACS Appl. Mater. Interfaces*, 2014, **6**, 14008-14015.

CHAPTER TWO:

Thienyl Arylated Iridium *bis*- and *tris*-cyclometallated $Ir(C\hat{}N\text{-}Ar)_3$ and $Ir(Me\ ppy)_2(tta\text{-}Ar)$ Complexes

1. Arylated *facial* tris-cyclometallated thienylpyridine iridium complexes *fac*-Ir(thpy-Ar)$_3$

In the following section, the different procedures used for the preparation of the complex *fac*-Ir(thpy)$_3$ and its functionalized derivatives reported in the literature will be presented. The absorption and luminescence properties of these complexes will be discussed together with the effects of functionalization on these properties.

1.1. Synthesis of the precursor complex *fac*-Ir(thpy)$_3$

1.1.1. Classical method, first example of complex *fac*-Ir(thpy)$_3$

In 1994, Colombo *et al.* reported the first example of *tris*-cyclometallated 2-2′-thienylpyridine iridium complex *fac*-Ir(thpy)$_3$, **1** (**Scheme 1**).[1] This complex was obtained in 58 % yield by reacting the chloro-bridged dimer [Ir(thpy)$_2$(μ-Cl)]$_2$ with an excess of 2-2′-thienylpyridine ligand in the presence of $AgCF_3SO_3$.[2]

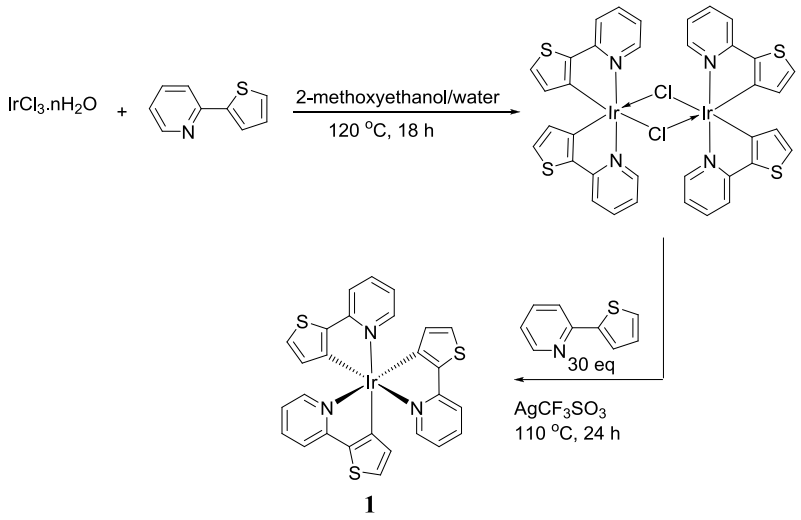

Scheme 1. Synthetic route for the formation of ***fac*-Ir(thpy)$_3$** [2]

The ^{1}H NMR spectrum of complex **1** shows a set of six signals corresponding to one thienylpyridine environment indicating that the three ligands are magnetically equivalent due to a C_3-fold symmetry axis of the molecule, which is consistent with a *facial* arrangement of the ligands.

1.1.2. Synthesis of the complex *fac*-Ir(thpy)$_3$ using alternative methods

In 2007, McGee *et al.* reported the preparation of *fac*-Ir(thpy)$_3$ at 90-115 °C using a multi-step procedure with longer reaction time starting from the chloro-bridged dimer (**Scheme 2**).[3] Dissolving the chloro-bridged dimer in acetonitrile produces the *mono-*

acetonitrile-*mono*-chloro complex **2**. The resulting complex was heated in acetonitrile in the presence of $AgPF_6$ to form the cationic *bis*-acetonitrile complex **3**. Starting from complex **3**, it was possible to prepare complex **1** in one or two steps depending on the solvent and the temperature used.

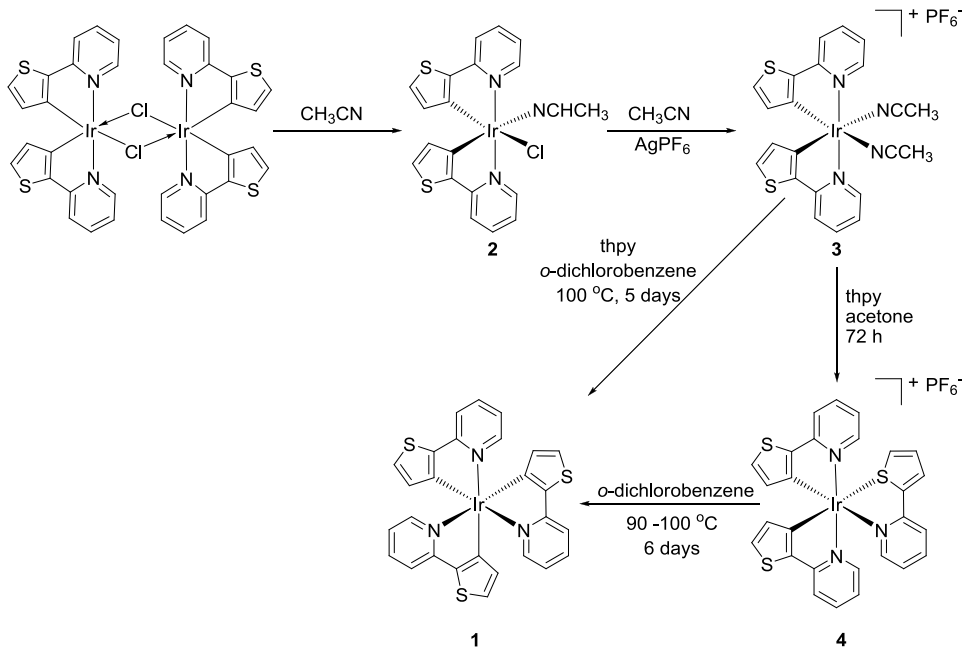

Scheme 2. McGee's synthetic route for the formation of ***fac*-Ir(thpy)$_3$** [3]

Heating **3** with thienylpyridine at 100 °C in *o*-dichlorobenzene for five days led to the formation of complex **1**. On the other hand, stirring complex **3** with an excess of 2-2′-thienylpyridine in acetone at room temperature for 72 h allowed the coordination of thienylpyridine through the lone pair of the sulfur atom to give the complex [Ir(*C*^*N*-thpy)$_2$(*S*^*N*-thpy)]PF_6, **4**. Heating **4** at 90-100 °C in *o*-dichlorobenzene for six days allowed the cyclometallation process to occur to give a mixture of complexes **1** and **4** in 2:1 ratio.

In our laboratory, the *fac*-Ir(thpy)$_3$ complex **1** was prepared with a slight modification of the two-step procedure reported by Colombo *et al.*[1] The metallic precursor $IrCl_3.nH_2O$ was reacted with an excess of 2,2′-thienylpyridine ligand in 2-ethoxyethanol to obtain the chloro-bridged dimer in 76 % yield. The dimer was then reacted with a slight excess of 2,2′-thienylpyridine (2.5 equivalents were used instead of 15 equivalents reported) in the presence of a base (K_2CO_3 instead of $AgCF_3SO_3$) in glycerol at reflux (200 °C). Complex **1** was isolated as an orange powder in 67 %.

1.2. Photophysical properties of complex *fac*-Ir(thpy)$_3$, 1

The absorption spectrum of complex **1** shows an intense band in the UV region at 300 nm corresponding to the π-π* transitions of the thienylpyridine ligand (**Figure 1**). A broad and moderately intense band is observed at 385 nm corresponding to the spin-allowed Metal-to-Ligand-Charge-Transfer ^{1}MLCT accompanied by a shoulder extending into the visible region corresponding to the spin-forbidden ^{3}MLCT.[1] Complex **1** presents a structured emission at 550 nm arising from a primarily LC ^{3}(π-π*) excited state. It has a photoluminescence quantum yield (ϕ) of 17 % and lifetime (τ) of 2.4 μs.

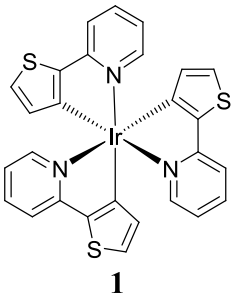

1

λ_{em} = 545 nm, ϕ = 17 %, τ = 2.4 μs.

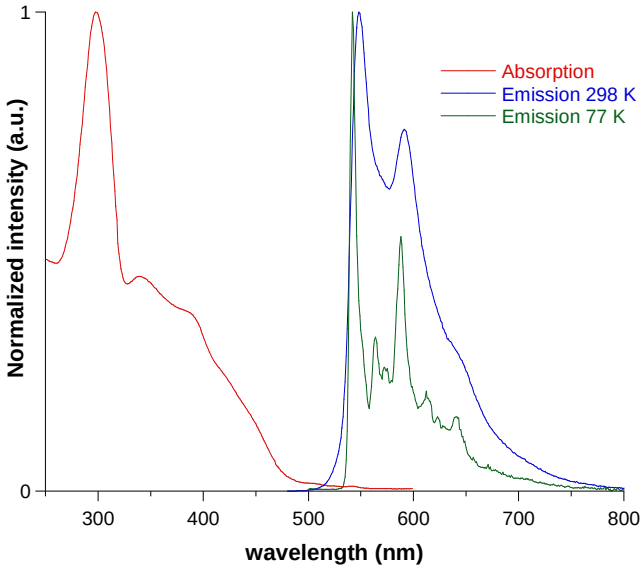

Figure 1. Absorption and emission spectra of 1 in CH_2Cl_2 at 298 K and in EPA solution at 77 K.

The luminescence properties of the complex *fac*-Ir(thpy)$_3$ (**1**) can be compared with that of the complex *fac*-Ir(ppy)$_3$, (**5**) having three cyclometallated phenylpyridine ligands. At 298 K, complex **5** presents a green emission originating from an MLCT excited state (**Figure 2**). The emission spectrum shows a featureless band at λ_{max} = 508 nm. In degassed DCM solution, complex **5** has a quantum yield of 100 % and lifetime τ = 1.6 μs.[4] Replacing the phenyl by the thienyl ring changes the emission color from green to orange. Complex **1** has a quantum yield which is much lower than that of complex **5** whereas it shows a longer lifetime (τ = 2.4 μs). Structural modification on the *C^N* ligand induces a change in the phosphorescence properties (emission wavelength, quantum yield and lifetime) as a result of changing the nature of the

excited state: the metal character in the excited-state decreases compared to **5** and becomes more ligand-centred with a concomitant reduction in k_r.

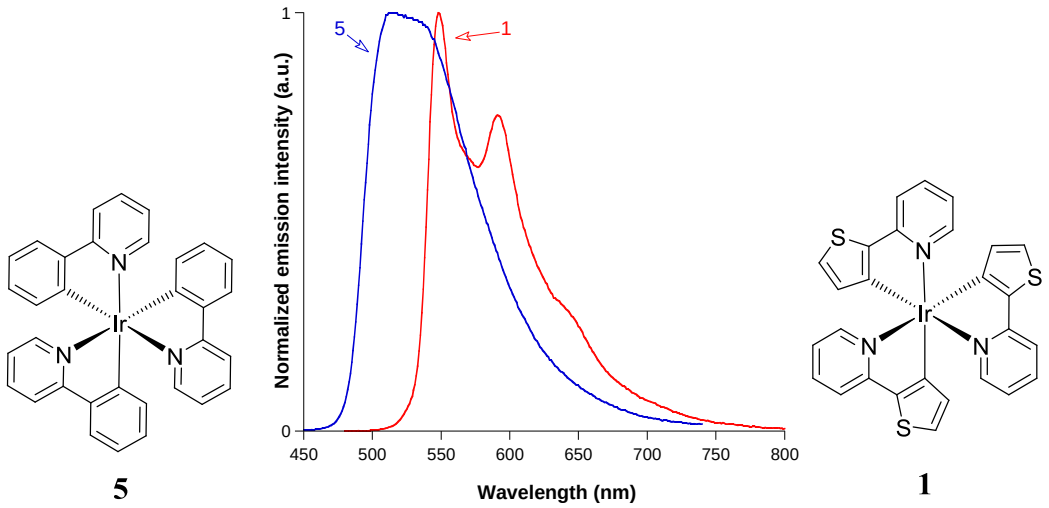

5 **1**

Figure 2. Emission spectra of complexes ***fac*-Ir(thpy)$_3$**, **1** and ***fac*-Ir(ppy)$_3$**, 5 in CH2Cl2 at 298K.

1.3. Synthesis and photophysical properties of functionalized *fac*-Ir(thpy)$_3$ complexes

1.3.1. Functionalization on the proligand

Few examples of functionalized *fac*-Ir(thpy)$_3$ derivatives have been reported. In 2003, Tsuboyama *et al.* showed that the substituted derivatives of *fac*-Ir(thpy)$_3$, **6**, **9** and **10** are accessible in a one-step procedure starting from Ir(acac)$_3$ and an excess of ligand in glycerol at reflux (**Figure 3**).[5] A new series of luminescent derivatives having yellow, orange and red colours have been prepared for application in OLEDs. The ligands were first prepared using Suzuki cross-coupling reaction between thienyl, 5-methylthienyl or benzothienyl boronic acids and the appropriate chloropyridine derivative.

In 2013, Lin *et al.* described the synthesis and the photophysical properties of the boryl-thienylpyridine iridium complexes **7** and **8**, for OLEDs applications (**Figure 3**).[6] The corresponding ligands were prepared using Stille palladium cross-coupling.

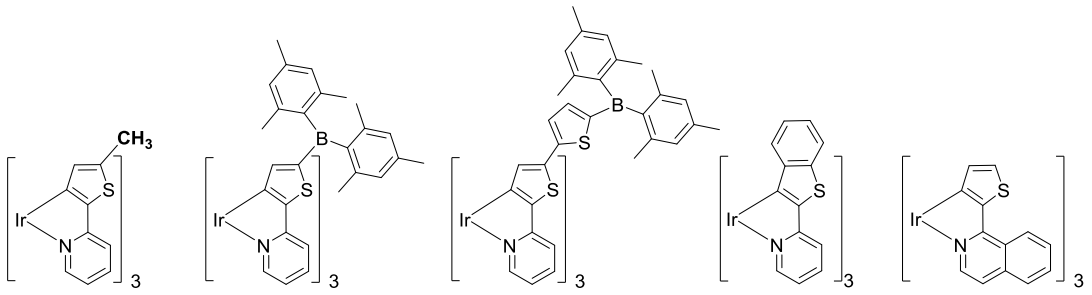

λ_{max} = 558 nm	λ_{max} = 700 nm	λ_{max} = 800 nm	λ_{max} = 596 nm	λ_{max} = 644 nm
τ = 0.99 µs	τ = 6.9 µs	τ = 6.2 µs	τ = 4 µs	τ = 0.74
Φ = 0.08	Φ = 0.396	Φ = 0.057	Φ = 0.12	Φ = 0.17
$Ir(5m\text{-}thpy)_3$	$Ir(DMSB\text{-}thpy)_3$	$Ir(DMSBth\text{-}thpy)_3$	$Ir(btpy)_3$	$Ir(tiq)_3$
6	**7**	**8**	**9**	**10**

Figure 3. Functionalised $Ir(thpy)_3$ complexes **6-10.** [6]

The complexes were substituted by electron-donor or -acceptor groups introduced at the thienyl or the pyridine rings, or *via* extended π-conjugated systems. Complex **6** is functionalized by the weak electron-donating methyl group on the C5 position of the thienyl ring, while complexes **7** and **8** bear strong electron-acceptor groups. Complexes **9** and **10** have extended π-conjugated systems due to the replacement of the thienyl ring by benzothienyl and the pyridine ring by isoquinoline.

Functionalization of the thpy ligand involves a modification of the photophysical properties. Introducing the methyl group on the C5 position of the thienyl ring of complex **6** results in a bathochromic shift of 8 nm in the emission wavelength compared to complex **1**. The photoluminescence quantum yield and lifetime are strongly influenced by this structural modification, the quantum yield decreased to 8 % and the lifetime decreased to 0.99 µs.[4]

The boryl group attached on the C5 position of the thiophene ring revealed a bathochromic-shift of 98 nm for complex **7** (λ_{em} = 643 nm) and 196 nm for complex **8** (λ_{em} = 741 nm), with respect to **1**. This substitution has also an influence on the photoluminescence quantum yield and lifetime of the resulting complexes (ϕ = 39.6 %, τ = 6.9 µs for complex **7** and ϕ = 5.7 %, τ = 6.2 µs for complex **8**).

Extending the π-conjugated system, by introducing aromatic rings to either the thienyl or the pyridyl part of the *C^N* ligand, also has an influence on the photophysical properties. Replacing the thienyl ring by a benzothienyl in complex **9** induces a bathochromic shift of 46 nm compared to complex **1**, while replacing the pyridyl ring by isoquinoline in complex **10** induces a bathochromic shift of 99 nm.[4] Extending the π-conjugated system changes the emission color from yellow-orange (compex **1**) to orange-red (complex: **9** λ_{em} = 596 nm and **10:** λ_{em} = 644 nm). The luminescence lifetime for complex **9** is increased to 4 µs while a decrease of the luminescence lifetime to 0.74 µs is observed for complex **10**. Interestingly, the

photoluminescence quantum yield is only weakly influenced by these structural modifications (ϕ (**8**) = 12 %, ϕ (**10**) = 12 %).

1.3.2. Functionalization using "*Catalysis- on-the-complex*"

Thiophene-containing *fac*-Ir(thpy)$_3$ complexes form an attractive class of luminophores.[7] They possess interesting phosphorescence properties that can be tuned by a simple modification of the thienylpyridine ligand. Developing a new synthetic strategy for the functionalization of this ligand would open the door for better modulation of the optical properties of the resulting complex.

An efficient and direct method to functionalize the cyclometallated ligands is the "*Chemistry-on the-complex*" strategy. This method was used in Rennes to prepare *tris*-styryl-phenylpyridine substituted Ir(III) complexes (**Scheme 3**). But the scope of the organic reactions that can be used is rather limited. Moreover, it is not always possible to control the selective *mono-*, *bis-* or *tris*-substitution in the presence of more than one reactive site on the complex such as in *tris*-cyclometallated Ir(III) complexes.[8a]

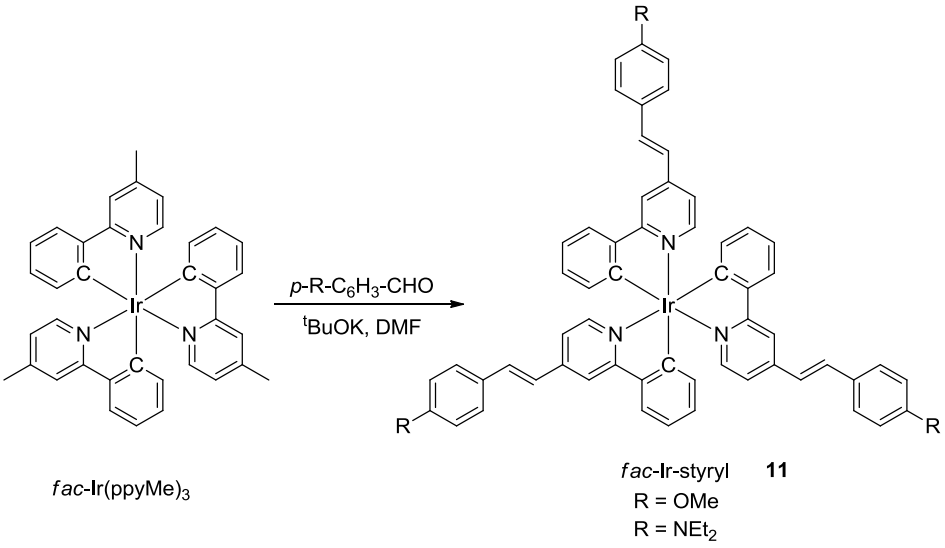

Scheme 3. Synthesis of *tris*-styryl-phenylpyridine iridium complexes[8a]

Catalytic reactions can be also a useful tool for the access to new luminophores that cannot be prepared using the classical organic reactions. The well-known cross coupling reactions (Suzuki, Negishi...) can lead to the functionalization of the complex by introducing different substituents. In addition, a C-C cross-coupling reaction between two organometallic species allows access to multi-nuclear complexes.

In 2009, Williams *et al.* reported the palladium-catalyzed Suzuki cross-coupling reaction between two cyclometallated iridium complexes to form a dinuclear complex with

interesting photophysical properties (**Scheme 4**).[9] This example shows that catalytic reactions can be applied directly on metallated ligands.

The two building blocks that are necessary for a Suzuki reaction were first prepared, the bromo-substituted *bis*-terdentate (N^N^N) iridium complex **12** and the iridium *bis*-terdentate Ir(*N^N^C*)(*N^C^N*)$^+$ complex **13** incorporating a boronic acid. The two complexes were coupled in the presence of $Pd(PPh_3)_4$ to produce the bimetallic complex **14** in 16 % yield. This example opens access to new classes of dinuclear complexes through performing catalytic reactions on the metallated ligands.

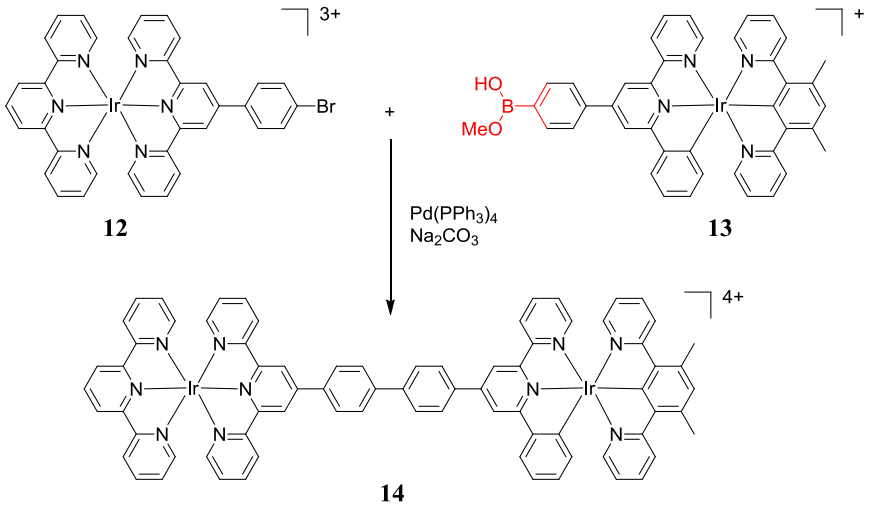

Scheme 4. Synthesis of dinuclear iridium complex **14** [9]

In 2012, Amouri reported the palladium-catalyzed Sonogashira cross-coupling reaction for the preparation of an iridium-polyoxometalate hybrid complex (**Scheme 5**).[8b] In this example, the heteroleptic iridium complex **15** incorporating two phenylpyridine ligands and picolinate ancillary ligand incorporating a terminal alkynyl group was prepared. The organotin polyoxometalate compound **16**, featuring a $PW_{11}O_{39}$ moiety connected *via* the tin center to 4-iodobenzene group, was synthesized. The Sonogashira cross-coupling between the two components **15** and **16** produced the hybrid iridium-polyoxometalate complex **17**.

These two examples show that performing catalysis directly on the metallated ligands is an efficient way to build up new multi-metallic species.

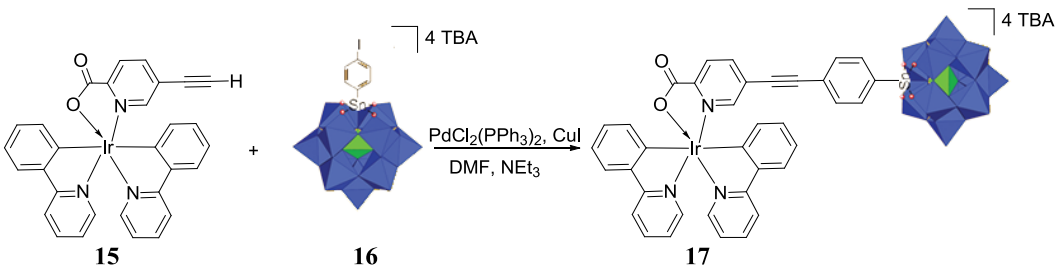

Scheme 5. Synthesis of of iridium-polyoxometalate hybrid complex **17** [8b]

1.3.3. Palladium-catalyzed arylation/C–H bond activation

As demonstrated above, Pd-catalysed cross-coupling reactions can be readily used, but more interestingly Pd-catalyzed arylation/C–H bond activation is also an efficient tool to functionalize Ir complexes.

- **Palladium-catalyzed C-H bond activation of free thiophenes**

Pd-catalyzed arylation/C–H bond activation can be applied to various heterocycles such as furans, thiophenes, pyrroles. In Rennes, H. Doucet and co-workers developed the direct arylation of α-substituted thiophenes using palladium-catalyzed C–H bond activation (**Scheme 6**).[10] They also showed that the C^5–H bond of thiophene can be activated by a ligand-free palladium catalyst.[10b] Blocking the α-position of the heterocycle restrains the possible side-reaction that would give the symmetrical *bis*-arylated product. Using this method, different aryls or heteroaryls (phenyl, pyridyl, naphthalenyl) substituted by a wide range of electron-donating (CH_3, NH_2) or electron-accepting groups (CN, COMe, COOMe, Cl, CF_3…) were introduced into the thiophene in very good yields (52 % to 84 %).

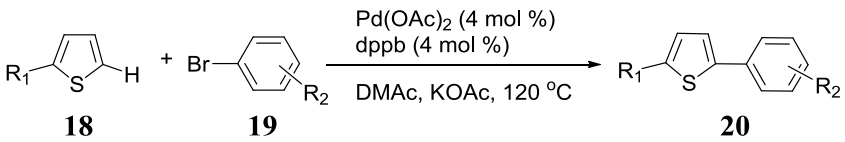

Scheme 6. Direct arylation of α-substituted thiophenes using palladium-catalyzed C-H bond activation [10]

- **Palladium-catalyzed C-H bond activation of *fac*-Ir(thpy)$_3$ complex: access to *mono-, bis-* and *tris*-arylated complexes**

The group in Rennes, in collaboration with H. Doucet, has developed the palladium-catalyzed C–H bond activation/arylation of *fac*-Ir(thpy)$_3$, **1**.[11] This method opens the door for the access to new class of functionalized complexes through the C–H bond activation of the

metallated thiophene rings. It provides the easy access to substituted complexes without the preparation of intermediates or metallic precursors. Furthermore, it allows the selective *mono*, *bis*, or *tris*-functionalization with various aryl or heteroaryl rings incorporating electron-acceptor-end groups.

1.3.4. Synthesis of *mono*-, *bis*- and *tris*-benzonitrile *fac*-Ir(thpy)$_3$ derivatives

For example, the coupling of complex **1** with 4-bromobenzonitrile has been performed in DMAc at 130 ^{o}C, using Pd(OAc)$_2$ as the catalyst and KOAc as the base (**Scheme 7**).[11] These conditions were previously optimized for the palladium-catalyzed direct arylation of α-substituted thiophenes. The phosphine-free palladium catalyst was selected in order to avoid a possible decomposition of the iridium complexes due to ligand exchange reaction with phosphines.

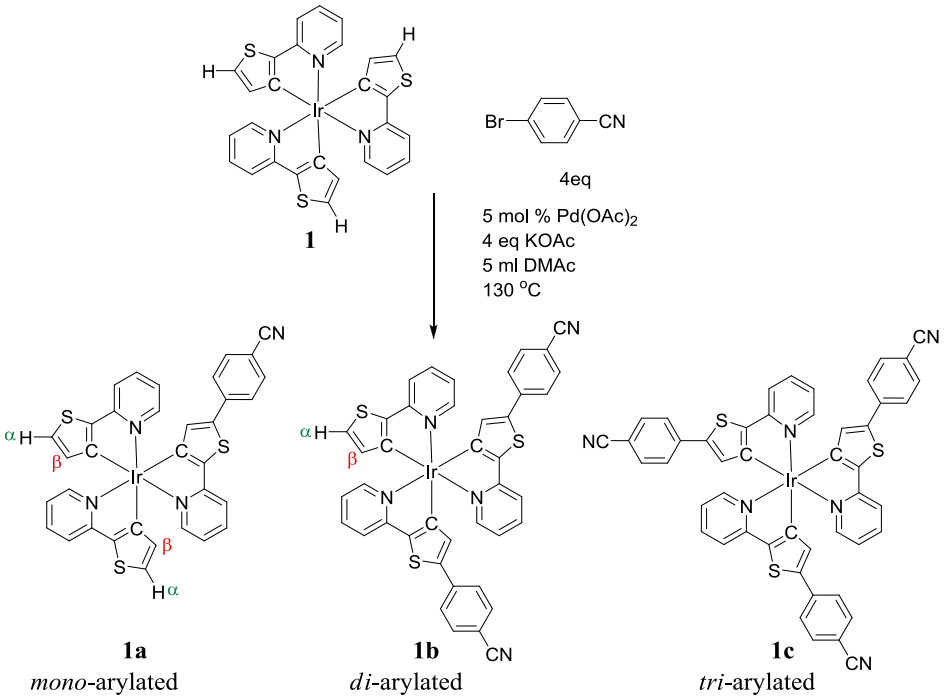

Scheme 7. Synthesis of *mono*-, *bis*- and *tris*-benzonitrile ***fac*-Ir(thpy)$_3$**[11]

The distribution of the product ratio appeared to be strongly dependent on reaction time. Upon heating the reaction up to 8 h, the ratio increases towards more arylated complexes: a mixture of **1a**:**1b** and **1c** was produced in 0:2:8. Further increase of the reaction times (48 h) produced selectively the *tris*-arylated complex **1c** (64 % isolated yield). This method has been extended to the preparation of complexes *fac*-Ir(thpy-Ar)$_3$ containing various aryl rings (phenyl, naphthalenyl) or heteroaryl rings (pyridyl, pyrimidyl) incorporating different substituents (**Figure 4**).

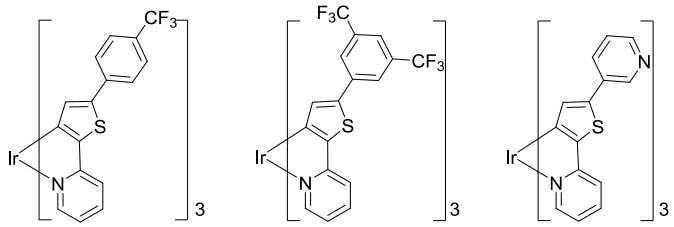

1d **1e** **1f**

Yield	48 %	63 %	52 %

Figure 4. ***fac*-Ir(thpy-Ar)$_3$** derivatives [11]

However, this method cannot be used for the preparation of *tris*-cyclometallated iridium thienylpyridine complexes with aryl rings incorporating donor-end groups. A possible explanation could be that the high electron density on the arylbromide incorporating donor end-group prevents their oxidative addition to the palladium catalyst.

1.4. Photophysical characterization of arylated *fac*-Ir(thpy-Ar)$_3$ complexes

The incorporation of an aryl substituent has a direct effect on the absorption properties of the resulting complexes. The absorption wavelengths as well as their molar extinction coefficients increase upon introducing stronger electron-accepting groups onto the complex.

The emission spectra of complexes **1**, **1c**, **1d**, **1e** and **1f** are presented in **Figure 5** and their characteristic emission data are summarized in **Table 1**.[11] The functionalized complexes **1c**, **1d**, **1e** and **1f** are luminescent at room temperature with emission spectra that have similar shape as that of complex **1,** indicating that their lowest energy excited states have the same nature. The arylated *fac*-Ir(thpy-Ar)$_3$ complexes show interesting photophysical properties, they present phosphorescence both at 298 K and 77 K originating primarily from the $LC^3(\pi\text{-}\pi^*)$ excited state that resides on the functionalized ligand. These complexes show a fine tuning of emission wavelength depending on the type of the aryl or heteroaryl and on the acceptor-end-group used. The presence of stronger acceptor end-groups induces a stronger red-shift of emission wavelength; on the other hand, it results in a decrease of photoluminescence quantum yield and lifetime

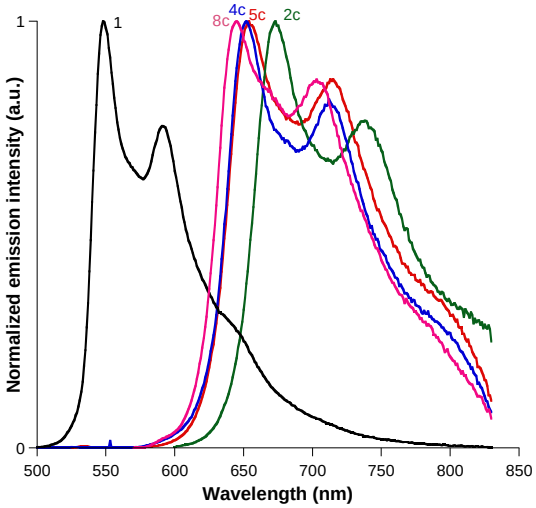

Figure 5. Emission spectra of complexes **1**, **1a**, **1b**, **1c** in CH_2Cl_2 at 298 K. [11]

The phosphorescence quantum yields and lifetimes of the arylated complexes were found to decrease together with a red shift of the emission wavelength. An estimation of the radiative (k_r) and non-radiative (Σk_{nr}) decay constants from the quantum yield and the lifetime suggests that there is an increase in Σk_{nr} and decrease in k_r upon arylation. This effect can be attributed to the more extended π-conjugated system; it is likely that the influence of the metal in promoting intersystem crossing through spin-orbit coupling is reduced.

Table 1. Emission data for the complexes **1, 1c**, **1d**, **1e** and **1f** in CH_2Cl_2 at 298 K.

	λ_{max} / nm	ϕ_{lum} (%)	τ / ns degassed [aerated]	$k_r \times 10^{3\,a}$ / s^{-1}	$\Sigma k_{nr} \times 10^{4\,a}$ / s^{-1}
1	548, 592, 643(sh)	40	7100 [87]	56	8.5
1c	673, 738	1.1	1500 [420]	7.3	66
1d	652, 712, 795(sh)	2.0	2400 [370]	8.3	41
1e	654, 714, 798(sh)	1.7	2100 [350]	8.1	47
1f	645, 703, 784(sh)	1.9	2800 [390]	6.8	35

(a) k_r and Σk_{nr} are the estimated radiative and non-radiative rate constants estimated from the Φ_{lum} and τ values, assuming that formation of the emitting state occurs with unitary efficiency.

Our objective in the present work was to extend the Pd catalyst synthesis method to more extended π systems as the chromophores (pyrene, naphthalimide, perylene…). They have large Stokes shifts and high extinction coefficients. The results will be useful for the design of visible-light-harvesting transition-metal complexes that show long-lived triplet excited states and for their applications as triplet sensitizers for various photophysical processes, such as triplet-triplet annihilation upconversion, photovoltaics, photocatalysis…

1.5. Iridium complexes functionalized with polycyclic-aromatic dyes

1.5.1. Neutral iridium complexes

In order to produce *tris*-cyclometallated Ir complexes that show strong absorption in the visible region along with long-lived triplet excited states, Zhao *et al.* prepared the neutral Ir(III) complex **22** featuring a ppy ligand connected to a naphthalimide (NI) group through an acetylide bond (**Scheme 8**).[12]

Complex **22** was synthesized in two steps: the N-alkyl NI moiety was first attached to 2-(4-ethynylphenyl)pyridine by using a Pd-catalyzed Sonogashira coupling reaction to produce the pro-ligand **21.** The heteroleptic Ir complex **22** was then obtained in 58% yield by reacting the chloro-bridged dimer $[Ir(\mu\text{-}Cl)(thpy)_2]_2$ with **21** in the presence of silver triflate. Compared to the parent complex $Ir(ppy)_3$ **5** which weakly absorbs in the visible region and is highly luminescent at 510 nm, complex **22** shows an intense absorption in the visible light range (ε = 39 600 L $mol^{-1}cm^{-1}$ at 402 nm), a room temperature red emission at 640 nm with a weak luminescence quantum yield (ϕ = 1.4 %), and a long-lived T_1 excited state (τ = 9.30 μs) which was identified as mainly an intraligand triplet excited state (^{3}IL). This complex was used as triplet photosensitizer for triplet-triplet annihilation (TTA) upconversion.

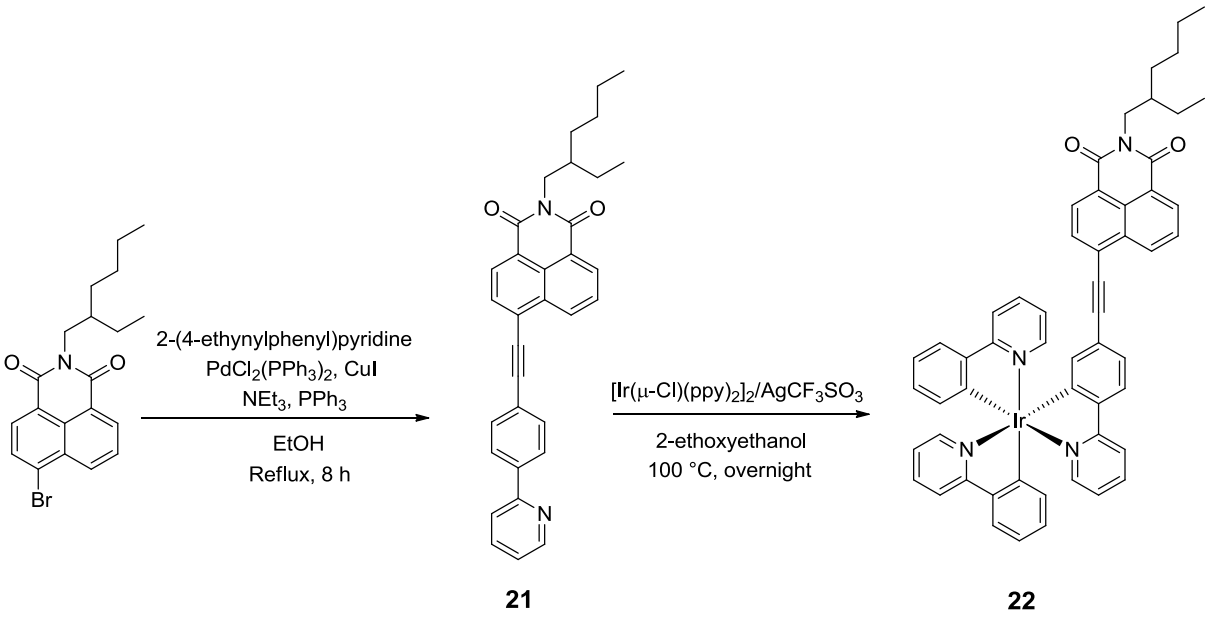

Scheme 8. Synthesis of the neutral Ir(III) complex **21** [12]

1.5.2. Cationic iridium complexes

In the same way, the synthesis and photophysical behavior of a series of cationic *bis*-cyclometallated Ir(III) complexes incorporating 2,2'-bipyridine ligands connected *via* a C≡C-bond to different dyes such as Bodipy, coumarin or naphthalenediimide (NDI) were recently reported.[13,14, 15, 16] Some representative complexes **23**-**27** are shown in **Figure 6**.

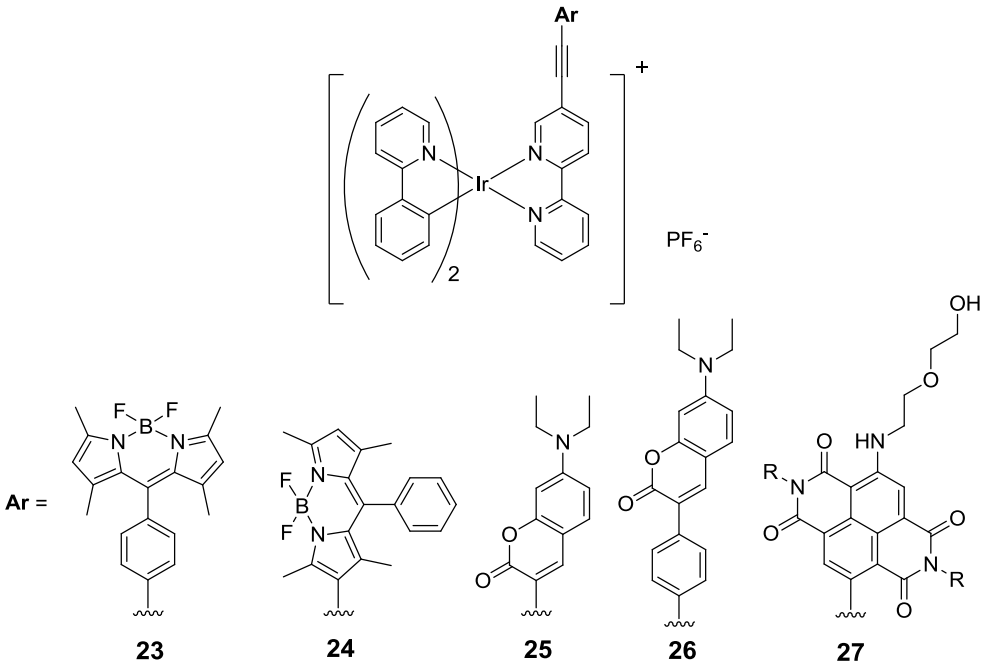

Figure 6. Cationic *bis*-cyclometallated Ir(III) complexes **23-27** [13-16]

Their preparations were quite similar to that of the parent iridium complex **28**, and the first step also involved the preparation of the bipyridyl ligand by a Sonogashira coupling reaction between the 5-ethynyl-2,2'-bpy and the dye (**Figure 7**). The photophysical properties of these complexes are summarized in **Table 2** and are compared to those of the parent complex $[(ppy)_2Ir(bpy)]PF_6$ **28**.

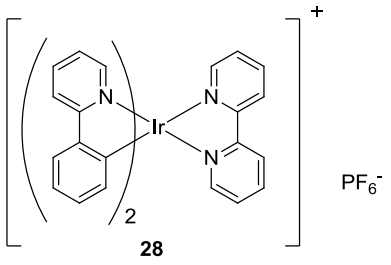

Figure 7. Cationic iridium complex 28

In contrast to **28**, all the dye-containing iridium complexes display strong absorption in the visible region: for example, complexes **23** and **24** tethered to a Bodipy moiety show broad absorption bands at 499 and 527 nm, respectively, similar to the correspondingly functionalized bpy-Bodipy ligands.[17] By contrast, these two complexes show different luminescence properties: whereas only room-temperature fluorescence of the Bodipy ligand is observed for **23** at 514 nm with a luminescence lifetime of 0.9 ns, both weak fluorescence and phosphorescence (assigned to a Bodipy-localized ^{3}IL state) can be seen for **24** at 553 and 742 nm, respectively. This different behavior can be explained by the structure of the two Bodipy-bpy ligands: in **23** there is no π-conjugation between the Bodipy and the coordination centre, whereas in **24** the Bodipy unit is directly π-conjugated to the bpy ligand via a C≡C triple bond.

The two diethylamino coumarin-containing Ir(III) complexes **25** and **26** (which only differ from **25** by the presence of an extra phenyl unit between the coumarin moiety and the C≡C triple bond) also show room temperature phosphorescence emission at ~ 640 nm.[15] However the lifetime of **25** ($\tau = 36.7$ μs) was found to be much longer than that of **26** ($\tau = 7.3$ μs), showing that a subtle variation of the molecular structure of the dye may affect the photophysical properties. The Ir(III) complex **27** featuring a naphthalenediimide dye exhibits the most red-shifted absorption band at 542 nm attributed to the NDI moiety. Like complex **24**, the RT emission spectrum of **27** shows two emission bands at 572 nm and 732 nm, respectively.[16] The first band is fluorescence with a short luminescence lifetime of 5.0 ns, whereas the near IR emission is phosphorescence with a very long lifetime up to 130 μs which is due to the NDI-localized intraligand triplet excited state. Finally, it is noteworthy that all these complexes were used as triplet photosensitizers for triplet-triplet annihilation (TTA), and upconversion quantum yields ranging from 1.2% (for **23**) to up to 22.8 % (for **25**) were observed.

Table 2. Photophysical data for the complexes **23-28** in CH_2Cl_2 at 298 K. [13-16]

Complex	λ_{abs}/nm; ε / L mol^{-1} cm^{-1}	λ_{em} / nm	τ / μs	ϕ
23	499 (7.14 ×10^4)	514	0.009	0.018
24	527 (8.30×10^4)	553, 742	0.026, -[a]	0.00003/0.003
25	487 (4.20 ×10^4)	645	36.7	0.065
26	437 (4.58×10^4)	640	7.3	0.011
27	542 (1.71 ×10^4)	572, 732	0.005, 220.3	0.001
28	405 (0.5 ×10^4)	578	0.3	0.04

[a]too weak to be measured accurately

1.5.3. Iridium complexes incorporating cyclometalated aromatic dyes

In 2012, Pope *et al.* described the synthesis and photophysical properties of new iridium(III) complexes incorporating cyclometalated pyrene units (**Scheme 9**).[18] The synthesis of the pro-ligands **30** was achieved in two steps: condensation of 1-pyrenecarboxaldehyde with 1,2-diaminobenzene gave the benzimidazole intermediates and subsequent N-alkylation (using phase transfer conditions) afforded a variety of pyrene-benzimidazole derivatives **29**. The mixed-ligand cationic iridium(III) species **31** were classically prepared in two steps from $IrCl_3.xH_2O$. An X-ray diffraction study of **31** (R = Bz) revealed a highly unusual coordination mode for the pyrenyl ligand with a metalation at position C10 (instead of C2) resulting in the formation of a six-membered ring. Compared to the parent complex $[(ppy)_2Ir(bpy)]PF_6$ (**28)**, these complexes display enhanced absorption features in the visible region which are attributed to the presence of cyclometalated pyrenyl chromophores (^{1}IL and ^{1}MLCT transitions). The emission properties show emission profiles between 407 and 446 nm with short lifetimes (<5 ns) suggestive of a fluorescent emitting state localized on the pyrene moieties. Interestingly, these complexes appeared to be extremely effective $^1O_2$ photosensitizers.

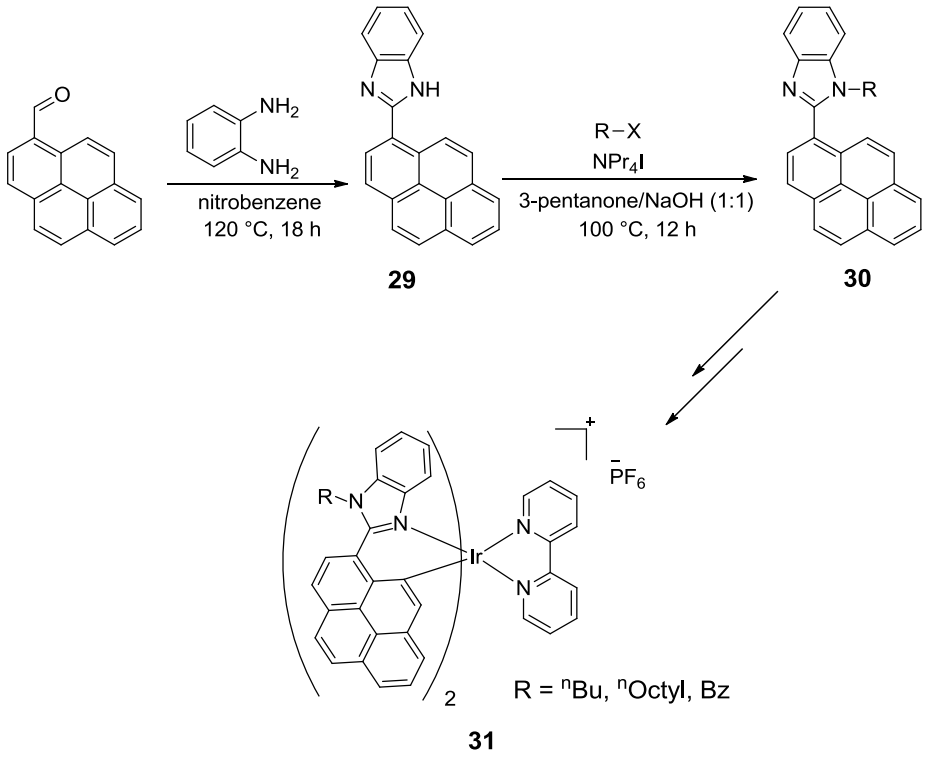

Scheme 9. Preparation of cationic iridium(III) complex **31**[18]

A series of neutral and cationic Ir(III) complexes comprising two cyclometallating 3-(2-benzothiazolyl)-7-(diethylamino)coumarin ligands and either one acac or diimine (2,2'-bipyridine, 1,10-phenanthroline) ancillary ligand were prepared and their photophysical properties were reported (**Figure 8**).[19, 20] Again, the UV-vis absorption spectra show intense bands in the visible region, at ca. 480 nm. The molar absorptivity of the cationic complexes **32b,c** was much larger than that of the neutral complex **32a**, and this enhancement is presumably due to the combined effects of the ILCT transition of the coumarin ligand and the MLCT/LLCT transitions related to the diimine ligands. At room temperature all these complexes exhibit a strong emission band at 565-589 nm. Again, their relatively long emission lifetimes (between 6.2 and 7 μs) as compared to that of complex **27**, as well as the vibronic fine structures observed in the emission spectra, indicate that the excited states of these complexes possess ^{3}IL nature rather than ^{3}MLCT character. Interestingly, these complexes were used as efficient photosensitizers for visible-light driven hydrogen generation.[20]

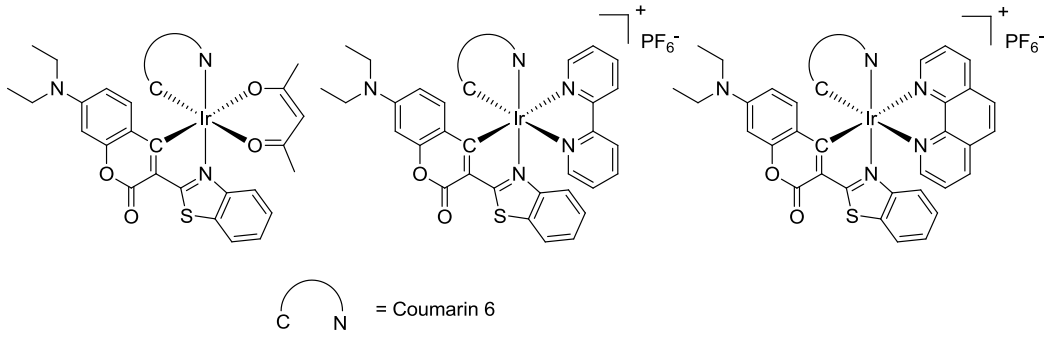

32a **32b** **32c**

Figure 8. Neutral and cationic iridium complexes **32a 32b** and **32c** [19, 20]

Table 3. Photophysical data of complexes **30a-c** in CH_2Cl_2/MeOH at 298 K. [19, 20]

Compounds	Absorption λ_{max} / nm, ε/ L mol^{-1} cm^{-1}	Emission λ_{max} / nm	Lifetime τ / μs	Quantum yield ϕ
32a	472 (83200)	565	6.57	0.60
32b	483 (129000)	589	6.21	0.26
32c	485 (126000)	589	7.06	0.18

2. Results and discussion

Initially, the synthesis of the following bromo aromatic chromophores, **NI-Br**, **Per-Br**, **Pyr-Br**, **Coum-Br** (**Figure 9**) will be presented. Subsequently, the Pd-catalyzed arylation reactions, on methylthiophene and directly on the complex *fac*-Ir(thpy)$_3$, **1** with these bromo derivatives will be describe. In the last part, I will describe the photophysical properties, absorption and emission studies, of the arylated methylthiophene and the arylated *fac*-Ir(thpy)$_3$ will be discussed.

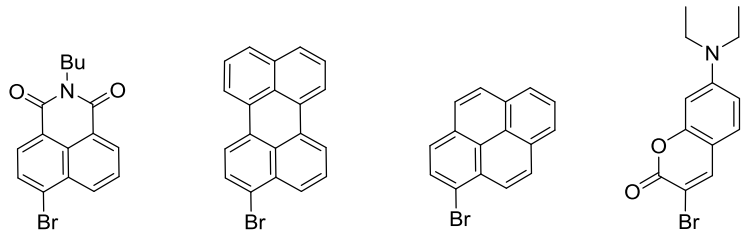

NI-Br **Per-Br** **Pyr-Br** **Coum-Br**

Figure 9. Bromo aromatic chromophores, **NI-Br**, **Per-Br**, **Pyr-Br** and **Coum-Br**

2.1. Synthesis of the bromoaryl derivatives

- *N*-butyl-4-bromonaphthalimide, **NI-Br**

The 4-bromonaphthalene anhydride was used as starting material for the synthesis of naphthalimide (**Scheme 10**).[21] The reaction with N-butylamine in ethanol at 60 °C gave the corresponding imide in 70 % yield. The *N*-butyl-4-bromonaphthalimide, **NI-Br** was isolated as a pale brown powder. The ^{1}H NMR spectrum of **NI-Br** shows the signals of the alkyl protons (δ = 0.98, 1.45, 1.71 and 4.17 ppm). In the aromatic region, three doublets and one triplet are attributed to the naphthalene protons.

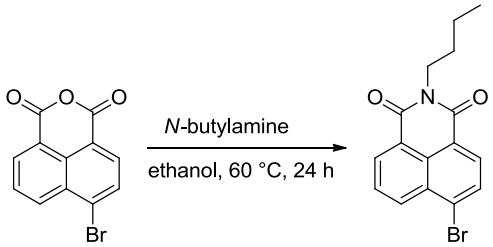

NI-Br

Scheme 10. Synthesis of **NI-Br** [21]

- 1-Bromoperylene, **Per-Br**

The bromination of perylene was achieved by the addition of *N*-bromosuccinimide (NBS), the bromination occurs at the C1 position of perylene (**Scheme 11**).[22] The reaction was performed in DMF at room temperature for 24 h. After purification, the 1-bromoperylene, **Per-Br** was obtained as a white powder in 78 % yield.

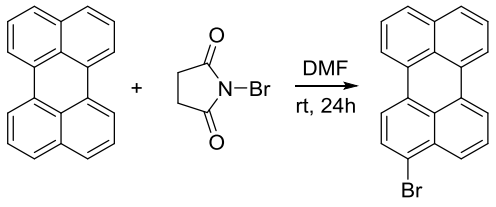

Per-Br

Scheme 11. Synthesis of **Per-Br** [22]

- 1-bromopyrene, **Pyr-Br**

The bromination of pyrene was achieved by the reaction between pyrene and bromine generated *in situ* by the action of hydrogen peroxide on hydrogen bromide (**Scheme 12**).[23] The compound 1-bromopyrene, **Pyr-Br** was isolated as a white powder in 90 % yield.

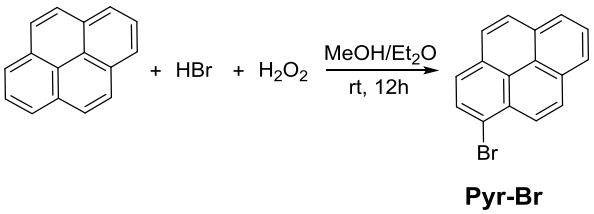

Scheme 12. Synthesis of **Pyr-Br** [23]

- Bromo-coumarin, **Coum-Br**

The synthesis of bromo-coumarin, **Coum-Br** was performed in three steps (**Scheme 13**).[24,25] The first step is an aldol condensation of salicylaldehyde with diethylmalonate in basic conditions. After purification by column chromatography, the desired product **34** was obtained in 70 % yield. The treatment of **33** with HCl led to the lactone **34** in 80 % yield. Finally, the bromination proceeds by the addition of Br_2 in acid solution over 3 h. The collected white solid was dried under vacuum and then recrystallized in acetonitrile to afford the bromo-diethylamino coumarin, **Coum-Br**, in 78 % yield. The ^{1}H NMR spectrum shows two singlets at δ = 7.67 and 8.18 ppm corresponding to the proton in the α position to bromine and the singlet proton adjacent to the amino group, respectively. In addition, a triplet observed at δ = 1.29 ppm (J = 7.1 Hz) was assigned to the CH_3- and a quartet at δ = 3.37 ppm was assigned to the CH_2- of the coumarin.

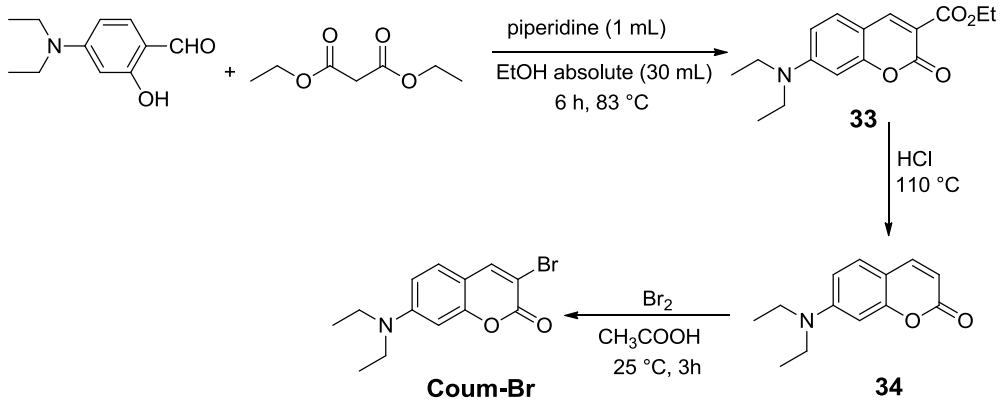

Scheme 13. Synthesis of **Coum-Br** [24,25]

2.2. Pd-Catalyzed arylation of 2-methylthiophene

We have investigated the Pd-catalyzed arylation of methylthiophene with the following bromo aromatic chromophores, previously prepared: *N*-butyl-4-bromonaphtalimide, 3-bromoperylene, 1-bromopyrene, 3-bromo-7-(diethylamino)chromen-2-one (**Scheme 14**). Generally the C^2 and C^5 positions of the thiophene are susceptible to palladium-catalyzed activation. However, in the present instance, the C^2-position is blocked by a methyl group (or, in subsequent sections, a pyridyl ring), and hence the C^5-position is the only available site for arylation.

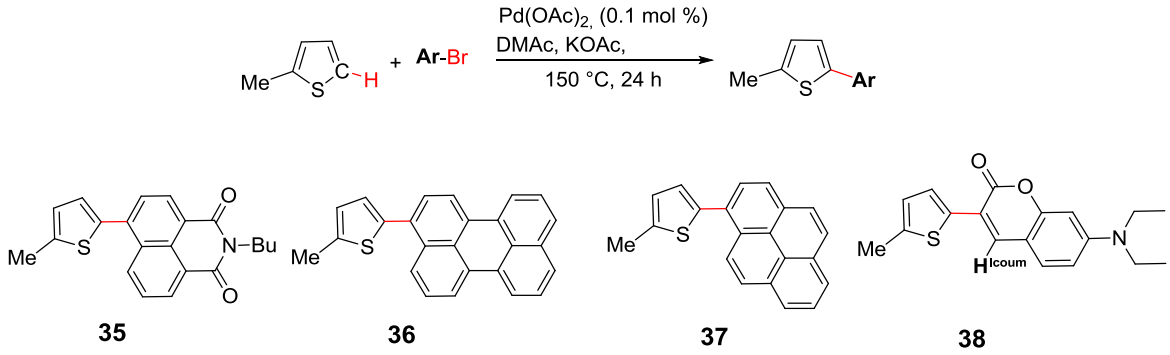

Scheme 14. Pd-Catalyzed arylation of 2-methylthiophene

The reactions were performed in the presence of 0.1 mol % of $Pd(OAc)_2$ in DMAc with KOAc for 24 h at 150 °C. The C^5-arylated methylthiophene derivatives **35-38** were isolated in 63 to 65 % yields after purification by column chromatography on silica gel using a gradient of Et_2O/ pentane or dichloromethane. All products were characterized by ^1H and ^{13}C $\{^1H\}$ NMR spectroscopy using CD_2Cl_2 as the solvent. In general, the ^1H NMR spectra show two characteristic doublets around δ = 6.90-7.00 ppm and 7.10-7.20 ppm corresponding to the H^4 and H^3 of the thiophene ring. In addition, the signal at δ = 6.77 ppm corresponding to H^2 of the thiophene ring disappears. As an example, the ^1H NMR of the **38** shows the characteristic singlet of H^{1coum} at δ = 7.62 ppm.

2.3. Catalytic arylation of the complex *fac*-Ir(thpy)$_3$

The advantage of doing the direct arylation on the iridium complex is the selectivity of the on-metal approach which can lead to the formation of the *mono* and or the *bis*-arylated iridium complex. Moreover, this reaction allows keeping the geometry (*facial* or *meridional*) of the complex.

2.3.1. Synthesis

The synthetic procedure used to prepare these arylated complexes involved the use of 6 equivalents of the aryl bromide (**35**, **36**, **37**, **38**) relative to the iridium complex *fac*-Ir(thpy)$_3$ **7**, 5 % of Pd(OAc)$_2$ as the catalyst and a large excess of base (KOAc) in DMAc as the solvent (**Scheme 15**). The mixture was heated at 130-150 °C for 48 h. Compared to the off-metal reaction (see section **2.2**) the catalytic reaction on the complex required more palladium catalyst. In fact, with less than 5 % of Pd(OAc)$_2$, there is no formation of the *tris*-arylated iridium complex.

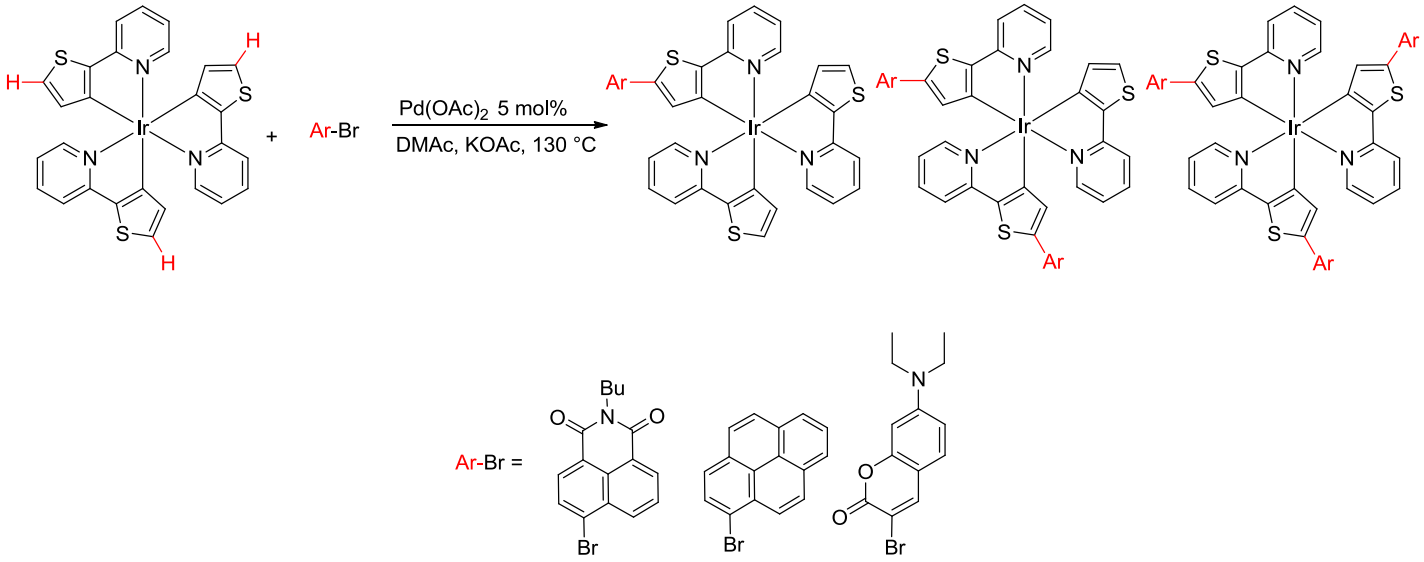

Scheme 15. Catalytic arylation of ***fac*-Ir(thpy)$_3$**

The purification was performed by column chromatography on silica gel. All compounds were characterized by ^{1}H and ^{13}C{^{1}H} NMR spectroscopy in CD_2Cl_2. It was noticed that the capacity to obtain the *mono*- *bis*- and *tris*-arylated products depends on the reactivity of the aryl bromide, the temperature and the reaction time.

- *fac*-Ir(thpy)$_3$ complex bearing naphthalimide or pyrene units

The treatment of the *fac*-Ir(thpy)$_3$ complex with *N*-butyl-4-bromonaphthalimide leads to a mixture of *bis*- and *tris*-arylated compounds which were separated by column chromatography on silica (Eluent = pentane / Et_2O (4:6)). The *bis*-arylated complex was isolated in 40 % yield whilst only a small amount of the *tris*-arylated complex was collected (**Figure 10**).

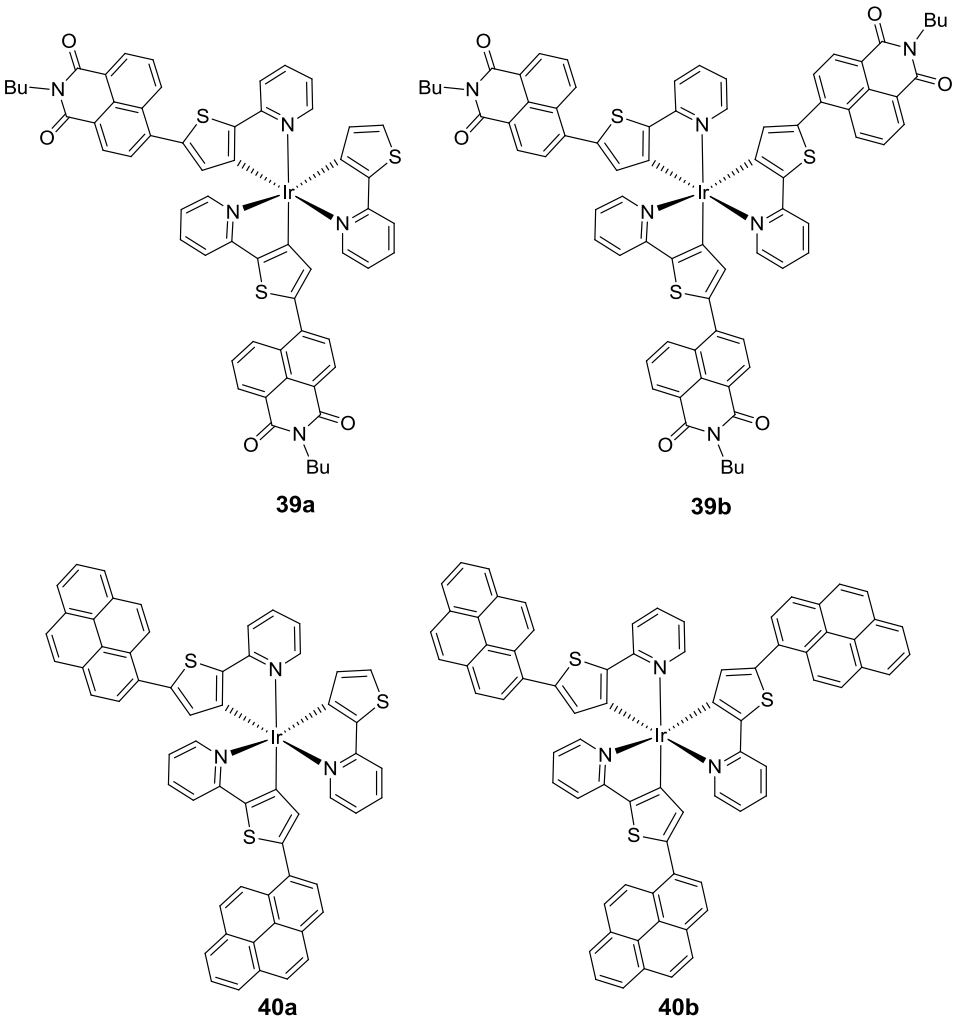

Figure 10. Arylated ***fac*-Ir(thpy)$_3$** complexes **39a-b** and **40a-b**

The two products were characterized by ^{1}H and ^{13}C{^{1}H} NMR in CD_2Cl_2. The *tris*-cyclometallated complex was identified due to the presence of the C^3-axis of symmetry: as a result, one set of signals corresponding to one ligand was observed. However, the *bis*-arylated complex *fac*-Ir(thpy)(thpy-NI)$_2$ (**39a**), featuring no axis of symmetry, showed three different sets of signals corresponding to the three non-magnetically equivalent ligands. Indeed, the *bis*-arylated complex shows two doublets at δ = 6.69 and 6.74 ppm (J = 6.7 Hz) corresponding to H^4 and H^5 protons of non-arylated thienyl ring. The *tris*-arylation of the iridium complex (**39b**) presents a singlet at δ = 8.59 ppm corresponding to the H^4 proton of the thienyl ring. The same case was observed with the arylation between *fac*-Ir(thpy)$_3$ and the bromopyrene.

However, due to a difficult separation of the mixture of *bis*- and *tris*-arylated iridium complexes, it was impossible to isolate either one of the species in suffcient purity to allow photophysical studies to be performed.

- *fac*-Ir(thpy)$_3$ complex bearing a coumarin unit

Upon treating *fac*-Ir(thpy)$_3$ with the bromo-coumarin for 48 h, the apparence of one new spot on TLC was observed, while the spots corresponding to the starting materials stayed unchanged (**Figure 11**). After workup, the new spot was isolated and identified using ^{1}H and ^{13}C{^{1}H} NMR spectroscopy to be the *mono*-arylated complex **41**.

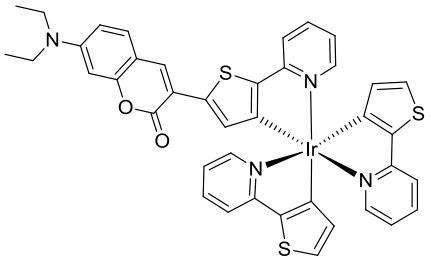

41

Figure 11. *mono*-Arylated complex **41**

Two characteristic doublets of the thienyl ring at δ = 6.43 ppm and 6.53 ppm were observed and a singlet at δ = 6.86 ppm corresponding to the proton of the arylated thienyl ring. The singlet at δ = 7.88 ppm is attributed to the proton of the coumarin. In addition, a triplet observed at δ = 1.26 ppm (J = 7.1 Hz) was assigned to the CH_3- and a quartet at δ = 3.46 ppm (J = 7.1 Hz) was assigned to the CH_2- of the coumarin. We assume that the presence of strong donating amino group used has decreased the efficiency of the reaction. A similar observation has been made in previous work done in the laboratory, where introducing aryl groups incorporating donor ends to the *fac*-Ir(thpy)$_3$ complex was not possible.[11]

2.3.2. Photophysical studies

- **Absorption studies**
  - **Methylthiophene derivatives**

The absorption spectra of the different organic compounds have been registered at room temperature in CH_2Cl_2 solution (**Figure 12**). The ligand **37** has a main absorption band at 268 nm and a second at 327 nm (**Table**). The ligand **36** presents a red-shifted absorption at 447 nm. It is interesting to note that the molar extinction coefficient (absorption table)

increases from the pyrene (**37**) to the perylene (**36**) group. It can be attributed to the extension of the π system. The ligands **38** and **35** absorb in the blue region with maxima at 399 nm and 378 nm, respectively.

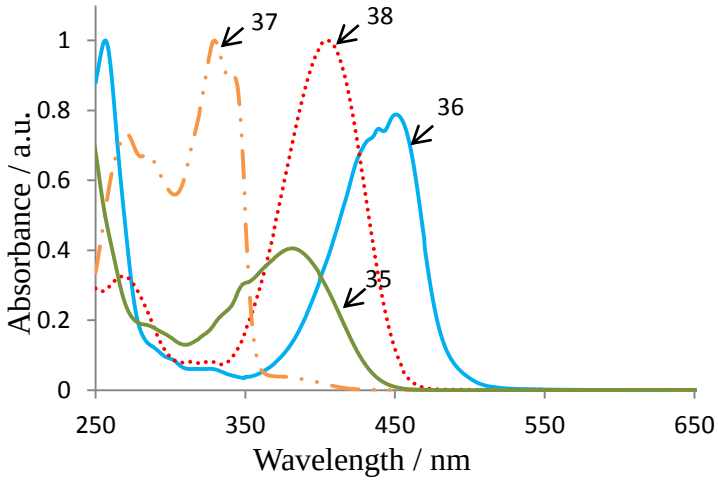

Figure 12. UV-visible absorption spectra of **35** (dashed), **36** (plain), **37** (dashed/dotted), **38** (dotted) in CH_2Cl_2 solution at 298 K.

Table 4. Absorption data of **35-38** in CH_2Cl_2 solution at 298 K.

Compound	Absorption λ_{max} / nm (ε/ 10^3 L mol^{-1} cm^{-1})
35	329 (5.40), 345 (8.07), 378 (11.3)
36	254 (34.4), 435 (25.4), 447 (26.9)
37	268 (17.0), 280 (15.7), 327 (23.0), 337 (21.4)
38	260 (8.25), 399 (25.2)

- **Iridium complexes**

Figure 28 presents the superposition of the absorption spectra of the non-functionalized complex **2** and complexes with two or three ligands bearing a naphthalimide group (*fac*-Ir(thpy)(thpy-NI)$_2$ (**39a**), *fac*-Ir(thpy-NI)$_3$ (**39b**), respectively).

The *bis*- and *tris*-arylated complexes *fac*-Ir(thpy)(thpy-NI)$_2$ (**39a**), *fac*-Ir(thpy-NI)$_3$ (**39b**), respectively show different absorption profiles in the UV region and similar profiles in the visible region, with molar extinction coefficients that increase with the increasing number of arylated ligands. There is an influence of the number of arylated ligands. The *bis*-arylated complex *fac*-Ir(thpy)(thpy-NI)$_2$ (**39a**) shows three bands in the UV region at 306 nm (24.2 L

mol^{-1} cm^{-1}), 351 nm (27.8 L mol^{-1} cm^{-1}) and 373 (26.4 L mol^{-1} cm^{-1}). The *tris*-arylated complex shows one band in the UV region at 354 nm (45.1 L mol^{-1} cm^{-1}).

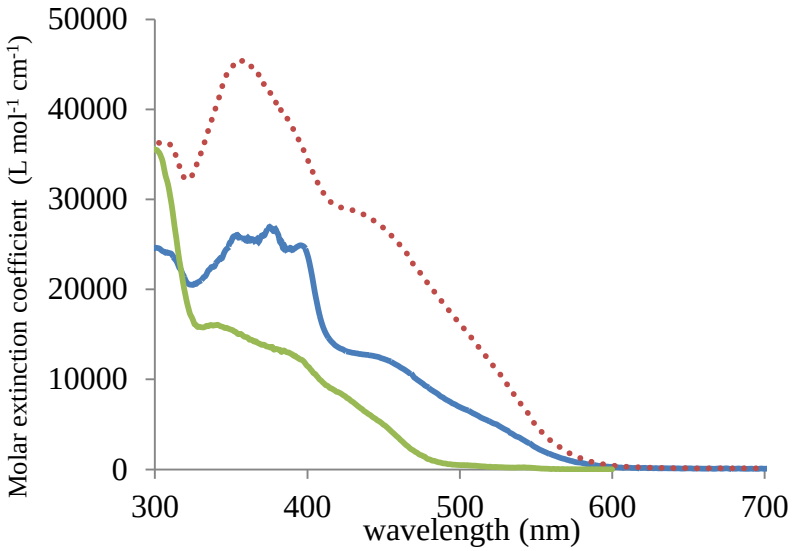

Figure 13. UV-Visible absorption spectra of **1** (plain), **39a** (dashed) and **39b** (dotted) in CH_2Cl_2 solution at 298 K.

The absorption spectra of different iridium complexes have been recorded at room temperature in CH_2Cl_2 solution (**Figure 13**).

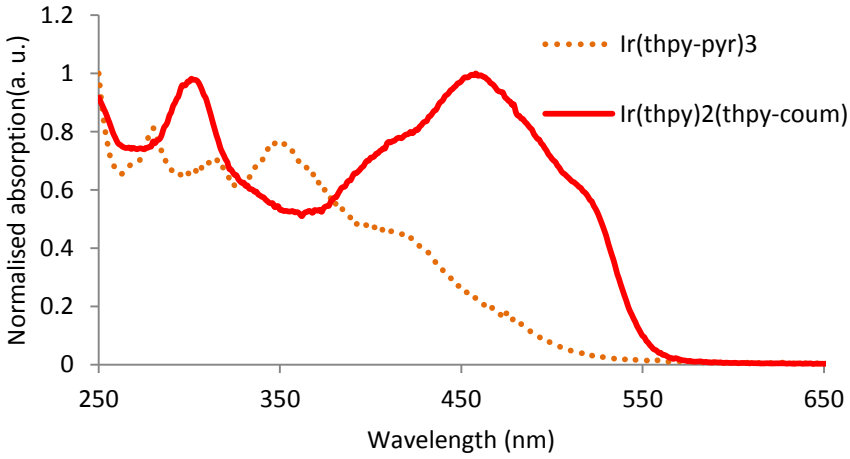

Figure 14. UV-visible absorption spectra of **40a** (dotted) and **41** (plain) in CH_2Cl_2 solution at 298 K.

Table 5. Molar extinction coefficients (L mol^{-1} cm^{-1}) of iridium complexes

Complex	Absorption λ_{max} / nm (ε/ 10^3 L mol^{-1} cm^{-1})
39a	298 (24.3), 306 (24.1), 351 (27.7), 373 (26.4), 394 (12.5), 445 (12.5), 522 (5.12)
39b	296 (35.4), 305 (36.1), 354 (45.1), 443 (27.7), 520 (11.9)
40a	260 (49.5), 400 (28.7)
40b	262 (49.2), 394 (29.7)
41	400 (14.1), 453 (25.6), 513 (15.6)

- **Emission studies**
  - **Methylthiophene derivatives**

The emission spectra of the aryl-substituted methylthiophenes have been recorded at room temperature in CH_2Cl_2 solution (**Figure 15**). Complexes **37** and **36** emit at 447 nm and 505 nm, respectively. A red-shift can be observed in the case of perylene. Compared to these, **35** presents an emission band at 482 nm. This compound has a larger Stokes shift than **38** which displays an emission band at 468 nm (**Table 6**).

↙35

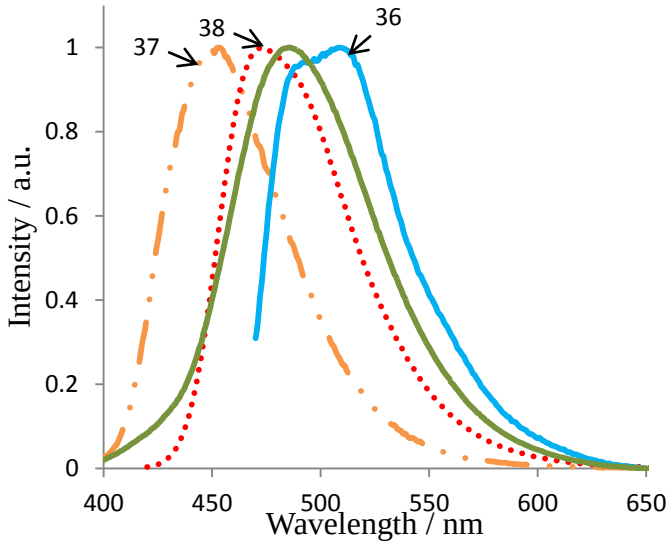

Figure 15. Emission spectra of methylthiophenes derivatives **35** (dashed), **36** (plain), **37** (dashed/dotted), **38** (dotted) in CH_2Cl_2 solution at 298 K

Table 6. Emission wavelengths of complexes **35-38** in CH_2Cl_2 at 298 K.

Complexes	Emission λ_{max} / nm	$\Delta\lambda$ / nm
35	482	104
36	505	58
37	447	110
38	468	69

- **Iridium complex derivatives**

Unfortunately, none of the complexes are emissive at room temperature. At 77 K the emission of these species is weak. This particular behavior can be attributed a quenching effect induced by the presence of the aromatic substituents. Indeed if the substituent possesses a lower triplet state than the one of the complex, the emission process goes from the complex to the ligand triplet state. This thermodynamic transfer leads to a phosphorescence quenching as this ligand triplet state is non-emissive at room temperature.

2.4. Catalytic arylation of the complex $Ir(Meppy)_2(tta)$

As an extension of this work, it was decided to investigate the access to arylated $Ir(C^N\text{-}Meppy)_2(O^O\text{-}tta\text{-}\mathbf{Ar})$ complexes where the incorporated aryl group is an aromatic chromophore such as naphthalene, pyrene, naphthalimide, and coumarine, and to study the

photophysical properties of the resulting complexes. There are several reports of the combination of organic dyes with *bis*-cyclometallated complexes $[Ir(C^N)_2(N^N\text{-bpy})]^+$. Various designs have been reported where the 2,2'-bipyridine ligand is connected *via* a C≡C– bond to different dyes such as Bodipy, coumarin or naphthalenediimide (NDI), leading to intriguing triplet-triplet annihilation (TTA) based upconversions.[26] Direct cyclometallation of the fluorophore has also been reported such as complexes incorporating cyclometalated pyrene units which resulted in enhanced absorption in the visible as compared to benchmark complexes like $[Ir(C^N\text{-ppy})_2(bpy)]^+$ and $[Ir(ppy)_2(acac)]$.[27] The synthesis and photophysical properties of a series of neutral and cationic Ir(III) complexes comprising two cyclometallating 3-(2-benzothiazolyl)-7-(diethylamino)coumarin ligands and either one acac or diimine ancillary ligands have also been recently described and their use as efficient photosensitizers for visible-light driven hydrogen generation demonstrated.[28,29] In addition, the fluorescent coumarin 343 has been connected to the O^O-ancillary ligand of a phosphorescent *bis*-cyclometallated iridium complex for monitoring oxygen levels in living cells and tissues, using a tetraproline linker to separate the phosphor from the fluorophore.[30] In contrast, to our knowledge the molecular engineering of heteroleptic cyclometallated Ir(III) complexes featuring functionalized "acac-type" ligands directly conjugated with the aromatic dyes has never been investigated.

2.4.1. Synthesis

We found two routes to the naphthalimide-based complex $Ir(C^N\text{-Meppy})_2(O^O\text{-tta-NI})$, **Ir-NI**: (*i*) Pd-catalysed direct arylation of the coordinated tta ligand of $Ir(C^N\text{-Meppy})_2(O^O\text{-tta})$ **Ir-1**, (MeppyH = 4-methyl-2-phenylpyridine), and (*ii*) the synthesis of the proligand **ttaH-NI** involving a Pd-catalysed arylation step. The desired complex **Ir-NI** was formed from **Ir-1** *via* the route (*i*), in the presence of a 6-bromonaphthalimide using the Pd-catalysed direct arylation reaction conditions previously operative for aryl bromides ($Pd(OAc)_2$, K_2CO_3 in DMA). Complex **Ir-NI**, where the naphthalimide group is incorporated onto the C^5-position of the thiophene ring of the coordinated ligand tta, was isolated as a red powder in 16 % yield (**Scheme 16**). The ^1H NMR of **Ir-NI** exhibits the typical signals in the aromatic region of the NI group at δ 8.63 8.54 and 8.47 ppm. The protons of the thiophene ring appear at δ 7.73 and 7.20 ppm. It should be mentioned that the purification of **Ir-NI** was very tedious, as several chromatography columns were needed in order to get a pure compound. Moreover, some degradation occurred due to a long reaction time at 100 °C. As a consequence, we decided to investigate the route (*ii*) i.e. to perform the catalytic arylation on

thiophene derivatives, precursors of the ttaH proligand.

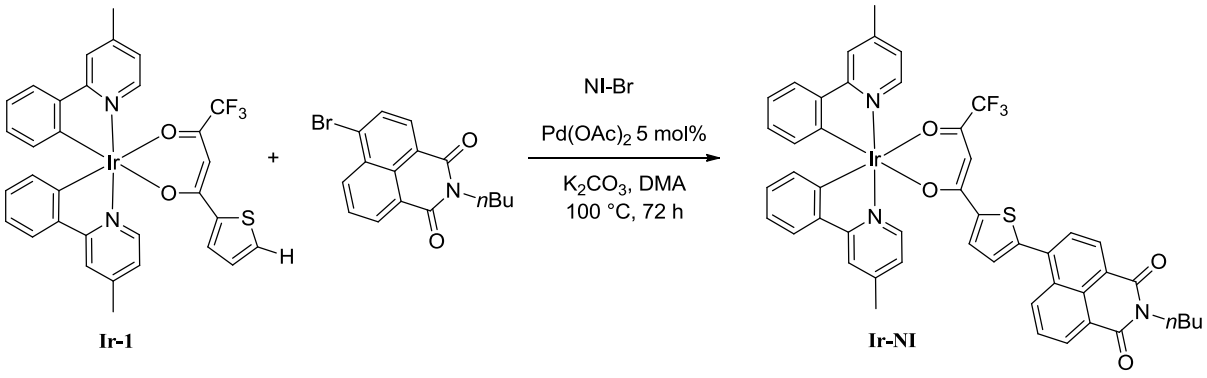

Scheme 16. Synthesis of **Ir-NI** *via* Pd-arylation of **Ir-1**

The arylated complexes **Ir-Ar** were synthesized upon treatment of the chloro-bridged dimer $[Ir(\mu\text{-}Cl_2)(C\text{^}N\text{-}Meppy)_2]_2$ with the appropriate diketone **ttaH-Ar** in the presence of Na_2CO_3 (**Scheme 17**). The reaction was performed under mild conditions (t = 80 °C) as there is no need to obtain the facial geometry (required for the formation of the *fac*-$Ir(thpy)_3$ complex). All complexes were isolated in low to moderate yields due to their high solubility and were characterized by standard techniques. The formation of the **tta-Ar**-based complexes was verified by the appearance of the aryl-thiophene protons and the formation of two sets of signals for the magnetically non-equivalent 4-methyl-2-phenylpyridine ligands in the ^1H NMR spectra (see Experimental part).

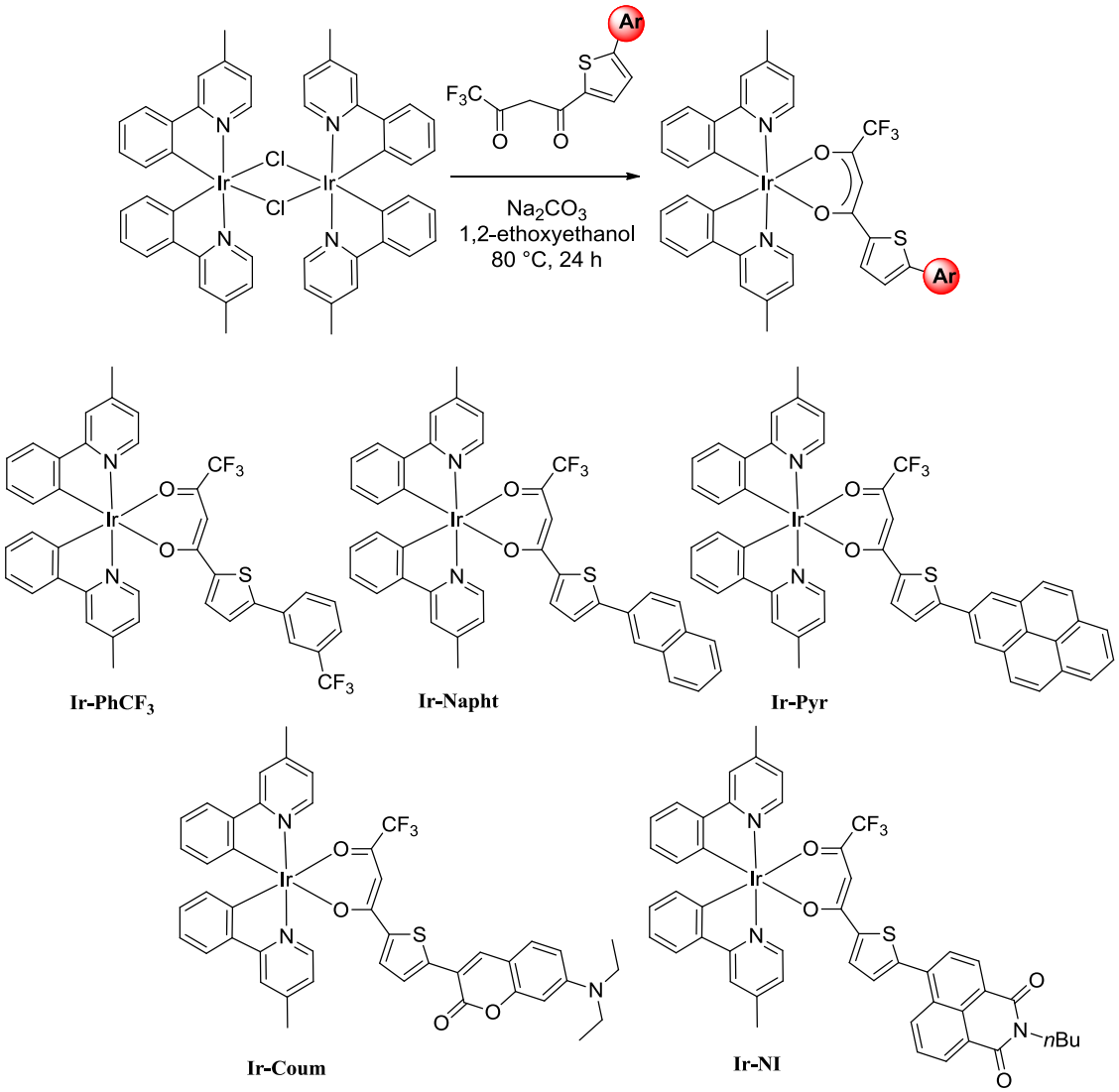

Scheme 17. Synthesis of the complexes **Ir-Ar**.

2.4.2. Photophysical properties of arylated thiopheneketones th-Ar and their Ir(III) complexes.

The electronic absorption spectra of the newly prepared arylated thienylketones **th-Ar** have been performed in dichloromethane solution at room temperature (**Figure 16**, **Table 7**). The thiophene derivatives **th-NI** and **th-Pyr** exhibit an intense absorption band at 365 nm (32100) and 367 nm (33700), respectively, whereas the absorption band of **th-Napht** appears at higher energy at 344 nm. Compounds **th-Per** and **th-Coum** show maxima at ~450 nm, their absorption being more into the visible. Note that the absorption band of **th-PhCF$_3$** (λ_{max} = 322 nm) is blue-shifted compared to those of the other arylated compounds of the series, due to the absence of a π-conjugated system. All compounds are fluorescent in fluid CH_2Cl_2 solution

under excitation with UV or visible light. The corresponding emission spectra are broad and featureless (**Figure 16**). Interestingly, changing the nature of the appended aryl group allows a fine modulation of the emission wavelength (from 360 to 514 nm). The emission from the coumarine- and perylene-based compounds (λ_{em} = ~515 nm) are the most red-shifted, as they absorb more into the visible.

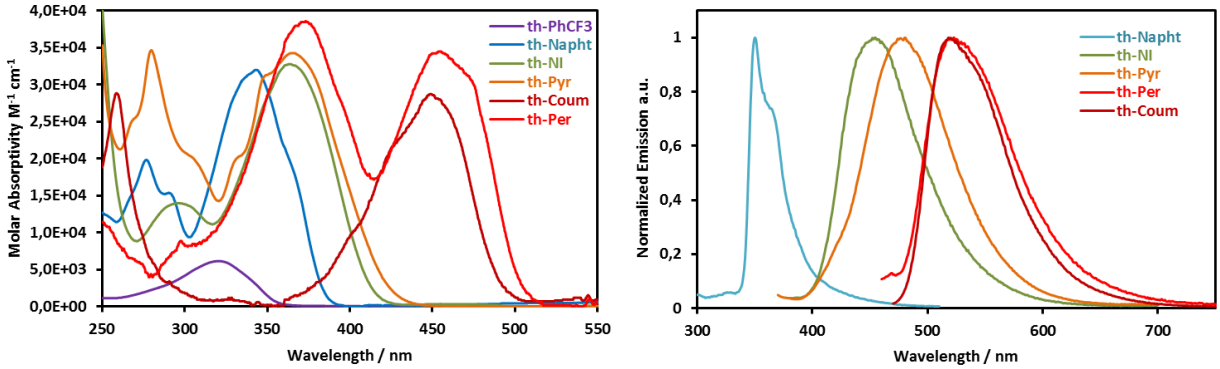

Figure 16. Absorption spectra (left) and Emission spectra (right) of **th-PhCF$_3$**, **th-Napht**, **th-NI**, **th-Pyr**, **th-Per** and **th-Coum** in CH_2Cl_2 solution at 298 K.

Table 7. Photophysical data of **th-PhCF$_3$, th-Napht, th-NI, th-Pyr, th-Per** and **th-Coum** in (a) degassed DCM and (b) in EPA solution.

Compound	λ_{abs} / nm ($10^3.\varepsilon$ / L mol^{-1} cm^{-1})[a]	λ_{em} / nm 298 K[a]	λ_{em} / nm 77 K[b]
th-PhCF$_3$	322 (6.1)	-	374
th-Napht	344 (32.1)	349	393,414
th-Pyr	367 (33.7)	470	450
th-Per	425 (23.4), 450 (28.4)	518	490,518
th-NI	365 (32.1)	445	440
th-Coum	450 (34.0)	514	511,532

The electronic absorption spectra of the arylated Ir(III) complexes in dichloromethane solution at room temperature are displayed **Figure 17**, and the characteristic data are listed in **Table 8**. All complexes present similar absorption profiles to one another. In the UV region the spectra are dominated by an intense absorption band at around λ = 270 nm, attributed to ligand-centered transitions (^{1}LC). In the lower energy region (λ > 320 nm), absorption spectra are characteristic of Ir(III) complexes with a moderately-intense and broad band (320 to 450 nm) tailing up to 500 nm. This broad band could be assigned as ^{1}MLCT transition (dπ(Ir)→π*(C^N)).

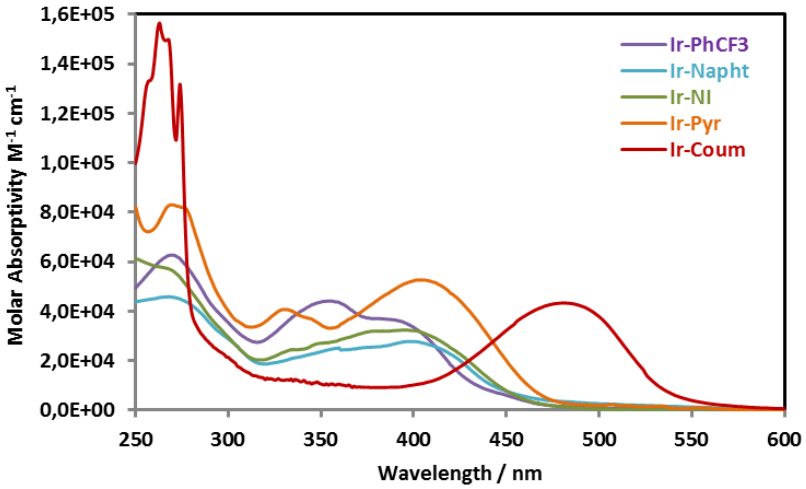

Figure 17. Absorption spectra of **Ir-PhCF$_3$**, **Ir-Napht**, **Ir-Pyr**, **Ir-NI** and **Ir-Coum** in CH_2Cl_2 solution at 298 K.

All the arylated complexes **Ir-Ar** display fluorescence in fluid solution at room temperature upon photoirradiation, the phosphorescence emission being quenched (**Figure 18**). This feature was previously observed for the tta-arylated complexes containing electron-donating substituents in the aryl group attached to the thiophene ring (C_6H_4-*p*OMe, C_6H_4-*p*-NH_2, 3-Cl-5-NH_2-C_6H_3).[31] All the emissions are insensitive to O_2, due to short-lived spin-allowed fluorescence from the singlet state. These results show the dramatic effect of incorporating an aromatic chromophore into the ancillary ligand. It is believed that extension of the π-conjugation of the ancillary ligand leads to a decrease of the spin-orbit coupling influence of the metal ion. Compared to the free ligands **ttaH-Ar**, the emission bands are red shifted (Δ = 86-124 nm), except for the NI-based derivatives for which the emission bands are located at the same energy. The quantum yields are very low in all cases ($\phi \leq 0.01$), except for the Ir-Coum complex which is strongly emissive (ϕ = 0.49). In order to detect emission from the triplet excited states, we performed luminescence studies at 77 K (EPA). Hovewer, no emission data could be obtained.

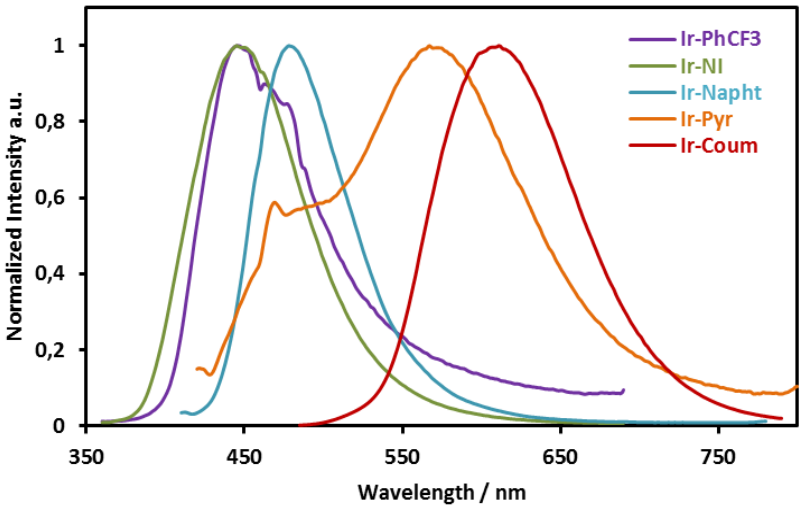

Figure 18. Normalized fluorescence spectra in CH_2Cl_2 at 298 K: **Ir-PhCF$_3$** (λ_{exc} = 350 nm) (purple), **Ir-Napht** (λ_{exc} = 400 nm) (Blue), **Ir-Pyr** (λ_{exc} = 410 nm) (orange), **Ir-NI** (λ_{exc} = 350 nm) (green), **Ir-Coum** (λ_{exc} = 475 nm) (red).

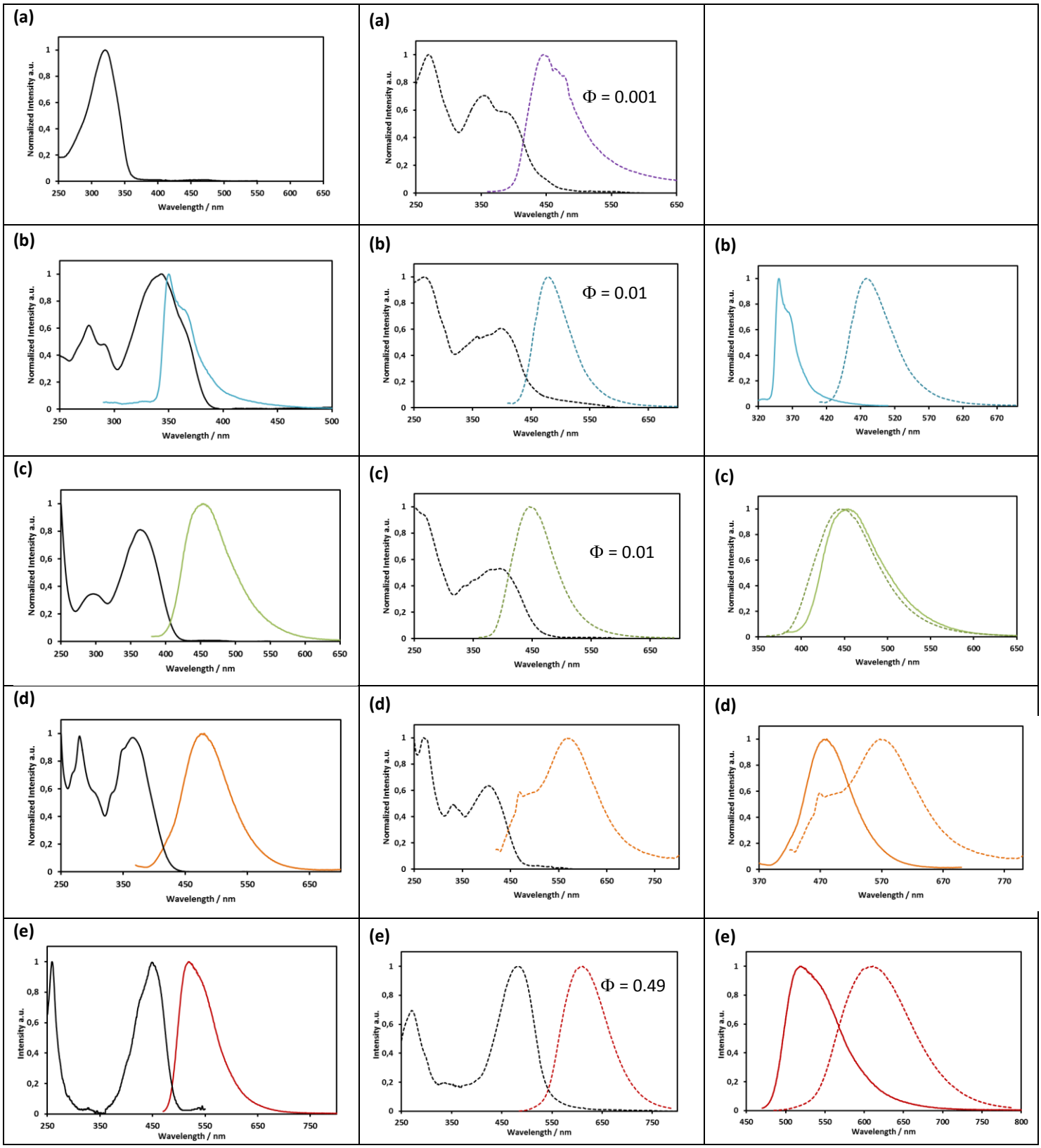

Normalized absorption spectra (black) and fluorescence spectra (in colour) in CH_2Cl_2 at 298 K **Left** (a) th-$PhCF_3$ (b) th-Napht (λ_{exc} = 320 nm) (Blue) (c) th-NI (λ_{exc} = 365 nm) (green) (d) th-Pyr (λ_{exc} = 360 nm) (orange) (e) th-Coum (λ_{exc} = 460 nm) (red). **Middle** (a) Ir-$PhCF_3$ (λ_{exc} = 350 nm) (purple) (b) Ir-Napht (λ_{exc} = 400 nm) (Blue) (c) Ir-NI (λ_{exc} = 350 nm) (green) (d) Ir-Pyr (λ_{exc} = 410 nm) (orange) (e) Ir-Coum (λ_{exc} = 475 nm) (red) **Right** Comparison of the normalized emission spectra of the ligands (plain) and the complexes (dotted) (b) th-Napht and Ir-Napht (c) th-NI and Ir-NI (d) th-Pyr and Ir-Pyr (e) th-Coum and Ir-Coum.

The emission spectrum of **Ir-PhCF$_3$** in EPA solution (ether/isopentane/ethanol (2:2:1 v/v)) at 77 K is displayed in **Figure 19**. The spectrum displays two sets of bands: a structured band around 500 nm and bands at 650 nm showing a vibrational structure. By comparison with the behaviour of the precursor complex Ir(C^N-Meppy)$_2$(O^O-tta), the high-energy band is likely to be due to the usual mixed d-π* / π-π* excited state associated with this core unit. The vibrational structure within the low-energy band is not clearly resolved and could be attributed to the triplet IL($\pi \rightarrow \pi^*$) state of state of the **tta-PhCF$_3$** ligand.

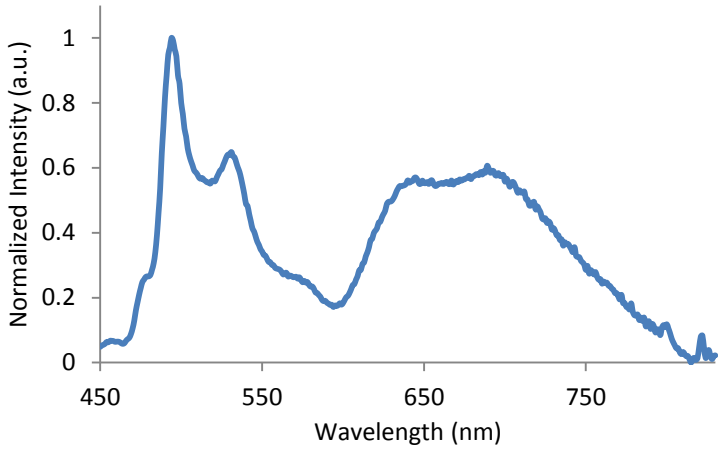

Figure 19. Emission spectrum at 77 K of **Ir-PhCF$_3$** in EPA solution

Table 8. Photophysical data of **Ir-tta-Ar** complexes

Complex	λ_{abs} / nm ($10^3.\varepsilon$ / L mol^{-1} cm^{-1})^a	ϕ	λ_{em} / nm 298 K^b
Ir-PhCF$_3$	275 (61.4), 359 (42.8), 394 (33.8)	0.001	440
Ir-Napht	275 (39.1), 364 (21.4), 400 (27.7)	0.01	473
Ir-Pyr	277 (87.1), 337 (42.0), 408 (52.2)	-	563
Ir-NI	270 (55.2), 400 (31.2)	0.01	440
Ir-Coum	260 (31.4), 482 (38.6)	0.49	600

3. Concluding Remarks

The direct approach of the arylation of chromophores on *fac*-I(thpy)$_3$ complex shows the selective formation of mono bis and tris- arylated iridium complexes (formation of *bis* and *tris* cyclometallated iridium complexes containing a naphthalimide or a pyrene unit and the unique mono arylated *fac*-Ir(thpy)$_3$ containing a coumarine unit). A yield of 40 % was observed for the preparation of the **39a**. Two different routes for the formation of the arylated

Ir(C^N-Meppy)$_2$(O^O-tta) were studied. The direct arylation of the naphthalimide on the metal complex requires mild conditions to avoid the degradation of the complex. Ir-NI was obtained in 16 % yields. The catalytic reaction on the organic compound was then used because of the better catalytic reaction yield.

The aromatic chromophore possesses a lower triplet state than the one of the complex *fac*-Ir(thpy)$_3$, leading to a phosphorescence quenching as this ligand triplet state is non-emissive at room temperature. The combination of these two – organic and organometallic – chromophores, leads to fluorescence at room temperature. The quantum yield of triplet *formation* is reduced in these systems, owing to the extension of the π-conjugation of the tta ligand, minimizing the heavy atom effect, whilst the efficency of triplet emission will be reduced for the same reason.

4. References

[1] M. G. Colombo, T. C. Brunold, T. Riedener, H. U. Güdel, M. Fortsch, H. B. Burgi, *Inorg. Chem.*, 1994, **33**, 545.

[2] M. G. Colombo, H. U. Güdel, *Inorg. Chem.*, 1993, **32**, 3081.

[3] K. A. McGee, K. R. Mann, *Inorg. Chem.*, 2007, **46**, 7800.

[4] T. Sajoto, P. I. Djurovich, A. B. Tamayo, J. Oxgaard, W. A. Goddard, M. E. Thompson, *J. Am. Chem. Soc.*, 2009, **131**, 9813.

[5] A.Tsuboyama, H. Iwawaki, M. Furugori, T. Mukaide, J. Kamatani, S. Igawa, T. Moriyama, S. Miura, T. Takiguchi, S. Okada, M. Hoshino, K. Ueno, *J. Am. Chem. Soc.*, 2003, **125**, 12971.

[6] C.-L. Ho, B. Yao, B. Zhang , K.-L. Wong, W.-Y.Wong, Z. Xie, L. Wang, Z. Lin, *J. Organomet. Chem.*, 2013, **730**, 144.

[7] V. L. Whittle, J. A. G. Williams, *Dalton Trans.*, 2009, **20**, 3929.

[8] (a) M. Lepeltier, H. Le Bozec, V. Guerchais, T. K.-M. Lee, K. K.-W. Lo, *Organometallics*, 2005, **24**, 6069.

(b) B. Matt, J. Moussa, L.-M. Chamoreau, C. Afonso, A. Proust, H. Amouri, G. Izzet, *Organometallics*, 2012, **31**, 35.

[9] (a) Y.-Q. Fang, M. I. J. Polson, G. S. H. Hanan, *Inorg. Chem.*, 2003, **42**, 5.

(b) K. J. Arm, J. A. G. Williams, *Chem. Commun.*, 2005, **2**, 230.

[10] (a) L. Chen, J. Roger, C. Bruneau, P. H. Dixneuf, H. Doucet, *Chem. Commun.*, 2011, **47**, 1872.

(b) J. Roger, F. Pozgan, H. Doucet, *Green Chem.*, 2009, **11**, 425.

[11] K. Beydoun, M. Zaarour, J. A. G. Williams, H. Doucet, V. Guerchais, *Chem. Commun.*, 2012, **48**, 1260.

[12] J. Sun, W. Wu, J. Zhao, *Chem. Eur. J.*, 2012, **18**, 8100.

[13] A. A. Rachford, R. Ziessel, T. Bura, P. Retailleau, F. N. Castellano, *Inorg. Chem.*, 2010, **49**, 3730.

[14] J. Sun, F. Zhong, X. Yi, J. Zhao, *Inorg. Chem.*, 2013, **52**, 6299.

[15] X. Yi, C. Zhang, S. Guo, J. Ma, J. Zhao, *Dalton Trans.*, 2014, **43**, 1672.

[16] L. Ma, S. Guo, J. Sun, C. Zhang, J. Zhao, H. Guo, *Dalton Trans.*, 2013, **42**, 6478.

[17] J. Sun, W. Wu, J. Zhao, *Chem. Eur. J.*, 2012, **18**, 8100.

[18] A. J. Hallett, N. White, W. Wu, X. Cui, P.N. Horton, S. J. Coles, J. Zhaob, S. J. A. Pope, *Chem. Commun.*, 2012, **48**, 10838.

[19] S.-Y. Takizawa, C. Pérez-Bolívar, P. Anzenbacher, S. Murata, *Eur. J. Inorg. Chem.*, 2012, 3975.

[20] L. Ma, H. Guo, Q. Li, S.Guo, J. Zhao, *Dalton Trans.*, 2012, **41**, 10680.

[21] G. Huimin, M.-S. Maria, W. Wenting, L. Xin, Z. Jianzhang, *Dalton Trans.*, 2011, **49**, 6802.

[22] R. H. Mitchell, Y.-H. Lai, R. V. Williams, *J. Org. Chem.*, 1979, **44**, 4733.

[23] S. Muhammadi, S. Reimann, K. Wittler, P. Langer, *Eur. J. Org. Chem.*, 2011, **27**, 5261.

[24] R. Debbas, P. K. Bharadwaj, *Inorg. Chem.*, 2008, **47**, 2252.

[25] S. Haiyang, G. Huimin, W. Wenting, L. Xin, Z. Jianzhang, *Dalton Trans.*, 2011, **40**, 7834.

[26] (a) A. A. Rachford, R. Ziessel, T. Bura, P. Retailleau, F. N. Castellano, *Inorg. Chem.*, 2010, **49**, 3730.

(b) J. Sun, F. Zhong, X. Yi, J. Zhao, *Inorg. Chem.* 2013, **52**, 6299.

(c) X. Yi, C. Zang, S. Guo, J. Ma, J. Zhao, *Dalton Trans*, 2014, **43**, 1672.

(d) L. Ma, S. Guo, J. Sun, C. Zhang, J. Zhao, H. Guo, *Dalton Trans*, 2013, **42**, 6478.

[27] A. J. Hallett, N. White, W. Wu, X. Cui, P. N. Horton, J. S. Coles, J. Zhao, S. J. A. Pope, *Chem. Commun.* **2012**, *48*, 10838.

[28] S. M. Borisov, I. Klimant, *Anal. Chem.*, 2007, **79**, 7501.

[29] S.-Y. Takizawa, C. Pérez-Bolivar, P. Anzenbacher, S. Murata, *Eur. J. Inorg. Chem.* **2012**, 3975.

[30] (a) M. C. DeRosa, D. J. Hodgson, G. D. Enright, B. Dawson, C. E. B. Evans and R. J. Crutchley, *J. Am. Chem. Soc.*, 2004, **126**, 7619.

(b) T. Yoshihara, Y. Yamaguchi, M. Hosaka, T. Takeuchi, S. Tobita, *Angew. Chem. Int. Ed*., 2012, **51**, 4148.

[31] K. Beydoun, M. Zaarour, J. A. G. Williams, T. Roisnel, V. Dorcet, A. Planchat, A. Boucekkine, D. Jacquemin, H. Doucet, V. Guerchais, *Inorg. Chem,*. 2013, **52**, 12416.

CHAPTER THREE:

Heavy-Metal Complexes Containing Tetradentate Ligands

1. Introduction

1.1. Cyclometallated Platinum Complexes of a Bidentate Ligands

The first cyclometallated Pt(II) complexes studied involved bidentate N^C type ligands (**Figure 1**).[1,2] These complexes can be divided into two classes: homoleptic complexes, which contain two identical N^C ligands simultaneously bound to platinum, *i.e.* $Pt(N^C)_2$,[1] and heteroleptic complexes,[2,3,4] which contain one N^C ligand and either a second bidentate ligand, L^L or L^X (examples include bipyridine or acetylacetonate, respectively), or two monodentate ligands L and X (*e.g.* CO and Cl). There are only a few examples of homoleptic complexes, probably due – at least in part – to the fact that their synthesis typically requires the use of lithiated ligands, a route that is intolerable to many functional groups. Such homoleptic complexes are always formed as the *cis* isomer, *i.e.* with the metallated carbon *trans* to the coordinated nitrogen of the other ligand, due to the large *trans* effect of cyclometallating carbon atoms which disfavours their disposition *trans* to one another.[5,6] $Pt(thpy)_2$ (thpy = 2-thienylpyridine) is phosphorescent at room temperature (λ_{max} = 578 nm) whereas Pt(ppy) is only emissive at 77 K (λ_{max} = 491 nm).[7] The literature contains more examples of heteroleptic complexes, as these are generally easier to synthesize. Unfortunately complexes involving these bidentate ligands are still prone to D_{2d} distortions in the excited state, which provide a pathway of non-radiative decay. As a consequence, the photophysical properties are often far from optimum, with quantum yields no more than 0.22 for the most luminescent of such systems.[2]

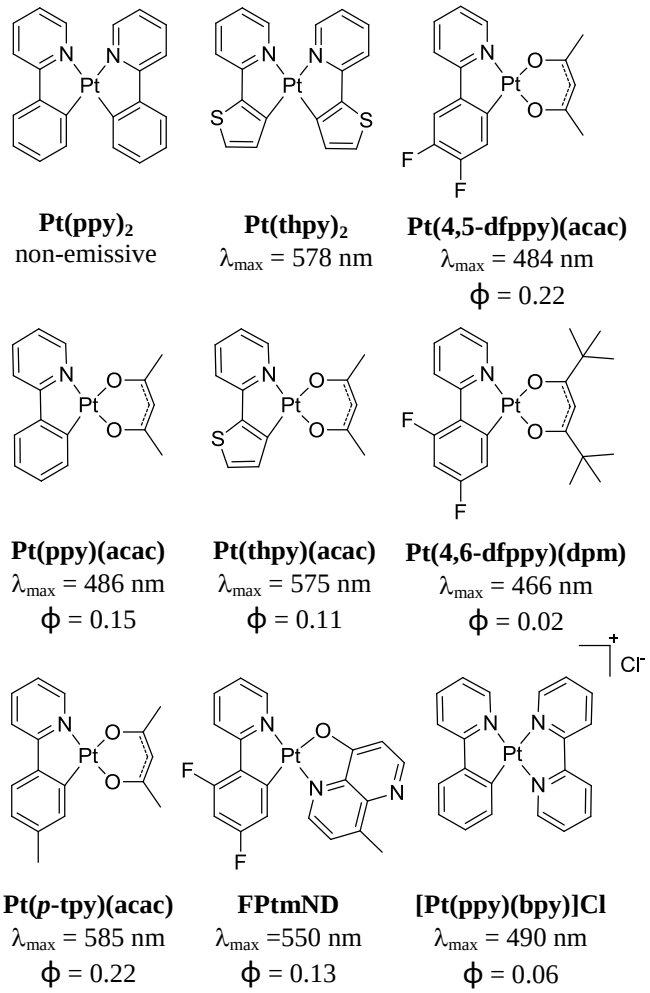

Figure 1. Examples of *bis*-cyclometallated platinum(II) complexes and their luminescent properties (λ_{max} and ϕ) at 298 K in acetonitrile (**Pt(ppy)$_2$** and **Pt(thpy)$_2$**); DCM (**FPtmND**), DMF (**[Pt(ppy)(bpy)]Cl**) and 2-methyltetrahydrofuran (**Pt(4,5-dfppy)(dpm), Pt(4,6-dfppy)(dpm)**, **Pt(ppy)(acac)**, **Pt(thpy)(acac)** and **Pt(*p*-tpy)(acac)**)[1,2,3,4,7]

1.2. Cyclometallated Platinum Complexes with Terdentate Ligands

An increase in the rigidity of the cyclometallating system may lead to enhanced luminescence quantum yields. Terdentate platinum complexes have been investigated to enhance the rigidity. Much of the work on Pt(N^N^C) systems has been developed by Che and co-workers, who have gone on to put the luminescence of such complexes to use in a number of applications.[8,9,10] In an early study, Che reported on the cyclometallation of 2,9-diphenyl-1,10-phenanthroline (dpp) to Pt(II) as a terdentate N^N^C-coordinating ligand, in which one of the two pendent phenyl rings cyclometallated, coplanar with the Pt(N^N) plane, whilst the other remains uncoordinated.[11] In their synthesis, the product isolated contained a labile MeCN molecule in the fourth coordination site (**Figure 2**).

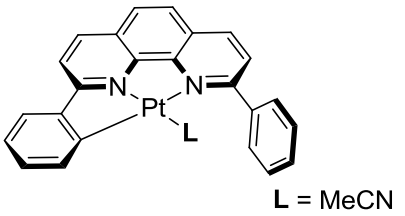

Figure 2. Terdentate C^N^N platinum(II) complex[11]

The perchlorate salt of this cationic complex proved to be highly emissive with a vibrationally structured spectrum, λ_{max} = 550 nm, τ = 14 μs and ϕ = 0.21 in dilute solution in DCM at room temperature. At higher concentrations, the monomer emission (*i.e.* luminescence from isolated molecules behaving independently of one another) is quenched, accompanied by the formation of an excimer that emits at about λ_{max} = 700 nm.

The chloride ligand in Pt(N^N^C)Cl complexes is quite labile, and can be displaced by other ligands. Yip *et al.* examined a series of four pyridyl adducts, [Pt(phbpy)(L)]ClO_4 where R = pyridine (py), 4-aminopyridine (4-ap), 2-aminopyridine (2-ap), and 2,6-diaminopyridine (dap) (**Figure 3**).[12] On the basis of absorption spectroscopy, the order of energy of the MLCT excited states was established as py ~ 4-ap > 2-ap > dap.

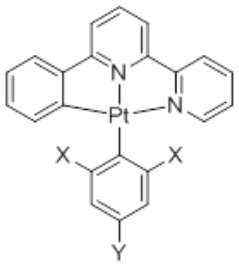

compound	X	Y
py	H, H	H
4-ap	H, H	NH_2
2-ap	NH_2, H	H
dap	NH_2, NH_2	H

Figure 3. Terdentate C^N^N platinum(II) complex[12]

In emission, the py and 4-ap complexes displayed structured, high-energy emission spectra (λ_{max} ~ 494 nm in MeCN at room temperature), assignable to $^3\pi$-π^* states. In contrast, the 2-ap complex emitted at substantially lower energy (λ_{max} = 534 nm), even though the σ-donating ability of 2-ap was similar to 4-ap. The results were interpreted in terms of the role of the *ortho*–NH_2 groups in destabilizing the Pt dπ orbitals, through intramolecular interactions of their lone pairs with the metal centre (**Figure 4**).

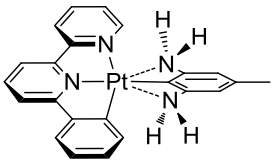

Figure 4. Geometry effect on the C^N^N platinum(II) complex[12]

The synthesis of a platinum complex with a single tetradentate ligand, offering four donor atoms to the metal, will simultaneously avoid the labile effect and the D_{2d} distortions in the excited state. Enhanced luminescent properties can be anticipated because of both stronger inhibition of the D_{2d} distortion caused by a high rigidity of the planar complex, and the elimination of a labile monodentate coordination site, which compromises the chemical stability and limits use in applications such as OLEDs or bio-imaging. Furthermore, since the metal is coordinated by only one ligand, the complex may also be advantageous in terms of thermal stability than bidentate and terdentate metal complexes.

1.3. Tetradentate Cyclometallated Platinum Complexes

1.3.1. Platinum complexes of "pseudocyclometallated" tetradentate Schiff-base ligands

- **O^N^N^O Systems**

In 2003, Wang *et al.* presented the synthesis of two Pt(O^N^N^O) complexes bearing *bis*(phenoxy)diimine ligands (where the diimine unit was 4,7-diphenyl-1,10-phenanthroline **1** or 4,4'-di-t-butyl-2,2'-bipyridine **2**). They are tetradentate relatives of the 8-hydroxyquinoline or quinolinolato (q) ligand, as found in the famous fluorescent metal complex Alq_3 for example (**Figure 5**).[13] These neutral Pt(II) complexes exhibit moderately intense, low-energy UV/Vis absorptions around 400-500 nm that undergo slight negative solvatochromic shifts (**Table 1**). Both derivatives are highly luminescent in solution at 298 K with emission lifetimes in the μs range. The functionalization on the pyridyl rings (*i.e. t*-butyl versus phenyl) does not affect the emission wavelength. However, a higher quantum yield and a longer luminescence lifetime was observed for **1** compared to **2**, attributed to the enhanced rigidity associated with the phen over the bpy unit.

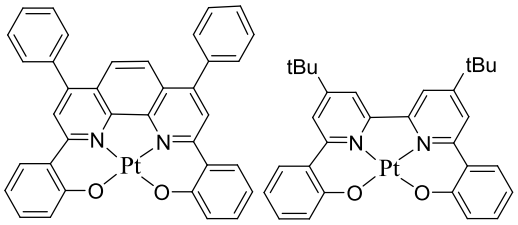

1 **2**

Figure 5. Tetradentate platinum(II) complexes **1** and **2** [13]

Table 1. Photophysical data for platinum(II) complexes **1** and **2** in degassed DCM solutions at 298 K [13]

Complex	λ_{abs}/nm (ε/ 10^3 L mol^{-1}cm^{-1})	λ_{em} / nm	τ / μs	ϕ
1	291 (39.2), 315 (34), 325 (32.3), 352 (25.8), 375 (24.7), 420 (5.2), 488 (sh, 6.7), 504 (7.2)	586	5.3	0.60
2	253 (41), 313 (18.4), 397 (8.4), 479 (2.94), 504 (sh, 2.52)	595	1.9	0.12

Many platinum(II) complexes of tetradentate Schiff base ligands have been investigated due to their good photophysical properties and the facile synthesis and functionalization of the Schiff base ligand.[14,15,16,17,18] A Schiff base is essentially a carbon-nitrogen double bond with the nitrogen connected to an aryl or an alkyl unit. For example, the synthesis of the platinum complexes **3**, **4** and **5** (**Figure 6**) consists of the reaction of K_2PtCl_4 with the appropriate ligand in the presence of a weak base to deprotonate the phenol, at 70 °C to 90 °C giving yields of 65 % to 85 %. All complexes showed good thermal stability and exhibited intense absorption bands with λ_{max} in the range 417–546 nm, which were assigned to states of metal-to-ligand charge-transfer ^{1}MLCT character mixed with *intra*-ligand charge-transfer ^{3}ILCT character. They exhibited emission between 550 and 592 nm with relatively low quantum yields (0.19 (**3**), 0.14 (**4**) and 0.087 (**5**)).

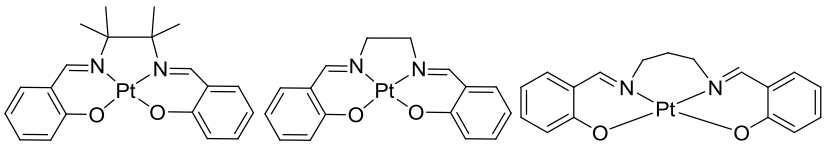

3 **4** **5**

Figure 6. Tetradentate platinum(II) complexes **3**, **4** and **5** [15]

- **N^N^N^N Systems**

All-nitrogen-coordinated (N^N^N^N) systems, where the nitrogen atoms can be provided by a combination of Schiff bases and heterocycles such as pyrrole or pyridine, have been developed and used for biology and OLEDs applications.[19,20,21,22,23] For example, in 2003, Lai *et al.* described the synthesis and the application in organic optoelectronics of neutral tetradentate *N*-donor platinum complexes **PtPren**, **6**, **PtPrtmen**, **7** and **PtPrdmPhen**, **8** (**Figure 7**).[24] These structures bear some resemblance to a porphyrinic unit, featuring two deprotonated pyrroles. **PtPrdmphen** emits at the lowest energy close to the NIR region, presumably due to its extended π-conjugated ligand system, but the quantum efficiency is very low (ϕ = 0.001). **PtPren** shows a yellow emission with a peak maximum at 566 nm and a shoulder at 613 nm in CH_3CN at 298 K. Compared with Pt(II) porphyrins, which often display long-lived red emission (τ ~ 80 μs), **PtPren** and **PtPrtmen** exhibit shorter luminescence lifetimes (τ = 4.2 and 3.6 μs, respectively) and reasonable quantum yields (ϕ = 0.09 and 0.10 respectively).

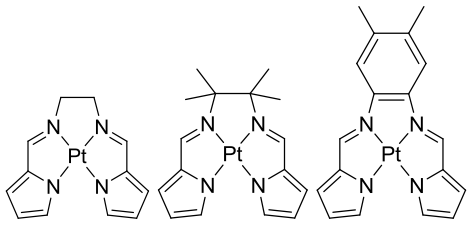

6 **7** **8**

Figure 7. Tetradentate platinum(II) complexes **6**, **7** and **8** [24]

- **N^C^C^N Systems**

In 2013, Che *et al.* have reported a series of new platinum(II) complexes functionalised with two carbenes and two phenolic units (**Figure 8**).[25] The photophysical investigation of these complexes showed that complex **14** does not emit at room temperature in solution whereas complex **11** shows an emission at λ_{em} = 460 nm with a quantum yield of 0.07. This difference was attributed to the higher distortion of complex **14** compared to complex **11,** leading to a high value of k_{nr} at room temperature and hence to a lack of detectable emission under these conditions. Complex **13** displays a red-shift of its absorption and emission (λ_{em} = 531 nm) compared to **11** due to the π extension. The interesting long lifetime (τ = 47.3 μs) was attributed to the lack of geometrical change in the molecule

between its ground state S_0 and triplet excited state T_1.This quasi-symmetry is postulated to lead to a low k_{nr} and a long lifetime.

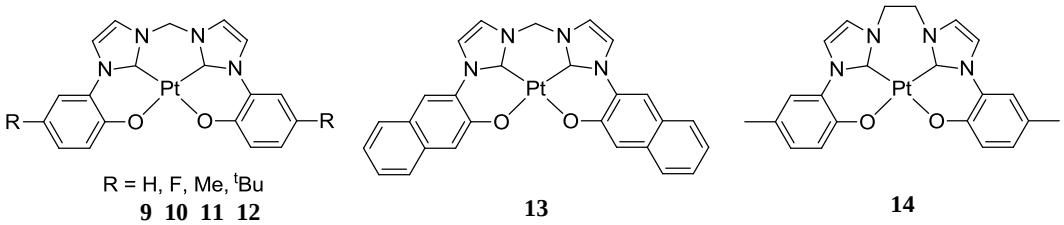

Figure 8. Platinum(II) complexes **9**, **10**, **11**, **12**, **13** and **14** bearing a tetradentate carbene ligand [25]

1.3.2. Cyclometallated Platinum Complexes

- **O^N^C^N**

Che and Li have recently investigated tetradentate O^N^C^N platinum complexes for application in OLEDs.[16,26,27,21] The formation of this kind of tetradentate complex was described as one deprotonation of an –OH group and a C–H activation at the position *trans* to the –OH unit. Double C–H activation in mutually *trans* positions is generally more difficult than in *cis* positions, as noted in **Section 1.1**, but the deprotonation of the relatively acidic –OH group (pK_a around 10) facilitates the formation of the Pt(II) complex, whilst leading to a charge-neutral product. A series of highly robust platinum(II) complexes **9-17** supported by tetradentate O^N^C^N ligands have been readily synthesized in high yields (≥ 80 %) and they have high thermal stabilities (Td >400°C).[27,28]

The first series of O^N^C^N Pt(II) complexes **15-19** (**Figure 9**) feature one 6-membered metallacycle and two 5-membered metallacycles. All complexes showed blue-green emissions and good photophysical properties with high emission quantum yields (ϕ = 0.72 to 0.93) and long luminescence lifetimes (τ = 11 μs to 28 μs, see **Table 2**).

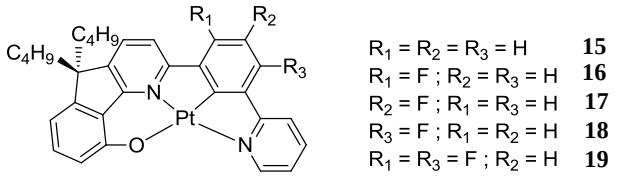

Figure 9. Tetradentate platinum(II) complexes **15-19** [28]

Table 2. Photophysical data for platinum complexes **9**-**13** in degassed DCM solution at 298 K [28]

Complex	λ_{abs}/ nm (ε/ 10^3 L mol^{-1}cm^{-1})	λ_{em} / nm	τ / μs	ϕ
15	254 (4.59), 280 (3.16), 354 (1.77), 390 (1.46), 426 (0.91)	485, 517, 557	12.0	0.72
16	254 (4.24), 261 (4.18), 290 (2.51), 352 (1.71), 388 (1.42), 429 (0.57)	488, 522	28.0	0.80
17	247 (3.72), 261 (3.43), 279 (2.67), 356 (1.52), 395 (1.15), 439 (0.70)	508, 543, 594	11.0	0.89
18	251 (4.82), 261 (4.55), 294 (2.07), 350 (1.83), 381 (1.40), 424 (0.86)	488, 518	13.2	0.93
19	245 (4.58), 259 (4.45), 289 (2.65), 3.01 (1.86), 349 (1.78), 376 (1.35), 424 (0.66)	482, 512	17.7	0.75

The second series of O^N^C^N Pt(II) complexes incorporate one 5-membered metallacycle and two 6-membered metallacycles. Complexes **20**, **21** and **22** (**Figure 10**) absorbed and emitted at lower energy (λ_{max} = 553 nm and 552 nm) than complexes **23** and **24** (λ_{max} = 526 nm and 527 nm) as the π extended conjugation is better for the carbazole than the phenoxazine or the phenothiazine (**Table 3**). The introduction of a bulky –^{t}Bu group on complexes **21** and **22** did not significantly change the photophysical properties.

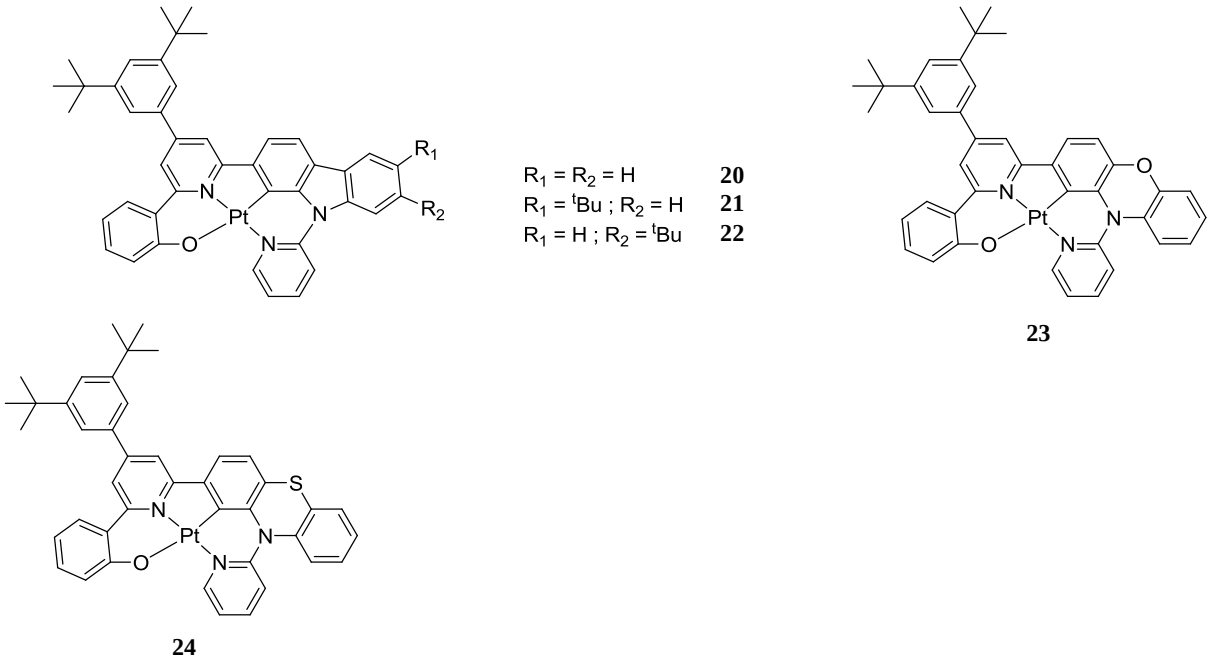

Figure 10. Tetradentate platinum(II) complexes **20**-**24** [27]

Table 3. Photophysical data for platinum complexes **14-18** in degassed DCM solution at 298 K [27]

Complex	λ_{abs}/nm (ε/ 10^3 L mol^{-1}cm^{-1})	λ_{em} / nm	τ / μs	ϕ
20	277 (5.21), 298 (4.78), 334 (4.07), 358 (2.34), 418 (0.92), 461 (0.41), 488 (0.35)	553 , 587	6.6, 6.8	0.86
21	278 (5.12), 298 (4.48), 336 (4.10), 358 (2.11), 415 (0.90), 460 (0.34), 487 (0.32)	553 , 590	7.4, 7.2	0.67
22	278 (5.27), 296 (4.52), 337 (4.32), 360 (2.12), 416 (1.08), 462 (0.39), 486 (0.34)	552 , 590	8.0, 7.6	0.82
23	280 (5.22), 322 (3.03), 385 (1.46), 443 (sh, 0.47)	526	5.9	0.47
24	281 (4.67), 327 (2.85), 354 (1.46), 379 (1.45), 453 (sh, 0.32)	527	8.8	0.49

- **C^N^N^C, N^C^C^N and C^C^N^N Systems**

➢ **C^N^N^C Systems**

bis-Cyclometallated platinum complexes with tetradentate C^N^N^C ligands are formed by the association of two bidentate N^C ligands through a linker Y (Y = CR_2, NR or O) in the examples reported to date.[29,30,31,32,33] Two C–H activations are necessary to form the final complex, whereas a simple deprotonation of oxygen, sulfur or nitrogen was involved for the synthesis of some of the previous tetradentate platinum complexes. Due to the linker, the rigidity of these complexes is expected to be higher than that of a *bis*-cyclometalled platinum complex with two bidentate ligands, and a structure forced closer to planarity might be anticipated.

Different coordination geometries of these tetradentate platinum complexes are possible (**Figure 11**): two symmetrical conformations named as C^N^N^C and N^C^C^N systems, featuring a C_2 axis through the metal and linker atom Y, and non-symmetrical named C^C^N^N and C^N^C^N systems. To date, examples of the first three are known, but no C^N^C^N tetradentate platinum complex has yet been synthesized.

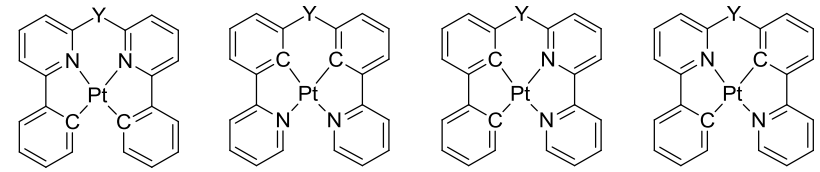

Figure 11. The « parent » complexes of the C^N^N^C, N^C^C^N, C^C^N^N and C^N^C^N systems

In 2009, Weck *et al.* investigated the first *bis*-cyclometallated tetradentate platinum complexes for application in OLEDs.[29] The interest was to append the platinum complexes onto a polymer through ring-opening metathesis co-polymerisation of norbornene-appended complexes with a norbornene-appended carbazole. Such an approach is feasible owing to the broad tolerance of most ruthenium olefin metathesis initiators, allowing for the direct covalent grafting of metal complexes onto poly(norborene)s in a "chemistry-on-the-complex" approach. (**Figure 12**). Complexes **25** and **26** were synthesized as models for complexes **27** and **28**. The synthesis of the functionalized poly(norborene) ligands involved a Grignard reaction between *bis*(2-(6-bromopyridyl))ketone and (norbornenylpentyl magnesium bromide)

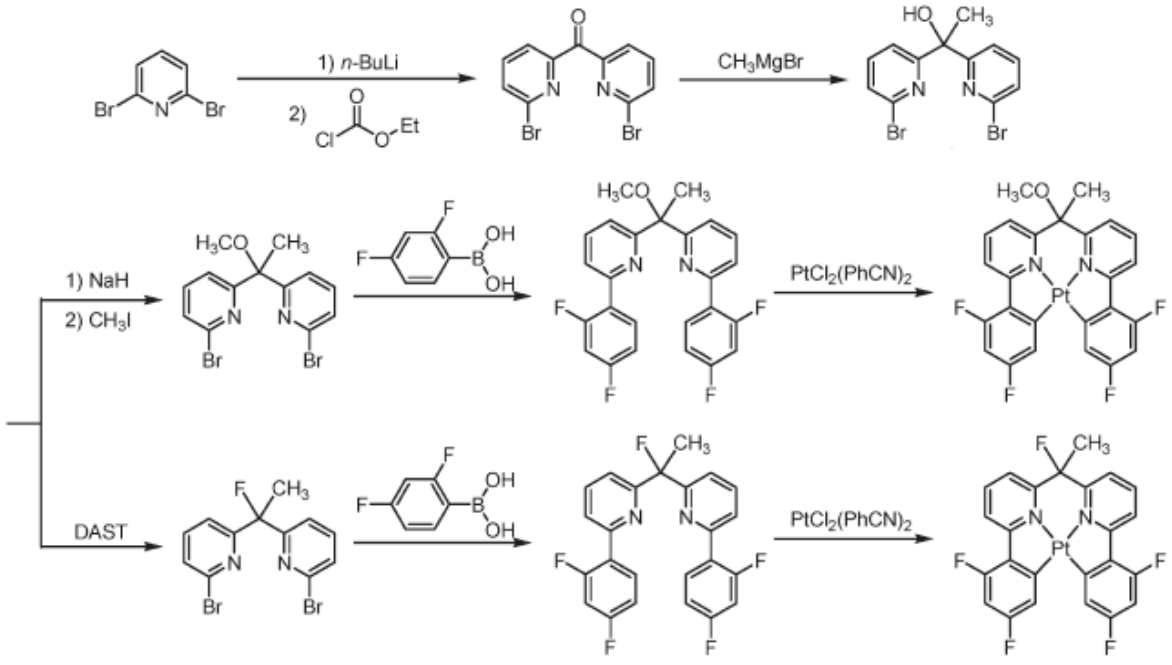

Scheme 1. Synthesis of C^N^N^C platinum complex **26**

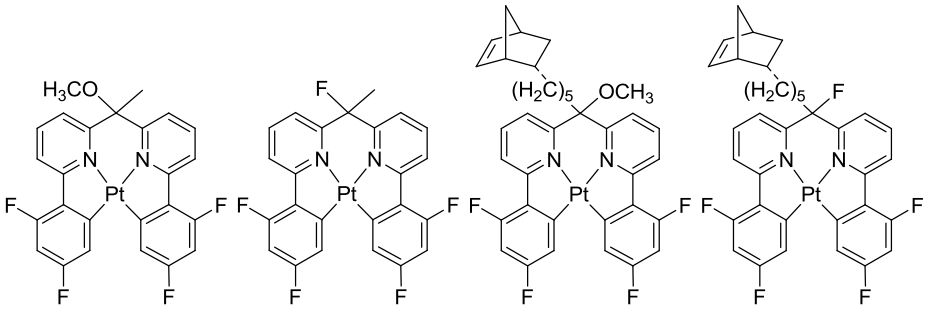

25 **26** **27** **28**

Figure 12. C^N^N^C platinum complexes **25-28**

The absorption and emission spectra were recorded in dichloromethane at 298 K (**Table 4**). All complexes exhibited intense structured absorption bands between 250 nm and 340 nm corresponding to the ILCT π-π* transitions and a medium-strength absorption band around 390 nm corresponding to the MLCT transition (**Figure 13**). They all emitted at λ_{max} = 492 nm, consistent with a ^{3}MLCT excited state, with quantum yields between 0.54 and 0.58 and lifetimes in the range 0.3-0.4 μs. The photophysics and the electrochemical studies of the non-functionalized and the norborene-substituted platinum complexes **25** and **26** showed similar results to the functionalized platinum complexes **27** and **28**. Thus, the functionalized polymer is a good host for the platinum complexes because of its lack of influence on the platinum-based properties.

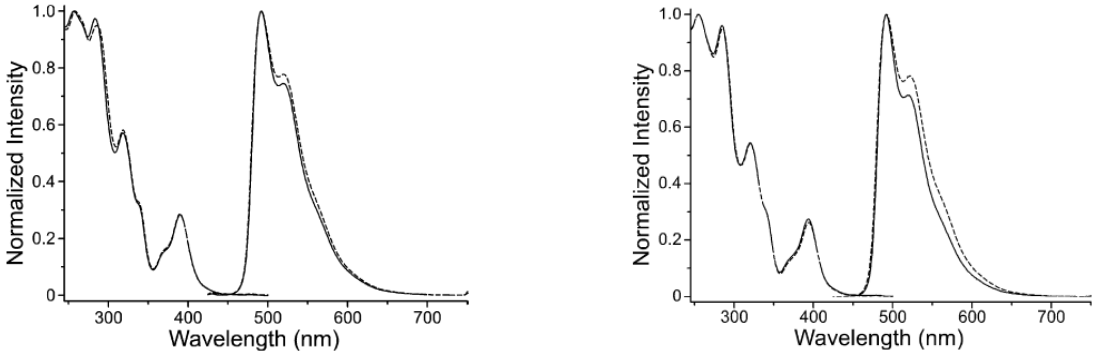

Figure 13. Comparison of the absorption and emission spectra between **25** (plain) and **26** (dashed) (left), and **27** (plain) and **28** (dashed) (right) in DCM at 298 K

Table 4. Photophysical data for platinum(II) complexes **25**, **26**, **27** and **28** in degassed dichloromethane solution at 298 K [29]

Complex	λ_{abs}/nm (ε/ 10^3 L $mol^{-1}cm^{-1}$)	λ_{em} / nm	τ / μs	ϕ
25	257 (33.2), 284 (32.3), 319 (19.0), 339 (10.5), 368 (4.92), 390 (9.42), 478 (0.89)	493, 525, 560 (sh)	0.38	0.54
26	255 (33.8), 284 (32.4), 320 (18.4), 340 (10.3), 369 (4.41), 394 (9.27), 478 (0.78)	492, 520, 564 (sh)	0.32	0.58
27	258 (33.3), 285 (31.6), 318 (19.3), 339 (10.8), 369 (5.24), 390 (9.52), 477 (0.81)	492, 520, 560 (sh)	0.39	0.56
28	255 (33.6), 285 (33.4), 321 (18.2), 341 (10.0), 370 (4.25), 394 (8.84), 478 (0.77)	492, 522, 564 (sh)	0.38	0.55

Huo *et al.* later showed the effect of the functionalization of tetradentate platinum complexes on the photophysical properties.[30] They used an amine linker as opposed to the carbon of the complexes of **Figure 12.** An amine linker is interesting for the high modularity it offers in ligand design and the simplicity of ligand synthesis. The complexes were prepared from the ligands using K_2PtCl_4 as the metal source, in the presence of a phase-transfer catalyst (Bu_4NCl) to facilitate the solubilisation in refluxing acetic acid.[31] DFT calculations of complexes **29** and **30** showed that the amine linker did not have any influence on the HOMO-LUMO energy gap. Furthermore, the HOMO was based on the phenyl rings and the metal while the LUMO was localized on the pyridine rings (**Figure 14**). The photophysical studies of complexes **29** and **30** were performed in 2-methyltetrahydrofuran solution at 298 K (**Table 5**). The presence of the fluorine in complex **30** had a hypsochromic effect on the absorption and the emission wavelengths (λ_{max} = 488 nm for complex **30** and λ_{max} = 512 nm for complex **29**), but the quantum yield was not affected (ϕ = 0.74 and 0.75, respectively). The luminescence lifetime slightly increased for complex **30** (τ = 11.4 μs) compared to complex **29** (τ = 7.6 μs).

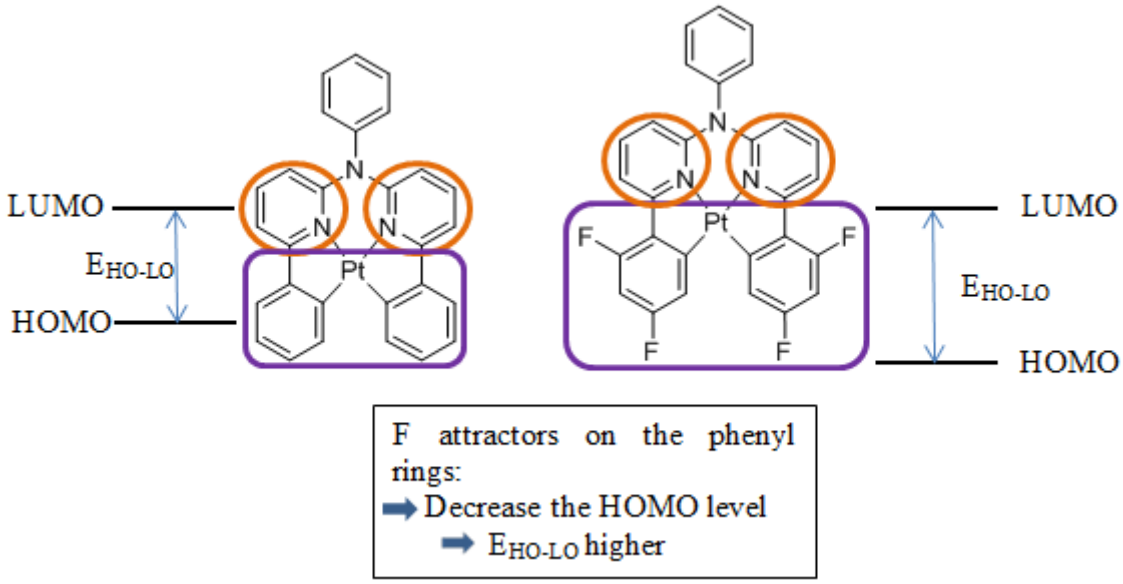

Figure 14. $E_{HO/LO}$ comparison between C^N^N^C platinum(II) complexes **29** (left) and **30** (right)

Table 5. Photophysical data for platinum(II) complexes **29** and **30** in degassed 2-methyltetrahydrofuran solution at 298 K [30]

Complex	λ_{abs}/nm (ε/ 10^3 L $mol^{-1}cm^{-1}$)	λ_{em} / nm	τ / μs	ϕ
29	324 (25229), 342 (26272), 384 (4903), 407 (5969)	512, 548	7.6	0.74
30	268 (29196), 329 (18970), 387 (3891)	488, 523	11.4	0.75

➢ N^C^C^N Systems

In the same paper, Huo *et al.* also studied the influence of the relative disposition of the ligating atoms on the photophysical properties.[24] They synthesized four N^C^C^N platinum(II) complexes **31**–**34** (**Figure 15**) based on the same procedure as that used for the C^N^N^C platinum(II) complexes. The DFT calculations again showed a HOMO based on the phenyl rings and the metal and a LUMO on the pyridyl or pyrazole rings. The luminescence was attributed to either MLCT, ILCT or mixed charge transfer (MMLLCT) transitions. The comparison between **31** and **32**, **33** and **34** showed a strong bathochromic shift of the luminescence (139 nm between **31**and **32**, for which λ_{max} = 613 and 474 nm respectively) (**Table 6**). As pyridine is a better acceptor than pyrazole, it will decrease the level of the LUMO and reduce the HOMO-LUMO gap to give a red-shift of the luminescence. The functionalization on the C^3 or C^4 position by a weak donor group such as methyl, does not have a significant effect on the emission wavelength.

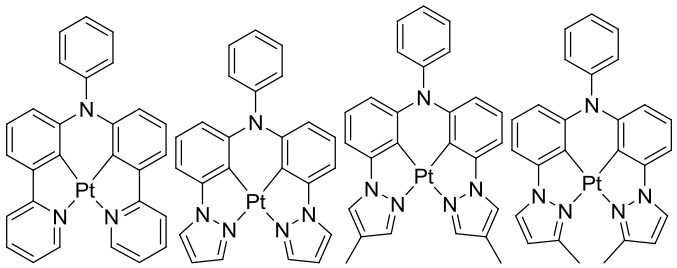

31 **32** **33** **34**

Figure 15. N^C^C^N platinum(II) complexes **31-34** [24]

Table 6. Photophysical data for platinum(II) complexes **31-34** in degassed 2-methyltetrahydrofuran solution at 298 K [24]

Complex	λ_{abs}/nm (ε/ 10^3 L $mol^{-1}cm^{-1}$)	λ_{em} / nm	τ / μs	ϕ
31	274 (28533), 324 (17411), 338 (17435), 409 (9656), 507(1350)	613	7.6	0.14
32	304 (21396), 334 (10307), 348 (13294), 365 (5021), 408 (1656), 428 (1401)	474	3.4	0.37
33	302 (34401), 335 (16243), 351 (28521), 370 (8493), 421 (3367), 442 (2880)	484, 512	4.9	0.56
34	307 (28076), 342 (10328), 357 (18193), 376 (4722), 428 (1835), 451 (1560)	486, 516	5.7	0.63

Li *et al.* demonstrated in 2013, the synthesis and the photophysical properties of three related tetradentate platinum complexes for application in OLEDs that incorporate oxygen linkers between the two N^C-coordinating units (**Figure 16**).[32] The emission of complex **37** in DCM was red-shifted (λ_{max} = 512 nm) compared to complexes **36** and **35** (λ_{max} = 430 nm and 468 nm respectively) and gave a higher quantum yield (**Table 7**). The greater electron-withdrawing ability of pyridine accounts for this shift. Pyridine is more electron-deficient than pyrazole or imidazole, so the LUMO level is lower in complex **37** than in complexes **35** and **36**. As a consequence, the HOMO-LUMO gap of complex **37** is lowest and its emission is red shifted.[24,32]

(Poorer acceptor) pyrazole < Imidazole < pyridine **(Better acceptor)**

When we compare complexes **37** and **29**, we can observe that the emission wavelength of complex **29** is similar to that for complex **37**, but its lifetime and quantum yield are longer and higher respectively (**Table 5 and 7**). The presence of two 6-membered and one 5-membered metallacycles for **31** compared to one 6-membered and two 5-membered

metallacycles for complex **29** may account for this difference, since **29** can be expected to be the more rigid system.

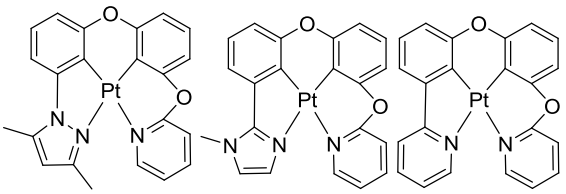

35 **36** **37**

Figure 16. N^C^C^N platinum(II) complexes **29-31** [32]

Table 7. Photophysical data for platinum(II) complexes **35-37** in degassed DCM solution at 298 K [32]

Complex	λ_{em} / nm	τ / μs	ϕ
35	430,456	3.0	0.39
36	468	9.0	0.64
37	512	2.0	0.63

- **C^C^N^N Systems**

In 2013, Huo *et al.* developed two platinum(II) complexes with the configuration C^C^N^N (**Figure 17**).[33] Complexes **38** containing a pyridyl ring and **39** a pyrazole unit were obtained in 38 % and 22 % yields, respectively. The photophysical data for complexes **38** and **39** in degassed DCM at 298 K (**Table 8**) show that the emission of complex **39** is blue-shifted (λ_{max} = 555 nm) compared to **39** (λ_{max} = 660 nm). Again, this can be rationalised in terms of the pyridine unit being a better acceptor than the pyrazole unit. Furthermore, the quantum yield of complex **39** is higher than that of **38** (ϕ = 0.17 and 0.001, respectively). Quantum yields are generally highest in the green region: they fall off towards the blue because of the role of higher-lying states and towards the red because of vibrational decay.

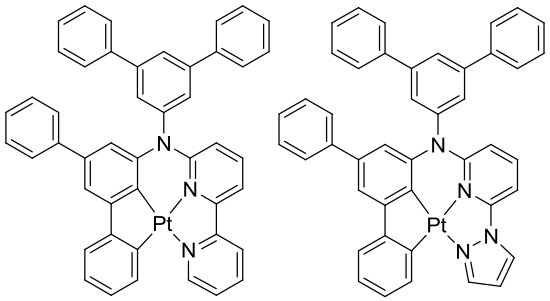

38 **39**

Figure 17. C^C^N^N platinum(II) complexes **38** and **39** [33]

Table 8. Photophysical data for platinum(II) complexes **38** and **39** in degassed DCM solution at 298 K [33]

Complex	λ_{abs}/nm (ε/ 10^3 L mol^{-1}cm^{-1})	λ_{em} / nm	τ / μs	ϕ
38	261 (27.3), 392 (10.3), 418 (8.5), 519 (2.3)	660	0.85	0.001
39	260 (26.5), 371 (12.9), 456 (2.7)	555	4.4	0.17

1.4. Tetradentate Palladium Complexes

Few palladium(II) complexes are luminescent in solution at room temperature. The smaller spin-orbit coupling (SOC) compared to platinum leads to smaller radiative rate constants, and very rigid systems are likely to be required to ensure that non-radiative decay is not overly competitive.[34] It is therefore not surprising that palladium(II) porphyrins are the most well-known Pd-based phosphors to date, typically emitting deep into the red region of the spectrum.

Klimant *et al.* have worked on luminescent Pd^{II}-porphyrins as oxygen sensors, and they recently prepared complexes of tetradentate O^N^N^O-coordinating Schiff base ligands for the same purpose.[35,36] A selection of these complexes (**48**, **49** and **50)** is shown in **Figure 18**.

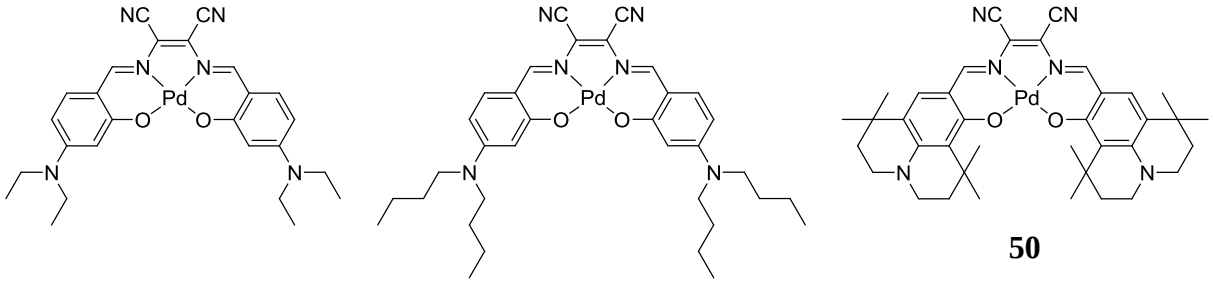

48 **49** **50**

Figure 18. O^N^N^O palladium(II) complexes **48**, **49** and **50** [35, 36]

The photophysical properties of these complexes were investigated in degassed toluene at 298 K (**Table 9**). All are weakly emissive in the red region (λ_{max} = 762 to 792 nm, $\phi \sim 10^{-2}$). Due to the long radiative decay constants associated with the smaller SOC of Pd(II) compared to Pt(II), the luminescence lifetimes (45 to 70 μs) are much longer than those of their platinum(II) analogues, which exhibit luminescence lifetimes of around 10 μs.

Table 9. Photophysical data of palladium(II) complexes **48**, **49** and **50** in degassed toluene solution at 298 K [35, 36]

Complex	λ_{max}em / nm	τ / μs	ϕ
48	763	45	0.012
49	762	70	0.023
50	792	57	0.016

In 2013, Che *et al.* synthesized and studied the first luminescent tetradentate O^N^C^N palladium complexes for applications in oxygen sensing, photocatalysis, or OLEDs (**Figure 19**).[37] To synthesize these palladium(II) complexes, they proceeded by the reaction between $Pd(OAc)_2$ and the corresponding ligand in acetic acid at reflux. Complexes **40**-**47** were obtained in yields of 50 to 80 %.

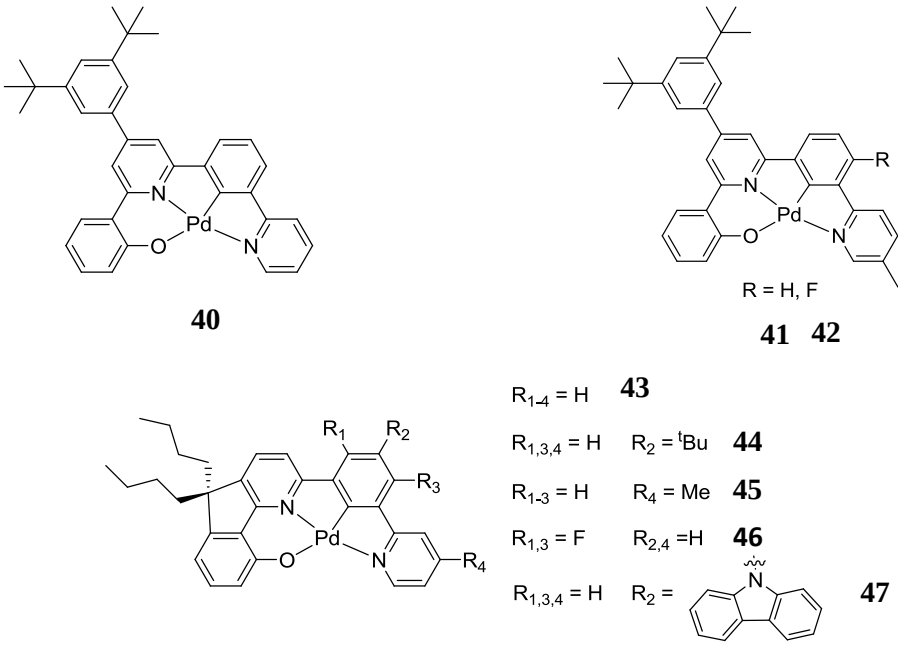

Figure 19. O^N^C^N palladium(II) complexes **40**-**47** [37]

The luminescence properties of these complexes were measured in degassed DCM at 298 K (**Table 10**). They are all moderately emissive under these conditions, exhibiting a green-yellow luminescence with λ_{max} between 517 and 540 nm. Compared to the platinum(II) analogue **9**, complex **40** showed a bathochromic shift of 55 nm and a decrease of its luminescence lifetime and its quantum yield.

Table 10. Photophysical data of palladium(II) complexes **40-47** in degassed DCM solution at 298 K, together with platinum(II) complex **15** for comparison. [28, 37]

Complex	λ_{max}^{em}/ nm	τ / μs	ϕ
40	540	0.4	0.0019
41	543	0.2	0.002
42	535	< 0.2	0.0016
43	527	105	0.15
44	498	121	0.20
45	527	122	0.17
46	517	62	0.22
47	536	83	0.14
15	485	12	0.72

The data in **Table 10** refer to degassed solutions. The luminescence of complex **44** showed a drastic decrease in intensity and lifetime in the presence of air, demonstrating the potential of such compounds for oxygen sensing. Furthermore, it was possible to oxidize a secondary amine by oxygen under light irradiation with complexes **43**-**46** as catalysts. Complex **46** showed the highest activity and generated the products with up to about 1650 turnovers in 2 h. Singlet oxygen sensitized by the triplet-excited Pd(II) complex is proposed to be the active oxidant.[38,39] This finding reveals that Pd(II) complexes containing non-porphyrin ligands may also possess rich photochemical properties analogous to those displayed by their Pt(II) counterparts. Notably, their smaller radiative decay constants can lead to exceptionally long lifetimes that may offer utility for applications to which Pt(II) analogues are less suited.

1.5. Objectives

It is clear from the overview given in the preceding sections that platinum(II) and palladium(II) complexes of tetradentate ligands may possess interesting photophysical properties, offering scope in diverse applications (*e.g.* OLEDs, catalysis, oxygen sensing, *etc*). Different ways to synthesize these complexes are possible. Depending on the rigidity and the functionalization of the tetradentate metal complex, we can observe a modulation of the luminescence properties.

In a first section of results presented in this Chapter, the synthesis, characterization and photophysical properties of platinum(II) and gold(III) complexes of a non-porphyrinic N^N^N^N-coordinating tetradentate ligand will be described (**Figure 20**). Their

photophysical data will be compared with corresponding metalloporphyrins and Pt(II) complexes with other tetradentate ligands.

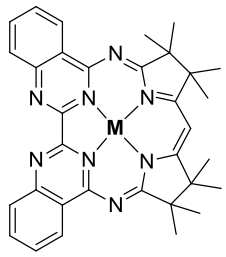

Figure 20. N^N^N^N heavy-metal complexes prepared and studied in this work

Secondly, a study of new C^N^N^C tetradentate platinum(II) complexes will be described (**Figure 21**). More electron rich and delocalized aryl rings have been introduced compared to previously described complexes, with a view to extending the emission wavelength into the red.

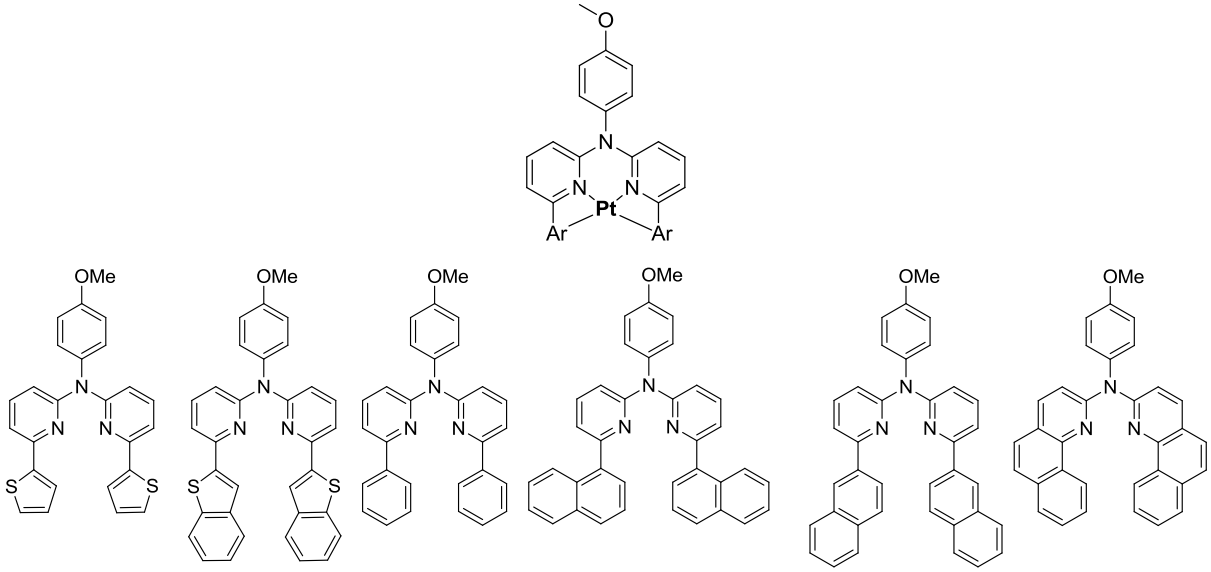

Figure 21. Summary of tetradentate C^N^N^C-coordinating ligands and their cyclmetallated platinum(II) complexes investigated in this work

The possible metallation of a palladium atom into such C^N^N^C tetradentate ligands will then be discussed, and the photophysical properties of the resulting complexes described (**Figure 22**).

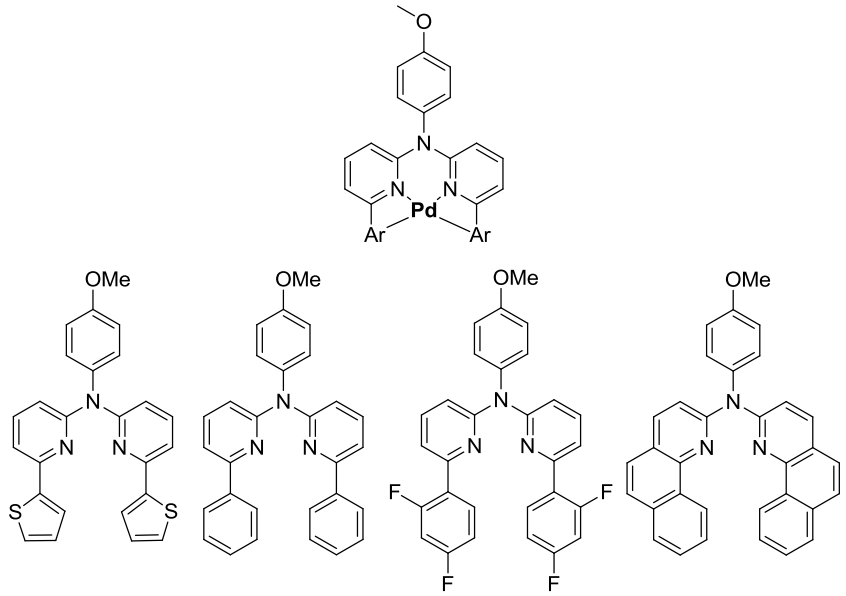

Figure 22. Summary of tetradentate C^N^N^C-coordinated palladium(II) complexes investigated in this work

Finally, the results of a preliminary exploration into the synthesis of iridium(III) and gold(III) complexes of such ligands will be presented.

2. Synthesis and Characterization of Tetradentate Heavy-Metal Complexes

2.1. N^N^N^N Tetradentate Heavy-Metal Complexes

2.1.1. Background

Porphyrin and phthalocyanine are both symmetrical macrocycles (C_4 axis when coordinated to a metal ion) used for dyes or application in biology. Porphyrins are comprised of four pyrrole units linked by CH units at the so-called *meso* positions. Phthalocyanine, in contrast, is composed of four iminoisoindoline units linked *via* nitrogen atoms at each of the four *meso* positions (**Figure 23**). Both macrocycles are dianionic and can bind metal atoms such as Fe, Co or Zn. The macrocycle known as MabiqH (**Figure 23**) is similar to porphyrin and phthalocyanine, but it is *mono*anionic (only one N–H available to deprotonate) and it incorporates an exocyclic N^N unit by virtue of the presence of the bipyrimidine, which could potentially coordinate a second metal ion. Von Zelewsky *et al.* first with cobalt complexes, and then Hess and coworkers with iron complexes demonstrate that the redox non-innocence of the diketiminates is a matter for consideration in the chemistry of metal complexes containing such ligands. Only a few T.M. complexes of this ligand have been prepared, and it was of interest in our work to explore, firstly, whether Pt(II), Pd(II) and

Au(III) complexes of Mabiq could be synthesised and secondly, how their photophysical properties would compare with those of metalloporphyrins. Although the main focus of this chapter is the synthesis and study of palladium and platinum complexes, Au(III) is also of interest, as it isoelectronic with Pt(II).

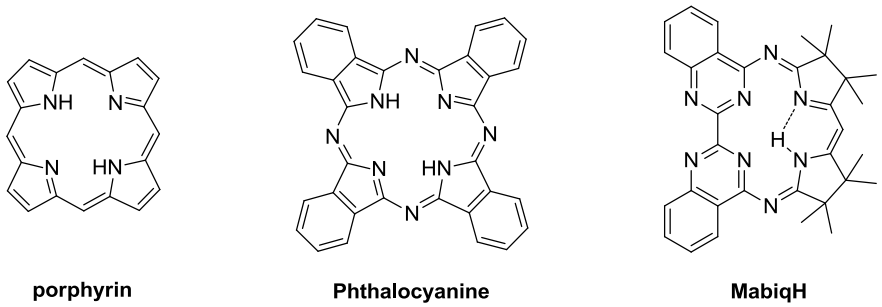

Figure 23. Representation of a porphyrin (dianionic), a phthalocyanine (dianionic) and a MabiqH (monoanionic) ligand

2.1.2. Synthesis

A sample of the proligand (H)Mabiq was provided by the group of Dr C. Hess at Durham. It was prepared according to the route originally devised by von Zelewsky (**Scheme 2**).[40] Two equivalents of 2-aminobenzamide reacted with acyl chloride to give an intermediate **I** which was sublimed at 350 °C to form **II**, and then chlorinated with PCl_5 to obtain the first bipyrimidine moiety **III** of the final product. Product **III** was finally reacted with (*bis*)amidine to give the H(Mabiq) ligand in 55 % yield.

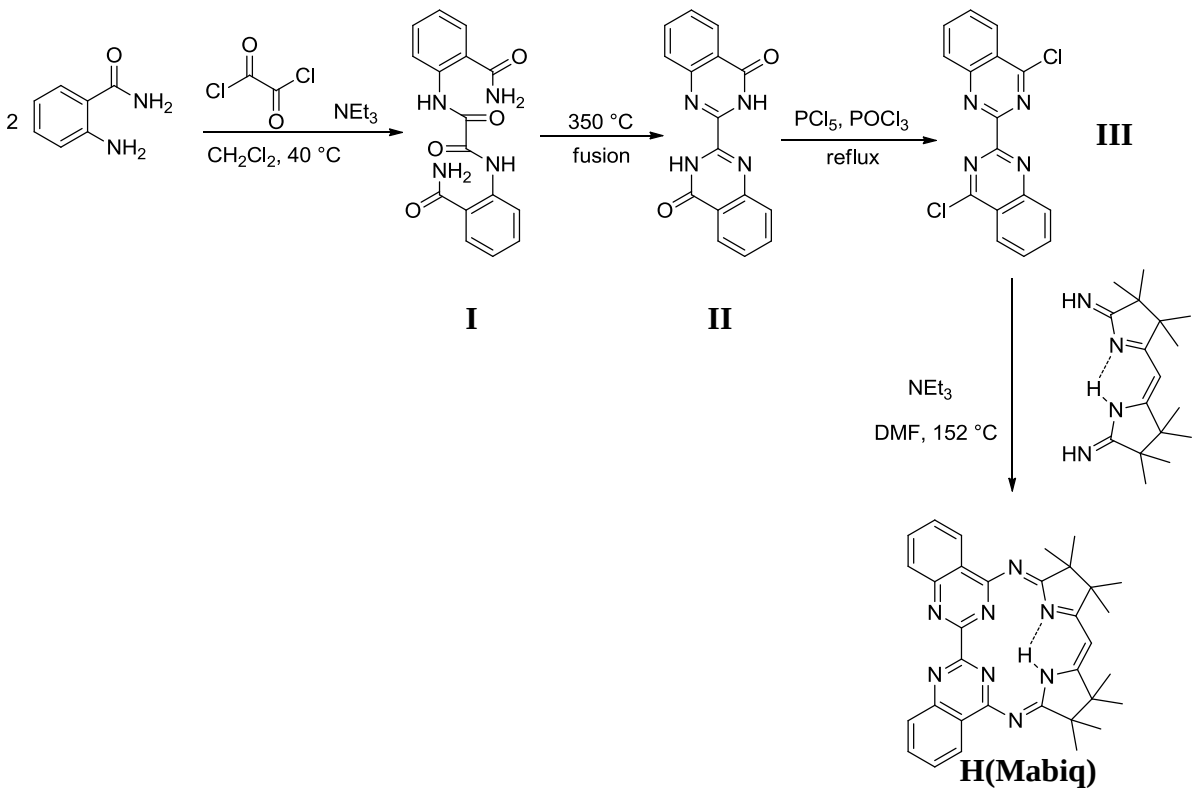

Scheme 2. Synthetic route of **H(Mabiq)** synthesis [40]

- **Synthesis of the platinum(II) complex of Mabiq**

The synthetic pathway to prepare **[PtMabiq]PF_6** has been inspired by the work of Yeaman's group on platinum tetraphenylporphyrins (TPP). **H(Mabiq)** and $PtCl_2(dmso)_2$ were dissolved in benzonitrile and heated at 190°C for 3 h (**Scheme 3**).[41] After cooling to room temperature, distilled water was added. The counterion exchange from Cl^- to PF_6^- was made after several washings of the crude product with EtOH and Et_2O. The orange-coloured complex was finally obtained by recrystallization from CH_3CN/ Et_2O, in 65 % yield.

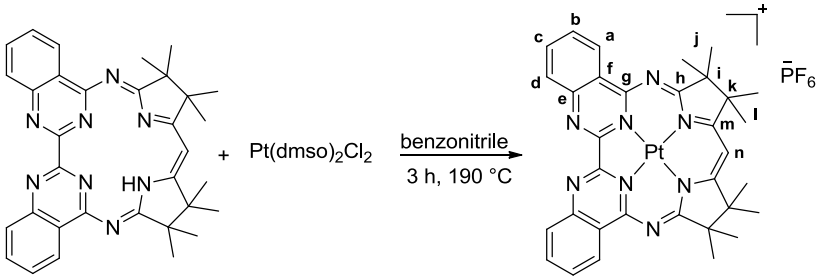

Scheme 3. Synthesis of **[PtMabiq]PF_6** [41]

- **Synthesis of the gold(III) complex of Mabiq**

The synthesis of **[AuMabiq](PF$_6$)$_2$** was performed following a similar procedure to that used by Kadish *et al.* for the preparation of gold(III) porphyrin.[42] A mixture of (**H)Mabiq**, potassium tetrachloroaurate(III) and NaOAc was heated at reflux in a mixture of toluene and glacial acetic acid for 10 min (**Scheme 4**). To exchange the chloride counterion to hexafluorophosphate and thus obtain a more soluble salt, the residue was dissolved in chloroform and stirred with a saturated solution of potassium hexafluorophosphate in water for 18 h. The yellow precipitate was isolated in 67 % yield.

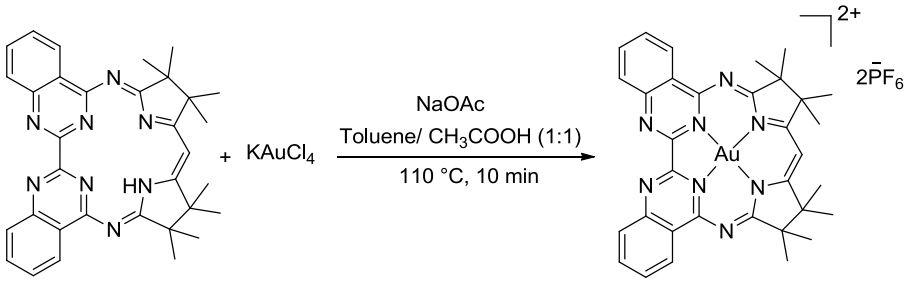

Scheme 4. Synthesis of **[AuMabiq](PF$_6$)$_2$** [42]

- **Attempted synthesis of the palladium(II) complex of Mabiq**

The synthesis of **[PdMabiq]PF$_6$** was attempted using a method inspired by Harvey *et al.*[43] Pd(OAc)$_2$ (1.1 equiv.) was added slowly to a solution of **H(Mabiq)** in 1,2-dichloroethane. The reaction mixture was heated at 110 °C for 12 h. The presence of the product was detected by an ^{1}H NMR spectrum of the crude reaction (as the major product) and by mass spectrometry, but all attempts to purify the crude product to date have been unsuccessful.

2.1.3. Characterization

- **NMR spectroscopy**

The ^{1}H NMR spectrum of **[PtMabiq]PF$_6$** was recorded in CD_3CN solution and **[AuMabiq](PF$_6$)$_2$** in DMSO-d_6 solution. Spectra are shown in **Figure**s **24** and **25**. The ^{1}H NMR spectrum of **[PtMabiq]PF$_6$** showed a slight shift in the aromatic protons and of the C–H protons of the diketiminate backbone compared with those spectra of the free ligand. The signal for the acidic cavity N–H proton of the free ligand, at 13.7 ppm, disappears upon

coordination of the metal ion. The same observation was made for the gold complex. For **[PtMabiq]PF_6**, two peaks in the alkyl region corresponded to the methyl protons of the dihydropyrrole backbone due to the C_2 symmetry axis through the Pt(II) and methane carbon of the molecule. **[AuMabiq]$(PF_6)_2$** displayed seven peaks in the aliphatic (methyl) region between 1.2 and 1.6 ppm, which suggests a lack of symmetry in the Au(III) complex in contrast to the Pt(II) analogue. An elemental analysis will show if the molecule is five-coordinate **[AuMabiqCl]PF_6** and not square-planar **[AuMabiq]$(PF_6)_2$** by oxidation with chloroform. The presence of the chloride ion on one face of the molecule would lead to the inequivalence of these methyl protons.

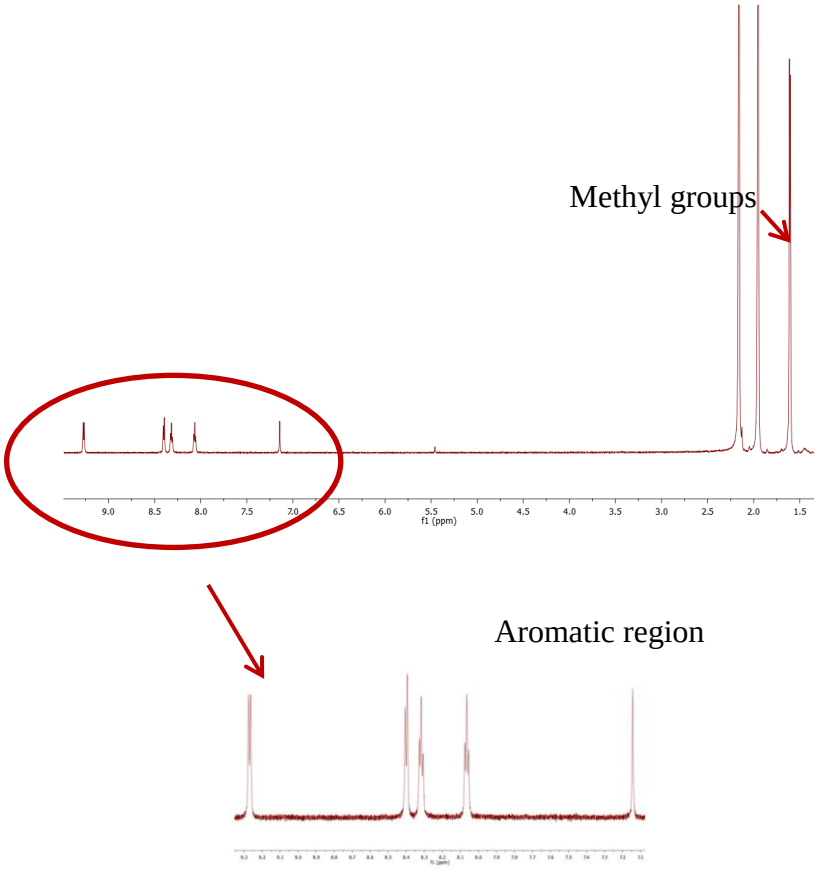

Figure 24. ^{1}H NMR of **[PtMabiq]PF_6** recorded at 700 MHz in CD_3CN at 298 K

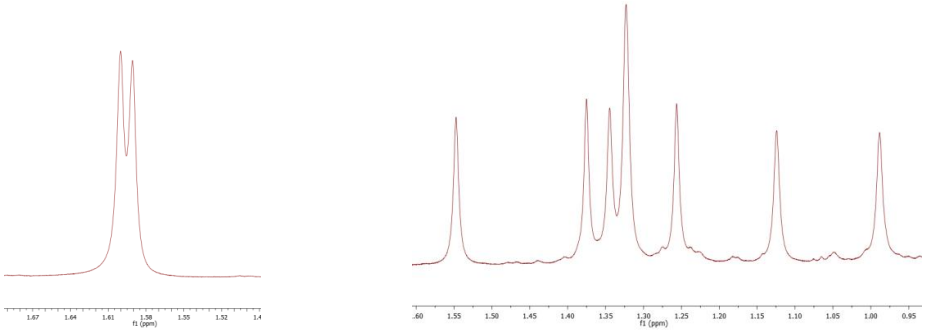

Figure 25. Aliphatic region of the ^{1}H NMR spectrum of **[PtMabiq]PF_6** (left) and **[AuMabiq]$(PF_6)_2$** (right) recorded at 700 MHz in CD_3CN and DMSO-d6 respectively at 298 K

- **Crystal structure**

Crystallisation of the platinum(II) complex was performed in MeCN by slow evaporation. The molecular structure of **[PtMabiq]PF_6** was determined by single crystal X-ray diffraction analysis at 100 K, which confirmed the tetradentate coordination structure and the cationic form of the platinum complex with the presence of PF_6 anions (**Figure 26**). The selected bond lengths and angles are listed in **Tables 11**.

A slight asymmetry is observed in the Pt–N bonds, with a distance of 1.97 Å to the bipyrimidine nitrogen atoms (N1, N2) versus a 1.95 Å bond to the diketiminate N atoms (N3, N4). The asymmetry in metal-nitrogen bond lengths arises from differences in the basicity of the two types of nitrogen donors, as observed for the previously reported **[Zn^{II}(Mabiq)Cl]** complex.[44] No Pt···Pt interactions were observed but **[PtMabiq]PF_6** displayed a quasi planarity of the PtN_4 core. In fact, the bipyrimidine unit was distorted at an angle of only ~ 3.63° from the coordinating diketiminate N-atoms whereas **[Zn^{II}(Mabiq)Cl]** showed a corresponding distortion of ~ 11.5°.

Figure 26. Molecular structure of **[PtMabiq]PF_6** complex

Table 11. Selected bond lengths (Å) and torsion angles (°) of **[PtMabiq]PF_6** (structure was acquired at 100 K). Data for **[ZnMabiqCl]** are included for comparison. [44]

Complex	**[PtMabiq]PF_6**	**[ZnMabiqCl]**
Torsion angle (°)	3.63	11.5

Complex	Bond lengths **Pt**–N^1	Bond lengths **Pt**–N^2	Bond lengths **Pt**–N^3	Bond lengths **Pt**–N^4

[PtMabiq]PF_6	1.974(3)	1.972(2)	1.958(3)	1.957(3)
[ZnMabiqCl]	2.090	2.090	2.030	2.030

- **Photophysical characterization**

The ground state absorbance spectrum of **[PtMabiq]PF_6** in dichloromethane solution is shown in **Figure 27** and photophysical data are summarized in **Table 12**. It showed two intense bands in the near UV region between 250 and 300 nm and between 300 and 400 nm corresponding to the $^1\pi$-π^* transitions of the ligands. These are accompanied by a weaker, lower energy feature centred at 452 nm, assigned to the ^{1}MLCT bands. The emission spectra in DCM at 298 K and in EPA at 77 K showed structured bands with maxima at 530 nm and 521 nm respectively. The well-defined vibronic structure that is observed even in solution at room temperature is typical of emission from ligand-centred excited states in rigid aromatic systems. The small hypsochromic shift on cooling to 77 K is typical of the rigidochromic effect associated with rigidification of the environment of the molecule when in a frozen glass. The complex displayed a lifetime of 2.3 μs and a quantum yield of 0.04. Whilst the quantum yield is comparable to that of, for example, PtTPP under the same conditions (TPP = tetraphenylporphyrin), the lifetime is much shorter (for PtTPP in DCM, t = 59 μs, ϕ = 0.046).[45]

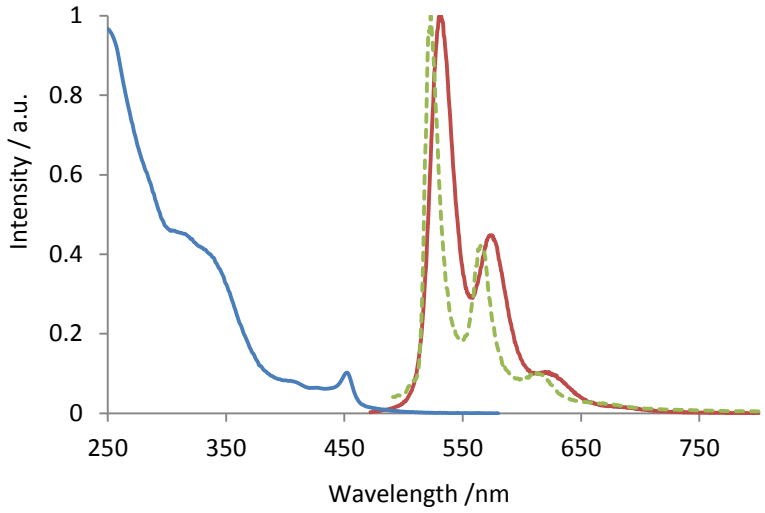

Figure 27. Normalized absorption spectrum of **[PtMabiq]PF_6** in DCM (blue line) and emission spectra in degassed DCM and in EPA solutions at 298 K and 77 K respectively (solid red and dashed green lines respectively).

Table 12. Photophysical data for **[PtMabiq]PF_6** in degassed DCM and EPA solution at 298 K and 77 K

Complex	λ_{abs} / nm	λ_{em} / nm	τ / μs	ϕ	λ_{em} / nm

[PtMabiq]PF_6	255, 335, 452	530, 574, 625	2.3	0.04	521, 563, 612
PtTPP[(a)]	400, 508, 538	668, 734	59	0.04	655, 728

(a) data from ref 45

- **Electrochemistry**

The cyclic voltammogram (CV) of **[PtMabiq]PF_6** was recorded in DCM (0.1 M $TBAPF_6$ as electrolyte) at 50, 100 and 200 mV s^{-1}. The CV exhibited two reversible waves centered at – 1.00 V and –1.85 V versus Fc^+/Fc (**Figure 28**). No oxidation wave was observed up to 2 V. Both electron transfer processes are assigned as ligand-centered reductions. The cyclic voltammogram (CV) of **[Zn(Mabiq)Cl]** showed a reversible one-electron redox wave centered at –1.4 V and an irreversible reductive process at –2.19 V. Both electron transfer processes were also assigned as ligand-centered reductions. CV of previously reported **[Fe(Mabiq)]** in THF displayed four distinct electron transfer processes, centered at 0.45 V, –0.93 V (one-electron oxidations), -1.79 and –2.45 V (one-electron reduction processes, 0.1 V s^{-1}, 0.2 M $TBAPF_6$).[44]

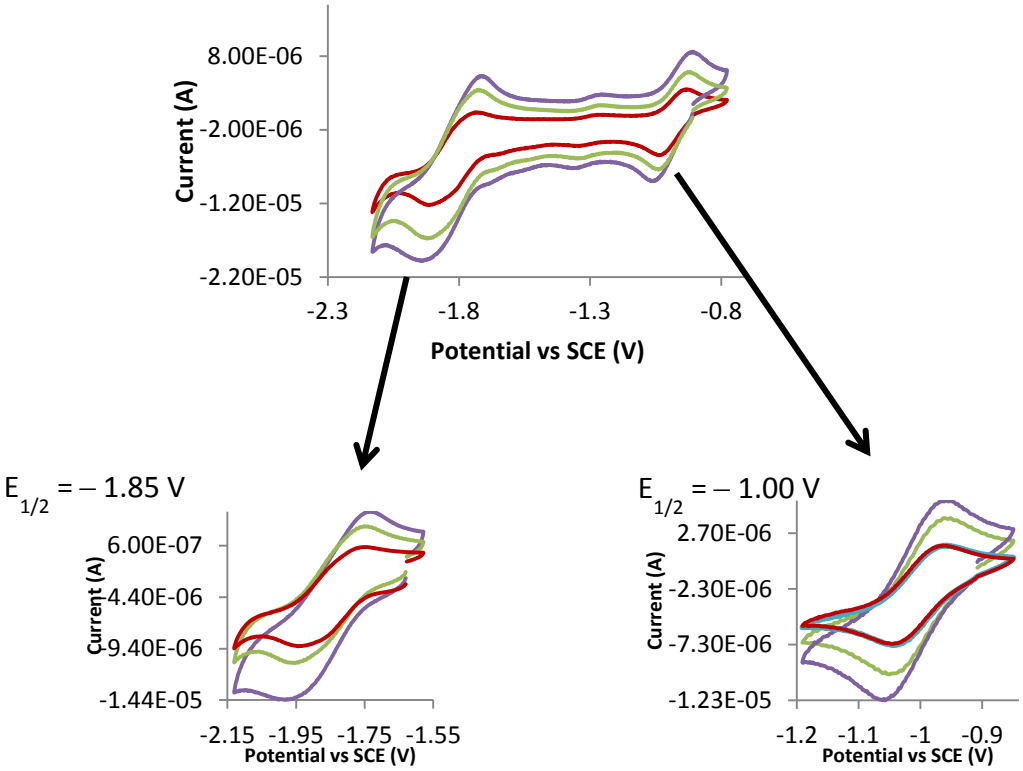

Figure 28. Cyclic voltammogram showing the two reversible reductions observed for **[PtMabiq]PF_6**. The scans were performed in degassed DCM, in the presence of a 0.1 M tetrabutylammonium hexafluorophosphate background electrolyte, at scan rates of 50, 100 and 200 mV s^{-1}.

2.2. C^N^N^C Tetradentate Platinum Complexes

2.2.1. Synthesis of the tetradentate ligands

The method used to prepare the tetradentate ligands was based on that used by Huo *et al*.[30] The first step for most of the ligands consists of a double Buchwald-Hartwig amination of a primary aryl amine with two equivalents of 2,6-dibromopyridine catalysed by palladium (**Scheme 5**).[46] In the present work, the aryl amine used was *p*-methoxyaniline – as opposed to unsubstituted aniline used by Huo – leading to bis(6-bromopyridin-2-yl)-N-(4-methoxyphenyl)-amine (**IV**) which features two mutually parallel C–Br bonds. The presence of the electron-donating methoxy group in the *para* position increases the nucleophilicity of the amine and facilitates the amination. In contrast, it has been found that electron-withdrawing groups at this position greatly retard the reaction, and indeed other side-products may form.[47]

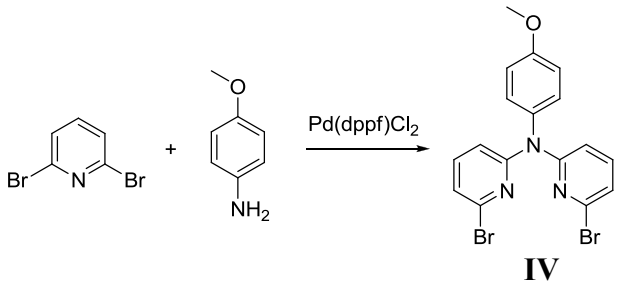

IV

Scheme 5. Synthesis of precursor **IV** *via* a Buchwald-Hartwig reaction

The subsequent step of the synthesis involves the Pd-catalysed coupling of the precursor either with aryl boronic acids (as used by Huo) or aryl stannanes. In general, the former are preferred owing to the benign nature of the boronate side products. The conditions are similar, although the Suzuki reaction requires the addition of base to convert the boronic acid into a boronate.

Ligands $\mathbf{L^1H_2}$-$\mathbf{L^6H_2}$ (**Scheme 6**) were prepared by Suzuki coupling with the requisite boronic acid, commercially available in each case. The general procedure involved the use of 3 equivalents of aryl boronic acid per equivalent of precursor **IV**, and an excess of sodium carbonate as the base. After prior degassing of this mixture, the palladium catalyst $Pd(PPh_3)_4$ was added under nitrogen flow and the reaction mixture was heated for 24 h. Dimethoxyethane at 80˚C was used as the solvent for $\mathbf{L^1H_2}$, $\mathbf{L^2H_2}$ and $\mathbf{L^3H_2}$, and toluene at 110˚C for $\mathbf{L^4H_2}$, $\mathbf{L^5H_2}$ and $\mathbf{L^6H_2}$, where a higher temperature was required in order to bring about the desired reaction. The crude product was obtained after addition of H_2O and extraction with CH_2Cl_2, and purification was carried out by column chromatography on silica.

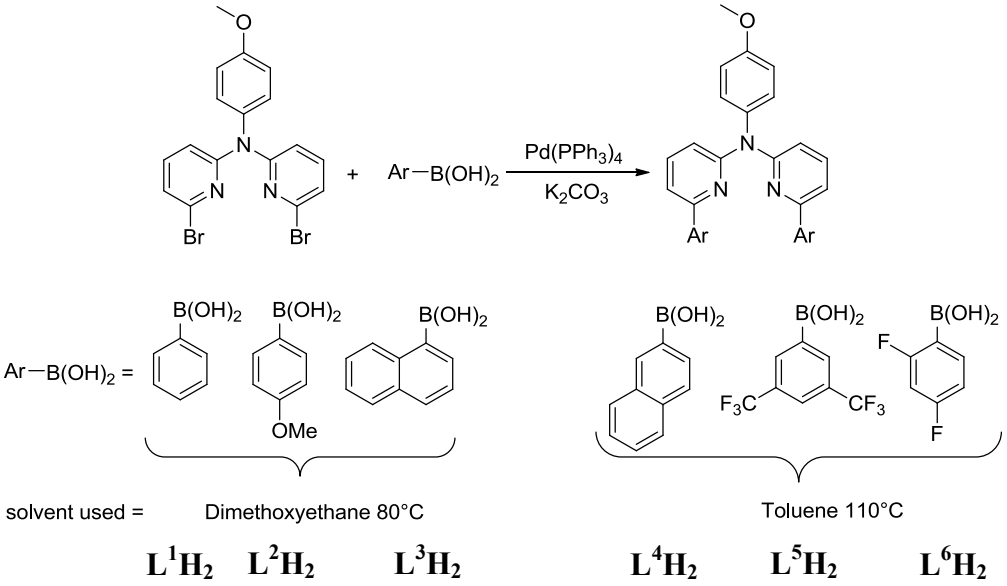

Scheme 6. Synthesis of $\mathbf{L^1H_2}$-$\mathbf{L^6H_2}$ tetradentate ligands *via* a Suzuki cross-coupling reaction

It is known that 2-thienylboronic acid is not always a good substrate for Suzuki reactions, showing a tendency to undergo competitive deboronation.[48] Ligand $\mathbf{L^7H_2}$ and its benzothienyl analogue $\mathbf{L^8H_2}$ were therefore prepared by Stille cross-coupling of precursor **IV** with the requisite aryl stannane, using *bis*(*tri*phenylphosphine)palladium(II) chloride as the catalyst, in the presence of lithium chloride (**Scheme 7**).

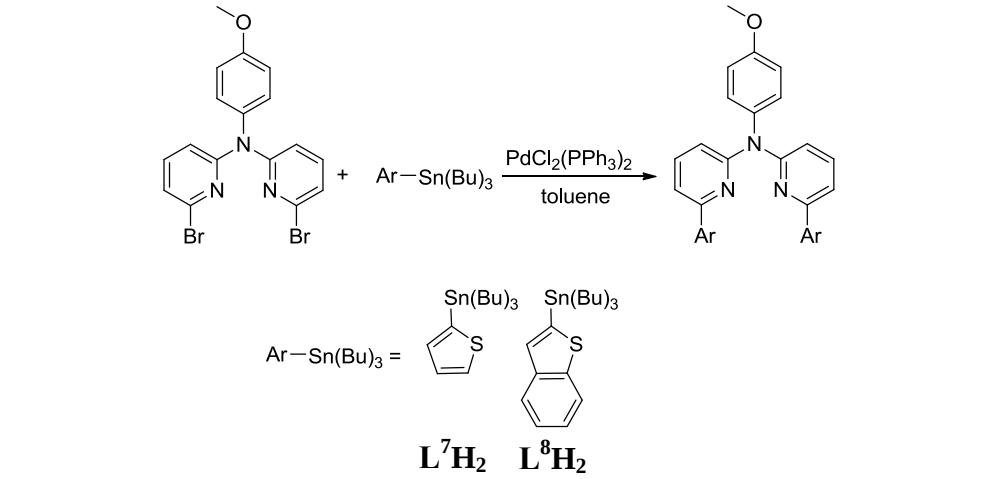

Scheme 7. Synthesis of $\mathbf{L^7H_2}$ and $\mathbf{L^8H_2}$ tetradentate ligands *via* a Stille cross-coupling reaction

A different synthetic method was used for the preparation of the tetradentate ligand incorporating benzoquinoline units $\mathbf{L^9H_2}$ (**Scheme 8**). Selective iodination of benzoquinoline at the 2-position was achieved, following a procedure reported by Mongin *et al.*[49] It consists

of directed lithiation at the position α to the nitrogen by BuLi in the presence of $ZnCl_2$TMEDA in hexane solution at 0 °C, followed by addition of iodine to give the precursor **V** in 78 % yield. Subsequent amination with *p*-methoxyaniline (0.5 equiv) under the same Buchwald-Hartwig conditions described earlier gave $\mathbf{L^9H_2}$ in 31 % yield.

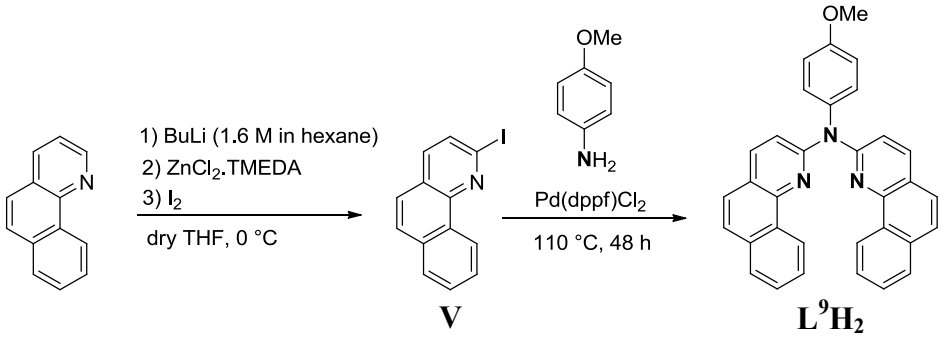

Scheme 8. Synthesis of precursor **V** and $\mathbf{L^9H_2}$ tetradentate ligand *via* regioselective iodination of benzoquinoline followed by Buchwald-Hartwig amination

2.2.2. Synthesis of platinum complexes

- Platinum(II) complexes

Cyclometallated platinum(II) complexes of arylpyridine ligands are typically prepared by reaction of the pro-ligand with K_2PtCl_4, often either in acetic acid as the solvent or a mixture of an organic solvent, such as MeCN, and water.[50,51] For the present series of compounds, the use of acetic acid was generally successful, after heating under reflux for 24 to 48 h under a nitrogen atmosphere (**Scheme 9**). Complexation of $\mathbf{L^6H_2}$ with K_2PtCl_4 was not performed.

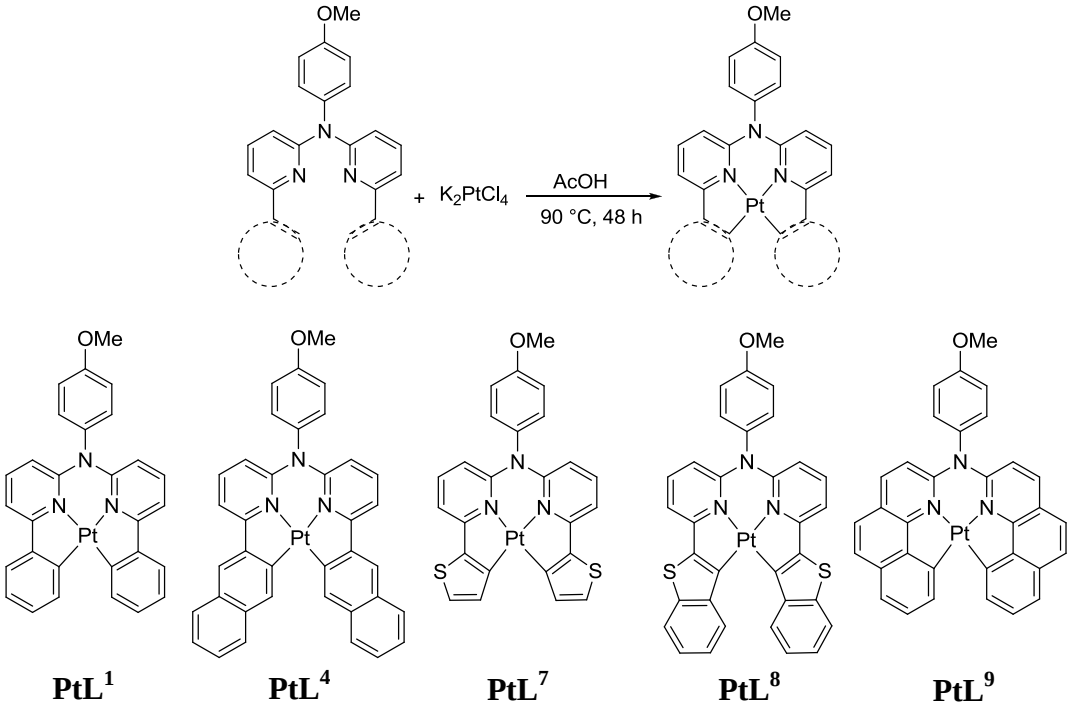

Scheme 9. Synthesis of platinum(II) complexes using $\mathbf{K_2PtCl_4}$ as reagent

In some cases, microwave irradiation was used instead. For example, the reaction of $\mathbf{L^4H_2}$ and K_2PtCl_4 in glacial acetic acid was performed under microwave irradiation at 160 °C for 30 min, giving a yield of 75 % compared to 55 % under conventional heating (**Scheme 10**). However, microwave irradiation was unsuccessful for the formation of $\mathbf{PtL^8}$, leading to degradation of the starting materials.

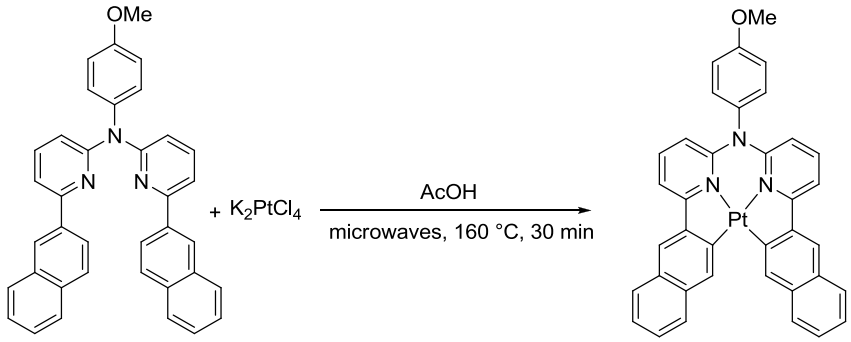

Scheme 10. Synthesis of platinum(II) complex *via* microwave reaction

In the case of $\mathbf{L^3H_2}$ and $\mathbf{L^5H_2}$, it did not prove possible to prepare the Pt(II) complexes. For $\mathbf{L^3H_2}$, a Pt(IV) complex was uniquely isolated (see below). Meanwhile, the attempted complexation of ligand $\mathbf{L^5H_2}$ to platinum under the same conditions as those used for $\mathbf{PtL^1}$ led to an unexpected product (**Figure 29**). On the basis of NMR spectroscopy and mass spectrometry, the product was identified as a pyrrolodipyridine compound **VI**. The ^{1}H NMR spectrum of the product **3** in $CDCl_3$ showed six signals in the aromatic region and one in the aliphatic region corresponding to the methyl of the compound. The six signals indicated symmetry of the molecule. In fact, there were four doublets, each integrating for two protons, and two singlets at 8.61 ppm and 7.92 ppm, integrating for four and two protons respectively. The comparison with the free ligand indicated that two protons are missing and a low frequency shift of all the protons.

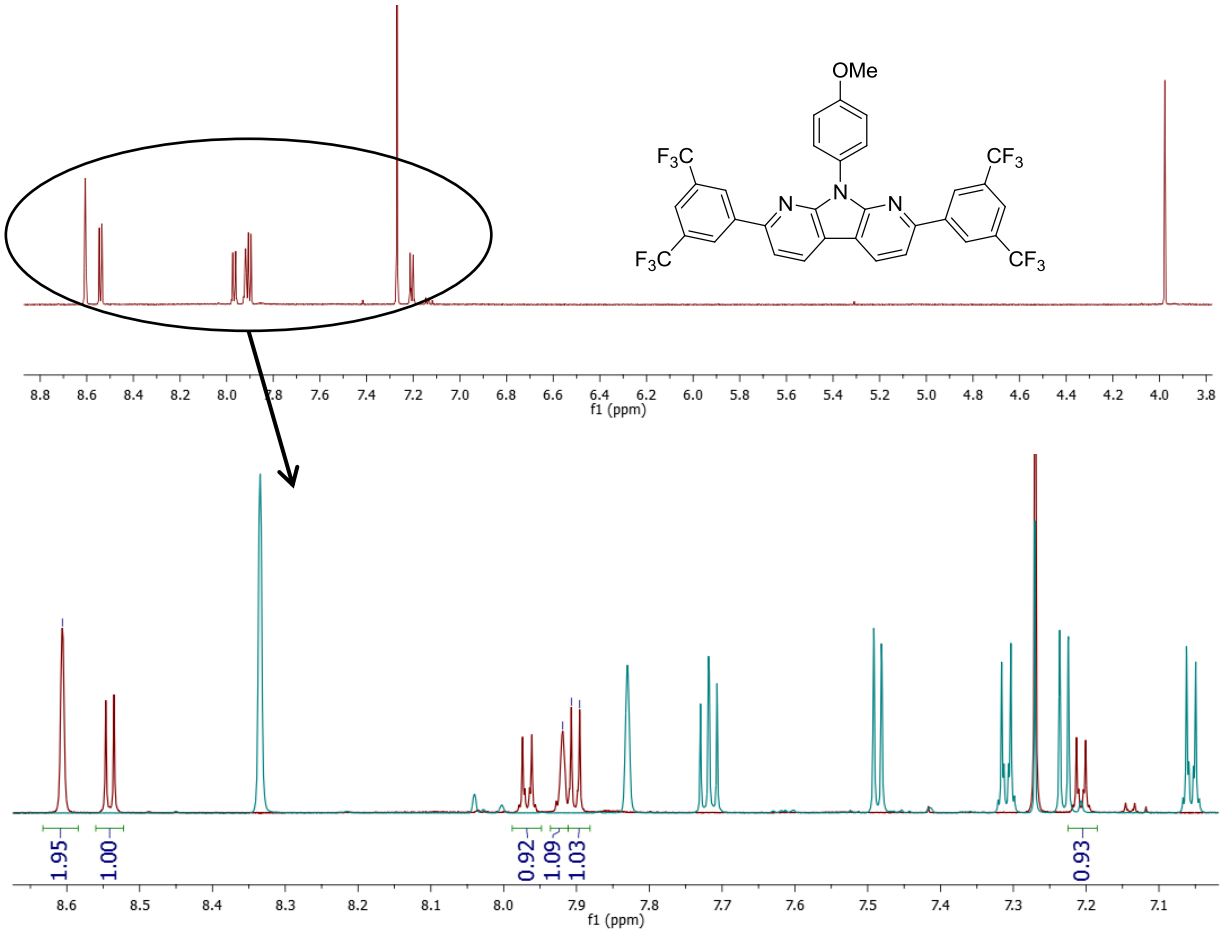

Figure 29. **TOP:** Full ^{1}H NMR spectrum of compound **VI** and **BOTTOM:** aromatic region of the overlaid ^{1}H NMR spectra of **VI** (red) and its precursor proligand $\mathbf{L^5H_2}$ (blue). Both spectra were recorded at 700 MHz in $CDCl_3$ at 298 K.

Previously, the synthesis of such pyrrolodipyridines has been performed by irradiation of the corresponding 2,2'-dipyridylamine for 48 h (yield = 53 %).[52] The generated product in our case was isolated in 53 % yield. There was no evidence of such a product being formed from the other proligands. Presumably, the CF_3 groups serve to deactivate the aryl rings to oxidative addition to Pt(II), and activation (metallation) of the 3 position of the pyridine occurs instead. [53,54] This leads to oxidative coupling of the two pyridyl units through the C^3 carbon atoms. It is noteworthy that the same proligand also gave an unexpected product with palladium too, different from the other proligands, showing metallation at one of the pyridyl C^3 positions (see Section **2.3.1** below).

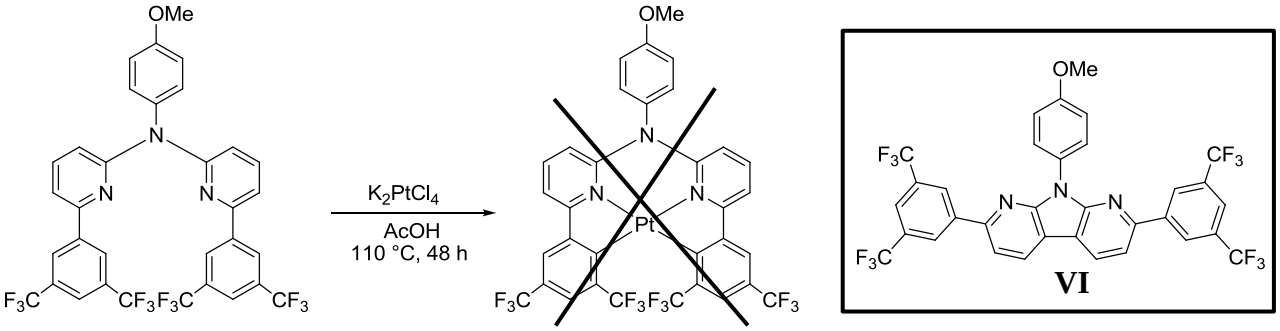

Scheme 11. Reaction between ligand $\mathbf{L^5H_2}$ and $\mathbf{K_2PtCl_4}$ leading to the unexpected organic product **VI**

Another metallation method was tested for $\mathbf{L^8H_2}$ to compare the reactivity and the yield of the final product obtained (**Scheme 12**).[55] The lithiation of the free ligand $\mathbf{L^8H_2}$ with a solution of BuLi (1.6 M in hexane) was performed at -78 °C in a mixture of THF/Et_2O. The lithiated precursor reacted with a platinum dimer $[PtMe_2(SMe_2)_2]_2$ at –10 °C to give $\mathbf{PtL^8}$ in 12 % yield.[56] The relative acidity of the α proton of the benzothiophene favored the regioselective lithiation, while a hazardous attack of the BuLi on the ligand $\mathbf{L^1H_2}$ or $\mathbf{L^7H_2}$ may not give the expected complexes. Indeed, following Holleman rules, when the substituent on the aryl reagent is an electron acceptor (as pyridyl) the electrophilic addition is favored in *meta* position. Nevertheless, the yield of the reaction is comparable to the reaction at high temperature in acetic acid.[57]

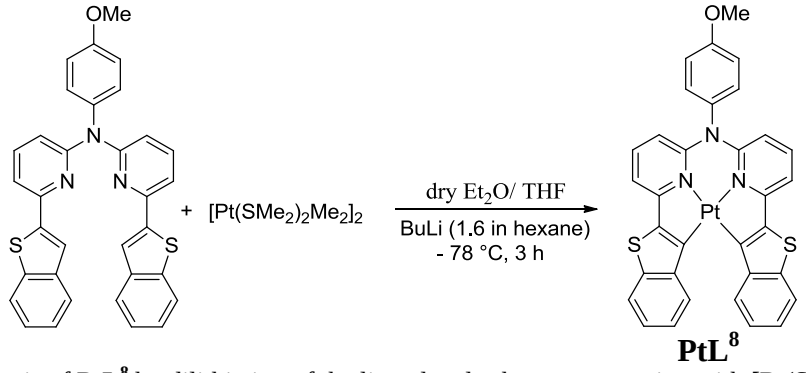

Scheme 12. Synthesis of $\mathbf{PtL^8}$ by dilithiation of the ligand and subsequent reaction with $\mathbf{[Pt(SMe_2)_2(Me)_2]_2}$

- **Platinum(IV) complexes**

$\mathbf{PtL^4}$ and $\mathbf{PtL^8}$ were oxidized to their corresponding Pt(IV) complexes $\mathbf{PtL^4Cl_2}$ and $\mathbf{PtL^8Cl_2}$ by bubbling Cl_2 gas through a solution of the Pt(II) complex in chloroform (**Scheme 13**). The reactions were performed in the dark to avoid the light-activated decomposition of the platinum(IV) complexes. The yellow colour of the initial solution was discharged within 1 hour of reaction, which provided a visual indication of the oxidation to Pt(IV).

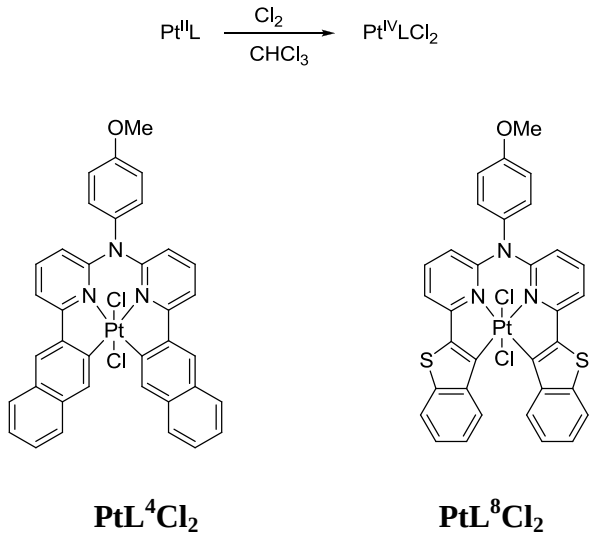

Scheme 13. Oxidation reaction of **PtL**^{4} and **PtL**^{8}

The reaction between K_2PtCl_4 and the free ligand $\mathbf{L^2H_2}$ and $\mathbf{L^3H_2}$ led *directly* to the oxidized Pt(IV) forms alone $\mathbf{PtL^2Cl_2}$ and $\mathbf{PtL^3Cl_2}$ (**Figure 30**). The identity of the compound $\mathbf{PtL^3Cl_2}$ was proved by the crystal structure showing the two chlorides in axial positions. The reaction was performed under the same conditions as for all the other ligands, namely in AcOH at reflux under a nitrogen atmosphere. The result was repeatable, ruling out the possibility of adventitious ingress of oxygen on one specific occasion, for example. Thus it seems that in this case, the stability of the Pt(IV) complex is higher than that of its Pt(II) analogue.

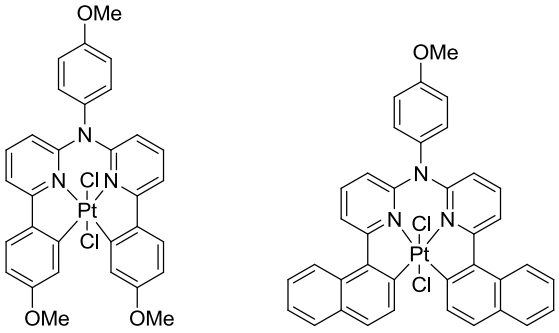

Figure 30. $\mathbf{PtL^2Cl_2}$ (left) and $\mathbf{PtL^3Cl_2}$ (right) complexes

2.2.3. Characterization of Platinum complexes

- **NMR spectroscopy**

➢ **Comparison of the proligand $\mathbf{L^1H_2}$ with its Pt(II) complex $\mathbf{PtL^1}$**

The ^{1}H and $^{13}C\{^{1}H\}$ NMR spectra of the ligands and their square-planar platinum(II) complexes showed the expected C_2 symmetry of the molecules along the anilino N···OMe

and the metal axis (**Figure 31**). This effect was apparent from the presence of 10 signals in the ^{1}H NMR and 16 signals in the ^{13}C {^{1}H} NMR spectra. The metallation of the ligand **L^{1}H$_2$** to **PtL^{1}** was clearly indicated by the integral value (two protons are "missing" relative to the proligand) and the appearance of characteristic satellites flanking the signal of H^{e} due to coupling to ^{195}Pt, ^{3}J (^{195}Pt–H) = 25 Hz.

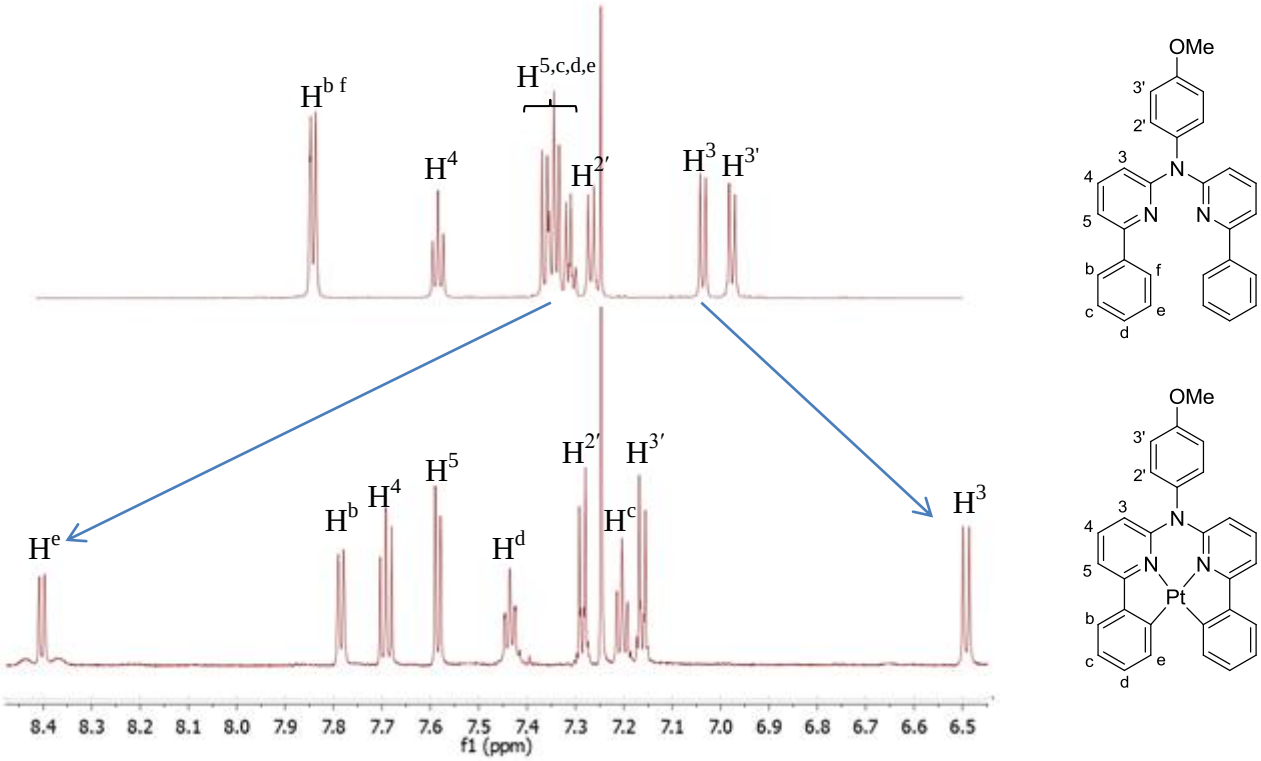

Figure 31. **TOP:** ^{1}H NMR spectrum (700 MHz) of the proligand **L^{1}H$_2$** and **BOTTOM:** ^{1}H NMR spectrum (600 MHz) of the corresponding platinum complex **PtL^{1}**. All spectra were recorded in $CDCl_3$ at 298 K. Notice the ^{195}Pt satellites observed around the peak corresponding to H^{e} in the complex: $^{3}J(^{195}\text{Pt–H}) = 25$ Hz.

In **PtL^{1}** complex, the aromatic ring current of the phenyl ring connected to the anisidine nitrogen atom influences the protons of the pyridyl ring. Indeed, the anisyl ring is expected to be essentially perpendicular to the rest of the complex (**Figure 32**), as confirmed by crystallography (see below). As a consequence, the chemical shift of H^{3} protons was shielded to δ = 6.5 ppm compared to the free ligand for which the corresponding value was 7.0 ppm. This phenomenon was not observed for the free ligand because of its free rotation about the C–N (pyridyl–anilino) bond. The metallation brings more rigidity to the molecule compared to the free ligand.

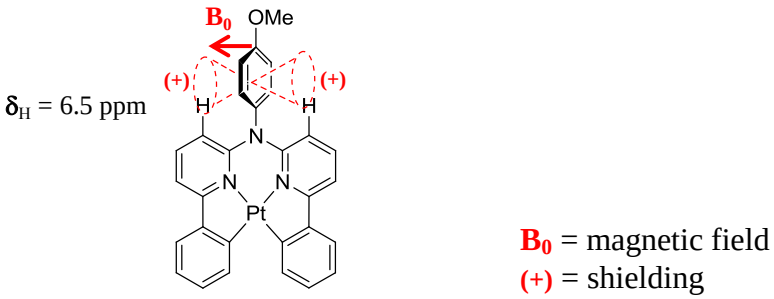

Figure 32. Aromatic ring current of the pendent phenyl ring leading to upfield shifts of the pyridyl H^3 signals in the NMR spectrum

Another characteristic of the platinum complexes was the deshielding of the proton in the metallated aryl ring that is α to the metal-carbon bond (labelled H^e in **Figure 33**). Upon cyclometallation with K_2PtCl_4, H^e *ortho* to the Pt–C bond exhibited an upfield shift of $\Delta\delta$ = 1.1 ppm reflecting an enhanced shifted effect. A valuable hypothesis was made by Selbin and coworkers as a through-space shielding caused by an adjacent aromatic ring defined as syn juxtaposition.[58] They observed for [μ-(OAc)Pd(ppy)]$_2$ that the C–H *ortho* to the C–Pd of the phenyl ring showed an upfield shift of $\Delta\delta$ = 0.5 ppm. The larger upfield shift observed for tetradentate platinum complexes may be due to the enhanced of rigidity.

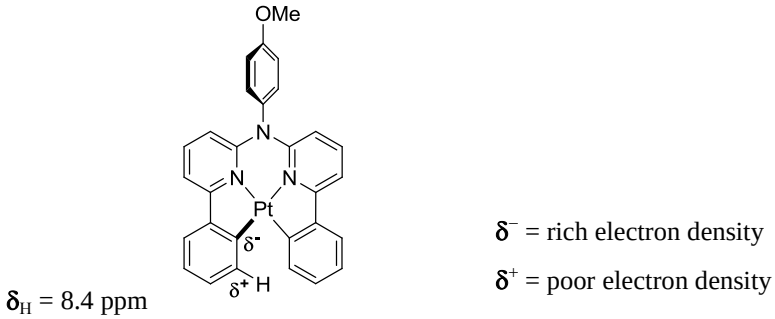

Figure 33. π backbonding effect on a tetradentate platinum complex

- **Oxidation from platinum(II) to platinum(IV)**

It was noted above how $\mathbf{L^3H_2}$ directly gave a Pt(IV) complex upon reaction with K_2PtCl_4. In fact, we observed that such Pt(IV) complexes could also be formed with the other ligands, indirectly via their Pt(II) complexes, without the need for Cl_2 or the presence of any obvious oxidant, in a process that seemed to involve the solvent and be activated by light. Chassot *et al.* showed that the orthometalated complexes $Pt(ppy)_2$ and $Pt(thpy)_2$ are photosensitive in several organic solvents, giving rise to oxidative addition reactions that lead to the formation of Pt(IV) complexes.[59,60]

We therefore tried to explore the reactivity of the platinum(II) complexes with solvent and under the influence of light. For example, the oxidation of **PtL^7** under light irradiation was monitored by ^{1}H NMR spectroscopy (**Figure 34**). A first ^{1}H NMR was made at t = 0 with 10 mg of **PtL^7** dissolved in $CDCl_3$. We observed one set of signals corresponding to the Pt(II) complex. The NMR tube was placed in a bath at 25 °C for all the experiment time in order to maintain the same temperature during the irradiation. After 30 min of light irradiation, we observed an additional new set of aromatic signals, corresponding to the partial oxidation to Pt(IV), and the diminution of the integration for the Pt(II) complex. The oxidation of the Pt(II) to the Pt(IV) analogue was almost complete after 19 h. The oxidation state of the complex had a direct impact on the ^{1}H NMR. In fact, the Pt–C bonds were stronger and the π-bonding is more important for the Pt(II) than the Pt(IV) so the electron density is lower for the Pt(IV) which induced a deshielding of the protons. As an example the most shielded proton (H^d) at 6.40 ppm for the Pt(II) is shifted to 6.46 ppm for the Pt(IV) complex.

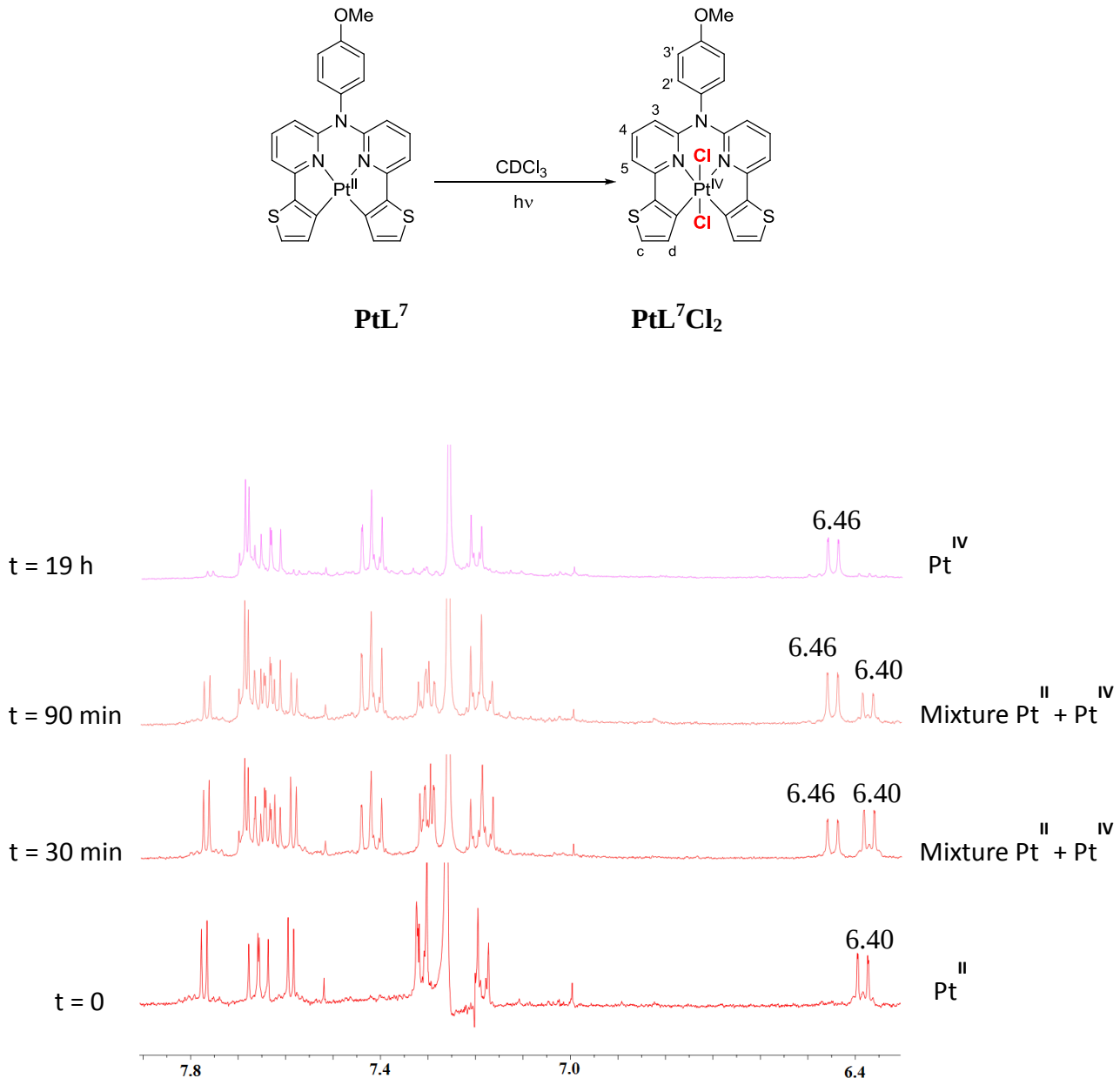

Figure 34. Evolution of the ^{1}H NMR spectrum (400 MHz) of **PtL^{1}** as it becomes oxidised to **PtL^{1}Cl$_2$** in $CDCl_3$ solution upon irradiation with light at 298 K

The same experiment was made with **PtL^{8}** complex. It appeared that the oxidation to Pt(IV) was faster for **PtL^{8}** than **PtL^{7}**. The planar **PtL^{8}** complex was oxidized in 2 h instead of 19 h for **PtL^{7}** oxidation. The more electron-rich benzothiophene unit apparently facilitates the oxidation of the platinum(II). The back reduction of the oxidized complex was attempted by leaving the NMR tube in the dark for several weeks, but no re-formation of the Pt(II) complex was observed.

- **Crystal structures**

➢ **Crystal structures of Platinum(II) Complexes**

The molecular structures of **PtL[1]**, **PtL[4]**, **PtL[7]** and **PtL[8]** were determined by single crystal X-ray diffraction analysis at 120 K, which confirmed the tetradentate coordination structure (**Figure 35** and **36**). Selected bond lengths and angles are listed in **Table 13**.

In all cases, the Pt–N bond lengths were slightly longer than the Pt–C bond lengths. For example, for **PtL[7]**, the Pt–N and Pt–C bond lengths are approximately 2.05 Å and 2.00 Å respectively (**Table 13**). The average of the Pt–C bond lengths of all complexes (~ 2.000 Å) is very close to that reported for *cis*-Pt(ppy)$_2$ (1.993 Å) and *cis*-Pt(thpy)$_2$ (1.986 Å), but the average of the Pt–N bonds (2.051 Å) is shorter than in *cis*-Pt(ppy)$_2$[61] (2.127 Å) and *cis*-Pt(thpy)$_2$ (2.159 Å). The formation of *three* metallacycle rings in the tetradentate complexes – two five-membered and one six-membered due to the nitrogen linker between the two C^N units – explains the relative shorter Pt–N bond lengths. The comparison with the tetradentate complexes synthesized by Huo *et al.* (**29** and **31**)[30] showed that the six-membered metallacycle ring formed with the two C^N units and the nitrogen as the linker, involved shorter bond lengths. Indeed, we observed that the distance Pt–C for **31** and Pt–N for **29** was shorter than Pt–N for **31** and Pt–C for **29**. The Pt bonds close to the N bridge are shorter than the other Pt bonds.

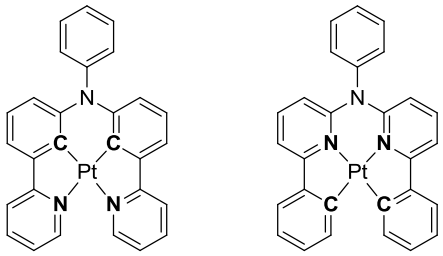

31 **29**

Figure 35. Pt(II) complexes **31** and **29** reported by Huo and co-workers [30]

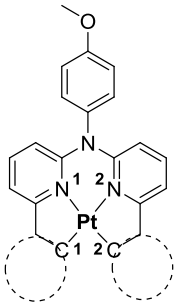

Figure 36. Representation of a tetradentate cyclometallated platinum(II) complex

Table 13. Selected bond lengths (Å) and angles (°) of Pt(II) complexes (All structures were acquired at 120 K). Data for ***cis*-Pt(ppy)$_2$, *cis*-Pt(thpy)$_2$, 29** and **31** are included for comparison.[1,30]

Complex	Bond angles / ° N^1^**Pt**^N^2	Bond angles / ° C^1^**Pt**^C^2	Bond angles / ° N^1^**Pt**^C^1	Bond angles / ° N^2^**Pt**^C^2
PtL^1	92.97(13)	103.51(16)	81.89(14)	81.78(14)
PtL^4	93.20(2)	102.10(3)	82.50(3)	83.00(2)
PtL^7	92.44(13)	102.56(17)	82.35(15)	82.66(15)
PtL^8	91.24(12)	106.27(16)	81.67(14)	82.01(14)
***cis*-Pt(ppy)$_2$**	101.9(1)	99.30(2)	79.30(1)	79.30(1)
***cis*-Pt(thpy)$_2$**	98.20(1)	103.30(3)	79.40(1)	79.10(1)

Complex	Bond lengths **Pt**–N^1	Bond lengths **Pt**–N^2	Bond lengths **Pt**–C^1	Bond lengths **Pt**–C^2
PtL^1	2.041(3)	2.046(3)	2.001(4)	2.001(4)
PtL^4	2.038(6)	2.031(6)	1.966(7)	1.986(7)
PtL^7	2.054(3)	2.058(3)	2.006(4)	1.995(4)
PtL^8	2.054(3)	2.048(3)	2.000(4)	2.002(4)
***cis*-Pt(ppy)$_2$**	2.127(3)	2.127(3)	1.993(4)	1.993(4)
***cis*-Pt(thpy)$_2$**	2.159(3)	2.161(3)	1.986(4)	1.992(4)
29	2.125(7)	2.130(6)	1.960(7)	1.959(8)
31	2.051(2)	2.050(2)	2.000(3)	2.007(3)

The anilino nitrogen adopted a planar geometry (a sum of 360º of the three C^N^C angles around the nitrogen) rather than a normal trigonal pyramidal geometry, indicating the feature of an sp^2 hybridized N for extended conjugation. Furthermore, the phenyl ring of the anisole group is clearly seen to be perpendicular to the plane of the rest of the complex (**Table 14**). This observation supports the earlier analysis of the NMR spectra, where the aromatic ring current induced in the phenyl ring explains the shielding of the H^3 protons of the pyridyl ring.

Table 14. Torsion angles between plane A and B (defined as in Fig. 15) for **PtL^1**, **PtL^4**, **PtL^7** and **PtL^8**

Complex	**PtL^1**	**PtL^4**	**PtL^7**	**PtL^8**
Angle between anisole group and the C^N^N^N^C plane	82.81	83.53	87.31	78.19

The non-planarity of the platinum complexes was observed by the torsion between the two C^N-coordinating units of the tetradentate ligand. Torsion data are shown in **Table 15**. For complex **PtL^7**, the torsion between the two thienylpyridine rings was quite small (3.23°) which provided a quasi-planarity of the complex. For complexes **PtL^1**, **PtL^4** and **PtL^8**, the two aromatic rings (phenyl, naphthalene and benzothiophene) were twisted probably because of the steric interaction of the two rings in the open end (tail) of the tetradentate complexes. The complexes had a twisted planar geometry around the metal center with a largest deviation of 24.90° for **PtL^8** between the two N^Pt^C planes.

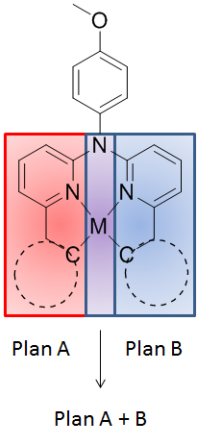

Table 15. Torsion angles between the two C^N units in the platinum complexes **PtL^1**, **PtL^4**, **PtL^7** and **PtL^8.** The torsion is measured as the angle between the planes of the two 5 membered rings (MCCCN)

Complex	**PtL^1**	**PtL^4**	**PtL^7**	**PtL^8**
Torsion angle (°)	15.79 °	21.13 °	3.23 °	24.90 °

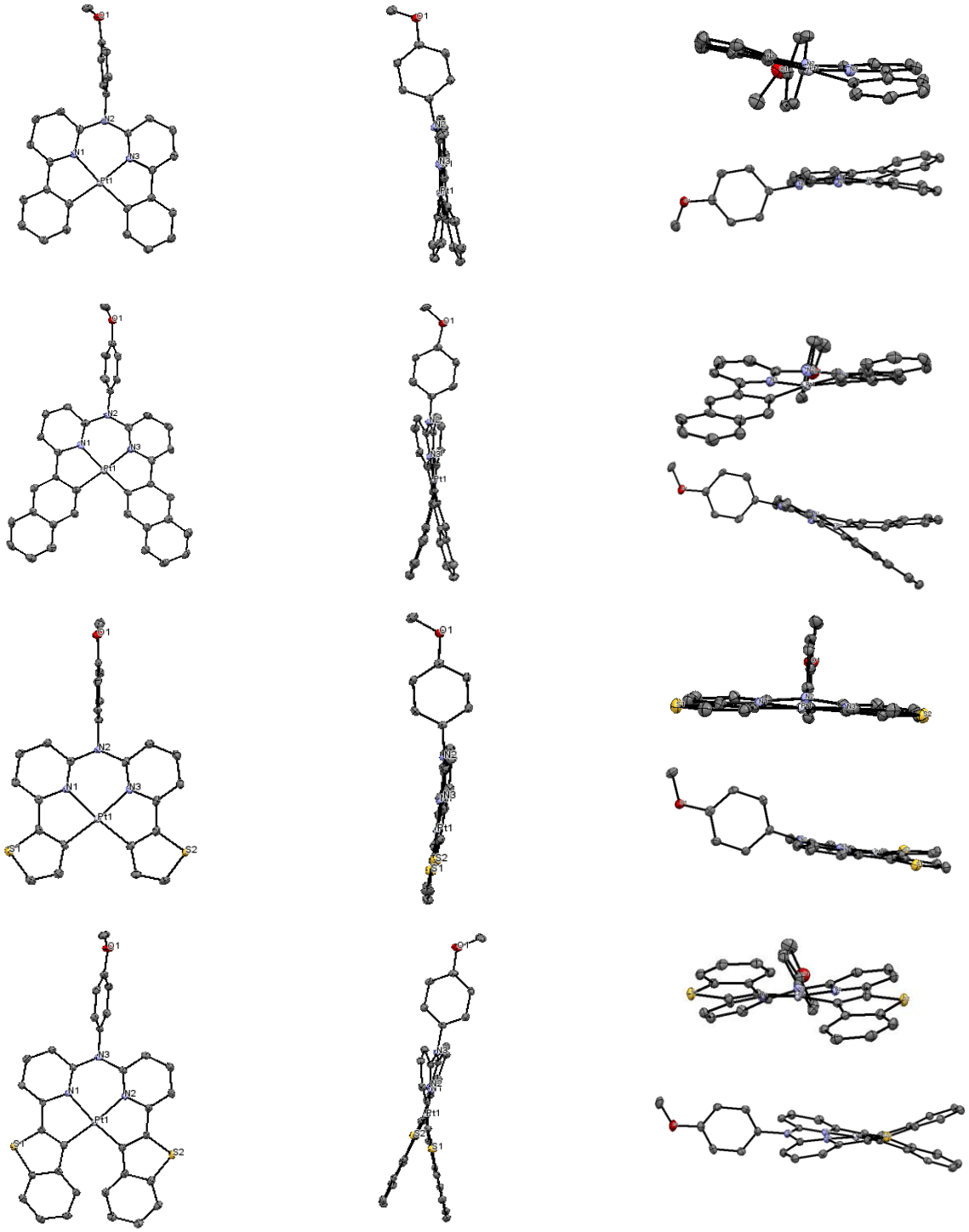

Figure 37. Molecular structures of **PtL**[1], **PtL**[4], **PtL**[7] and **PtL**[8] viewed at various orientations

PtL[1] and **PtL**[7] crystallised in a monoclinic system in $P2_{1/c}$ and $P2_{1/n}$ space groups respectively whereas **PtL**[4] and **PtL**[8] crystallised in a triclinic system in P1 space group due to the bulky complexes. They all adopted an antiparallel arrangement and packed in a head-to-tail fashion. To estimate whether any significant C–C or Pt–Pt interactions exist in the crystal packing, centroid-to-centroid distances were analysed. There is no evidence of Pt⋯Pt

interactions influencing the packing of any of the complexes, as distances are more than the threshold of 3.7 Å at which such interactions become plausible (**PtL^7** displayed the shortest distance with d = 3.983 Å).

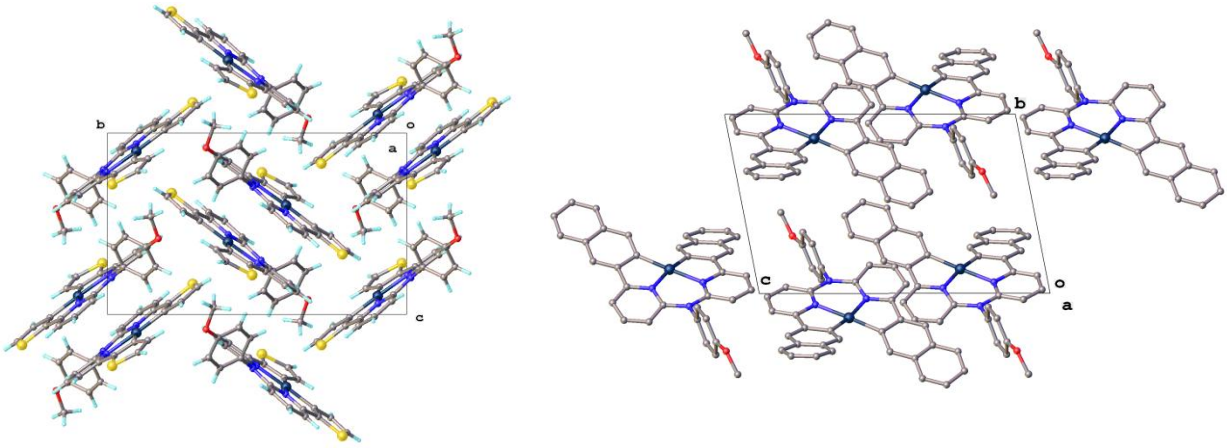

Figure 38. Crystal packing of **PtL^7** (left) and **PtL^4** (right)

- **Crystal structures of the Pt(IV) complexes**

PtL^{1}ClCN was obtained upon evaporation of a solution of **PtL^1** in CH_3CN and DCM. **PtL^{1}ClCN** and **PtL^{4}Cl$_2$** crystallised in a triclinic system in P1 space group due to the octahedral geometry (**Figure 39** and **Table 16**). Compared to **PtL^1**, Pt–N and Pt–C distances of **PtClCNL^1** were longer than the corresponding distances in the Pt(II) complex. Furthermore, the Pt–Cl distance is the longest of the metal-ligand bonds (2.3712 Å) and Pt–CN bond the shortest (1.884 Å). The plane formed by four coordinating atoms of the tetradentate ligand and the platinum ion showed N^Pt^N, C^Pt^C and C^Pt^N angles similar to those of the platinum(II) complexes. The C^Pt^Cl, N^Pt^Cl, C^Pt^CN and N^Pt^CN displayed angles closer to 90 ° than the previous angles cited. For **PtL^{4}Cl$_2$**, Pt–N and Pt–C distances are also longer than the distance of the analogous planar geometry. Pt–Cl bonds displayed the same distance as for **PtL^{1}ClCN** (d = 2.3258 Å) and the angles did not really show any modifications.

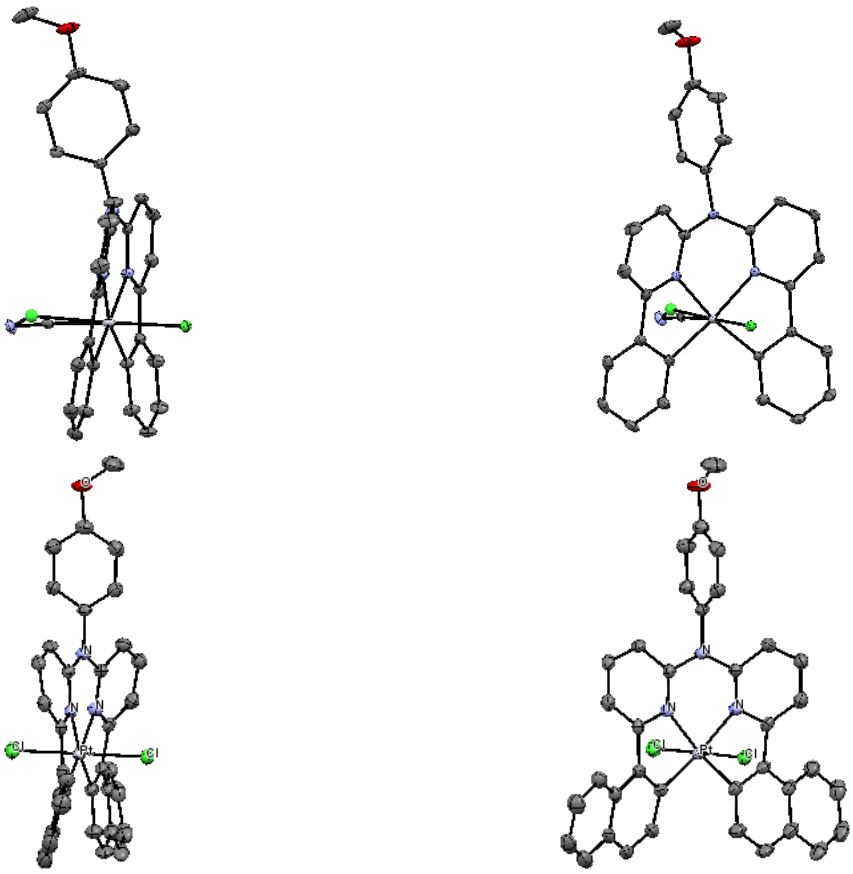

Figure 39. Molecular structures of **PtL^{1}CNCl** and **PtL^{4}Cl$_2$** viewed at various orientations

Table 16. Selected bond lengths (Å) and angles (°) of Pt(II) complexes **PtL^{1}CNCl** and **PtL^{4}Cl$_2$** (All structures were acquired at 120 K and 160 K respectively.

Complex	Bond lengths **Pt**–N^1	Bond lengths **Pt**–N^2	Bond lengths **Pt**–C^1	Bond lengths **Pt**–C^2	Bond lengths **Pt**–R	Bond lengths **Pt**–**Cl**
PtL^{1}ClCN R = CN	2.092(3)	2.094(3)	2.055(3)	2.058(3)	1.884(3)	2.371(9)
PtL^{4}Cl$_2$ R = Cl	2.083(4)	2.093(4)	2.024(5)	2.032(5)	2.315(13)	2.329(12)

Complex	Bond angles / ° N^1^**Pt**^N^2	Bond angles / ° C^1^**Pt**^C^2	Bond angles / ° N^1^**Pt**^C^1	Bond angles / ° N^2^**Pt**^C^2
PtL^{1}ClCN	92.27(10)	92.84(13)	80.76(12)	80.45(12)
PtL^{4}Cl$_2$	92.29(16)	105.7(2)	81.1(2)	80.88(19)

Complex	Bond angles / ° N^**Pt**^Cl	Bond angles / ° C^**Pt**^Cl	Bond angles / ° N^**Pt**^R	Bond angles / ° C^**Pt**^R	Bond angles / ° CN^**Pt**^Cl
PtL^{1}ClCN R = CN	88.46(8), 84.46(8)	87.00(9), 88.37(9)	95.42(12), 96.22(12)	92.84(13), 87.48(13)	175.63(2)
PtCl$_2$L^4 R = Cl	92.32(12), 91.10(12)	91.20(15), 88.44(15)	88.32(12), 88.90(12)	88.88(15), 90.92(13)	179.36(5)

- **Photophysical Characterization**

➢ **Absorption Spectroscopy at Room Temperature**

- **Platinum(II) Complexes**

The absorbance spectrum of the uncomplexed ligand $\mathbf{L^1H_2}$ was recorded in DCM solution at 298 K and compared with that of $\mathbf{PtL^1}$ (**Figure 40**). We observed a similarity between the peaks occurring in the region 230 nm-280 nm, indicating that bands occurring in this region of the complex absorption profile are due to ligand-localised $^1\pi$-π^* transitions. Lower intensity bands in the range 300 – 480 nm are observed in the spectrum of $\mathbf{PtL^1}$ but are absent in the ligand absorption, confirming that these bands arise upon ligand coordination to platinum. These bands are likely to include MLCT transitions and intraligand transitions, induced by the formal deprotonation of the two phenyl rings of the tetradentate ligand $\mathbf{L^1H_2}$ that accompanied metallation, and combinations of such transitions.

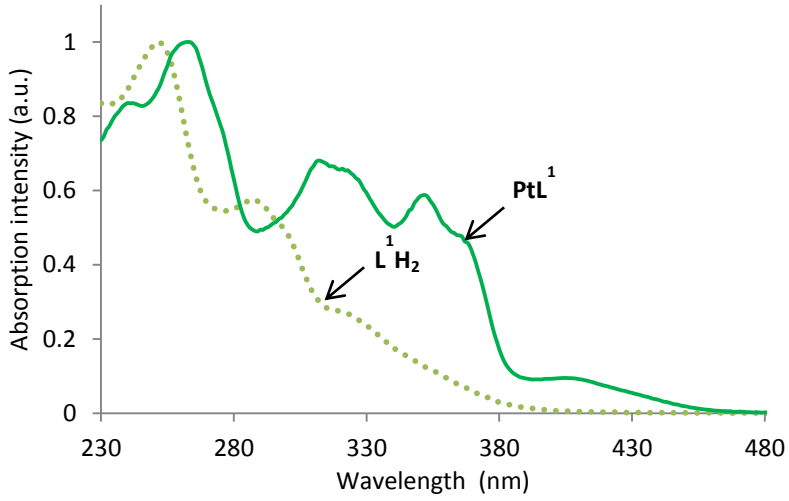

Figure 40. Normalized UV-visible absorption spectra of L^1H_2 and PtL^1 in DCM solution at 298 K

The ground-state absorbance spectra of $\mathbf{PtL^1}$, $\mathbf{PtL^4}$, $\mathbf{PtL^7}$ and $\mathbf{PtL^8}$ in dichloromethane solution are shown in **Figure 41**. (Unfortunately, it was not possible to obtain absorption data for $\mathbf{PtL^9}$ owing to its very low solubility in all solvents). They all showed intense bands in the UV region between 230 and 330 nm assigned to the $^1\pi$-π^* transitions of the ligands. A weaker set of bands are observed at lower energy extending into the visible region, assigned to metal-to-ligand charge transfer (MLCT). $\mathbf{PtL^7}$ and $\mathbf{PtL^8}$ showed significantly lower-energy MLCT bands than $\mathbf{PtL^1}$ and $\mathbf{PtL^4}$. DFT calculations previously made by Huo *et al.* predict that atoms of the aryl ring involving the C–Pt bond make a significant contribution to the HOMO, and a lesser contribution to the LUMO-based orbitals. Therefore, placing electron-withdrawing aryl rings around this ring can be expected to have a greater stabilising effect on

the HOMO, and lead to a blue shift. Conversely, electron-releasing rings may be expected to destabilise the HOMO, leading to a red shift.

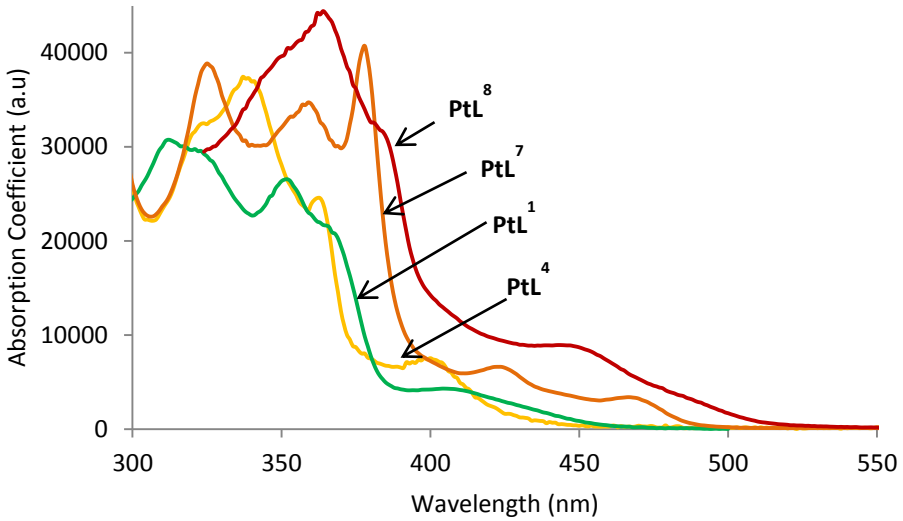

Figure 41. UV-visible absorption spectra of **PtL^1**, **PtL^4**, **PtL^7** and **PtL^8** complexes in degassed DCM at 298 K

- **Platinum(IV) Complexes**

Comparison of the absorption spectra of the tetradentate **Pt^{II}L$_1$** and **Pt^{IV}L^{1}Cl** showed that the absorption in the UV region had similar shape for both complexes (**Figure 42**). However, the lowest-energy absorption bands corresponding to the MLCT transitions observed in the Pt(II) complexes do not appear in the Pt(IV) analogues. This observation is consistent with the increase in the oxidation state of the metal, which should increase the energy associated with the MLCT transition, as it involves transient oxidation of the metal.

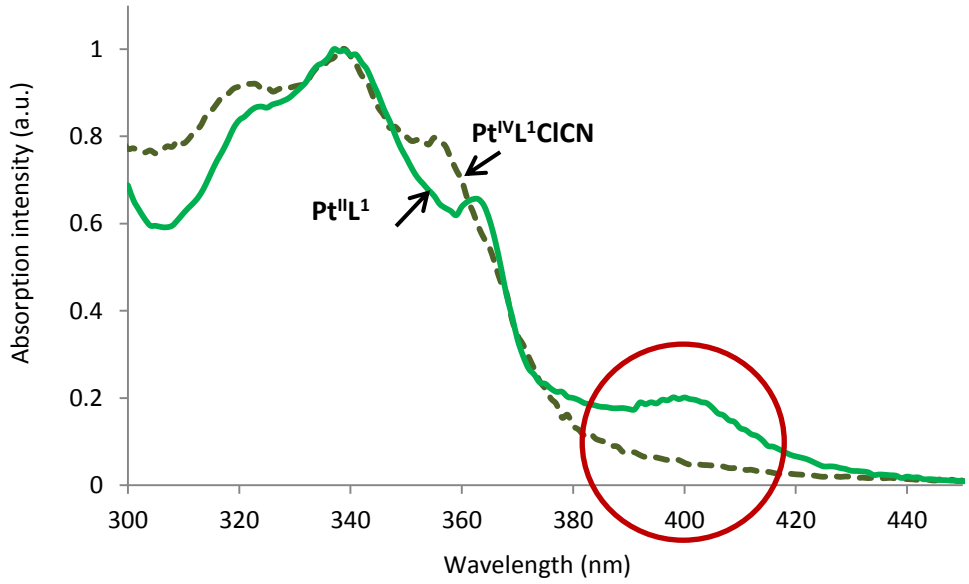

Figure 42. Normalized absorption spectra of **PtL^1**, and **PtL^{1}ClCN** complexes in DCM at 298 K

- **Emission Spectroscopy at Room Temperature**

Luminescence data for **PtL^1**, **PtL^4**, **PtL^7** and **PtL^8** are shown in **Table 18**. For all complexes, the emission spectra showed structured bands corresponding to the phosphorescence from a ^{3}MLCT state (**Figure 43**). The emission of **PtL^7** (λ_{max} = 557 nm) was red-shifted compared to **PtL^1** (λ_{max} = 499 nm), because the benzothiophene unit is more electron-rich which raises the HOMO. In emission, the highest intensity vibrational band was typically the one of highest energy, which corresponds to the 0–0 vibrational origin of the T_1 to S_0 transition. The bands at lower energy (and lower intensity) correspond to transitions to higher vibrational levels of the ground state. The shape and highly structured nature of the spectrum suggests that little geometric rearrangement occurs between the ground and excited states. The luminescence lifetimes were in the microsecond range with a significantly shorter lifetime for **PtL^4** probably due to an excimeric effect; deeper study of this phenomenon is required for confirmation (see Section **2.2.3**). Quantum yields of luminescence were higher for **PtL^1** and **PtL^7** than for **PtL^4** and **PtL^8.** The extended π conjugation of **PtL^4** and **PtL^8** may explain the decrease in the efficiency of such complexes.

ϕ and τ_0 are related to the radiative and non-radiative rate constants of the excited state. Relations between these radiative and non-radiative constants are given by **equations 1** and **2**.

Thus, the larger ϕ of **PtL^7** but comparable τ_0 between the two complexes means that k_r is larger and k_{nr} is smaller for **PtL^7**, and this complex is a more efficient emitter (values for k_r and k_{nr} are given in **Table 17**).

$$kr = \frac{\Phi}{\tau 0}$$ **Equation 1**

$$knr = \frac{1}{\tau 0} - kr$$ **Equation 2**

Equations 1: ϕ and τ_0 are related to the radiative constant (*kr*). **Equations 2**: Relations between radiative and non-radiative constants.

Platinum(IV) complexes **PtL^{2}Cl$_2$** and **PtL^{3}Cl$_2$** displayed undetectable luminescence at room temperature (see Section **2.2.3**).

Table 17. Radiative and non-radiative constants (k_r and k_{nr}) for **PtL^4**, **PtL^4**, **PtL^7** and **PtL^8** complexes

Complex	k_r / s^{-1}	k_{nr} / s^{-1}
PtL^1	9.4×10^4	1.2×10^5
PtL^4	2.0×10^3	1.5×10^4
PtL^7	4.9×10^4	1.8×10^4
PtL^8	6.8×10^3	1.6×10^4

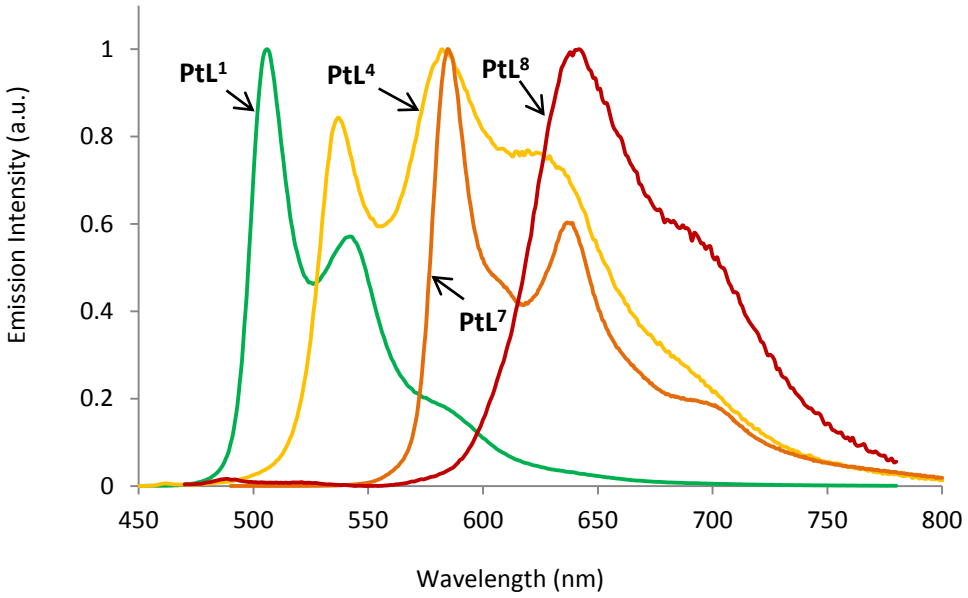

Figure 43. Normalized phosphorescence emission spectra of **PtL^1**, **PtL^4**, **PtL^7** and **PtL^8** complexes in degassed DCM at 298 K

- **Excimeric Emission**

An excimeric emission was observed for **PtL^4** at lower energy than the monomeric emission. This effect can be seen in **Figure 44**; the emission profile of a dilute sample

(degassed DCM at 298 K) was compared to emission profiles of solutions of increasing concentration. As the concentration was increased, the broad structureless excimeric emission grew in at lower energy at the expense of the monomeric emission. The overall colour of light observed depended on the ratio of the monomeric-to-excimeric emission, hence colour can be controlled simply by controlling concentration.

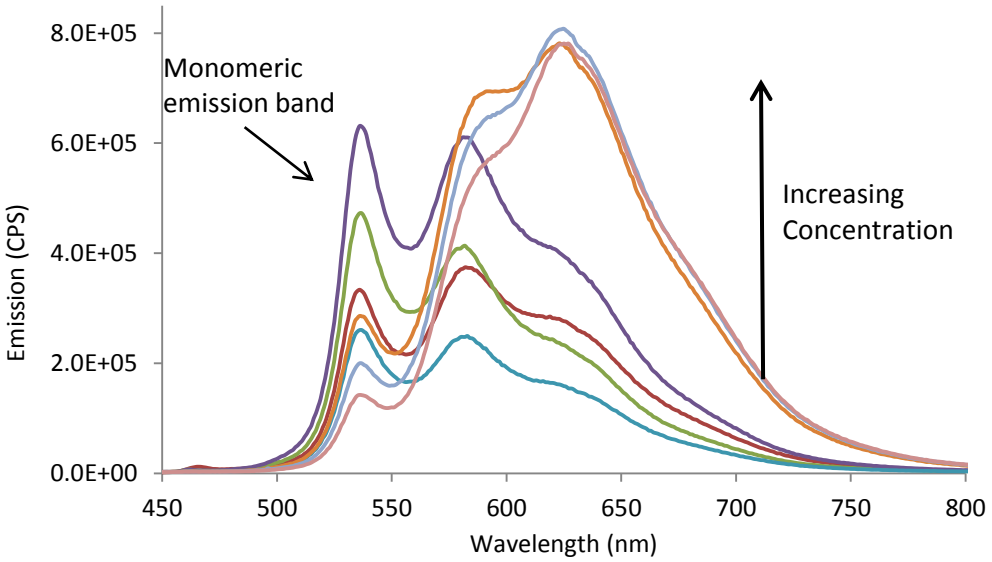

Figure 44. Emission spectra of various concentrations of **PtL^4** in degassed DCM at 298 K. Note the increasing contribution from excimer emission with increasing concentration

- **Low Temperature Spectroscopy**

- **Platinum(II) Complexes**

All the emission spectra at 77 K were recorded in a mixed solvent mix comprised of ether/isopentane/ethanol (2:2:1 v/v). This mixture forms an inert transparent glass at 77 K, which allows efficient and reproducible excitation of the solution and transmission of the signal to the detector. The emission spectra at 77 K were more structured than those obtained at 298 K (**Figure 45**). A small blue shift of the emission was observed for **PtL^1**, **PtL^4** and **PtL^7** at 77 K compared to 298 K ($\Delta\lambda_{em}$ = 7, 5 and 6 nm respectively). The larger Stokes shift (6522 cm^{-1}) between the emission (in the glass solution at 77 K) and absorption spectra of **PtL^7** when compared to that (6825 cm^{-1}) of the Pt(II) counterpart at 298 K is attributed to the more extensive excited state distortion in the former than in the latter complexes.

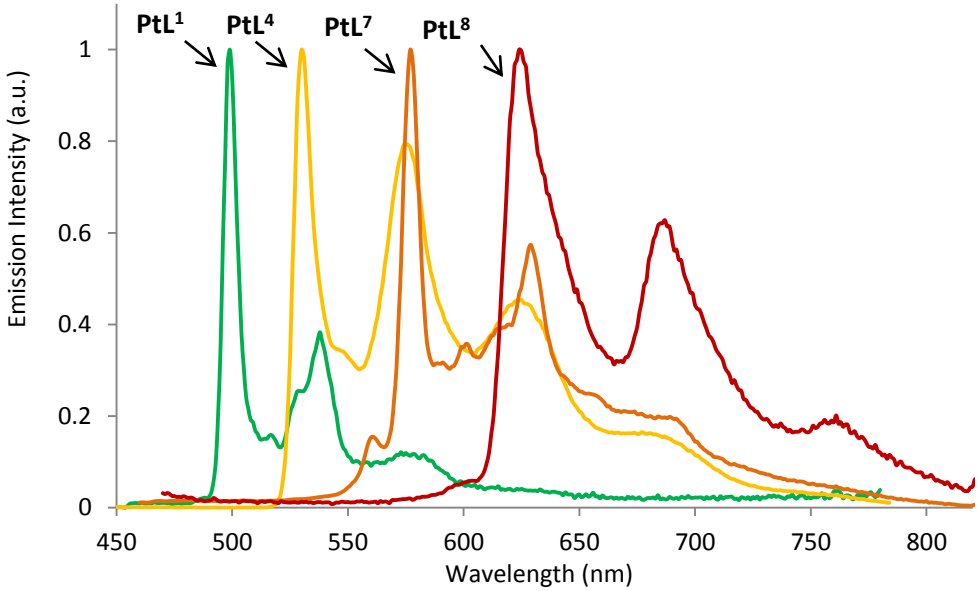

Figure 45. Normalized phosphorescence emission spectra of **PtL**[1], **PtL**[3]**Cl**$_2$, **PtL**[4], **PtL**[7] and **PtL**[8] complexes in EPA solution at 77 K

- **Platinum(IV) Complexes**

Platinum IV complexes are known to show luminescent properties at room temperature.[54,62,63] However, **PtL**[3]**Cl**$_2$ (IV) was only emissive at 77 K (there was no emission at 298 K),with λ_{max} = 543 nm and a long lifetime (τ = 319 ms). The metal-centred orbitals were contracted and interacted less with the ligand orbitals which involve a higher ^{3}LC contribution and a lower MLCT contribution. Chloride is a weak-field ligand, and the ligand field splitting is apparently insufficient to allow emission to be observed at room temperature.

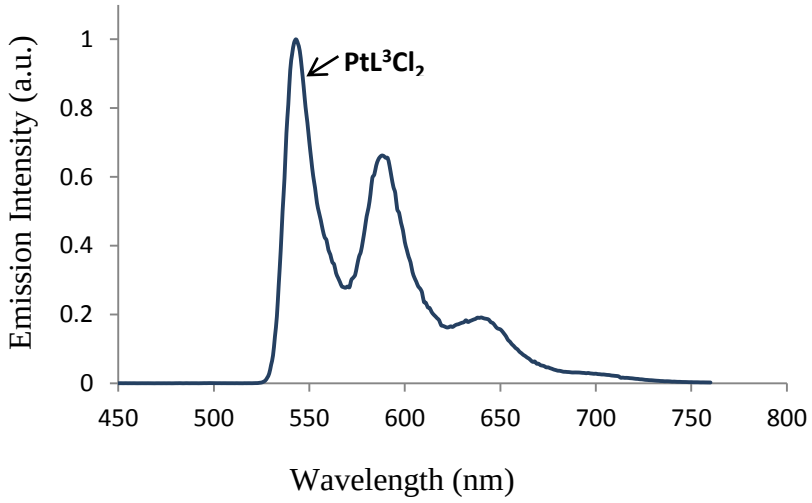

Figure 46. Phosphorescence spectrum of **PtL**[3]**Cl**$_2$ in EPA glass at 77 K

Table 18. Photophysical data of Pt(II) and Pt(IV) complexes in degassed DCM and EPA solution at 298 K and 77 K. [(a)] data collected in DCM at 298 K. [(b)] data collected in EPA solution at 77 K. [(c)] $[Ru(bpy)_3]^{2+}$ was used as reference for the calculation of the quantum yield ϕ

Complex	λ_{abs}/nm ($\varepsilon/10^3$ L mol^{-1}cm^{-1})[(a)]	λ_{em} / nm[(a)]	λ_{em} / nm[(b)]	τ / μs [(a)]	τ / μs [(b)]	ϕ [(a)(c)]
PtL^1	272 (72.4), 289 (57.5), 323 (34.6), 337 (38.9), 363 (24.5), 399 (7.58)	506, 541, 588 (sh)	499, 512, 524, 541, 572	8.3	12	0.78
PtL^{2}Cl$_2$	260 (66.0), 347 (28.8), 366 (20.8)	-	-	-	-	-
PtL^{3}Cl$_2$	237 (186.2), 270 (93.3), 365 (66.0)	-	543, 586, 636, 693	-	319	-
PtL^4	257 (75.9), 309 (38.9), 349 (25.9), 397 (6.37)	535, 580	530,543, 575, 623, 678	60	351	0.12
PtL^7	252 (45.7), 283 (74.1), 325 (38.9), 359 (34.6), 378 (40.7), 424 (6.7), 468 (3.8)	579, 599, 706 (sh)	559, 585, 598, 616, 628, 651, 685	15	17	0.74
PtL^8	358, 383, 443	635	623, 684, 756	5.9	12	0.04

2.3. Synthesis and Characterization of Palladium Complexes

We have shown that cyclometallated tetradentate platinum complexes have interesting photophysical properties. They showed long lifetimes and high quantum yields of luminescence. In contrast, luminescent palladium complexes are not well-known in the literature. Only a few examples of phosphorescent palladium(II) complexes containing non-porphyrin ligands have been reported. Thus we sought to synthesize cyclometallated palladium(II) complexes of the tetradentate ligands of Section **2.2.2.**, with a view to obtaining molecular materials that are emissive at room temperature.

2.3.1. Synthesis of the tetradentate palladium complexes

The palladium(II) complexes of ligands $\mathbf{L^1H_2}$, $\mathbf{L^7H_2}$, $\mathbf{L^6H_2}$ and $\mathbf{L^9H_2}$ were obtained upon reaction of the proligands with $Pd(OAc)_2$ (1.2 equiv.) in refluxing acetic acid for 48 h. (**Scheme 14**). A precipitate appeared after 12 h but a reaction time of 48 h is necessary to have the tetradentate palladium complex (see Section **2.2.2.**). Up to now, all the other ligands were not tested for the metallation to the palladium.

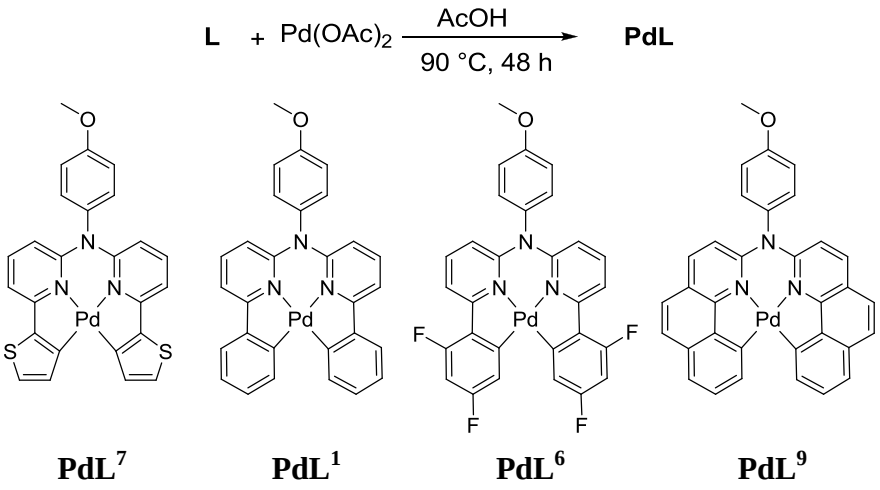

Scheme 14. Synthesis of palladium(II) complexes, $\mathbf{PdL^7}$, $\mathbf{PdL^1}$, $\mathbf{PdL^6}$ and $\mathbf{PdL^9}$

The same reaction was attempted using proligand $\mathbf{L^5H_2}$ (**Scheme 15**). However, the final product did not appear as the expected palladium complex but as a cluster containing two palladium atoms. A Pd–Pd bond is supported by acetate and chloride bridges. The molecule contains two ligands which were each coordinated through one pyridyl nitrogen and one carbon (C^3) of the other pyridyl ring. Apparently, the position 3 of the pyridyl ring is more reactive than the position f of the 3,5-bis(trifluoromethyl)benzene ring. The presence of the bulky and electron-withdrawing CF_3 unit on the position "e" evidently decreases the reactivity of the position "f" of the phenyl ring. This observation is consistent with the formation of the purely organic compound **3** upon reaction of the same proligand with K_2PtCl_4, where oxidative coupling of the C^3 positions of the two pyridyl rings has occurred (see Section **2.2.2** above).

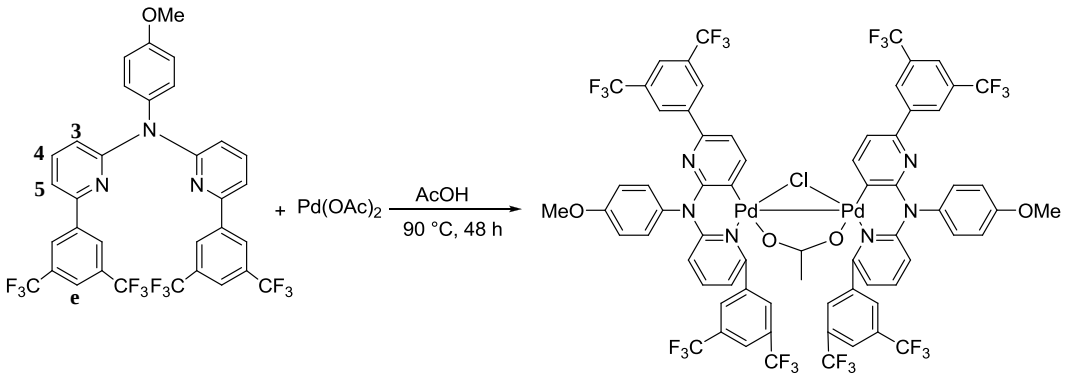

Scheme 15. Reaction between $\mathbf{L^5H_2}$ and $\mathbf{Pd(OAc)_2}$ leading to the Pd_2 cluster

2.3.2. Characterization of the Pd(II) complexes

- **NMR spectroscopy**

The ^{1}H NMR spectra of the palladium(II) complexes were similar to their platinum(II) analogues. We shall take the case of $\mathbf{PdL^7}$ as an example. The presence of seven aromatic signals and the strong shielding of H^3 due to the aromatic ring current of the phenyl ring are characteristic of a tetradentate metal complex. a shielding of the aromatic signals was observed when the metal changed from Pd → Pt. As an example, all signals in the aromatic region for $\mathbf{PdL^7}$ were shielded compared to its platinum analogue (Δδ was 0.2 ppm). Szłyk *et al.* observed the same weak effect of the metal atom with the analysis of *cis*-$Pt(ppy)_2Cl_2$ and *cis*-$Pd(ppy)_2Cl_2$ by NMR spectroscopy.[64]

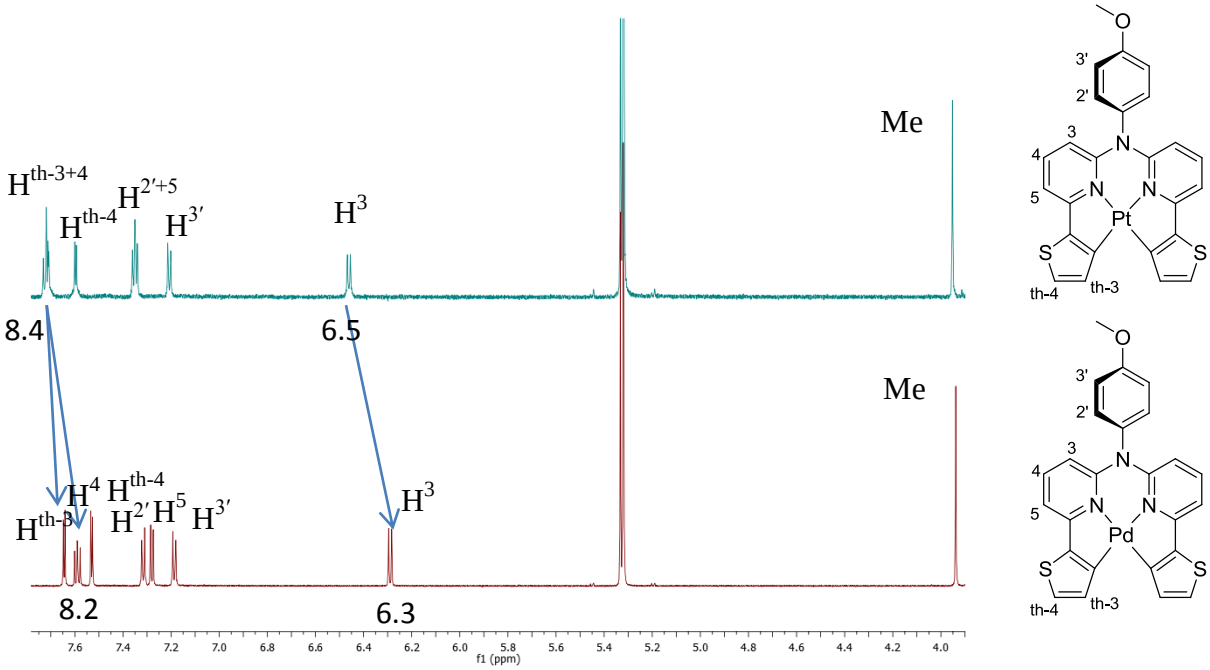

Figure 47. ^{1}H NMR spectra of $\mathbf{PtL^7}$ in blue (top) and of $\mathbf{PdL^7}$ in red (bottom), both recorded at 700 MHz in CD_2Cl_2 at 298 K

- **Crystal Structures**

Crystal structures of **PdL^1**, **PdL^7** and **PdL^9** were obtained by slow diffusion of DCM into a DMF solution of the complex and **PdL^6** was obtained by recrystallization in acetone.

The molecular structures of **PdL^1**, **PdL^7** and **PtL^9** were determined by single crystal X-ray diffraction analysis at 120 K, which confirmed the tetradentate coordination structure (**Figure 48**). Selected bond lengths and angles are listed in **Table 19**.

In all cases, the Pt–N bond lengths were slightly longer than the cyclometallated Pt–C bond lengths. For example, for **PdL^7**, Pd–N and Pd–C bond lengths were approximatively 2.05 and 2.00 Å respectively. Furthermore, the average of the bond lengths of all complexes (~ 2.00 Å) was very close to that reported for their platinum analogues **PtL^1** and **PtL^7**. A similar observation was made for the torsion angles (**Table 20**): Pt(II) and Pd(II) complexes adopted the same torsion angle (plan MCCN) with a *quasi*-planarity for **PdL^7** (3.03 °, for **PtL^7** torsion = 3.23 °). The distortion between the two planes of **PdL^1** seemed to be similar to **PdL^6**.

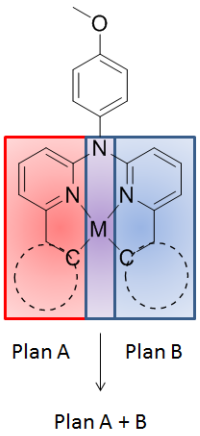

All these four complexes adopt a quasi-square planar geometry with N–Pd–C angles around 170 - 175°. Compared to the tetradentate palladium(II) complexes synthesised by Che *et al.*, where N^Pd^C angles of 160.14° to 162.09° were encountered, the current series of complexes are closer to planarity.

Table 19. Selected bond lengths (Å) and angles (°) of the Pd (II) complexes (All structures were acquired at 120 K). Corresponding data for **PtL^1** and **PtL^7** are listed for comparison

Complex	Bond angles / ° N^1^**M**^N^2	Bond angles / ° C^1^**M**^C^2	Bond angles / ° N^1^**M**^C^1	Bond angles / ° N^1^**M**^C^2	Bond angles / ° N^2^**M**^C^2	Bond angles / ° N^2^**M**^C^1
PdL^1	91.85	102.33	83.06	169.86	82.91	174.72
PdL^6	92.62	102.50	82.47	170.51	82.59	174.63
PdL^7	91.85	101.33	83.96	174.68	83.67	172.82
PdL^9	89.00	103.33	83.77	171.92	83.85	174.93
PtL^1	92.97	103.51	81.89	170.33	81.78	174.33
PtL^7	92.44	102.56	82.66	174.73	82.35	175.04

Complex	Bond lengths **M**–N^1	Bond lengths **M**–N^2	Bond lengths **M**–C^1	Bond lengths **M**–C^2
PdL^1	2.052	2.058	1.983	1.987
PdL^6	2.035	2.047	1.997	1.996
PdL^7	2.052	2.058	1.983	1.987
PdL^9	2.053	2.054	2.010	2.008
PtL^1	2.041	2.046	2.001	2.001
PtL^7	2.054	2.058	2.006	1.995

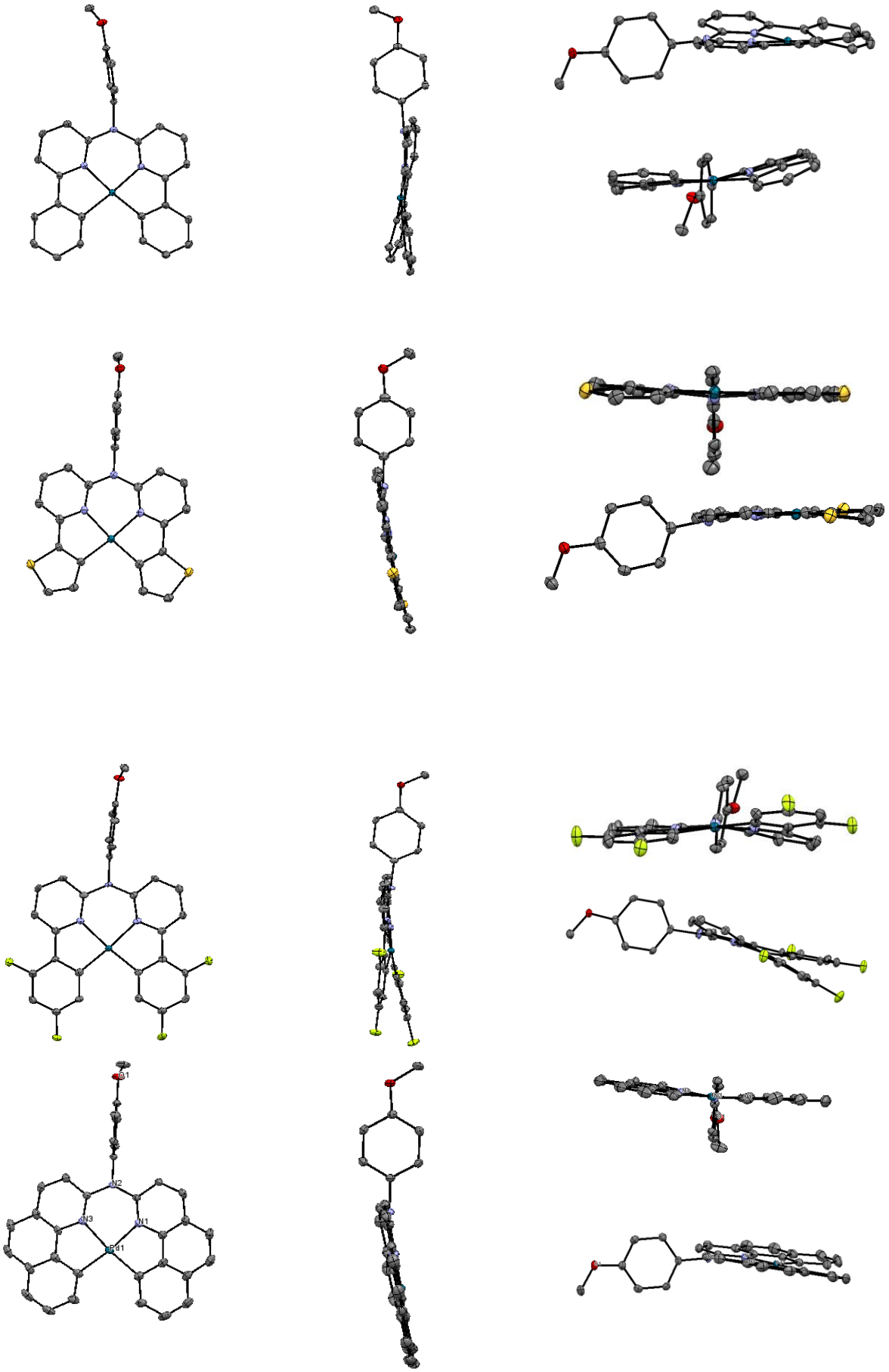

Figure 48. Molecular structures of **PdL**[1], **PdL**[6], **PdL**[7] and **PdL**[9] viewed at various orientations

Table 20. Torsion angles between the two C^N parts of the palladium complex for **PdL[1]**, **PdL[6]**, **PdL[7]** and **PdL[9].** The torsion is measured as the angle between the planes of the two 5 membered rings (PdCCCN)

Complex	**PdL[1]**	**PdL[6]**	**PdL[7]**	**PdL[9]**
Torsion angle (°)	16.31	15.41	3.03	7.08

All palladium(II) complexes showed head-to-tail crystal packing (**Figure 49**). They all showed weak stacking or π-π interactions between molecules, similar to the crystal packing of the previous tetradentate platinum(II) complexes.

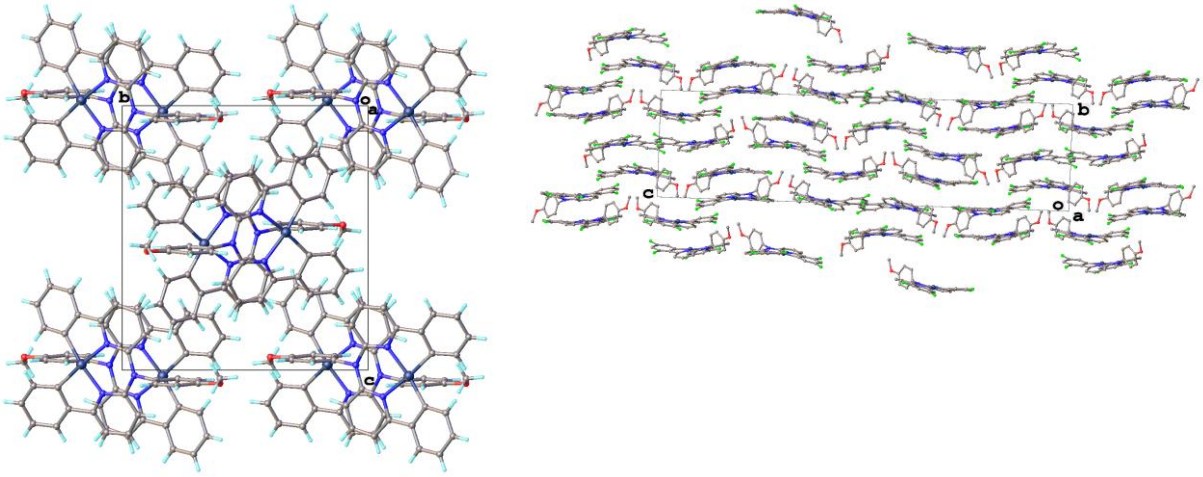

Figure 49. Crystal packing of **PdL[1]** (left) and **PdL[6]** (right)

$PdCl_2(L^1H_2)$ was obtained by the reaction of **L^1H_2** and $Pd(OAc)_2$ in acetic acid for 12 h. The precipitate formed was then recrystallized by slow evaporation from chloroform. The X-ray crystal structure of **$PdCl_2(L^1H_2)$** provides an indication of the mechanism of the reaction and how the metal initially binds to the ligand (**Figure 50**).

Figure 50. Representation of **$Pd(L^1H_2)Cl_2$** and its molecular structure

- **Photophysical Characterization**

➢ **Absorption Spectroscopy at Room temperature**

The ground state absorbance spectra of **PdL^1**, **PdL^6** and **PdL^7** in dichloromethane solution are shown in **Figure 51** (summarized in **Table 21**). Each complex showed intense bands in the near UV region between 230 and 300 nm corresponding to the $^1\pi$-π^* transitions of the ligands. These are accompanied by a series of weaker, lower energy features extending to the visible region, assigned to the ^{1}MLCT bands. **PdL^7** showed significantly lower energy ^{1}MLCT bands than those for **PdL^1**. This is attributed to the more electron rich nature of the thiophene compare to the phenyl ring. The MLCT transitions of the fluorinated **PdL^6** complex were blue-shifted with respect to the two other complexes, due to stabilization of the HOMO as a result of the electron-withdrawing nature of the fluorine substituents.

The complex **PdL^7** exhibited intense absorption bands at 230-370 nm ($\varepsilon = 2 \times 10^4$ L mol^{-1} cm^{-1}), and moderately intense absorption bands at 375-430 nm ($\varepsilon = 1 \times 10^4$ L mol^{-1} cm^{-1}). The absorption bands at 230-375 nm resembled those of the corresponding ligand, attributed to π-π^* transitions.

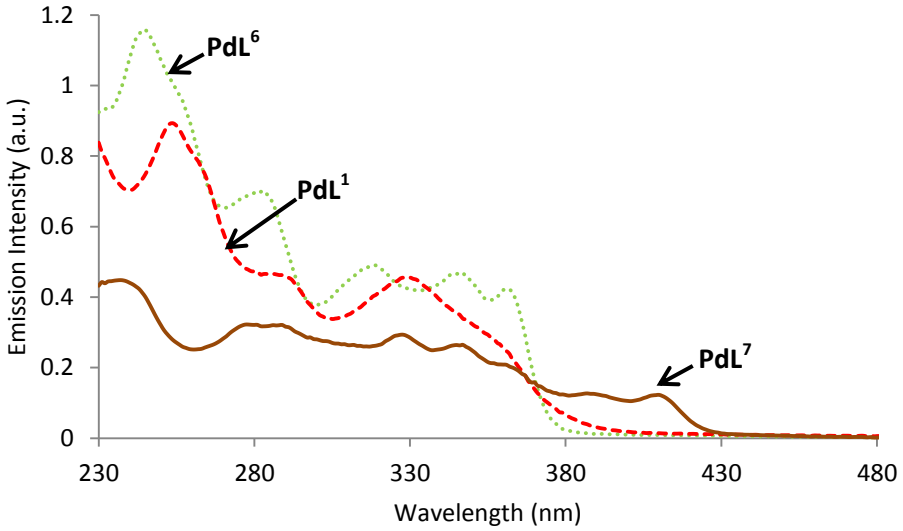

Figure 51. Normalized UV-visible absorption spectra of **PdL^1**, **PdL^6** and **PdL^7** complexes in DCM at 298K

The comparison between **L^{1}H$_2$**, **PdL^1** and **PdL^{1}H$_2$Cl$_2$** in DCM at 298 K (**Figure 52**) showed that the cyclometallation had an effect on the absorption properties. In fact, the palladium complex **PdCl$_2$L^{1}H$_2$** was only coordinated by the two nitrogens of the pyridine rings, and its absorption spectrum resembled that of the free ligand **L^{1}H$_2$**.

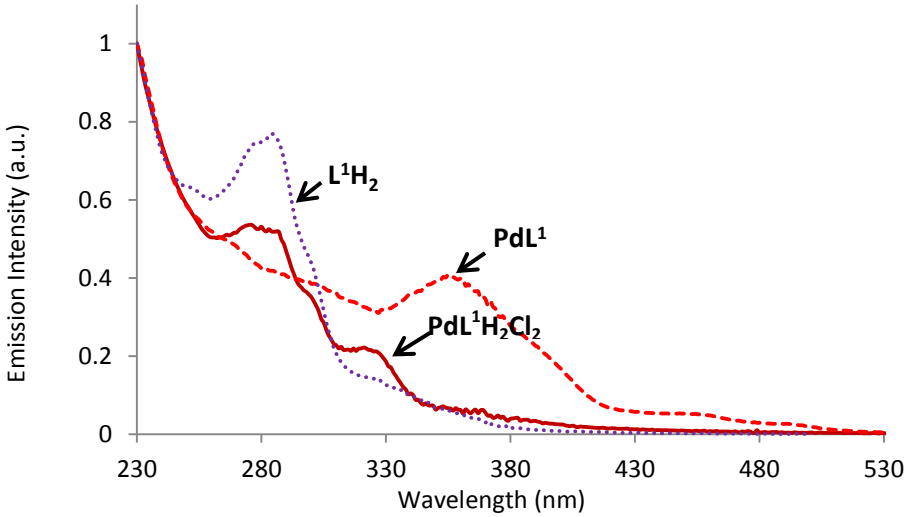

Figure 52. Normalized absorption spectra of $\mathbf{L^1H_2}$, $\mathbf{PdL^1}$ and $\mathbf{PdCl_2L^1}$ in DCM at 298 K

- **Emission Spectroscopy at room temperature**

$\mathbf{PdL^1}$, $\mathbf{PdL^6}$ and $\mathbf{PdL^7}$ are emissive at 298 K. In contrast, $\mathbf{L^6}$ is a weak field ligand in $\mathbf{PdL^6}$ which involved a weak emission from the complex at room temperature (ϕ = 0.0002). $\mathbf{PdL^9}$ was impossible to solubilize, as was found for its platinum analogue.[65] The emission was at lower energy for $\mathbf{PdL^1}$ (λ = 485 nm) compared to $\mathbf{PdL^7}$ (λ = 553 nm) due to the more electron rich thienyl group of $\mathbf{PdL^7}$. Furthermore, $\mathbf{PdL^1}$ was less emissive than $\mathbf{PdL^7}$ (ϕ = 0.012 and 0.15 respectively) and had a shorter lifetime (1.1 μs and 180 μs, respectively).

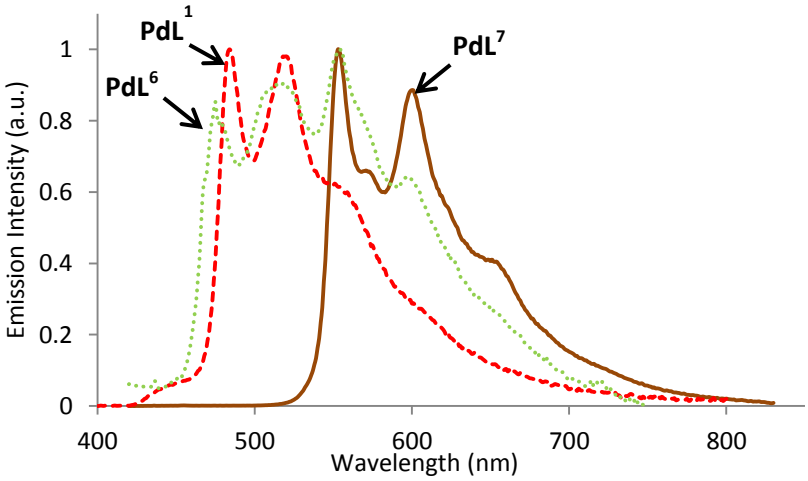

Figure 53. Normalized luminescent emission spectra of $\mathbf{PdL^1}$ and $\mathbf{PdL^7}$ complexes in degassed DCM at 298 K, following excitation into the lowest energy absorption band

Table 21. Photophysical data for **PdL^1**, **PdL^6** and **PdL^7** complexes in degassed DCM (a) and EPA solution (b) at 298 K and 77 K (c)

Complex	λ_{abs}/nm (ε /10^3 L mol^{-1} cm^{-1})	λ_{em} $^{(a)}$ nm	τ $^{(a)}$ µs	ϕ $^{(a)}$	λ_{em} $^{(b)}$ nm	τ $^{(b)}$ µs
PdL^7	233 (30.8), 279 (22.1), 325 (22.1), 342 (20.1), 364 (15.0), 386 (9.7), 407 (9.4)	553, 572, 600, 652	180 [c]	0.15	547, 566, 592, 611, 644	350
PdL^1	256 (49.2), 350 (8.0), 451 (0.8)	485, 520,550	1.1 [314]	0.012	479, 515, 553, 596, 653	350
PdL^6	241 (5.2), 276 (3.5), 311(1.5), 345 (1.4), 365 (1.4)	475, 517, 555, 597	76 [70]	0.0002	465, 500, 539, 580	640

➢ **Low Temperature Spectroscopy**

All the emission spectra at 77 K were recorded in an EPA glass. Data are reported in **Table 21**. All complexes emitted at 77 K and showed structured bands (**Figure 54**). **PdL^6** showed an emission at λ_{em} = 465 nm. This is attributed to the decrease of non-radiative effects (k_{nr}) at low temperature.[66] The emission spectrum of **PdL^6** was blue shifted compared to those for the complexes **PdL^1** and **PdL^7**. This was due to the weak field ancillary fluorinated ligand. The lifetimes of the **PdL^1**, **PdL^6** and **PdL^7** complexes are longer at 77 K than at 298 K.

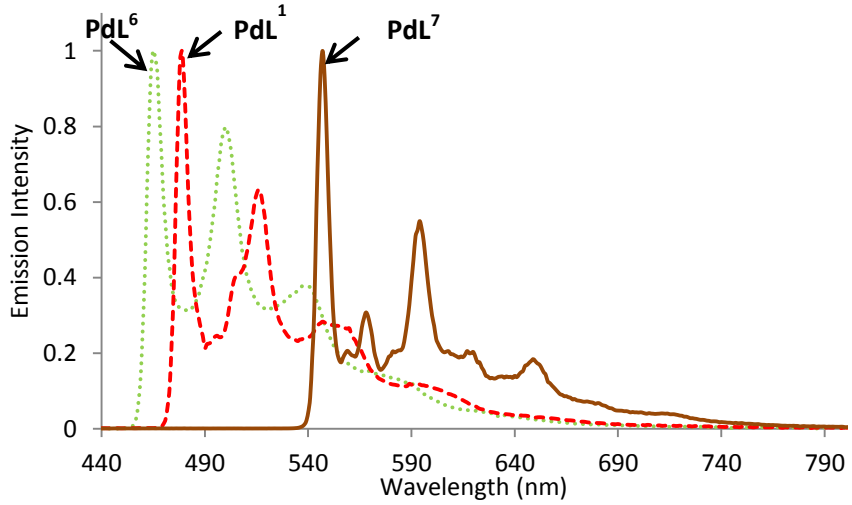

Figure 54. Normalized luminescence spectra of **PdL^1**, **PdL^6** and **PdL^7** complexes in an EPA glass at 77 K

➢ Comparison Between Platinum(II) and Palladium(II) Complexes

Comparison of the photophysical properties of the tetradentate Pt(II) and Pd(II) complexes showed that a lower absorption band maximum at $\lambda_{abs} > 430$ nm was observed for **PtL**^{7} (**Figure 55**). In fact, the 4d orbitals of palladium(II) systems are lower in energy than the 5d orbitals of their platinum(II) analogues: the higher energy absorption maxima are indicative of MLCT character in the excited states.[67] Despite similarly high molar absorption coefficients, the absorption bands in the UV region were much broader in the case of **PdL**^{7} complex. The emission bands had similar shapes for both complexes. Regarding the luminescence properties, the phosphorescence quantum yields of the **PtL**^{7} were significantly higher and the decay lifetimes shorter than for **PdL**^{7}. In fact, the higher ISC and better orbital match occuring in platinum(II) complexes will lead to a larger radiative constant (k_r) hence to shorter lifetime and higher quantum yield of luminescence.

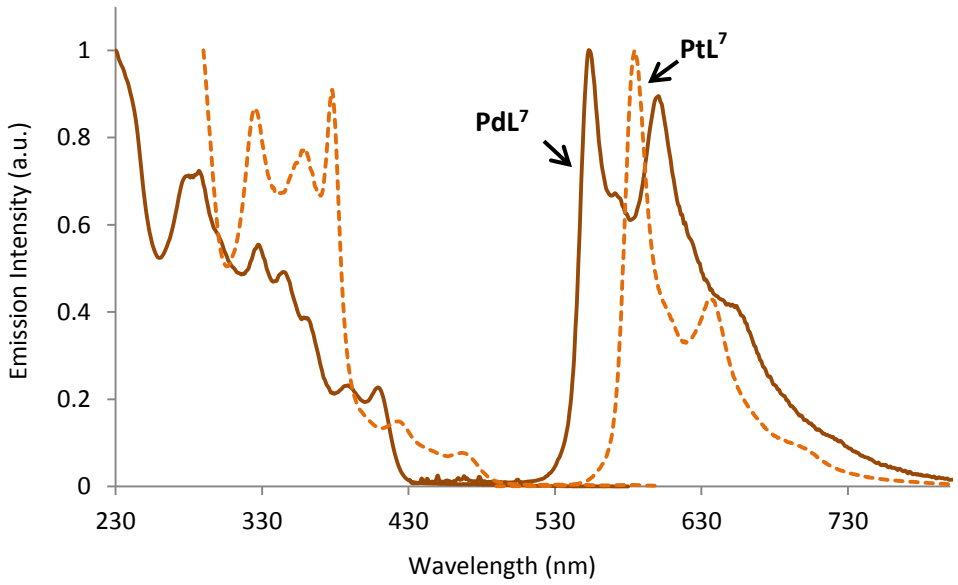

Figure 55. Normalized absorption and emission spectra for the **PtL**^{7} and **PdL**^{7} complexes in degassed DCM at 298 K

2.4. C^N^N^C Gold, Mercury and Iridium Complexes

2.4.1. Mercuric complex

The formation of a cyclometallated gold complex bearing a tetradentate ligand has often required the synthesis of a mercuric complex as a precursor.[68,69,70,71] Transmetallation from the mercuric complex to the gold is easier than the direct reaction between the ligand and inorganic gold salts such as $KAuCl_4$. Wenger *et al.* proposed a way to synthesize a cyclometallated tetradentate mercuric precursor (**HgL**) by heating the cyclometallated

tridentate ligand with $Hg(OAc)_2$ in EtOH at reflux for 3 days.[72] Adopting these conditions for the present case, when only a 1:1 ratio of mercuric reagent and ligand were reacted, the reaction after 24 h was not complete. The ^{1}H NMR spectrum of the mixture showed an exchange between the free ligand and the expected mercuric compound. We slightly changed the procedure. An excess of $Hg(OAc)_2$ (5 eq) was added to a mixture of $\mathbf{L^7H_2}$ dissolved in EtOH. The reaction time was reduced to 24 h (**Scheme 16**). A yellow precipitate was formed after 1 h of reaction at 78 °C. The NMR and mass spectra proved the formation of the mercuric complex.

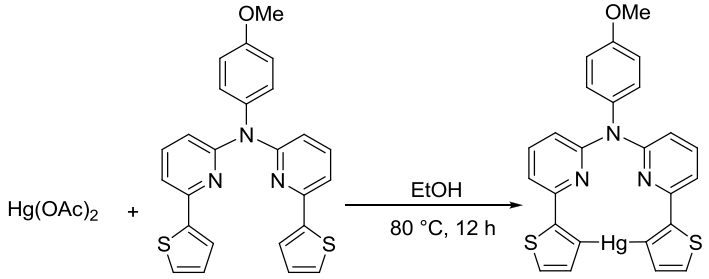

Scheme 16. Synthesis of $\mathbf{HgL^7}$ mercuric complex

2.4.2. Gold Complex

The *trans*-metallation between the mercuric complex and $KAuCl_4$ gave a final impure product, which may correspond to the tetradentate Au(III) complex. Stoichiometric amounts of the mercuric precursor and $KAuCl_4$ were stirred in acetonitrile at reflux for 12 h in the absence of light (**Scheme 17**). The ^{1}H NMR in DMSO-d6 recorded at 400 MHz of the resulting product, did not fit with the mercuric complex or the free ligand and it showed a shifted proton at 6.35 ppm, which may correspond to the proton of the pyridyl ring. Further studies are required to provide definitive identification of the product obtained (**Figure 56**).

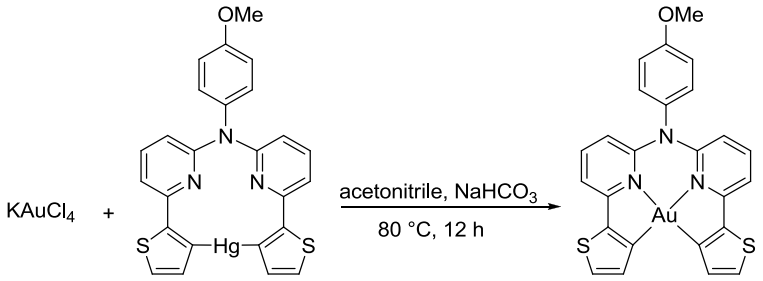

Scheme 17. Attempted synthesis of $\mathbf{[AuL^7]}$ gold (III) complex

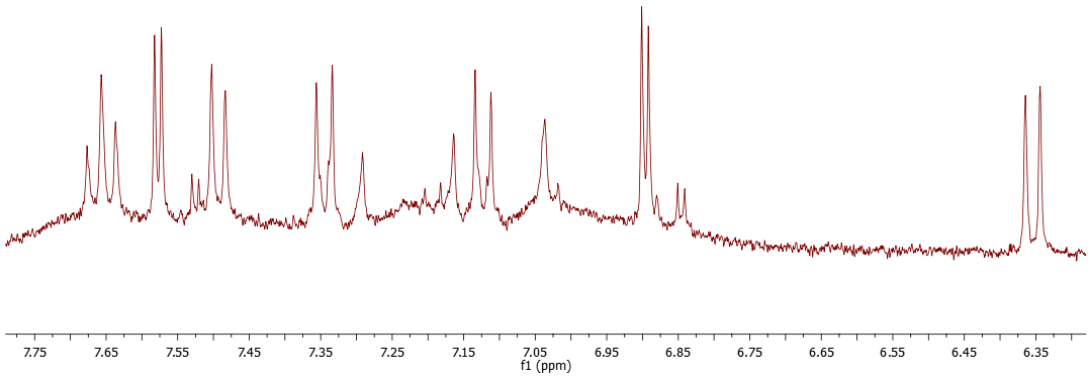

Figure 56. ^{1}H NMR spectrum of **AuL^{7}** recorded at 400 MHz in DMSO-d_6 at 298 K

3. Concluding Remarks

Huo *et al.* have performed DFT calculations on the parent platinum complex, **PtL^{1}** (Section 3.2). The calculations predict that the HOMO-based orbitals are localised along the platinum centre and the ancillary ligand, and the LUMO-based orbitals are mainly localised on the pyridyl rings. Using this as a starting point, rational structure modification has been employed to prepare complexes with tuneable emission.

On considering the tetradentate ligand, we realised that functionalisation of the phenyl ring should alter the energy of the HOMO-based orbitals more significantly than the LUMO-based orbitals. A series of Pt(II) complexes were synthesized and characterized.

All the Pt(II) complexes were emissive from DCM solution at 298 K, with quantum yields reaching as high as 0.78. The quantum yields of these complexes were found to be significantly higher than complexes involving analogous bidentate ligands, highlighting the importance of the extra rigidity conferred by the tetradentate system. **PtL^{1}** and **PtL^{7}** complexes show the best photophysical properties as they emit at low energy (**PtL^{1}** λ_{em} = 506 nm and **PtL^{7}** λ_{em} = 579 nm) with a high quantum yield (0.78 for **PtL^{1}** and 0.74 for **PtL^{7}**). By increasing the π-conjugating system, (**PtL^{4}** and **PtL^{8}**), we observed an emission into the lower energy compared to the emission of **PtL^{1}** and **PtL^{7}**. On the other hand, the quantum yield of luminescence decreased (from 0.78 for **PtL^{1}** to 0.12 for **PtL^{4}**). The deviation from planarity observed by X-ray diffraction for **PtL^{4}** may explain the decreased of the efficiency.

Palladium(II) complexes containing a cyclometallated tetradentate C^N^N^C ligand systems, **PdL^{1}**, **PdL^{6}**, **PdL^{7}** and **PdL^{9}** complexes, have been synthesised and characterized.

Photophysical properties of **PdL^{1}**, **PdL^{6}** and **PdL^{7}** display phosphorescence emission at 298 K emission with quantum yields 0.012, 0.0002 and 0.15 respectively. Their more rigid ligand scaffold which avoid the excited-state distortions efficiently. The lower radiative decay rate of palladium(II) complexes relative to platinum(II) complexes is explained as the heavy atom Pd(II)/Pt(II) in promoting radiative decay of the triplet state.

4. References

[1] M. Maestri, D. Sandrini, V. Balzani, L. Chassot, P. Jolliet, A. Von Zelewsky, *Chem. Phys. Lett.*, 1985, **122**, 375-379.

[2] J. Brooks, Y. Babayan, S. Lamansky, P. I. Djurovich, I. Tsyba, R. Bau, M. E. Thompson, *Inorg. Chem.*, 2002, **41**, 3055-3066.

[3] A. Poloek, C.-T. Chen, C.-T. Chen, *J. Mater. Chem. C*, 2014, **2**, 1376-1380.

[4] D. M. Jenkins, J. F. Senn, S. Bernhard, *Dalton Trans.*, 2012, **41**, 8077-8085.

[5] J. V. Quagliano., L. Schubert, *Chem. Rev.*, 1952, **50**, 201-260.

[6] F. R. Hartley, *Chem. Soc. Rev.*, 1973, **2**, 163-179.

[7] L. Chassot, E. Muller, A.Von Zelewsky, *Chem. Phys. Lett.*, 1985, **122**, 375-379.

[8] W. Lu, B.-X Mi, M. Chan, C. W. Z. Hui, C.-M. Che, N. Zhu, S.-L. Tong, *J. Am. Chem. Soc.*, 2004, **126**, 4958-4971.

[9] S. C. F. Kui, S. S.-Y. Chui, C.-M. Che, N. Zhu, *J. Am. Chem. Soc.*, 2006, **128**, 8297-8309.

[10] W. Lu, S. S.-Y. Chui, K.-M. Ng, C.-M. Che, N. Zhu, *Angew. Chem.*, 2008, **47**, 4568-4572.

[11] C.-W. Chan, T.-F. Lai, C.-M. Che, S.-M. Peng, *J. Am. Chem. Soc.*, 1993, **115**, 11245-11253.

[12] J. H. K. Yip, Suwarno, J. J. Vittal, *Inorg. Chem.*, 2000, **39**, 3537-3543.

[13] Y.-Y. Lin, S.-C. Chan, M. C. W. Chan, Y.-J. Hou, N. Zhu, C.-M. Che, Y. Liu, Y. Wang, *Chem. Eur. J.*, 2003, **6**, 1263-1272.

[14] C.-M. Che, S.-C. Chan, H.-F. Xiang, M. C. W. Chan, Y. Liu, Y. Wang, *Chem. Commun.*, 2004, **13**, 1484-1485.

[15] C.-M. Che, C.-C. Kwok, S.-W. Lai, A. F. Rausch, W. J. Finkenzeller, N. Zhu, H. Yersin, *Chem. Eur. J.*, 2010, **16**, 233-247.

[16] J. Zhang, F. Zhao, X. Zhu, W.-K. Wong, D. Ma, W.-Y. Wong, *J. Mater. Chem.*, 2012, **22**, 16448-16457.

[17] W.-L. Tong, S.-M. Yiu, M. C. W. Chan, *Inorg. Chem.*, 2013, **52**, 7114-7124.

[18] E. F. Reid, V. C. Cook, D. J. D. Wilson, C. F. Hogan, *Chem. Eur. J.*, 2013, **19**, 15907-15917.

[19] E. López-Torres, M. A. Mendiola, *Inorg. Chim. Acta*, 2010, **363**, 1735–1740.

[20] J. M. Hope, J. J. Wilson, S. J. Lippard, *Dalton Trans.*, 2013, **42**, 3176-3180.

[21] K. Li, X. Guan, C.-W. Ma, W. Lu, Y. Chen, C.-M. Che, *Chem. Commun.*, 2011, **47**, 9075-9077.

[22] A. Meyer, Y. Unger, A. Poethig, T. Strassner, *Organometallics*, 2011, **30**, 2980-2985.

[23] X.-C. Hang, T. Fleetham, E. Turner, J. Brooks, J. Li, *Angew. Chem. Int. Ed.*, 2013, **52**, 6753-6756.

[24] H.-F. Xiang, S.-C. Chan, K. K.-Y. Wu, C.-M. Che, P. T. Lai, *Chem. Commun.*, 2005, **11**, 1408-1410.

[25] K. Li, G. Cheng, C. Ma, X. Guan, W.-M. Kwok, Y. Chen, W. Lu, C.-M. Che, *Chem. Sci.*, 2013, **4**, 2630-2644.

[26] S. C. F. Kui, P. K. Chow, G. Cheng, C.-C. Kwok, C. L. Kwong, K.-H. Low, C.-M. Che, *Chem. Commun.*, 2013, **49**, 1497-1499.

[27] G. Cheng, P.-K. Chow, S. C. F. Kui, C.-C. Kwok, C.-M. Che, *Adv. Mater.*, 2013, **25**, 6765-6770.

[28] C. F. S. Kui, P. K. Chow, G. S. M. Tong, S.-L. Lai, G. Cheng, C.-C. Kwok, K.-H. Low, M. Y. Ko, C.-M. Che, *Chem. Eur. J.*, 2013, **19**, 69–73.

[29] K. Feng, C. Zuniga, Y.-D. Zhang, D. Kim, S. Barlow, S. R. Marder, J. L. Brédas, M. Weck, *Macromolecules*, 2009, **42**, 6855-6864.

[30] D. A. K. Vezzu, J. C. Deaton, J. S. Jones, L. Bartolotti, C. F. Harris, A. P. Marchetti, M. Kondakova, R. D. Pike, S. Huo, *Inorg. Chem.*, 2010, **49**, 5107-5119.

[31] I. J. Lin, M. D. S. Liaw, *J. Chin. Chem. Soc.*, 1993, **40**, 451-454.

[32] E. Turner, N. Bakken, J. Li, *Inorg. Chem.*, 2013, **52**, 7344-7351.

[33] C. F. Harris, D. A. K. Vezzu, J. P. Gagnier, M. E. Smith, R. D. Pike, Y. Li, S. Huo, *Polyhedron*, 2013, **52**, 1030-1040.

[34] C. Bronner, S. A. Baudron, M. W. Hosseini, C. A. Strassert, A. Guenet, L. De Cola, *Dalton Trans.*, 2010, **39**, 180-184.

[35] F. Niedermair, S. M. Borisov, G. Zenkl, O.T. Hofmann, H. Weber, R. Saf, I. Klimant, *Inorg.Chem.*, 2010, **49**, 9333-9342.

[36] S. M. Borisov, R. Saf, R. Fischer, I. Klimant, *Inorg. Chem.*, 2013, **52**, 1206-1216.

[37] P. K. Chow, C.Ma, W.-P. To, G. S. M. Tong, S.-L. Lai, S. C. F. Kui, W.-M. Kwok, C.-M. Che, *Angew. Chem. Int. Ed.*, 2013, **52**, 11775-1177.

[38] M. C. DeRosa, R. J. Crutchley, *Coord. Chem. Rev.*, 2002, **233**, 351-371.

[39] W.-P. To, Y. Liu, T.-C. Lau, C.-M. Che, *Chem. Eur. J.*, 2013, **19**, 5654-5664.

[40] E. Mueller, G. Bernardinelli, A. von Zelewsky, *Inorg. Chem.*, 1988, **27**, 4645-4651.

[41] L. M. Mink, M. L. Neitzel, L. M. Bellomy, R. E. Falvo, R. K. Boggess, B. T. Trainum, P. Yeaman, *Polyhedron*, 1997, **16**, 2809-2817.

[42] Z. Ou, T. Khoury, Y. Fang, W. Zhu, P. J. Sintic, M. J. Crossley, K. M. Kadish, *Inorg. Chem.*, 2013, **52**, 2474.

[43] D. Bellows, S. M. Aly, C. P. Gros, M. E. Ojaimi, J.-M. Barbe, R. Guilard, P. D. Harvey, *Inorg.Chem.*, 2009, **48**, 7613-7629.

[44] P. Banerjee, A. Company, T. Weyhermuller, E. Bill, C. R. Hess, *Inorg. Chem.*, 2009, **48**, 2944-2955.

[45] C. O. Paul-Roth, S. Drouet, A. Merhi, J. A. G. Williams, L. F. Gildea, C. Pearson, M. C. Petty, *Tetrahedron*, 2013, **69**, 9625.

[46] J. Louie, J. F. Hartwig, *Tetrahedron Lett.*, 1995, **36**, 3609-3612.

[47] J.-S. Yang, Y.-D. Lin, Y.-H. Lin, F.-L. Liao, *J. Org. Chem.*, 2004, **69**, 3517-3525.

[48] (a) A. Carpita, R. Rossi, Gazz. *Chim. Ital.*, 1985, **115**, 575.

(b) S. Gronowitz, D. Peters, *Heterocycles*, 1990, **30**, 645.

(c) B. Andrieu-Malapel, J.-Y. Merour, *Tetrahedron*, 1998, **54**, 11079.

(d) M. Haddach, J. R. McCarthy, *Tetrahedron Lett.*, 1999, **40** ,3109.

(e) M. Melucci, G. Barbarella, G. Sotgiu, *J. Org. Chem.*, 2002, **67**, 8877-8884.

[49] K. Snégaroff, S. Komagawa , F. Chevallier, P. C. Gros, S. Golhen, T. Roisnel, M. Uchiyama, F. Mongin, *Chem. Eur. J*., 2010, **16**, 8191-8201.

[50]V. N. Kozhevnikov, B. Donnio, B. Heinrich, D. W. Bruce, *Chem. Commun.*, 2014, ahead of print.

[51] W. Lu, V. A. L. Roy, C.-M. Che, *Chem. Commun.*, 2006, **38**, 3972-3974.

[52] V. M. Clark, A. Cox, E.-J. Herbert, *J. Chem. Soc.*, 1968, **7**, 831-833.

[53] M. Albrecht, *Chem. Rev.*, 2010,**110**, 576.

[54] F. Julia, D. Bautista, J. M. Fernandez-Hernandez, P. Gonzalez Herrero, *Chem. Sci.*, 2014, **5**, 1875.

[55] Z. M. Hudson, B. A. Blight, S. Wang *Org. Lett.*, 2012, **14**, 1700-1703.

[56] Z. M. Hudson, B. A. Blight, S. Wang, *Org.Lett.*, 2012, **14**, 1700.

[57] J. D. Scott, R. J. Puddephatt, *Organometallics*, 1983, **2**, 1643-1648.

(b) R. J. Puddephatt, M. A. Thomson, L. Manojlovic-Muir, K. W. Muir, A. A. Frew, M. P. Brown, *J. Chem. Soc., Chem. Commun.*, 1981, **15**, 805-806.

(c) F. B. Zhang, C. W. Kirby, D. W. Hairsine, M. C. Jennings, R. J. Puddephatt, *J. Am. Chem. Soc.*, 2005, **127**, 14196-14197.

(d) D. T. Song, S. Wang, *Organometallics*, 2003, **22**, 2187-2189.

(e) S. B. Zhao, D. T. Song, W. L. Jia, S. Wang *Organometallics*, 2005, **24**, 3290-3296. (f) D. D. Wick, K. I. Goldberg, *J. Am. Chem. Soc.*, 1997, **119**, 10235-10236.

[58] M. A. Gutierrez, G. R. Newkome, J. Selbin, *J. Organomet. Chem.*, 1980, **202**, 341-35.

[59] L. Chassot, A. Von Zelewsky, *Helv. Chim. Acta.*, 1986, **69**, 1855-1857.

[60] L. Chassot, A. von Zelewsky, D. Sandrini, M. Maestri, V. Balzani, *J. Am. Chem. Soc.*, 1986, **108**, 6085-6087.

[61] L. Chassot, E. Muller, A.Von Zelewsky, *Inorg. Chem.*, 1984, **23**, 4249-4253.

[62] L. Chassot, A. Von Zelewsky, D. Sandrini, M. Maestri, V. Balzani, *J. Am. Chem. Soc.*, 1986, **108**, 6084-6085.

[63] D. M. Jenkins, S. Bernhard, *Inorg. Chem.*, 2010, **49**, 11297-11308.

[64] L. Pazderski, J. Tousek, J. Sitkowski, L. Kozerski, E. Szłyk, *Magn. Reson. Chem.*, 2009, **47**, 658-665.

[65] C.-H. Tao, N. Zhu, V. W.-W. Yam, *J. Photochem. Photobiol. A*, 2009, **207**, 94–101.

[66] C. Bronner, S. A. Baudron, M. W. Hosseini, C. A. Strassert, A. Guenet, L. De Cola, *Dalton Trans.*, 2010, **39**, 180–184.

[67] S.-W. Lai, T.-C. Cheung, M. C. W. Chan, K.-K. Cheung, S.-M. Peng, C.-M. Che, *Inorg. Chem.*, 2000, **39**, 255-262.

[68] E. C. Constable, T. A. Leese, *J. Organomet. Chem.*, 1989, **363**, 419-424.

[69] S. Stoccoro, G. Alesso, M. A. Cinellu, G. Minghetti, A. Zucca, M. Manassero, C. Manassero, *Dalton Trans.*, 2009, **18**, 3467-3477.

[70] B. Soro, S. Stoccoro, G. Minghetti, A. Zucca, M. A Cinellu,. S. Gladiali, M. Manassero, M. Sansoni, *Organometallics*, 2005, **24**, 53-61.

[71] S. Lamansky, P. Djurovich, D. Murphy, F. Abdel-Razzaq, H. E. Lee, C. Adachi, P. E. Burrows, S. R. Forrest, M. E. Thompson, *J. Am. Chem. Soc.*, 2001, **123**, 4304-4312.

[72] A. Herbst, C. Bronner, P. Dechambenoit, O. S. Wenger, *Organometallics*, 2013, **32**, 1807-1814.

CHAPTER FOUR:

pH Sensitive Heavy-Metal Complexes

1. Introduction

Luminescent probes are crucial tools in cell biology, physiology, and related areas of the biomedical sciences. They can be utilised for the sensitive detection of species *in vitro* and *in vivo* and for the visualisation of intracellular structure, functions and tissue sections.

To date, most imaging agents are *fluorescent* organic compounds due to their intense emission and high color tunability.[1,2] Such compounds generally work well for conventional intensity-based imaging. A newer method of imaging is based on measuring the lifetimes at all points in the image, known as fluorescence lifetime imaging microscopy or FLIM. Lifetimes can provide additional information about the local environment of fluorescent molecules, for example, not available through intensities alone. However, as fluorescence has a lifetime typically in the range of nanoseconds, the studies of such small changes in lifetime involve sophisticated set-ups. Sub-nanosecond light sources and fast detectors are required. A further limitation of using fluorescence is that the natural fluorescence of endogenous biomolecules leads to interference in the image. This so-called *autofluorescence* becomes increasingly problematic as one goes from single cells to multicellular samples and particularly tissue sections.

In combating these limitations, it is of interest to incorporate a heavy metal atom (e.g. Ru, Rh Ir, Pt…) into the organic molecule in order to facilitate the analysis. Heavy metal complexes, thanks to the effect of spin-orbit coupling and fast intersystem crossing (ISC), may show a luminescence lifetime in the microsecond timescale.[3] The figure below shows how the luminescence of a long-lived probe can be detected without interference from fluorescent molecules (**Figure 1**).[4,5] As an example, in a cell containing a phosphorescent metal complex probe, the background fluorescence of the cell displays a shorter lifetime than the complex. The distinction between the two types of emission is facilitated as the intensity of the fluorescence decreases faster than that of the phosphorescent probe. A delay can be set between excitation and detection, during which the fluorescence decays to negligible values.

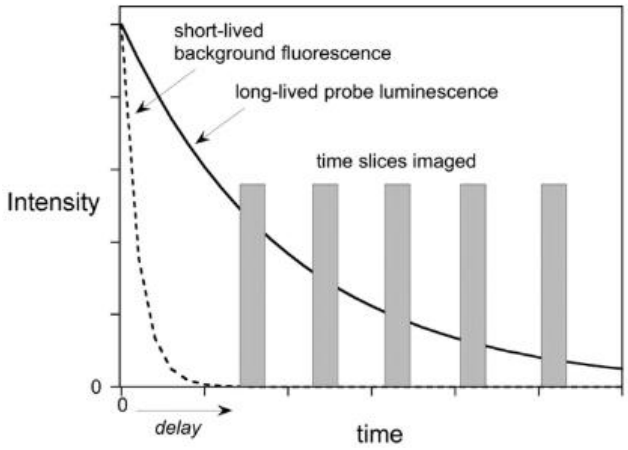

Figure 1. Illustrating the concept of time-resolved imaging and time-gated removal of background fluorescence [5]

Lanthanide complexes are also used as bio-imaging probes.[6,7,8,9] They show interesting photophysical properties such as a large Stokes shifts and narrow emission bands, a long emission lifetime and a good chemical stability profile. However, lanthanide ions are toxic, so a high complex stability is required by the synthesis of complexes bearing macrocyclic ligands. Another disadvantage is that the direct excitation of the lanthanide is very inefficient ($\varepsilon < 1$), so the incorporation of a sensitising chromophore is needed to absorb and transfer the energy to the lanthanide.

In the last decade, heavy metal complexes have been used as biosensor reagents.[10,11] Luminescent transition metal complexes are attractive candidates because of their intense, long-lived, and environment-sensitive emission with large Stokes shifts. In fact, they have been utilized to determine the concentration of substances and other parameters of biological interest (recognition of DNA or RNA, oxygen, cations, amino acids, sugar levels in cells and tissues).[12,13,14,15] Cyclometallated heavy metal complexes are often luminescent and show good stability; such complexes are often used in OLEDs but have only recently started to attract interest as luminescent sensors.[16,17,5]

In the present chapter, I will first introduce and briefly survey different applications of such complexes as biosensors. In the second part, I will present and discuss the synthesis, photophysical and bio-imaging studies of iridium complexes whose emission is modulated by acid or base and which thus have potential as sensory systems for pH and, by extension, other species such as metal ions.

1.1. Sensors for Amino Acids and Sugar Molecules

Thiols play important roles in biological systems. Cysteine (Cys) and homocysteine (Hcy) are mercapto biomolecules that play crucial roles in maintaining biological systems.[18] For example, Cys deficiency is involved in many syndromes including slow growth in children and liver damage. At elevated levels in plasma, Hcy is a risk factor for Alzheimer's or cardiovascular diseases.[19]

An off-on ruthenium complex was synthesized by Zhao *et al.* to detect the presence of sulfhydryl-containing compounds (**Figure 2**).[20] On itself, the ruthenium complex is not emissive due to an electron transfer (ET) from the ruthenium to the 2,4-dinitro-benzenesulfonyl (DNBS) acceptor unit via PET (photoinduced electron transfer). The cleavage of the DNBS unit by a thiolate compound leads to the phosphorescence of the ruthenium complex.

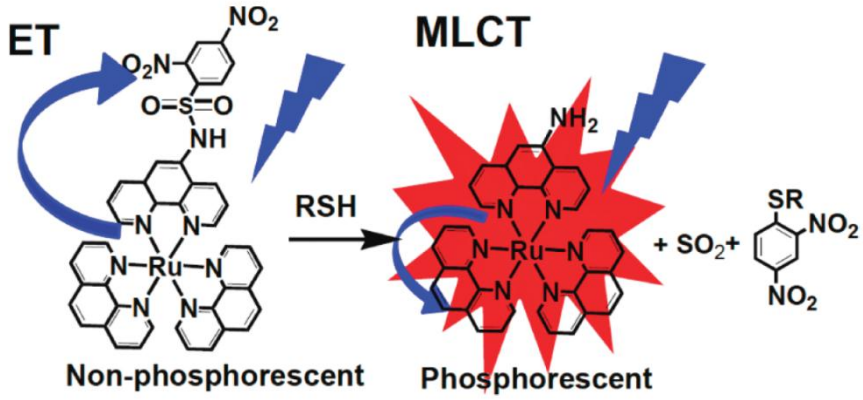

Figure 2. Excitation response of an off-on ruthenium complex[20]

Sugars are one of the most important energy sources for cells and organisms. As an example, the main energy source of the brain is glucose. To detect these sugars in cells, a series of cationic iridium complexes were synthesized as phosphorescent labelling reagents for reducing sugars.[21,22,23] Lo *et al.* have developed cyclometalated iridium(III) bipyridine complexes containing an *N*-methylamino-oxy group to allow reducing sugars to be detected. During this reduction process, the cationic iridium complex exhibits emission (**Figure 3**).[24] The amino-oxy group reacts with the reducing part of glucose, galactose, lactose, and maltose to increase the quantum yield of the luminescence. In fact, the emission of the non-conjugated iridium complex displays a quantum yield of 0.42. The reaction of the iridium complex with β-galactose, α-galactose, β -lactose and β -maltose will increase the quantum yield to 0.80, 0.80, 0.81 and 0.83 respectively.

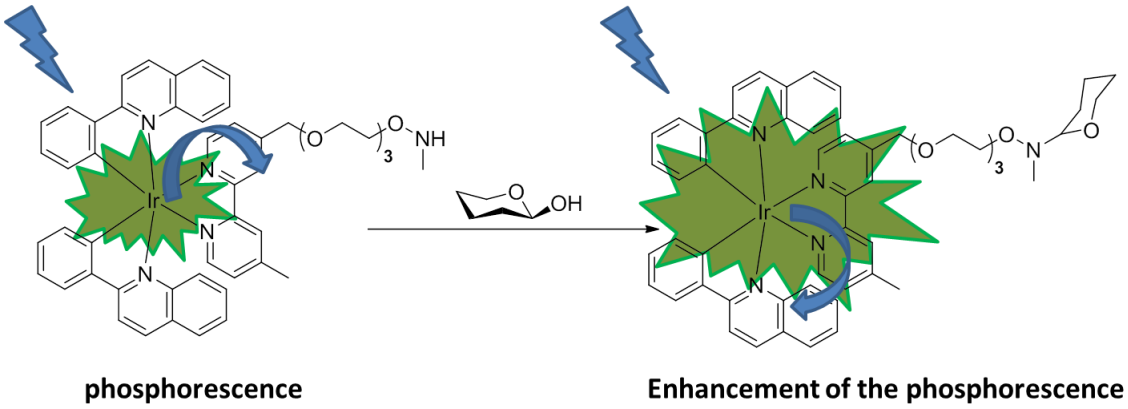

Figure 3. Iridium complexes for detection of reducing sugars [24]

1.2. DNA / RNA sensors

The majority of DNA/RNA sensors are metallointercalators. Intercalation was first proposed by L. S. Lerman and is defined as non-covalent insertion between base pairs.[25] The intercalator is usually a planar unit, typically an aromatic ring or polyaromatic, which can bind to the DNA/RNA (**Figure 4**).[26]

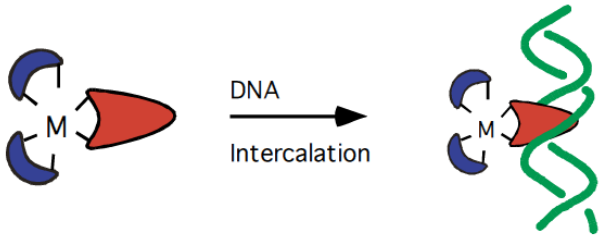

Figure 4. Metallointercalator introduced in DNA [26]

Simple iridium(III) complexes present an essentially spherical exterior, owing to the six-coordinate d^6 configuration of the metal. A more extended ligand protruding out from the core of the complex will thus be required for intercalation to occur. An example of an intercalating iridium complex was demonstrated by Lo and co-workers (**Figure 5**). Three cyclometallated iridium(III) dipyridoquinoxaline complexes were synthesized and studied as metallointercalators for DNA.[27] Upon the addition of DNA or the protein bovine serum albumin (BSA) in aqueous solution, the emission of the complexes increases. The enhancement effect of BSA arises from the binding of the complex to hydrophobic pockets in the protein, which reduces non-radiative decay processes.

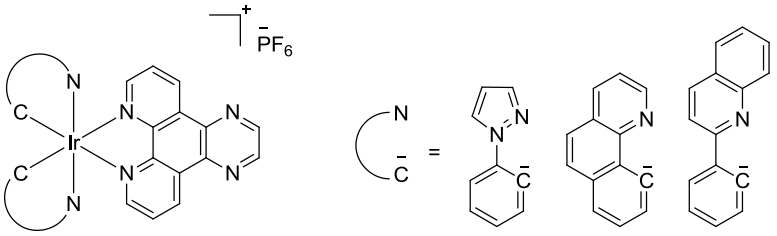

Figure 5. Metallointercalator iridium complexes [27]

1.3. Cation Sensors

The monitoring of bio-agent concentration in biological species is an important key to observing and understanding biological mechanisms. Zn^{2+} and Cu^{2+} are abundant elements in the human body; their concentrations play an important role in many cellular processes. For example a high level of Zn^{2+} is cytotoxic and may lead to skin diseases, diabetes, etc. Copper ions are important for the regulation of the human nervous system. To monitor the concentration of such cations *in vivo*, dipicolylamine can be used as an ion recognition unit in conjunction with an amine electron donor which quenches the luminescence of the free probes through a PET process.[28,29,30]

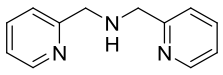

DPA

Figure 6. Representation of DPA molecule

A series of cyclometallated iridium(III) complexes were synthesized as sensors for Zn^{2+} by Lo *et al.* (**Figure 7**).[31] In the presence of Zn^{2+}, they observed an enhancement of the phosphorescence emission and the luminescence lifetime of the iridium complexes thanks to the coordination of the metal to the DPA unit.

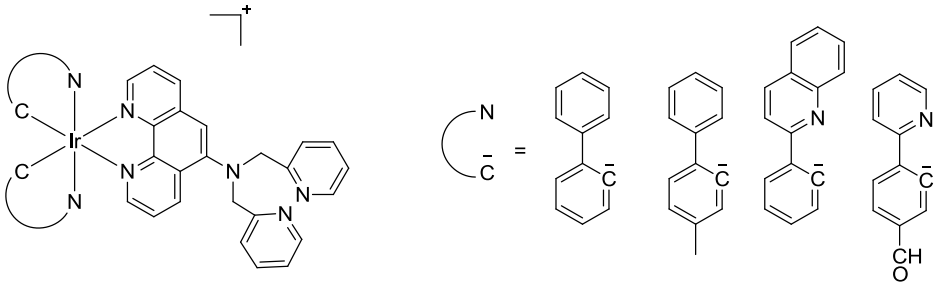

Figure 7. Zn^{2+} iridium complexes sensor [31]

In 2014, Nam *et al.* studied a series of phosphorescent cyclometalated iridium(III) complexes containing phenanthroline ancillary ligand as biosensor.[32] Metal-chelating receptors can readily be introduced into the ligand peripheries of the iridium(III) complexes to create phosphorescence sensors for detection of zinc, cupric, and chromium ions. Alterations in the structures of the C^N ligands produce varying extents of phosphorescence responses to metal ions. Mechanistic investigations establish that a nonradiative PET process is dominantly responsible for phosphorescence modulation. It is suggested that phosphorescence turn-on might result from the effective suppression of a non-radiative ILCT transition. The zinc probe based on the cyclometalated iridium(III) complex is cell-permeable when added to the culture media and is localized within the mitochondria of HeLa cells. The zinc-ion-sensing utility has been verified by carrying out phosphorescent visualization of intracellular zinc ions in mammalian cells.

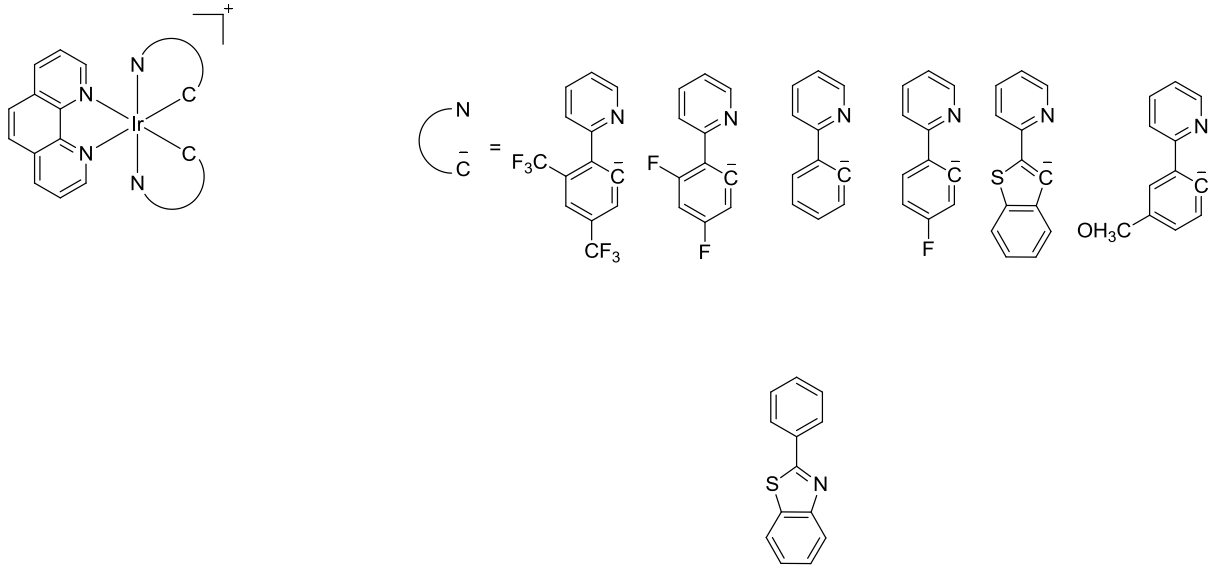

Figure 8. Cationic iridium complexes used as biosensors [32]

1.4. Intracellular pH sensors

Intracellular pH measurements provide important diagnostic information because a small deviation of the pH value may lead to cardiopulmonary and neurological diseases such as Alzheimer's disease, or may be associated with the formation of solid tumours. Cancer cells tend to be hypoxic which in turn leads to a lower pH. Luminescent pH sensors are attractive as pH probes due to their high sensitivity and convenience as well as the relatively non-invasive nature of fluorescence microscopy.

Excitation and emission profiles in the infrared and near infrared show better tissue penetration than UV, blue and green, which have a poor tissue penetration and (especially in the case of UV) may cause damage.

A water-soluble alkynylplatinum(II) terpyridine complex was synthesized and studied by Yam and co-workers (**Figure 9**).[33] They observed that the emission intensity can be modulated by the pH and the temperature (**Figure 10**).

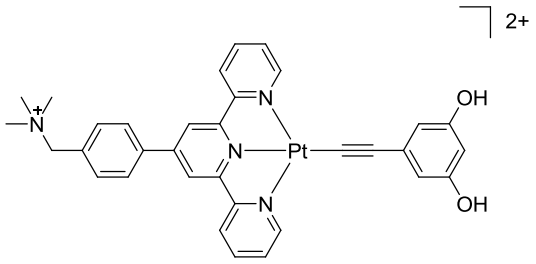

Figure 9. Alkynylplatinum(II) terpyridine complex [33]

In fact, they showed a pH-dependence of the complex's structure. For the complex in aqueous solution (50 mM NaCl) at 20˚C, the emission intensity in the NIR region remains relatively unchanged over the range from pH 3.5 to pH 5.6. The formation of aggregate explained the emission in the complex at lower pH. However, at pH above 5.6, the NIR emission shows a significant drop in intensity and becomes completely "turned-off" at or above pH 7.6 via PET. The decrease in the NIR emission intensity has been associated with the deprotonation of the phenolic protons of the complex. It is likely that the deprotonation leads to an increase in the hydrophilicity of the complex causing de-aggregation of the complex and hence a drop in its ^{3}MMLCT emission intensity. A temperature dependence of the complex's emission properties was also observed. At pH = 4, when the temperature was increased (from 10 °C to 80 °C), the emission intensity at 795 nm decreased. Below 50 °C, the de-aggregation of the complex and the increase of the non-radiative decay at high temperature gave rise to a significant decrease in the low-energy emission.

The NIR emission of the complex will be "off" at physiological pH (7.0-7.4) but will be "on" upon small changes of pH below 7, for example in tumour cells. The temperature below 50 °C will have no effect on the NIR emission; the aggregation of the complex moieties is negligible. A small change in physiological temperature would not have any interference on the detection of pH by the NIR emission spectral responses of the complex.

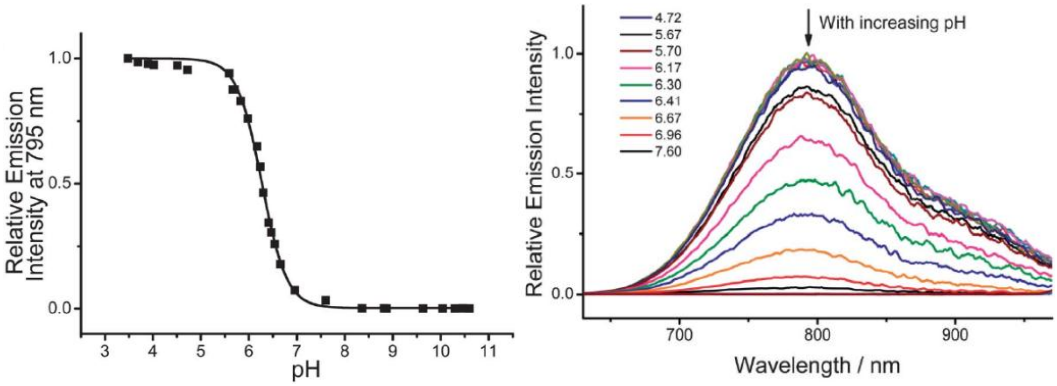

Figure 10. **Left**: Variation of the emission intensity of the complex shown in **Figure 9**, at 795 nm, as a function of pH. **Right**: emission spectra of the complex over the range of pH values indicated. The complex was at a concentration of 200 μM in 50 mM NaCl at 20 ˚C.[33]

Another example of a pH sensor was demonstrated in the laboratory at Durham. Two iridium complexes based on a pyridyl-benzimidazole (pybz and pybzH) were synthesized and studied (**Figure 11**).[34] The cationic and the neutral forms of the iridium complexes were obtained using two different synthetic methods. The photophysical properties of the neutral and the cationic complexes are different (**Table 1**). Indeed, the cationic complex shows a red-shift of the emission wavelength compared to the neutral complex (λ_{max} = 590 and 521 nm respectively). A pH titration in aqueous solution (DMSO / water 1:1) shows that a decrease of the intensity at 590 nm was observed after pH ≥ 5.6 (**Figure 12**). The introduction of the complex in the ovary cell of a hamster shows its localization in the lysosome. In co-staining experiments with a fluorescent nuclear stain (Hoechst 33342), image acquisition with no time delay shows only nuclear fluorescence associated with the fluorescent stain, whereas a short delay (10 ns) before image acquisition gives images with strong phosphorescence from cytoplasmic structures instead of the nucleus.

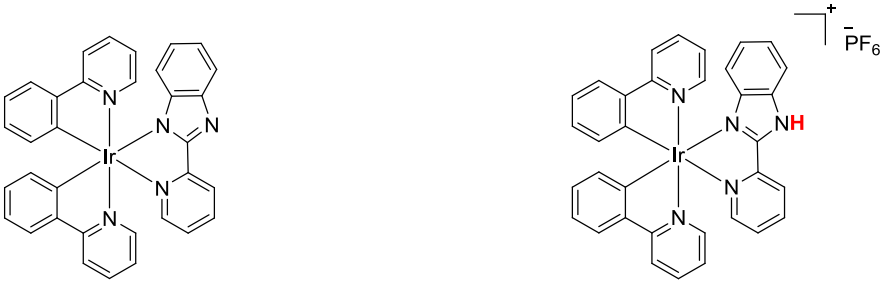

Ir(ppy)$_2$(pbz) **[Ir(ppy)$_2$(pbzH)]PF$_6$**

Figure 11. Neutral (left) and cationic (right) forms of pyridylbenzimidazole iridium complexes [34]

Table 1. Photophysical data of **Ir(ppy)$_2$(pbz)** and **[Ir(ppy)$_2$(pbzH)]$^+$** in degassed DCM at 298 K [34]

	Ir(ppy)$_2$(pbz)	**[Ir(ppy)$_2$(pbzH)]PF$_6$**
Absorption λ_{max}(nm) (ε (L mol^{-1}cm^{-1}))	340 (33100), 433 (5140), 476 (1270)	320 (30100), 380 (8670), 418 (4170), 470 (1100)
Emission λ_{max} (nm)	496, 521	590
Quantum yield ϕ_{lum}	0.48	0.22
Lifetime (ns)	3200 (100)	840 (210)

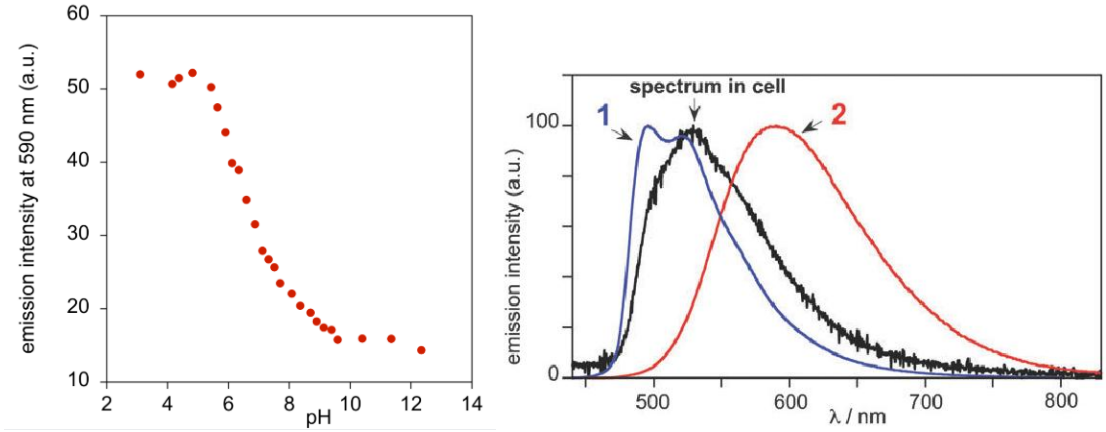

Figure 12. Titration of the neutral iridium complex **Ir(ppy)$_2$(pbz)** (**left**) and the comparison of the emission from inside a CHO cell with the emission of the neutral (**1**) and cationic (**2**) iridium complexes in solution.[34]

1.5. Objectives

New iridium complexes incorporating a *bis*-benzimidazole ligand (bbz) as potential phosphorescent reagents for bio-imaging will be report. In this case, *three* different forms may be anticipated in principle, namely a cationic, a neutral and an anionic form, according to the protonation state of the azole nitrogen atoms (**Figure 13**).

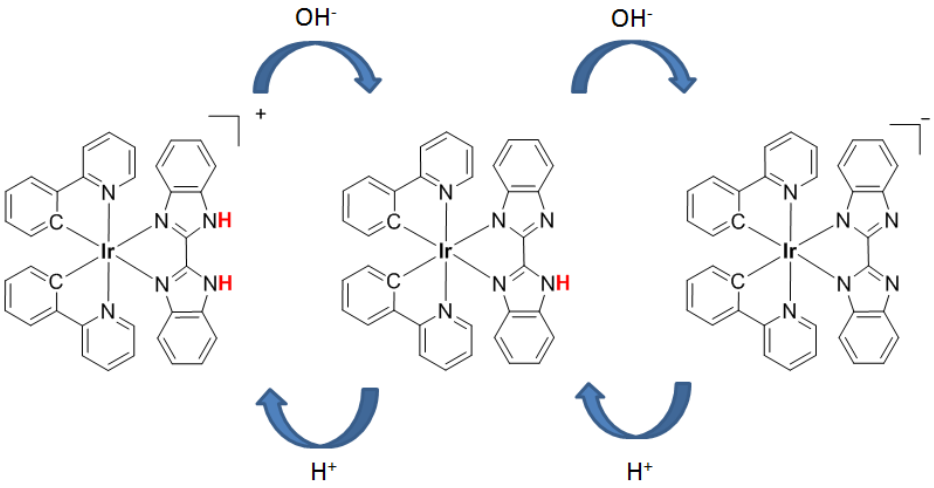

Figure 13. Protonation and deprotonation of iridium complex

A related series of isomeric complexes containing isoquinolyl-benzimidazoles (**L**^{10}**H**, **L**^{11}**H**, **L**^{12}**H**) will also be describe. The introduction of iso-quinolyl units leads to a red-shift in the emission compared to the pyridyl analogue, although the properties are dependent on the isomeric form. The complexes display pH-dependent absorption and emission properties.

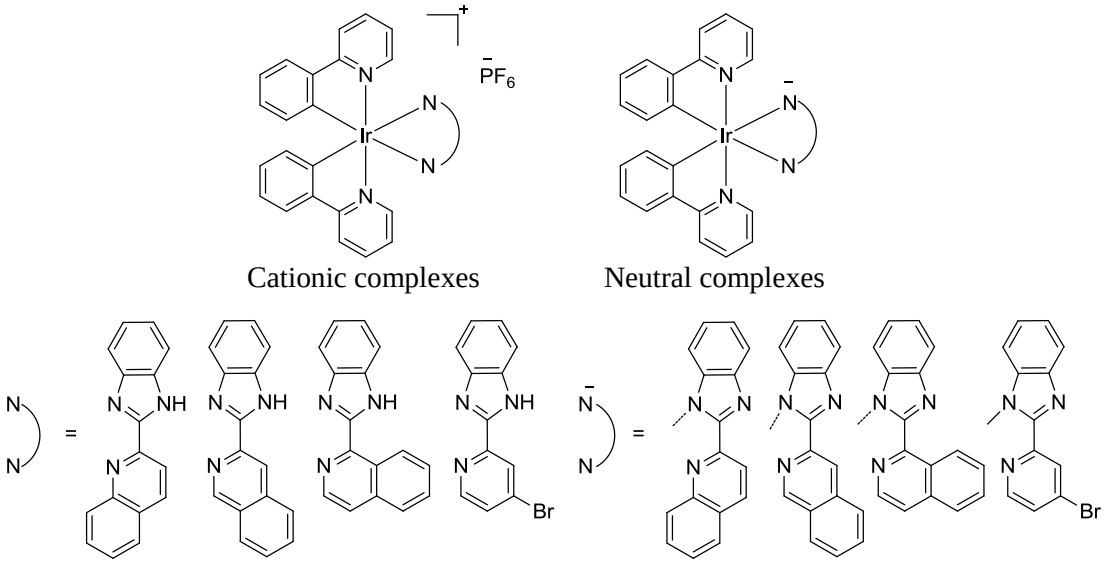

Figure 14. (Iso)-quinoline and bromo-pyridyl neutral and cationic iridium complexes

2. Synthesis and Characterizations

2.1. Preparation of the ligands/proligands

2.1.1. Benzimidazole derivatives

Benzimidazol-(iso)quinolyl derivatives **$L^{10}H$**, **$L^{11}H$**, **$L^{12}H$** and bromo-pyridylbenzimidazole **$L^{13}H$** were prepared using the Leavitt benzimidazole condensation (**Scheme 1**).[35] The reaction between *o*-phenylenediamine and the appropriate carboxylic acid was performed at 150 °C in polyphosphoric acid (PPA). It consists of the formation of the amide followed by the acid catalyzed-cyclisation thanks to the PPA.[36] Reactions gave the organic compounds **$L^{10}H$**, **$L^{11}H$**, **$L^{12}H$** and **$L^{13}H$** in 85 to 88 % yields.

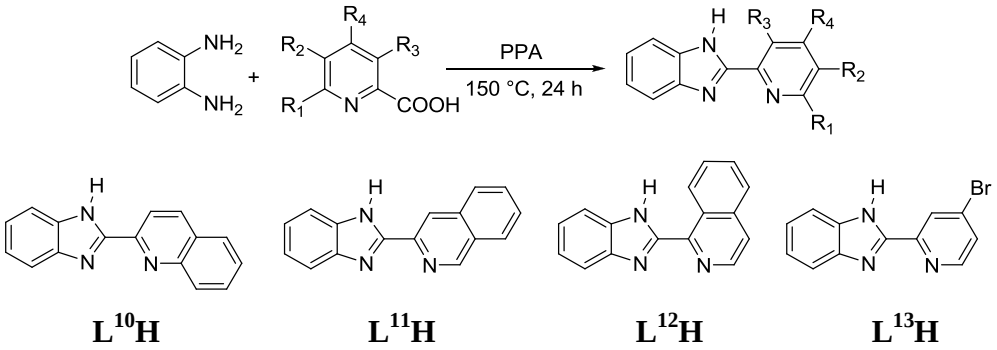

$L^{10}H$ **$L^{11}H$** **$L^{12}H$** **$L^{13}H$**

Scheme 1. Synthesis of benzimidazole derivatives via condensation

2.1.2. *Bis*-benzimidazole derivatives

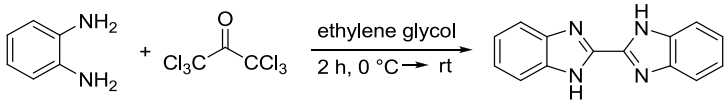

$L^{14}H_2$

Scheme 2. Synthesis of 2,2′- *bis*-benzimidazole via condensation

The synthesis of 2,2′-*bis*-benzimidazole **$L^{14}H_2$** was carried out by reaction of 1,2-benzenediamine with hexachloropropanone in ethyleneglycol at 0 °C (**Scheme 2**). A mechanism proposed by Meakins *et al.* was described as the formation of the amide followed by the condensation between the amine and the amide.[37] The product was dried under reduced pressure to give a white solid in 53 % yield. The dimethylated derivative **L^{15}** was also prepared. The methylation of the two azole rings was performed using the same procedure as Huang *et al.* (**Scheme 3**),[38] giving the product as a white solid in 75 % yield.

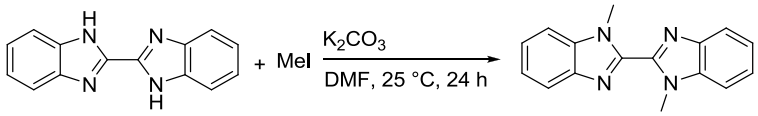

L[15]

Scheme 3. Synthesis of 1,1′-dimethyl-2,2′- *bis*-benzimidazole from **L**[15]

2.2. Preparation of the complexes

All the complexes were synthesized by the reaction of the well-known "iridium dimer" $[Ir(ppy)_2(\mu\text{-}Cl)]_2$ with the appropriate organic compound **L**[10]**H**, **L**[11]**H**, **L**[12]**H**, **L**[13]**H, L**[14]$\mathbf{H_2}$ or **L**[15]. The preparation of the chloride-bridged *di*-iridium(III) intermediate was usually performed with $IrCl_3.3H_2O$ and an excess of the proligand ppyH in a mixture of 2-ethoxyethanol and water at 146 °C (see **Chapter 1**).[39] The interest of using these ligands is the ability to protonate or deprotonate the azole ring leading to the formation of either a positively charged or charge-neutral iridium(III) complex. Similar behaviour has been observed for $[Ru(bpy)_2(pbzH)]^{2+}$.[40] The cationic and the neutral complexes, incorporating L^nH and L^n respectively (n = 1 to 6), were synthesized separately using two different methods.

2.2.1. Neutral Complexes

The synthesis of the neutral complexes required the deprotonation of the azolic nitrogen of the benzimidazole unit. The N^N⁻-coordinating pyridyl-azolate ligand resembles a cyclometallated N^C-coordinating ligand. This resemblance is well-established by the synthesis of iridium *bis*-phenylpyridyl complexes bearing 2-pyridyl pyrazolate, triazolate or tetrazolate, for example, from the work established by Chi and Chou.[41,42] The 2,2′- *bis*-benzimidazole acted as a primary amine ligand. The formation of the neutral complexes was realized under relatively aggressive conditions conditions in DMF at 152 °C (**Scheme 4**).[43] The addition of base such as K_2CO_3 was necessary to deprotonate the 2,2′- *bis*-benzimidazole and/or to remove the HCl liberated upon coordination of the ligand, which would protonate remaining ligand and inhibit further reaction. The cleavage and the coordination of the N^N ligand occurred within 24 h. The reaction was quenched with water and extracted with DCM. The final neutral complexes were obtained by recrystallization from THF in 45 % to 63 % yields.

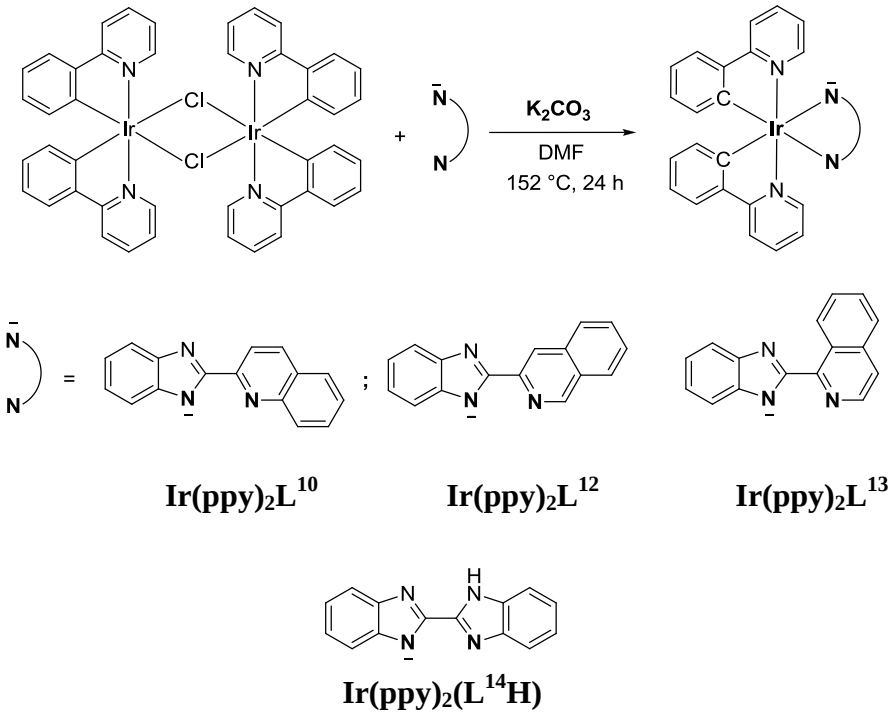

Scheme 4. Synthesis of neutral iridium complexes **Ir(ppy)$_2$L^{10}**, **Ir(ppy)$_2$L^{11}**, **Ir(ppy)$_2$L^{12}** and **Ir(ppy)$_2$(L^{14}H)** in DMF at 152 °C

2.2.2. Cationic Complexes

The cationic iridium complex is the conjugate acid of the corresponding neutral iridium complex. In the cationic complexes, the benzimidazole unit binds as a neutral imine-like =N- ligand, similar to a pyridine. The net coordination sphere is therefore comparable to that of [Ir(*N*^*C*–ppy)$_2$(*N*^*N*-bpy)]$^+$ for example, thus leading to the formation of a *bis*-cyclometallated cationic iridium complex. The synthesis of the cationic complexes was achieved under milder conditions, through reaction of the dimer with the benzimidazole ligand in a mixture of MeOH and DCM at 52 °C (**Scheme 5**).[44] The cleavage and the coordination of the N^N ligand was complete within 24 h. The solvent was evaporated and the residue was dissolved in the minimum volume of acetonitrile. At this point, the counterion is Cl^-. In order to obtain a more tractable, organic-soluble salt, the chloride can be exchanged for a larger ion such as PF_6^-. This was achieved by adding the acetonitrile solution dropwise to a saturated aqueous solution of KPF_6. The precipitate that formed was separated by centrifugation and washed several times with EtOH and Et_2O. Recrystallization in acetonitrile gave the iridium complexes as coloured powders in 40 to 78 % yields.

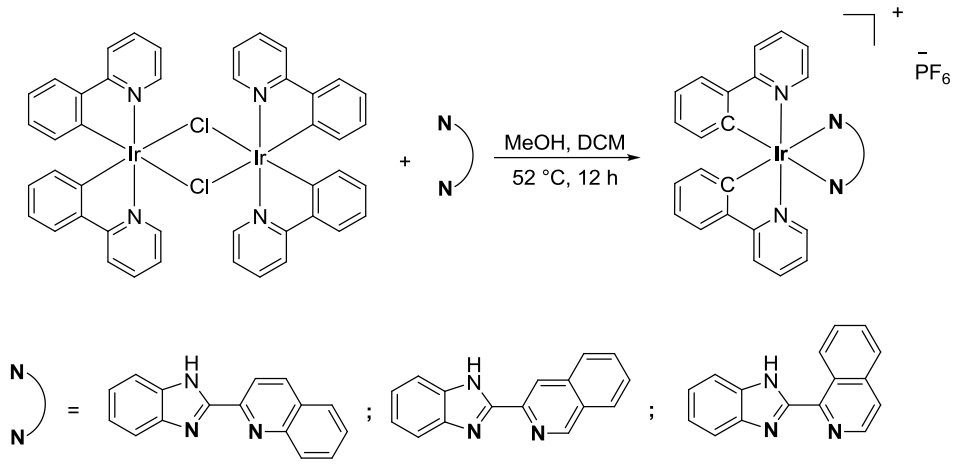

[Ir(ppy)$_2$(L^{10}H)]PF$_6$ **[Ir(ppy)$_2$(L^{11}H)]PF$_6$** **[Ir(ppy)$_2$(L^{12}H)]PF$_6$**

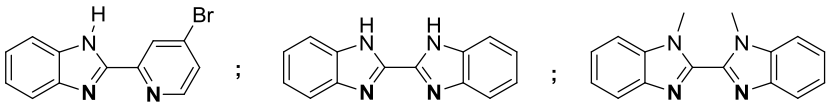

[Ir(ppy)$_2$(L^{13}H)]PF$_6$ **[Ir(ppy)$_2$(L^{14}H$_2$)]PF$_6$** **[Ir(ppy)$_2$L^{15}]PF$_6$**

Scheme 5. Synthesis of cationic iridium complexes **[Ir(ppy)$_2$(L^{10}H)]PF$_6$**, **[Ir(ppy)$_2$(L^{11}H)]PF$_6$**, **[Ir(ppy)$_2$(L^{12}H)]PF$_6$**, **[Ir(ppy)$_2$(L^{13}H)]PF$_6$**, **[Ir(ppy)$_2$(L^{14}H$_2$)]PF$_6$** and **[Ir(ppy)$_2$L^{15}]PF$_6$** under mild conditions: DCM/MeOH at 52˚C

2.3. Characterizations

2.3.1. NMR spectroscopy

The ^{1}H NMR spectra of **Ir(ppy)$_2$L^{10}** and **[Ir(ppy)$_2$(L^{10}H)]PF$_6$** displayed significant differences in the signals of the benzimidazole-based ligand (**Figure 15**) compared to the free ligand **L^{10}H**. The signals for protons **11** and **12** of the quinoline ring are slightly shifted for the neutral complex compared to the proligand **L^{10}H** and more shifted for the cationic iridium complex. On the other hand, the signal of proton **3** of the benzimidazole ring is shifted to lower frequency in both of the iridium complexes compared to the free ligand. The presence of the proton of the benzimidazole unit around 13 ppm confirmed the nature of the cationic iridium complex.

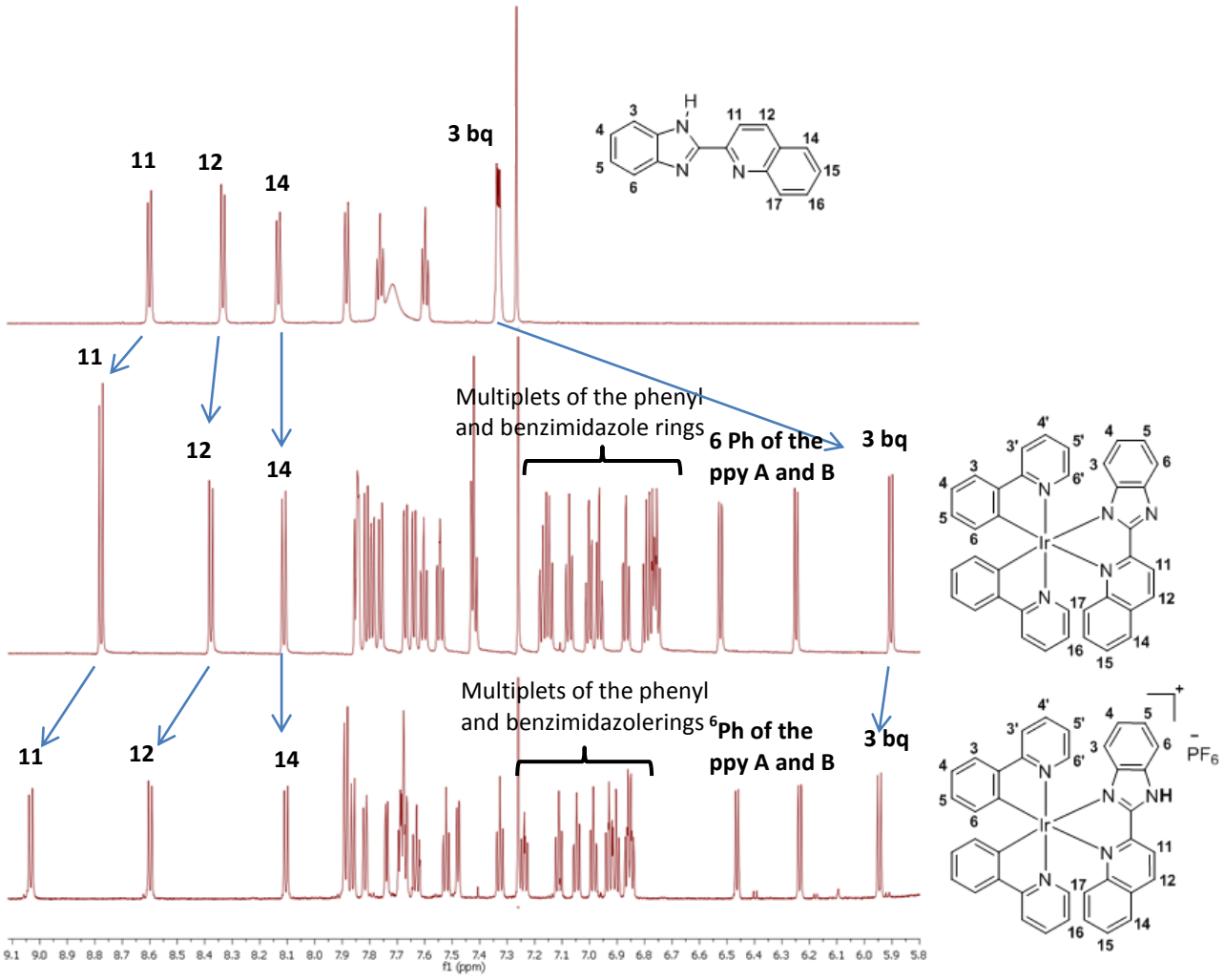

Figure 15. **TOP**: ^{1}H NMR of the ligand $\mathbf{L^{10}H}$, 2-(2-quinolyl)benzimidazole. **MIDDLE**: ^{1}H NMR of the corresponding neutral iridium complex, $\mathbf{Ir(ppy)_2L^{10}}$ and **BOTTOM**: ^{1}H NMR of the corresponding cationic iridium complex, $\mathbf{[Ir(ppy)_2(L^{10}H)]PF_6}$. All spectra were recorded in $CDCl_3$ at 298 K (700MHz)

The ^{1}H NMR in $CDCl_3$ of $\mathbf{Ir(ppy)_2(L^{14}H)}$ and $\mathbf{[Ir(ppy)_2(L^{14}H_2)]PF_6}$ are shown in **Figure 16**. Both iridium complexes, neutral and cationic, displayed twelve protons, despite the fact that $\mathbf{Ir(ppy)_2(L^{14}H)}$ would be expected to show one fewer than $\mathbf{[Ir(ppy)_2(L^{14}H_2)]PF_6}$. $\mathbf{[Ir(ppy)_2(L^{14}H_2)]PF_6}$ showed a clear C_2 symmetry, with twelve signals in the aromatic region, consistent with the two benzimidazole units being equivalent. $\mathbf{Ir(ppy)_2(L^{14}H)}$, due to the deprotonation of one of the two azole rings, should not be anymore symmetrical. However, the ^{1}H NMR still shows the two benzimidazole rings to be equivalent. The azolic proton is "shared" between the two azole nitrogen atoms, which confers symmetry.

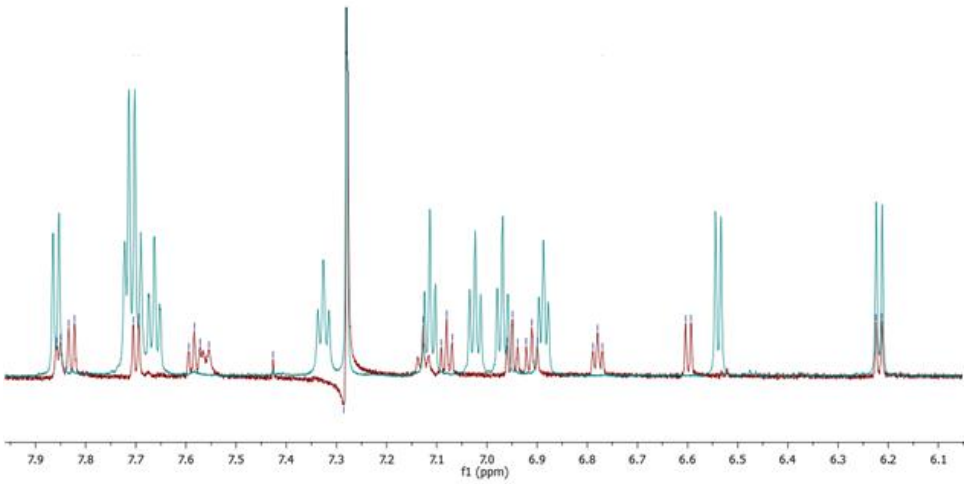

Figure 16. ^{1}H NMR of **Ir(ppy)$_2$(L^{14}H)** and **[Ir(ppy)$_2$(L^{14}H$_2$)]PF$_6$** overlayed to illustrate the observed differences in NMR spectra on the protonation of the benzimidazole unit. The blue spectrum is the neutral form of the iridium complex and the purple spectrum is the cationic form of the iridium complex. All spectra were recorded in $CDCl_3$ at 298 K (700 MHz)

2.3.2. Crystal structures

Crystals of **Ir(ppy)$_2$L^{12}**, **[Ir(ppy)$_2$(L^{12}H)]PF$_6$** and **Ir(ppy)$_2$L^{10}** were obtained by slow evaporation in acetone or chloroform. The molecular structures of **Ir(ppy)$_2$L^{12}**, **[Ir(ppy)$_2$(L^{12}H)]PF$_6$** and **Ir(ppy)$_2$L^{10}** were determined by single crystal X-ray diffraction analysis at 120 K for the cationic iridium complex **[Ir(ppy)$_2$(L^{12}H)]PF$_6$** and at 100 K for the neutral complexes **Ir(ppy)$_2$L^{10}** and **Ir(ppy)$_2$L^{12}**, which confirmed the pseudo-octahedral coordination structure (**Figure 17**). The trans angles at the metal centre range between 170.29 Å and 175.41 Å for **Ir(ppy)$_2$L^{10}**, 171.7 Å and 178.1 Å for complex **Ir(ppy)$_2$L^{12}** and 170.7 Å and 174.1 Å for **[Ir(ppy)$_2$(L^{12}H)]PF$_6$**. Furthermore, the presence of the PF_6 as a counterion of **[Ir(ppy)$_2$(L^{12}H)]PF$_6$** proved the protonated form of the complex. The selected bond lengths and angles are listed in **Table 2**.

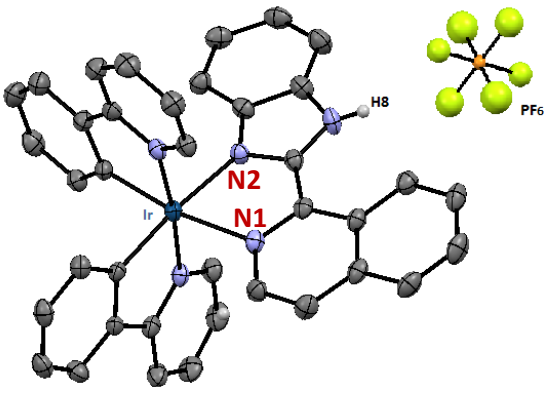

[Ir(ppy)$_2$(L^{12}H)]PF$_6$

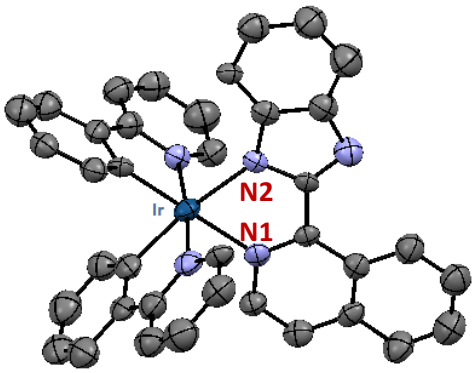

Ir(ppy)$_2$L^{12}

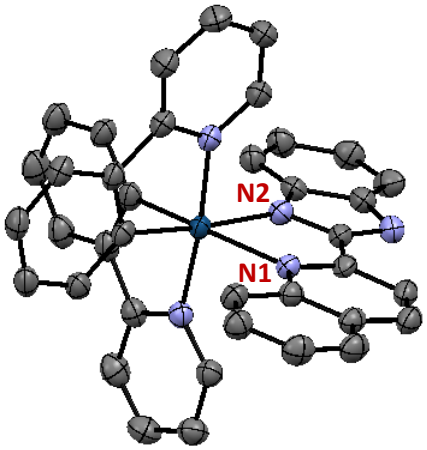

Ir(ppy)$_2$L^{10}

Figure 17. ORTEP structures of **[Ir(ppy)$_2$(L^{12}H)]PF$_6$**, **Ir(ppy)$_2$L^{12}** and **Ir(ppy)$_2$L^{10}**

All the bond angles of the neutral and the corresponding cationic complexes are similar. The Ir–N^2 bond was slightly shorter for the neutral complex **Ir(ppy)$_2$L^{12}** than for complex **[Ir(ppy)$_2$(L^{12}H)]PF$_6$** (2.090 Å and 2.123 Å respectively). In fact, due to the deprotonation of the azolic ring, the Ir–N bond of **Ir(ppy)$_2$L^{12}** is closer to that of *fac*-Ir(ppy)$_3$ (2.095 Å),whilst the Ir–N bond of **[Ir(ppy)$_2$(L^{12}H)]PF$_6$** is similar to the Ir–N(bpy) (2.135 Å).[45,46] However, all the metal-ppy bond distances were closer to the cationic [Ir(ppy)$_2$(bpy)]$^+$ complex than to *fac*-Ir(ppy)$_3$. Interestingly, the Ir–**N^1** bond distance was significantly longer than the other Ir–N bond distances of all the other complexes presented. The steric effect of the benzimidazole-quinoline ligand influenced its bond distances to the metal.

Table 2. Selected bond lengths (Å) and angles (°) of Ir(III) complexes. **[Ir(ppy)$_2$(bpy)]PF$_6$ and *fac*-Ir(ppy)$_3$** are included for comparison [44,45]

Complex	Bond lengths **Ir**–N^1	Bond lengths **Ir**–R	Bond lengths **Ir**–N	Bond lengths **Ir**–N	Bond lengths **Ir**–C	Bond lengths **Ir**–C
[Ir(ppy)$_2$(L^{12}H)]PF$_6$ R = N^2	2.161(4)	2.123(4)	2.046(4)	2.045(4)	2.003(5)	2.017(5)
Ir(ppy)$_2$L^{12} R = N^2	2.123(16)	2.090(15)	2.048(16)	2.018(18)	2.050(2)	1.985(19)
Ir(ppy)$_2$L^{10} R = N^2	2.252(3)	2.117(3)	2.042(3)	2.039(3)	2.010(4)	2.017(4)
[Ir(ppy)$_2$(bpy)]PF$_6$ R = N	2.142(5)	2.135(5)	2.042(7)	2.050(9)	2.011(5)	2.012(5)
***fac*-Ir(ppy)$_3$** R = C	2.095(9)	2.034(9)	2.086(8)	2.071(10)	2.032(9)	2.060(10)

Complex	Bond angles / ° N^1^**Ir**^R	Bond angles / ° C^1^**Ir**^C^2	Bond angles / ° N^1^**Ir**^C^1
[Ir(ppy)$_2$(L^{12}H)]PF$_6$ R = N^2	75.09(16)	80.71(19)	80.45(18)
Ir(ppy)$_2$L^{12} R = N^2	75.80(6)	80.45(8)	80.40(7)
Ir(ppy)$_2$L^{10} R = N^2	76.22(11)	80.40(15)	80.21(14)
[Ir(ppy)$_2$(bpy)]PF$_6$ R = N	76.50(6)	80.20(6)	80.40(4)
***fac*-Ir(ppy)$_3$** R = C	78.60(4)	79.00(4)	79.60(4)

2.3.3. DFT calculations

DFT and TD-DFT calculations for **Ir(ppy)$_2$L^{10}**, **[Ir(ppy)$_2$(L^{10}H)]PF$_6$**, **Ir(ppy)$_2$L^{11}**, **[Ir(ppy)$_2$(L^{11}H)]PF$_6$**, **Ir(ppy)$_2$L^{12}**, **[Ir(ppy)$_2$(L^{12}H)]PF$_6$** were carried out using the B3LYP functional, with 6-31G* as the basis set for the ligands and LanL2DZ for the iridium (**Figures 18** and **19**). According to the contour plots of the molecular orbitals of the neutral iridium complexes **Ir(ppy)$_2$L^{10}**, **Ir(ppy)$_2$L^{11}** and **Ir(ppy)$_2$L^{12}**, the HOMO is based on the benzimidazole unit and the metal centre and the LUMO essentially only on the (iso)-quinolyl part of the molecule. For the cationic iridium complexes, the LUMO is again based on the (iso)quinolyl unit, but now the HOMO is based on the phenyl rings of the ppy ligands. As a consequence, the functionalization of the ppy ligands by electron-withdrawing or -donating groups is expected to have little effect on the photophysical properties of the neutral iridium complexes. On the other hand, such functionalization may be anticipated to have a larger effect on the optical properties of the cationic iridium complexes, as it should influence the HOMO energy.

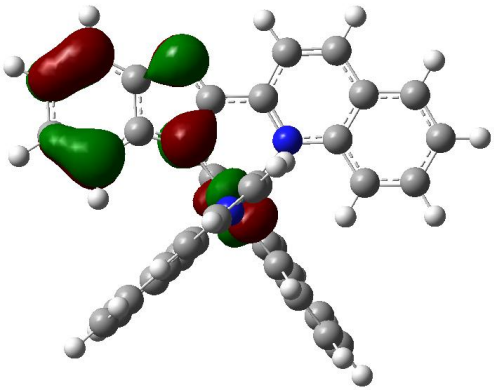

HOMO -5.29 eV

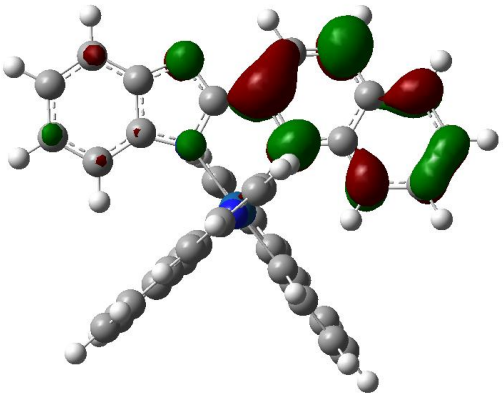

LUMO -2.10 eV

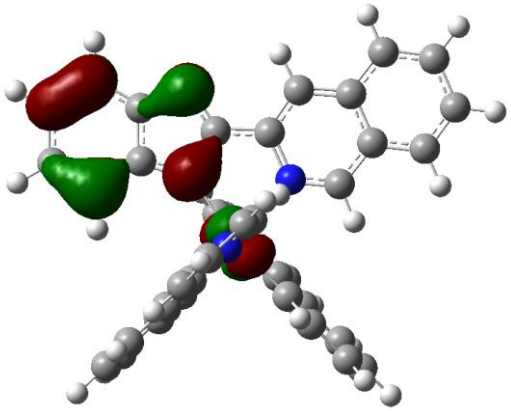

HOMO -5.21 eV

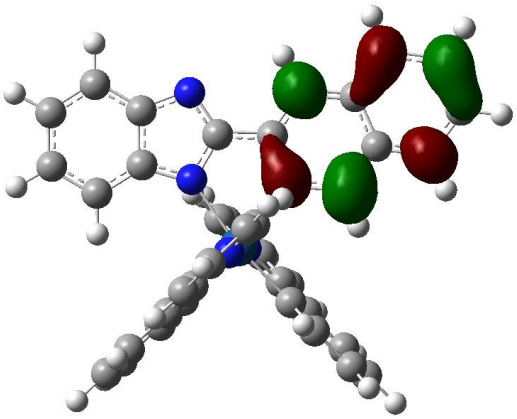

LUMO -2.08 eV

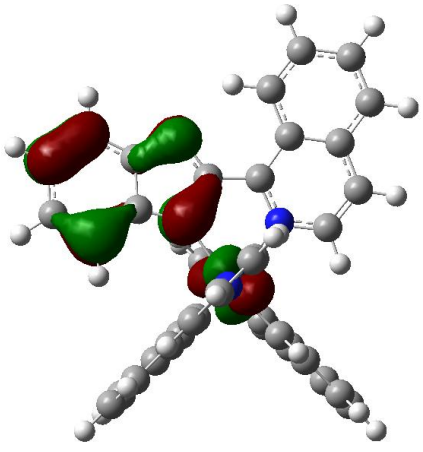

HOMO -5.32 eV

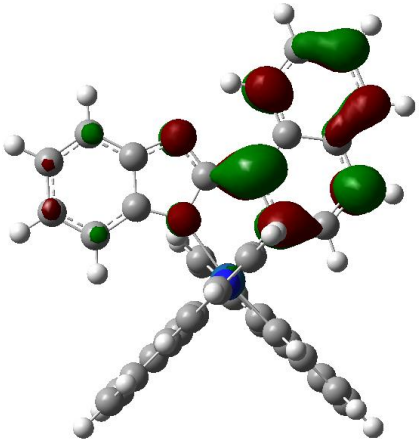

LUMO -2.12 eV

Figure 18. Contour plots of the HOMO and LUMO of neutral iridium complexes **Ir(ppy)$_2$L^{10}** (**TOP**), **Ir(ppy)$_2$L^{11}** (**MIDDLE**) and **Ir(ppy)$_2$L^{12}** (**BOTTOM**)

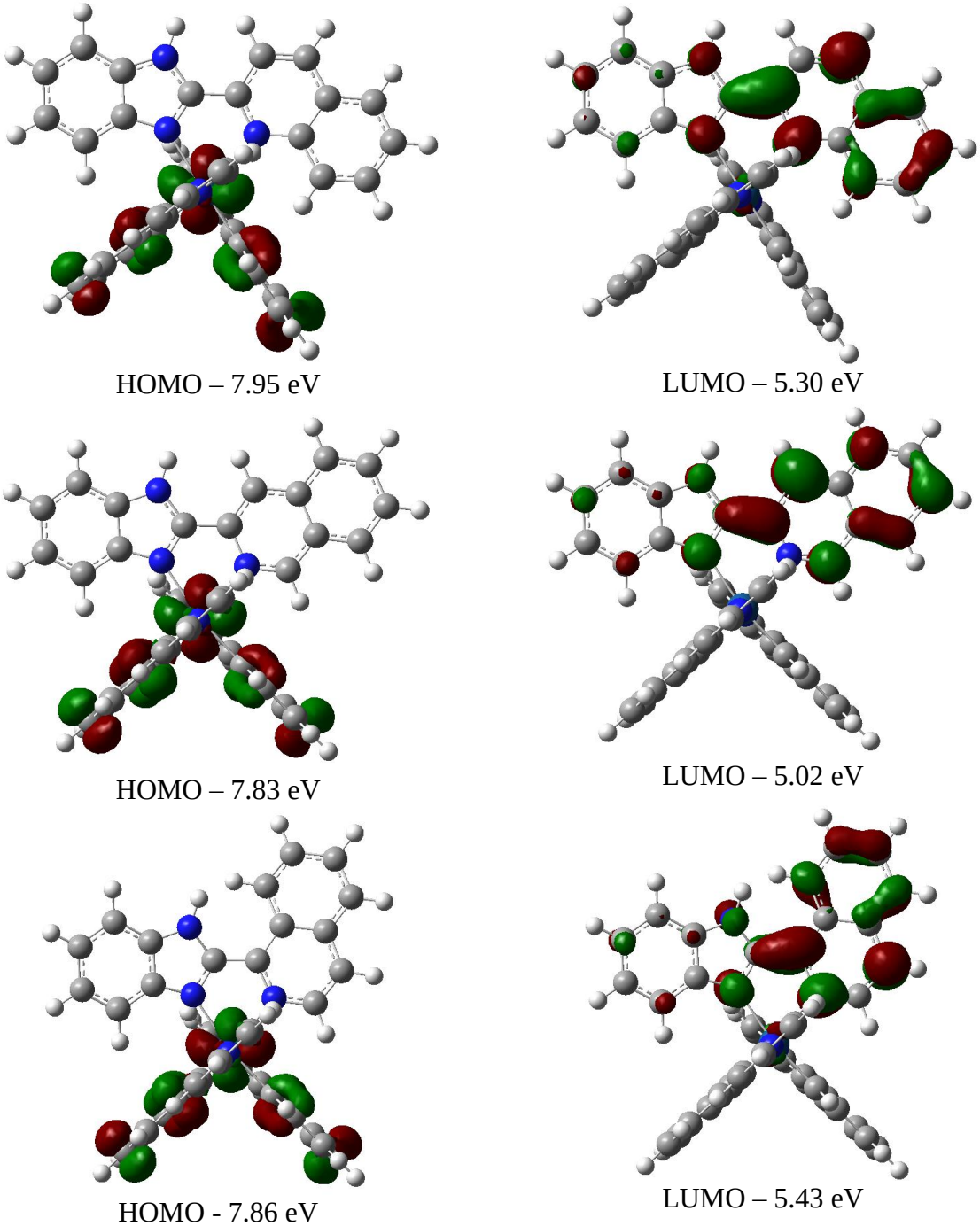

Figure 19. Contour plots of the HOMO and LUMO of cationic iridium complexes **[Ir(ppy)$_2$(L^{10}H)]PF$_6$** (**TOP**), **[Ir(ppy)$_2$(L^{11}H)]PF$_6$** (**MIDDLE**) and **[Ir(ppy)$_2$(L^{12}H)]PF$_6$** (**BOTTOM**)

2.3.4. Electrochemistry

Cyclic voltammetry was performed in DCM, with tetrabutylammonium hexafluorophosphate (0.1 M) as a supporting electrolyte, and the solutions were purged with nitrogen before each measurement. The nature of the ancillary ligands affects both the potentials and the reversibility of the redox processes. All compounds display at least one oxidation process. The formal half-wave potentials of the reversible processes and the peak potentials of the irreversible ones are reported in **Table 3**.

The CVs of **Ir(ppy)$_2$L^{10}**, **Ir(ppy)$_2$L^{11}** and **Ir(ppy)$_2$L^{12}** are shown in **Figure 20**. The CVs of **Ir(ppy)$_2$L^{11}** and **Ir(ppy)$_2$L^{12}** display two reversible anodic waves with $E_{½}$ = +1.15 V and +1.45 V for **Ir(ppy)$_2$L^{11}** and $E_{½}$ = +1.03 V and +1.27 V for **Ir(ppy)$_2$L^{12}**. In contrast, the CV of **Ir(ppy)$_2$L^{10}** exhibits also two anodic waves, one reversible at around +1.5 V and another at +1.45 V that do not display the corresponding backward wave either at 0.05 V s^{-1} or at higher scan rates, suggesting irreversibility. The nature of the ancillary ligand of these complexes has an impact on the oxidation process as the neutral **Ir(ppy$_2$)(pbz)** complex exhibits only one reversible oxidation ($E_{½}$ = +1.2 V). As far as the electrochemical behaviour of **Ir(ppy)$_2$L^{10}, Ir(ppy)$_2$L^{11}** and **Ir(ppy)$_2$L^{12}** is concerned, we can observe that the first oxidation process occurs at less anodic potentials than that of **Ir(ppy$_2$)(pbz)** because the quinoline and isoquinoline moiety is more electron-rich than the pyridine.

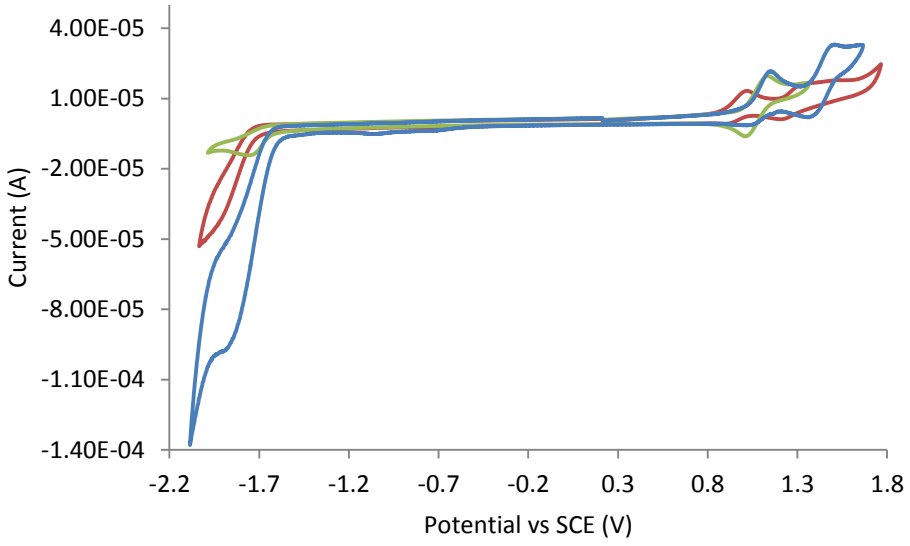

Figure 20. Cyclic voltammogram of **Ir(ppy)$_2$L^{10}** (green), **Ir(ppy)$_2$L^{11}** (blue) and **Ir(ppy)$_2$L^{12}** (red) in DCM/TBAPF$_6$ (0.1 M) versus Fc/Fc$^+$ at 100 mV s^{-1}

The CVs of **[Ir(ppy)$_2$(L^{10}H)]PF$_6$**, **[Ir(ppy)$_2$(L^{11}H)]PF$_6$** and **[Ir(ppy)$_2$(L^{12}H)]PF$_6$** are shown in **Figure 21**. All cationic complexes display one reversible oxidation with a formal potential of $E_{½}$ = +1.27 V, +1.06 V and +1.15 V respectively. On the cathodic side, **[Ir(ppy)$_2$(L^{10}H)]PF$_6$** exhibits a partially reversible reduction process around −1.4 V. The CV of **[Ir(ppy)$_2$(L^{12}H)]PF$_6$** displays two cathodic waves at −1.28 and −1.90 V which appear to be irreversible. One irreversible reduction wave was observed for **[Ir(ppy)$_2$(L^{11}H)]PF$_6$** around −1.8 V.

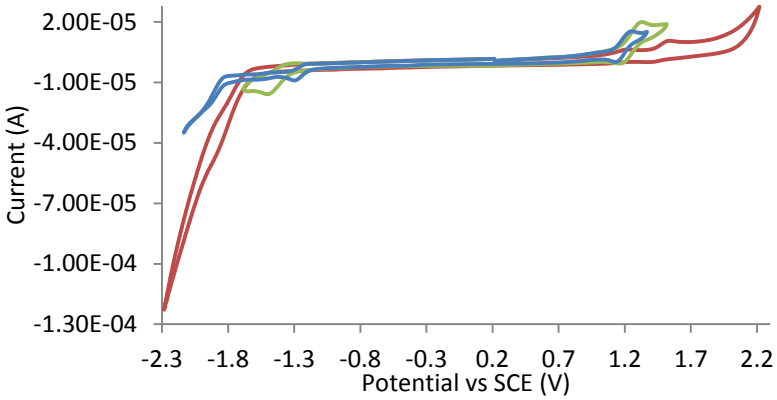

Figure 21. Cyclic voltammogram of **[Ir(ppy)$_2$(L^{10}H)]PF$_6$** (green), **[Ir(ppy)$_2$(L^{11}H)]PF$_6$** (blue) and **[Ir(ppy)$_2$(L^{12}H)]PF$_6$** (red) in dichloromethane/TBAPF$_6$ (0.1 M) versus Fc/Fc$^+$ at 50 mV s^{-1}

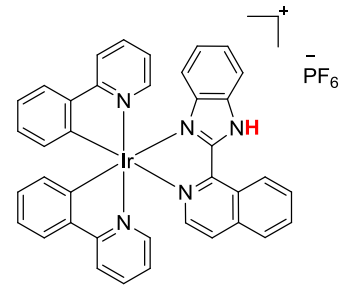

[Ir(ppy)$_2$(L^{12}H)]PF$_6$

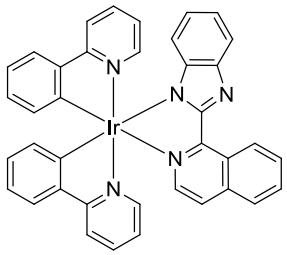

Ir(ppy)$_2$L^{12}

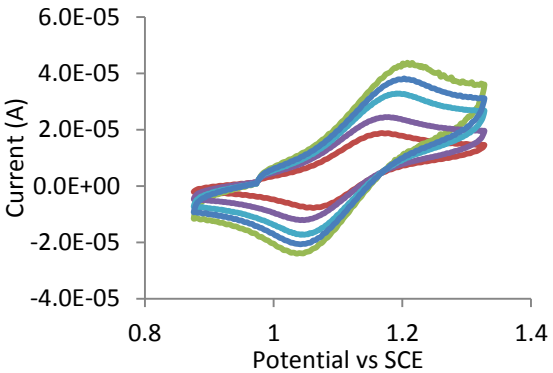

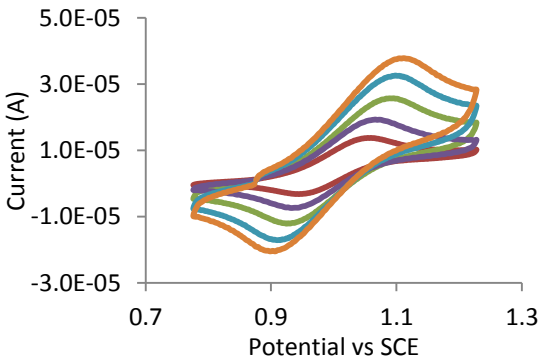

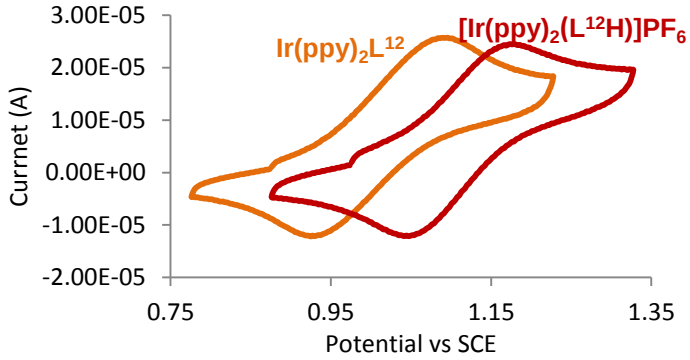

Figure 22. **TOP**: Representation of **[Ir(ppy)$_2$(L^{12}H)]PF$_6$** and **Ir(ppy)$_2$L^{12}**. **MIDDLE**: Cyclic voltammogram of the first oxidation of **[Ir(ppy)$_2$(L^{12}H)]PF$_6$** (left) and **Ir(ppy)$_2$L^{12}** (right) in DCM/TBAPF$_6$ (0.1 M) versus Fc/Fc$^+$ at 50 to 400 mV s^{-1}. **BOTTOM**: Overlay of the oxidation waves of **[Ir(ppy)$_2$(L^{12}H)]PF$_6$** and **Ir(ppy)$_2$L^{12}** in DCM/TBAPF$_6$ (0.1 M) versus Fc/Fc$^+$ at 100 mV s^{-1}

The first reduction of the Ir complexes usually occurs on the ancillary ligands, while the oxidation is centered on the Ir-aryl moiety. The redox gap of the whole series (calculated as the difference between the formal potentials of the cathodic and anodic systems) spans over a wide range, namely, ~2.3−2.7 V (**Figure 23**). The onset potentials of all complexes were estimated by analysing the intersection of the slope drawn at the rising oxidation and reduction current and the baseline. The oxidation potential onset was calculated in relation to E_{SCE} (-4.4 ± 0.1 eV) from the equation:[47,48]

$$\text{HOMO LEVEL} = E_{SCE} - \text{Eonset-ox}$$

$$\text{LUMO LEVEL} = E_{SCE} - \text{Eonset-red}$$

The electrochemical band gap (E_g) was defined as the difference between the onsets of oxidation (E_{ox}) and reduction (E_{red}). The reduction of **Ir(ppy)$_2$(L^{14}H)** and **[Ir(ppy)$_2$(L^{14}H$_2$)]PF$_6$** was not possible to observe but they both displayed reversible oxidation waves with $E_{½}$ = 1.01 V for **Ir(ppy)$_2$(L^{14}H)** and 1.05 V for **[Ir(ppy)$_2$(L^{14}H$_2$)]PF$_6$**.

Some conclusions can be made from the comparison between cationic and neutral complexes:

(i) The electrochemistry of the complexes is affected by the protonation state of the azolic ring. In fact, we observed that neutral complexes are easier to oxidise than the cationic complexes. This is due to the fact that it is difficult to remove electrons from an already charged complex as we observed the same case for the Ir(ppy)$_3$ and the Ir(ppy)$_2$(bpy)$^+$. Related to the DFT calculation (section **2.3.3**), the oxidation process of the neutral complexes involves the removal of one electron from the electron rich benzimidazole. In

contrast, the oxidation of the cationic iridium complexes occurs on the ppy units as the benzimidazolium became electron deficient. This matches the fact that neutral complexes are easier to oxidise than cationic complexes.

(ii) Cationic complexes are easier to reduce than neutral complexes. A lowering of the LUMO level occurs in the cationic complexes due to the proximity of the electron deficient benzimidazolium unit.

(iii) The drop of the LUMO level is more important than the evolution of the HOMO level for the cationic complexes. This involves a diminution of the HOMO-LUMO gap for the cationic complexes compared to the neutral complexes

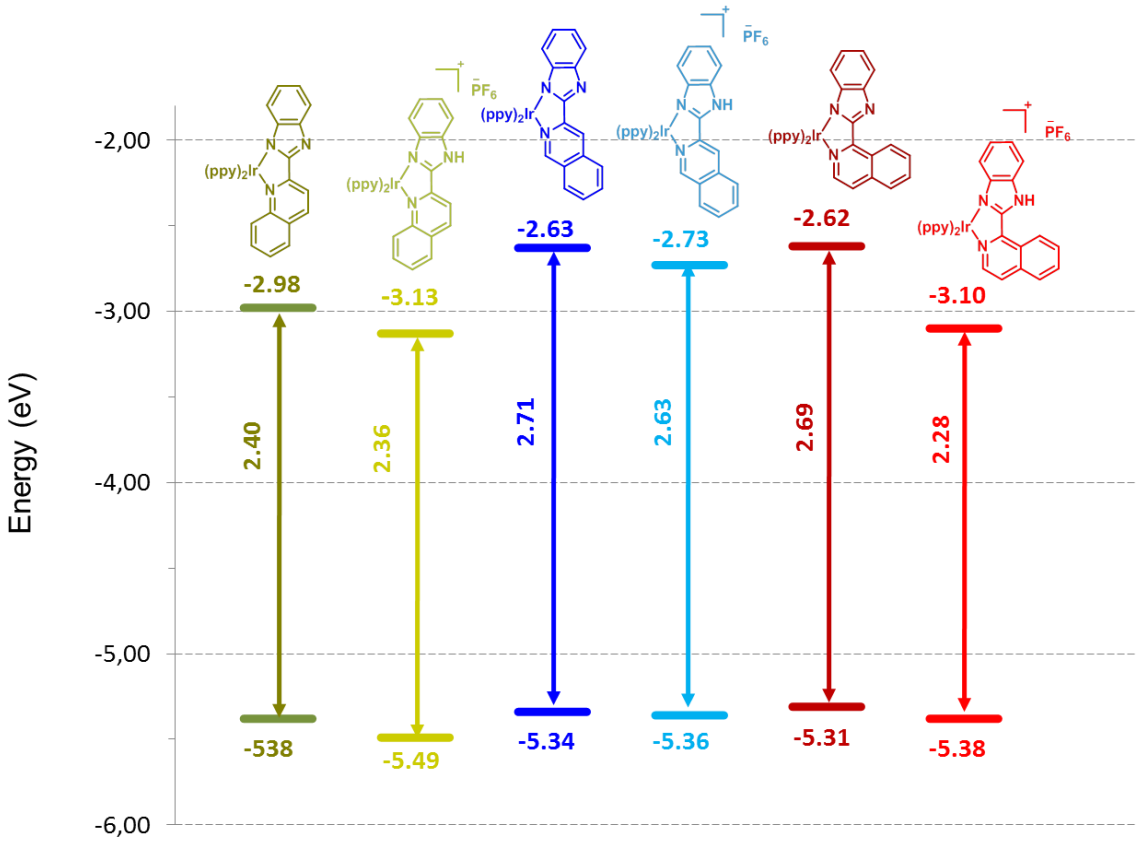

Figure 23. HOMO-LUMO energy levels for **[Ir(ppy)$_2$(L^{10}H)]PF$_6$**, **[Ir(ppy)$_2$(L^{11}H)]PF$_6$** and **[Ir(ppy)$_2$(L^{12}H)]PF$_6$** complexes and **Ir(ppy)$_2$L^{10}**, **Ir(ppy)$_2$L^{11}** and **Ir(ppy)$_2$L^{12}** complexes

Table 3. Electrochemical data for neutral and cationic Ir(III) complexes

Complex	$E_{1/2}$ ox (V)	$E_{1/2}$ red (V)	Eonset-ox (V) ; HOMO (eV)	Eonset-red (V) / LUMO (eV)	Energy gap E_g (eV)
$Ir(ppy)_2L^{10}$	1.10	-1.53	0.98 V ; -5.38 eV	-1.42 / -2.98 eV	2.40 eV
$[Ir(ppy)_2(L^{10}H)]PF_6$	1.27	-1.43	1.09 V; -5.49 eV	-1.27 / -3.13 eV	2.36 eV
$Ir(ppy)_2L^{11}$	1.15; 1.45	-1.82	0.94 V; -5.34 eV	-1.77 / -2.63 eV	2.74 eV
$[Ir(ppy)_2(L^{11}H)]PF_6$	1.06	-	0.96 V; -5.36 eV	-1.61 / -2.73 eV	2.63 eV
$Ir(ppy)_2L^{12}$	1.03; 1.27	-1.78	0.91 V; -5.31 eV	-1.78 / -2.62 eV	2.69 eV
$[Ir(ppy)_2(L^{12}H)]PF_6$	1.15	-	0.98 V; -5.38 eV	-1.30 / 3.10 eV	2.28 eV
$Ir(ppy)_2(L^{14}H)$	1.05	-	-	-	-
$[Ir(ppy)_2(L^{14}H_2)]PF_6$	1.01	-	-	-	-

The values were determined from DCM solutions at 298 K (~10^{-4} M), in the presence of a 0.1 M tetrabutylammonium hexafluorophosphate as the supporting electrolyte. A scan rate of 200 mV s^{-1} was employed and values are reported relative to SCE, using ferrocene as the standard ($E_{½}$ = 0.42 V *vs.* SCE).

2.4. Photophysical studies

2.4.1. Absorption in dichloromethane

2.4.1.1. Quinolyl and isoquinolyl iridium complexes

The ground-state absorbance spectra of cationic (**[Ir(ppy)$_2$(L^{10}H)]PF$_6$**, **[Ir(ppy)$_2$(L^{11}H)]PF$_6$**, **[Ir(ppy)$_2$(L^{12}H)]PF$_6$** and neutral (**Ir(ppy)$_2$L^{10}**, **Ir(ppy)$_2$L^{11}**, **Ir(ppy)$_2$L^{12}**) iridium complexes in DCM solution are shown in **Figures 24** and **25** respectively. They all showed intense bands in the UV region between 230 and 330 nm assigned to the $^1\pi$-π^* transitions of the ligands. Weaker bands at lower energy extending into the visible region (between 330 and 490 nm) were attributed to metal-to-ligand charge transfer (MLCT) transitions. **Ir(ppy)$_2$L^{11}** and **Ir(ppy)$_2$L^{11}** absorbed at higher energy than the other iridium complexes. In fact their absorption spectra were characterized by a broad band centered at 330 nm whereas **[Ir(ppy)$_2$(L^{12}H)]PF$_6$**, which absorbed at the lowest energy, was characterized by a broad band centered at 389 nm.

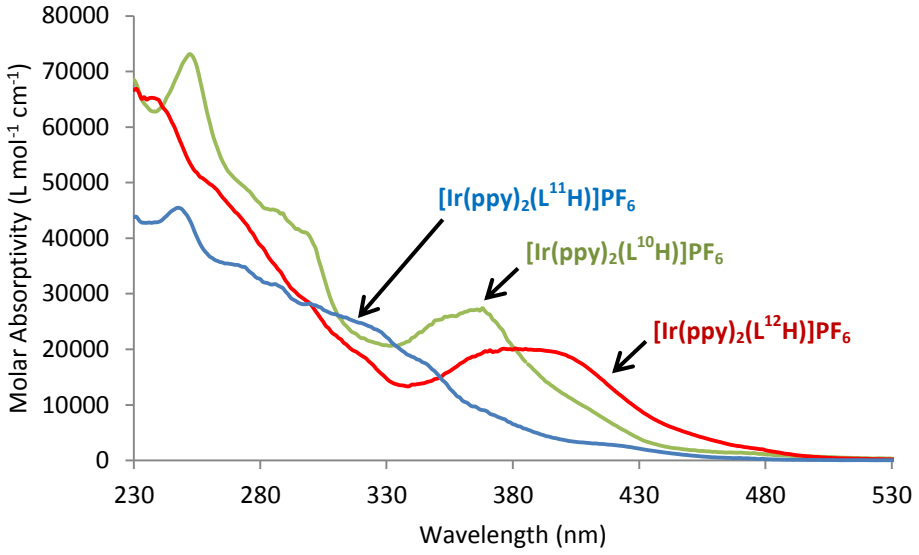

Figure 24. UV-visible absorption spectra of **[Ir(ppy)$_2$(L^{10}H)]PF$_6$**, **[Ir(ppy)$_2$(L^{11}H)]PF$_6$** and **[Ir(ppy)$_2$(L^{12}H)]PF$_6$**, complexes in DCM at 298 K

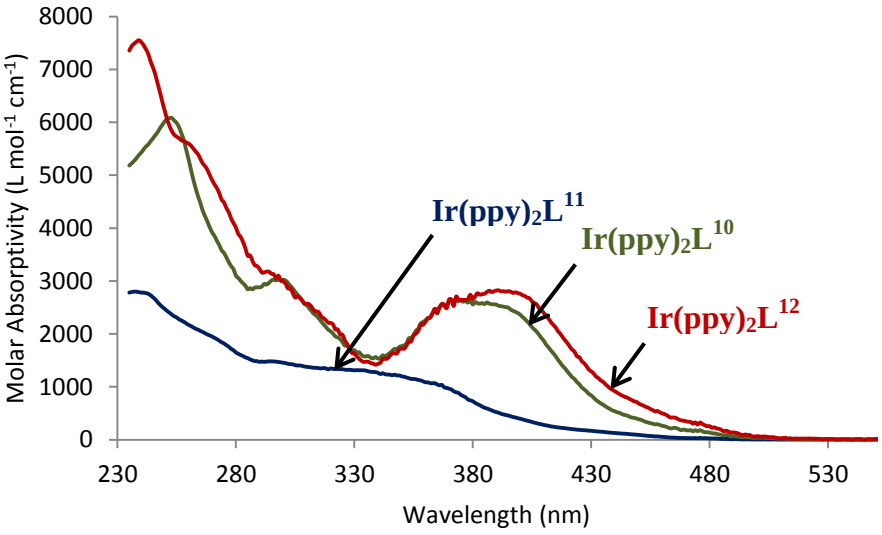

Figure 25. Normalized UV-visible absorption spectra of **Ir(ppy)$_2$L^{10}**, **Ir(ppy)$_2$L^{11}** and **Ir(ppy)$_2$L^{12}**, complexes in DCM at 298 K

The absorbance process measures the energy difference between the ground state and the excited state. Since there are a number of vibrational states associated with both the ground state and the excited state, the E_{00} band gap is the energy difference between the lowest vibrational states of the ground and excited states (**Figure 26**). The onset absorption wavelengths of all complexes were estimated by analysing the intersection of the slope drawn at the lowest energy and the baseline. The optical gap was calculated as the energy corresponding to the λ_{onset} wavelength. The calculated optical and electrochemical gap values are similar (difference from 0 eV for **Ir(ppy)$_2$L^{10}** to 0.21 eV for **[Ir(ppy)$_2$(L^{12}H)]PF$_6$, Table 4**), so we can conclude that the first transition observed in the absorption corresponds to a HOMO/LUMO transition. Moreover, from DFT calculation, we can see that this HOMO/LUMO transition corresponds to a metal-to-ligand charge-transfer (MLCT) transition.

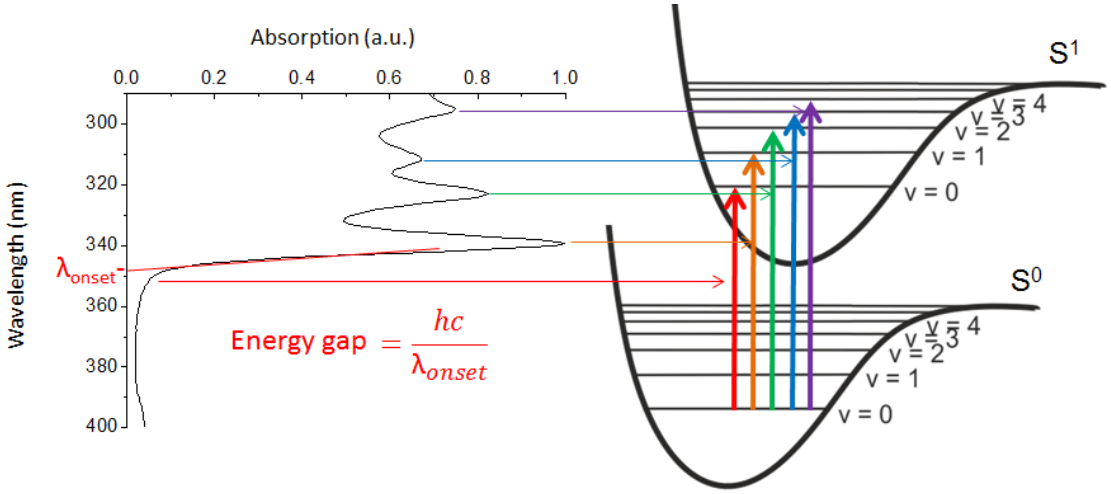

Figure 26. Relation between optical gap and the transition S_0-S_1

Table 4. Absorption and energy gap data of iridium complexes in DCM solution at 298 K.

Complex	λ_{abs} / nm (ε / 10^{-3} L mol^{-1} cm^{-1})	$E_g^{opt(a)}$	$E_g^{cv(b)}$
Ir(ppy)$_2$L^{10}	248, 293, 370 (2.6)	2.40	2.40
Ir(ppy)$_2$L^{11}	264, 346 (1.2)	2.74	2.63
Ir(ppy)$_2$L^{12}	235, 263, 290 (3.1), 395 (2.8)	2.59	2.55
[Ir(ppy)$_2$(L^{10}H)]PF$_6$	246, 294, 347, 360 (23)	2.36	2.35
[Ir(ppy)$_2$(L^{11}H)]PF$_6$	243, 317 (25), 422 (3.8)	2.58	2.63
[Ir(ppy)$_2$(L^{12}H)]PF$_6$	235, 294, 317, 389 (19)	2.24	2.55

[(a)]Optical gap
[(b)]Energy gap taken from the electrochemistry table

2.4.2. *bis*-benzimidazole iridium complexes

The ground-state absorbance spectra of cationic (**[Ir(ppy)$_2$(L^{14}H$_2$)]PF$_6$**, **[Ir(ppy)$_2$L^{15}]PF$_6$** and neutral **Ir(ppy)$_2$(L^{14}H)** iridium complexes in DCM solution are shown in **Figure 27**. They all show intense bands in the UV region between 230 and 360 nm assigned to the $^1\pi$-π^* transitions of the ligands. A weaker band at lower energy extending into the visible region (between 360 and 550 nm) is attributed to metal-to-ligand charge-transfer (MLCT) transitions. **[Ir(ppy)$_2$(L^{14}H$_2$)]PF$_6$** and **Ir(ppy)$_2$(L^{14}H)** display a weak, low-energy band around 430 nm that is not present for **[Ir(ppy)$_2$L^{15}]PF$_6$**.

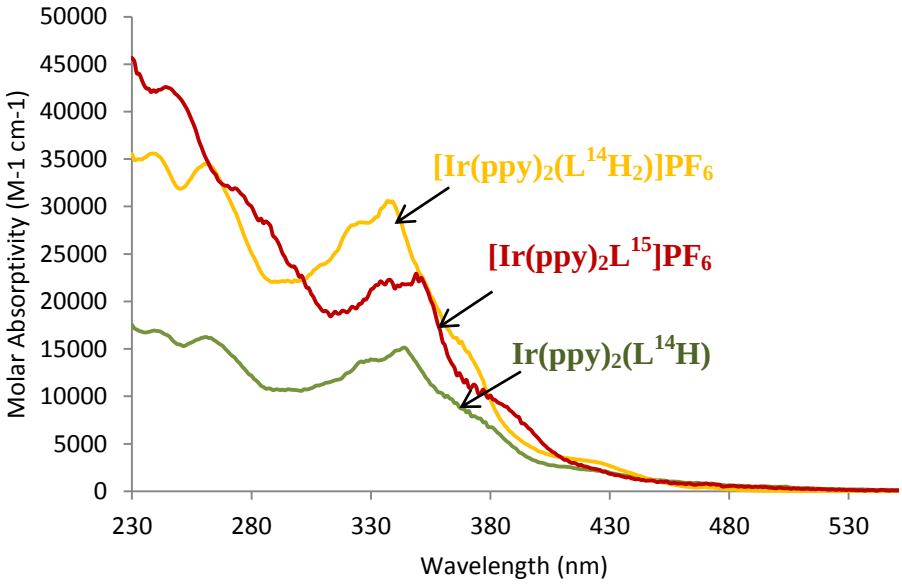

Figure 27. Normalized absorption spectra of **Ir(ppy)$_2$(L^{14}H)**, **[Ir(ppy)$_2$(L^{14}H$_2$)]PF$_6$** and **[Ir(ppy)$_2$(L^{15}H$_2$)]PF$_6$** complexes in DCM at 298 K

2.4.3. Emission studies in degassed DCM at 298 K

2.4.3.1. Neutral (iso)-quinolyl iridium complexes

Emission spectra of complexes **Ir(ppy)$_2$L^{10}**, **Ir(ppy)$_2$L^{11}** and **Ir(ppy)$_2$L^{12}** were recorded in degassed DCM solution at 298 K. Spectra of the neutral complexes are shown in **Figure 28** and luminescence data are collected in **Table 4**. All three complexes are strongly phosphorescent in degassed solution. The emission profiles of **Ir(ppy)$_2$L^{11}** and **Ir(ppy)$_2$L^{12}** are more structured than **Ir(ppy)$_2$L^{10}**. **Ir(ppy)$_2$L^{10}** and **Ir(ppy)$_2$L^{12}** are bright (ϕ = 0.50 and 0.42 respectively) and showed similar luminescence properties as **Ir(ppy)$_2$(pbz)** (ϕ = 0.48 and τ = 3.2 μs). However, **Ir(ppy)$_2$L^{10}** (λ_{em} = 619 nm) and **Ir(ppy)$_2$L^{12}** (λ_{em} = 575 nm) displayed a bathochromic shift of their emission compared to **Ir(ppy)$_2$(pbz)** due to the π extension on the pyridyl ring. The quantum yield of luminescence of **Ir(ppy)$_2$L^{11}** was low (ϕ= 0.15) compared to **Ir(ppy)$_2$L^{10}** and **Ir(ppy)$_2$L^{12}**, but its lifetime was much longer (τ = 25 μs, compared to τ = 4.4 μs and 7.6 μs, respectively). This specific characteristic has also been observed for a cyclometallated platinum(II) complex that contains an isoquinoline linked at position 3 to the metallated ring: platinum[2,6-di(3-isoquinolyl)-benzene]chloride displayed a luminescence lifetime (τ = 40 μs) much longer than its isomer in which the isoquinoline is linked at position 4 to the metallated ring (τ = 3.5 μs).[49] The effect in both cases appears to be derived from a much smaller k_r value for the 3-substituted isomer.

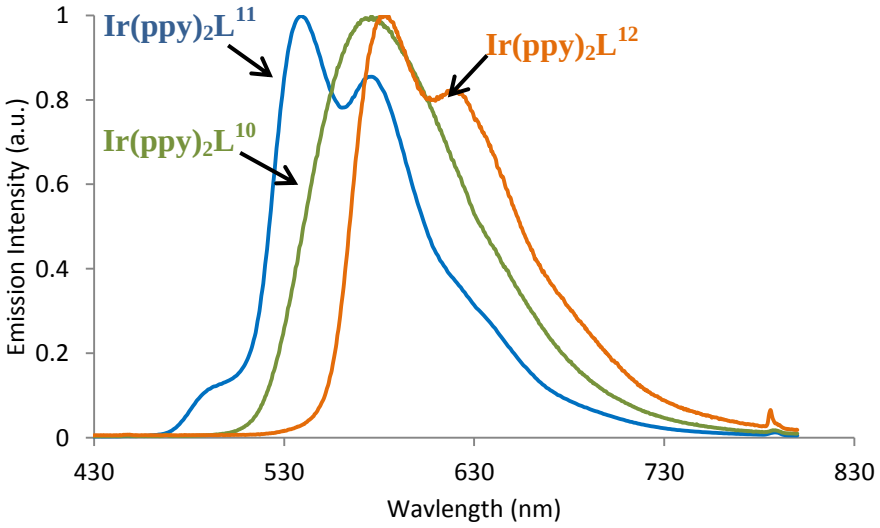

Figure 28. Normalized phosphorescence emission spectra of **Ir(ppy)$_2$L^{10}**, **Ir(ppy)$_2$L^{11}**, and **Ir(ppy)$_2$L^{12}** complexes in degassed DCM at 298 K

2.4.3.2. Cationic (iso)-quinolyl iridium complexes

Emission spectra of complexes **[Ir(ppy)$_2$(L^{10}H)]PF$_6$**, **[Ir(ppy)$_2$(L^{11}H)]PF$_6$** and **[Ir(ppy)$_2$(L^{12}H)]PF$_6$** were recorded in degassed DCM solution at 298 K (**Figure 29**). Luminescence data are compiled in **Table 5**. All three complexes are strongly phosphorescent in degassed solution. The emission spectrum of **[Ir(ppy)$_2$(L^{10}H)]PF$_6$** showed a broad brand characterized by a maximum at 625 nm whereas **[Ir(ppy)$_2$(L^{11}H)]PF$_6$** displayed a broad brand with a maxima at 566 nm and two shoulders at 530 nm and 615 nm. **[Ir(ppy)$_2$(L^{11}H)]PF$_6$** showed the most structured emission band with two maxima at 580 and 625 nm. However, the emission bands were less structured than for the neutral complexes. Emission of **[Ir(ppy)$_2$(L^{10}H)]PF$_6$**, **[Ir(ppy)$_2$(L^{11}H)]PF$_6$** and **[Ir(ppy)$_2$(L^{12}H)]PF$_6$** were also red-shifted compared to the neutral complexes (λ_{max} = 625 nm, 566 nm and 625 nm respectively). According to the DFT calculations, the LUMO was based on the quinolyl / isoquinolyl unit and the HOMO based on the phenyl rings of the cationic iridium complex. The luminescence lifetime of **[Ir(ppy)$_2$(L^{11}H)]PF$_6$** (τ = 14 µs) was higher than **[Ir(ppy)$_2$(L^{10}H)]PF$_6$** and **[Ir(ppy)$_2$(L^{12}H)]PF$_6$** complexes (τ = 3.9 µs and 7.0 µs, respectively). The quantum yields of luminescence of the cationic complexes were similar to their neutral analogues. The comparison with **[Ir(ppy)$_2$(pbz)]PF$_6$** showed that the emission wavelength was in the same range as **[Ir(ppy)$_2$(L^{12}H)]PF$_6$**. However, the quantum yield and lifetime of **[Ir(ppy)$_2$(pbz)]PF$_6$** luminescence were lower than all the other cationic complexes.

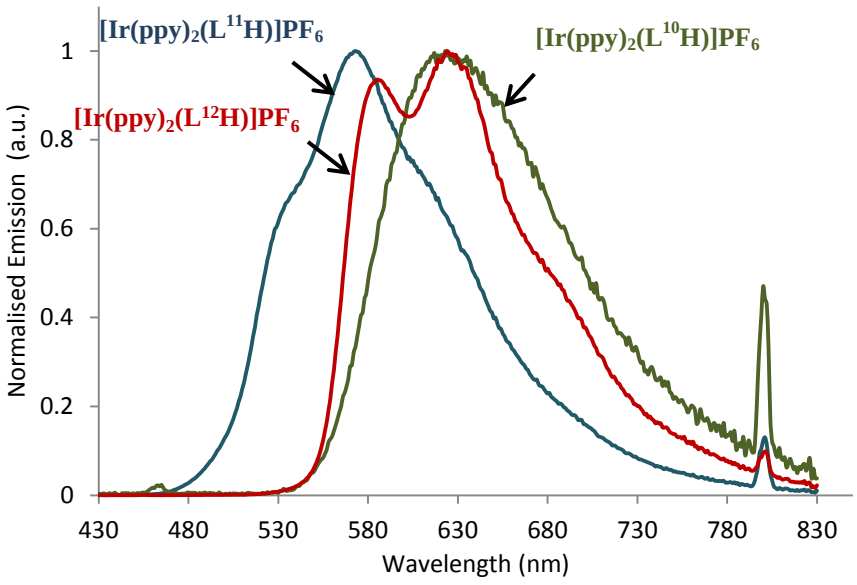

Figure 29. Normalized phosphorescence emission spectra of **[Ir(ppy)$_2$(L^{10}H)]PF$_6$**, **[Ir(ppy)$_2$(L^{11}H)]PF$_6$** and **[Ir(ppy)$_2$(L^{12}H)]PF$_6$** complexes in degassed DCM at 298 K

2.4.3.3. Comparison between $Ir(ppy)_2L^{10}$ and $[Ir(ppy)_2(L^{10}H)]PF_6$

The emission of the cationic and the neutral complexes showed a single broad band which corresponds to phosphorescence from an MLCT triplet state (**Figure 30**). For example, the cationic **$[Ir(ppy)_2(L^{10}H)]PF_6$** emission (λ_{max} = 625 nm) is red-shifted compared to the neutral **$Ir(ppy)_2L^{10}$**. This bathochromic shift is attributed to the protonation of the benzimidazole unit. In fact, the LUMO is lower in the cationic compared to neutral complex, because in the cationic complex the acceptor ligand (quin-bzH) is neutral whereas it is anionic in the neutral complex. It is the same as why $[Ir(ppy)_2(bpy)]^+$ is red-shifted compared to $Ir(ppy)_3$.[50]

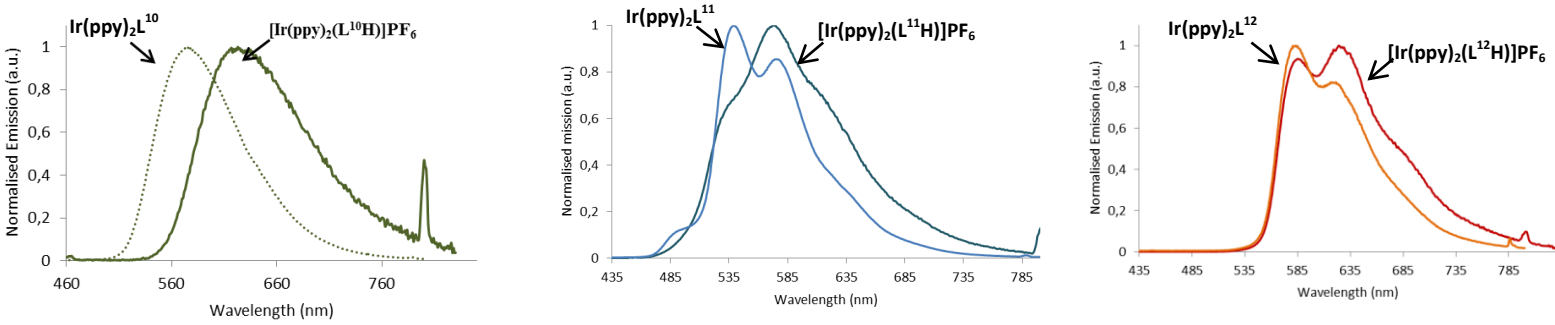

Figure 30. Normalized phosphorescence emission spectra of **$Ir(ppy)_2L^{10}$** and **$[Ir(ppy)_2(L^{10}H)]PF_6$** (left), **$Ir(ppy)_2L^{11}$** and **$[Ir(ppy)_2(L^{11}H)]PF_6$** (middle) and **$Ir(ppy)_2L^{12}$** and **$[Ir(ppy)_2(L^{12}H)]PF_6$** (right) complexes in degassed DCM at 298 K.

2.4.3.4. Emission of the *bis*-benzimidazole iridium deriatives

The emission spectra of **$Ir(ppy)_2(L^{14}H)$**, **$[Ir(ppy)_2L^{15}]PF_6$** and **$[Ir(ppy)_2(L^{14}H_2)]PF_6$** were recorded in degassed DCM at 298 K (**Table 5**). The comparison between **$Ir(ppy)_2(L^{14}H)$** and **$[Ir(ppy)_2(L^{14}H_2)]PF_6$** showed that there was a significant difference in the emission properties which was not apparent from the absorption studies (**Figure 31**). In fact, the emission wavelength of the protonated complex (λ_{max} = 535 nm) was red shifted compared to its non-protonated analogue (λ_{max} = 503 nm). Furthermore, **$[Ir(ppy)_2L^{15}]PF_6$** showed a strong bathochromic shift (λ_{max} = 593 nm) due to the methylation of the azole rings.

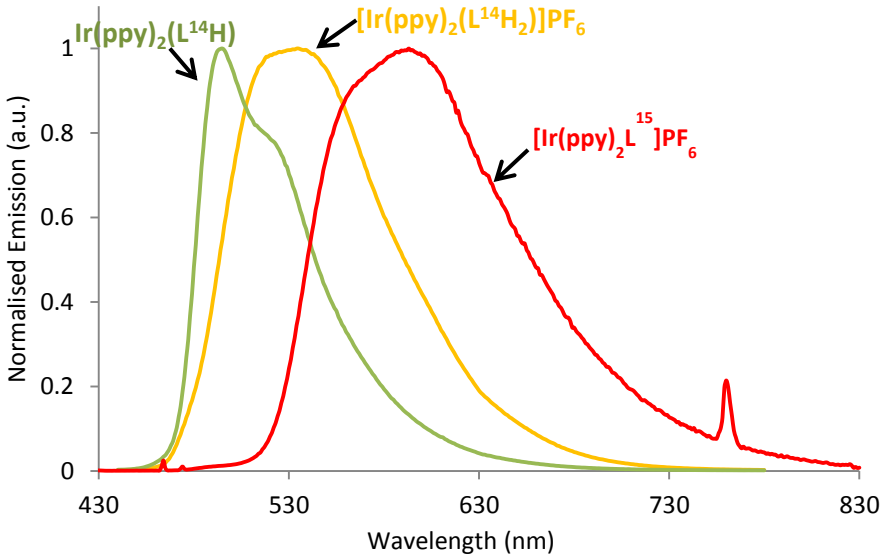

Figure 31. Normalized phosphorescence emission spectra of **$Ir(ppy)_2(L^{14}H)$**, **$[Ir(ppy)_2(L^{14}H_2)]PF_6$** and **$[Ir(ppy)_2(L^{15}H_2)]PF_6$** complexes in degassed DCM at 298 K

Table 5. Photophysical data of iridium complexes in degassed DCM at 298 K. **Ru(bpy)$_3$** was used as reference for the calculation of the quantum yield **ϕ,** Data for **[Ir(ppy)$_2$(pbz)]** and **[Ir(ppy)$_2$(pbzH)]PF$_6$** have been included for comparison[34]

	λ_{abs} / nm (ε / 10^{-3}L mol^{-1}cm^{-1})	λ_{em} / nm	τ / μs	ϕ	k_r / s^{-1}	k_{nr} / s^{-1}
Ir(ppy)$_2$L^{10}	248, 293, 370 (2.6)	579	4.4	0.50	113636	113636
Ir(ppy)$_2$L^{11}	264, 346 (1.2)	535, 568	25	0.15	6000	34000
Ir(ppy)$_2$L^{12}	235, 263, 290 (3.1), 395(2.8)	579, 629	7.6	0.42	52263	79316
Ir(ppy)$_2$(pbz)	340 (33), 433 (5.1), 476 (1.3)	496, 521	3.2	0.48	150000	162500
[Ir(ppy)$_2$(L^{10}H)]PF$_6$	246, 294, 347, 360 (23)	625	3.9	0.48	123711	134020
[Ir(ppy)$_2$(L^{11}H)]PF$_6$	243, 317 (25), 422 (3.8)	530, 566, 615	14	0.20	13870	55478
[Ir(ppy)$_2$(L^{12}H)]PF$_6$	235, 294, 317, 389 (18.9)	580, 625, 680 (sh)	7.0	0.38	54285	88571
[Ir(ppy)$_2$(pbzH)]PF$_6$	320 (30.1), 380 (8.6), 418 (4.2), 470 (1.1)	590	0.84	0.22	261904	928571
Ir(ppy)$_2$(L^{14}H)	255, 330 (13.8), 420 (1.5)	503, 520	2	0.24	120000	380000
[Ir(ppy)$_2$L^{15}]PF$_6$	284, 343 (19.9), 390 (7.4), 411 (2.6)	593	1	0.24	240000	760000
[Ir(ppy)$_2$(L^{14}H$_2$)]PF$_6$	255, 377 (11.6), 420 (3), 470 (0.5)	535	2	0.46	230000	270000
[Ir(ppy)$_2$(pbzH)]PF$_6$	320 (30.1), 380 (8.6), 418 (4.2), 470 (1.1)	590	0.80	0.22	261904	928572

2.4.4. Emission in EPA solution at 77 K

All the emission spectra at 77 K were recorded in an EPA solution (**Figure 32**). They show more pronounced structured than those obtained at 298 K.

The luminescence lifetimes of all complexes were longer at 77 K than at 298 K. A small difference was observed between the neutral and cationic iridium complexes, **Ir(ppy)$_2$L^{10}** and **[Ir(ppy)$_2$(L^{10}H)]PF$_6$** (**Ir(ppy)$_2$L^{10}** τ = 14.6 μs and **[Ir(ppy)$_2$(L^{10}H)]PF$_6$** τ = 9.8 μs, **Table 6**).

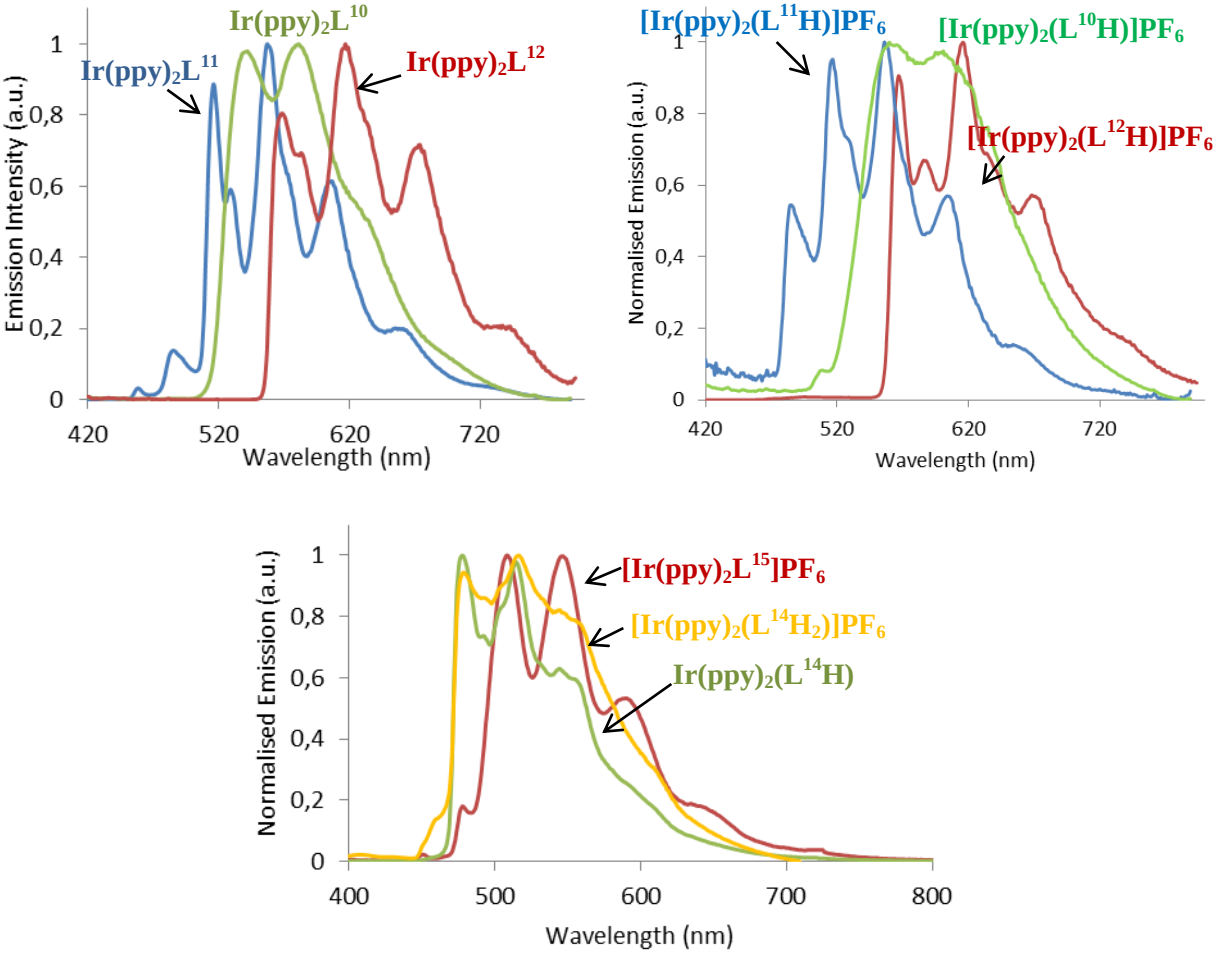

Figure 32. **TOP**: Normalized phosphorescence emission spectra of neutral iridium complexes (left) and cationic iridium complexes (right). **BOTTOM**: emission spectra of **Ir(ppy)$_2$(L^{14}H)**, **[Ir(ppy)$_2$(L^{14}H$_2$)]PF$_6$** and **[Ir(ppy)$_2$L^{15}]PF$_6$**. All spectra were acquired in EPA solution at 77 K

Table 6. Photophysical data of cationic and neutral iridium complexes in EPA solution at 77 K

	λ_{em} / nm	τ / μs
$Ir(ppy)_2L^{10}$	536, 572, 632	14.6
$Ir(ppy)_2L^{11}$	450, 481, 515, 525, 556, 602, 666, 718	132
$Ir(ppy)_2L^{12}$	564, 577, 612, 668, 736	7.8
$[Ir(ppy)_2(L^{10}H)]PF_6$	555, 597, 631	9.8
$[Ir(ppy)_2(L^{11}H)]PF_6$	484, 515, 525, 555, 599, 634	133
$[Ir(ppy)_2(L^{12}H)]PF_6$	566, 584, 614, 632, 665, 735	8
$Ir(ppy)_2(L^{14}H)$	476, 511, 544, 599	5.3
$[Ir(ppy)_2(L^{14}H_2)]PF_6$	452, 476, 511, 544, 605	4.1
$[Ir(ppy)_2L^{15}]PF_6$	476, 512, 542, 582, 636, 710	4.5

2.5. pH dependence of optical properties

Owing to the presence of the azole ring, which can undergo deprotonation / protonation (e.g. compare **$Ir(ppy)_2L^{10}$** and **$[Ir(ppy)_2(L^{10}H)]PF_6$** in the figure below), it was of interest to investigate the pH dependence of the optical properties of the iridium complexes. The UV-visible absorption and emission spectra of aqueous solutions of complexes **$Ir(ppy)_2L^{10}$**, **$Ir(ppy)_2L^{11}$**and **$Ir(ppy)_2L^{12}$** in the pH range between 12 and 2 have been recorded at various pH concentrations by adding H_2SO_4 at different concentrations to the buffer solution (DMSO/water, 1:1) at 298 K. Measurements were recorded with a glass pH electrode calibrated with standard buffer solutions.

2.5.1. $Ir(ppy)_2L^{10}$ and $[Ir(ppy)_2(L^{10}H)]PF_6$

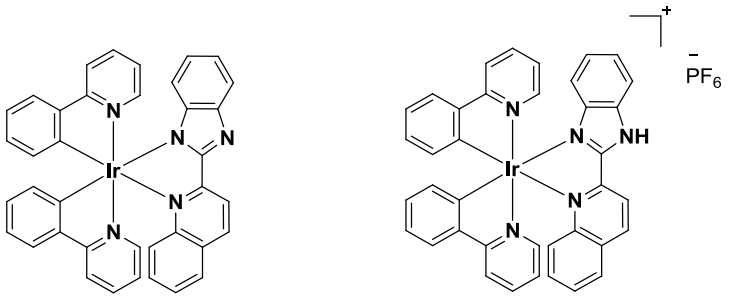

$Ir(ppy)_2L^{10}$ **$[Ir(ppy)_2(L^{10}H)]PF_6$**

Figure 33. Representation of the neutral (left) and the cationic (right) iridium complexes

The absorption spectra at different pH values and the variation of the absorption intensity at 400 nm with pH are shown in **Figure 34**, and corresponding data are compiled in **Table 7**. Over the pH range 12– 2, only one isosbestic point (namely, at 362 nm) can be clearly distinguished. An isosbestic point is a specific wavelength which is constant in intensity for all pH values in the experiment. The occurrence of isosbestic points provides a good indication of the presence of only two interchanging species. In basic solution, the UV-visible absorption spectrum was essentially composed of a broad band characterized by two maxima at 363 nm and 387 nm. From pH = 12 to 7, the absorption spectrum did not show any variations, indicating that the complex was uniquely in its neutral form over this range. Below pH = 7, the absorbance bands were blue-shifted, the absorbance intensity at 400 nm decreased with the pH, whereas the shoulder at 343 nm became more pronounced. These changes can be attributed to the protonation of the azolic ring. At pH around 5.0 until pH = 2, the spectrum shape did not change anymore and featured a single maximum at 349 nm. Over this range, the protonation is apparently complete and the cationic complex uniquely present.

The equivalence, where pH = pK_a, was determined by the graphical method.[51] A pK_a of 5.87 was found.

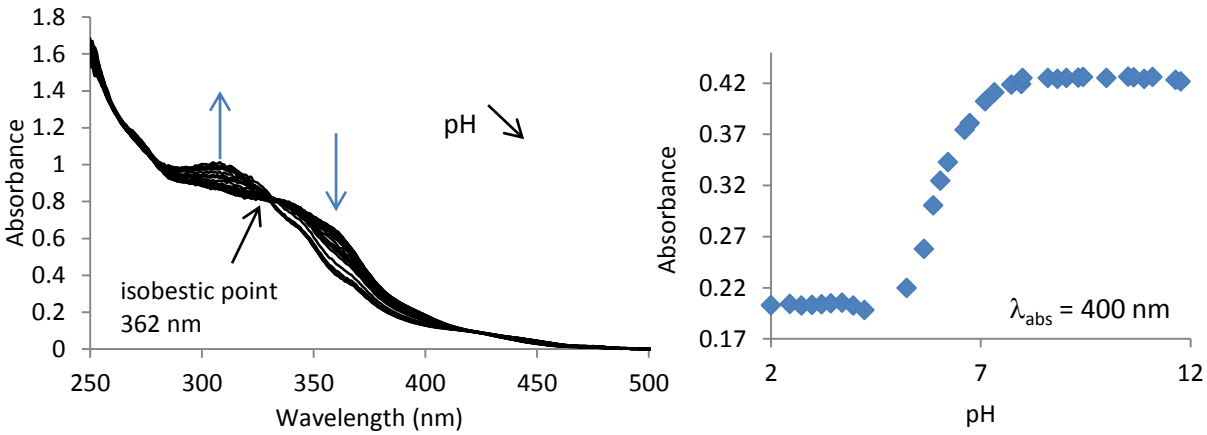

Figure 34. Variation of the absorption intensity of **$Ir(ppy)_2L^{10}$** (Concentration = 2.42 × 10–5 M) in DMSO / H2O (1:1, 100 mL) as a function of pH. trifluoroacetic acid and sodium hydroxide were used as acid and base respectively. The same profile was observed starting from the pre-formed sample of **$[Ir(ppy)_2(L^{10}H)]PF_6$**

The emission spectra during the titration of all complexes were recorded without degassing. The emission spectra showed a single broad band throughout (**Figure 35**). From pH = 12 to pH around 7, the spectral profile and intensity were essentially independent of pH, with λ_{max} = 590 nm. Below pH = 7.11, the emission intensity decreased and there was a progressive shift in λ_{max} towards longer wavelengths, until around pH 4 at which λ_{max} was around 640 nm. Further acidification led to no further discernible effect. These changes are consistent with the protonation of the azole ring. The equivalence, where pH = pK_a^*, was determined by the graphical method. A pK_a^* of 5.45 was found, a little lower than the corresponding value obtained from absorption data, indicating that the excited state is slightly less basic than the ground state. The lifetimes were determined at the extremes, namely at pH 12 and at pH 2, in degassed solutions, giving values of τ = 2.8 and 0.2 μs respectively, corresponding to the neutral and protonated forms respectively.

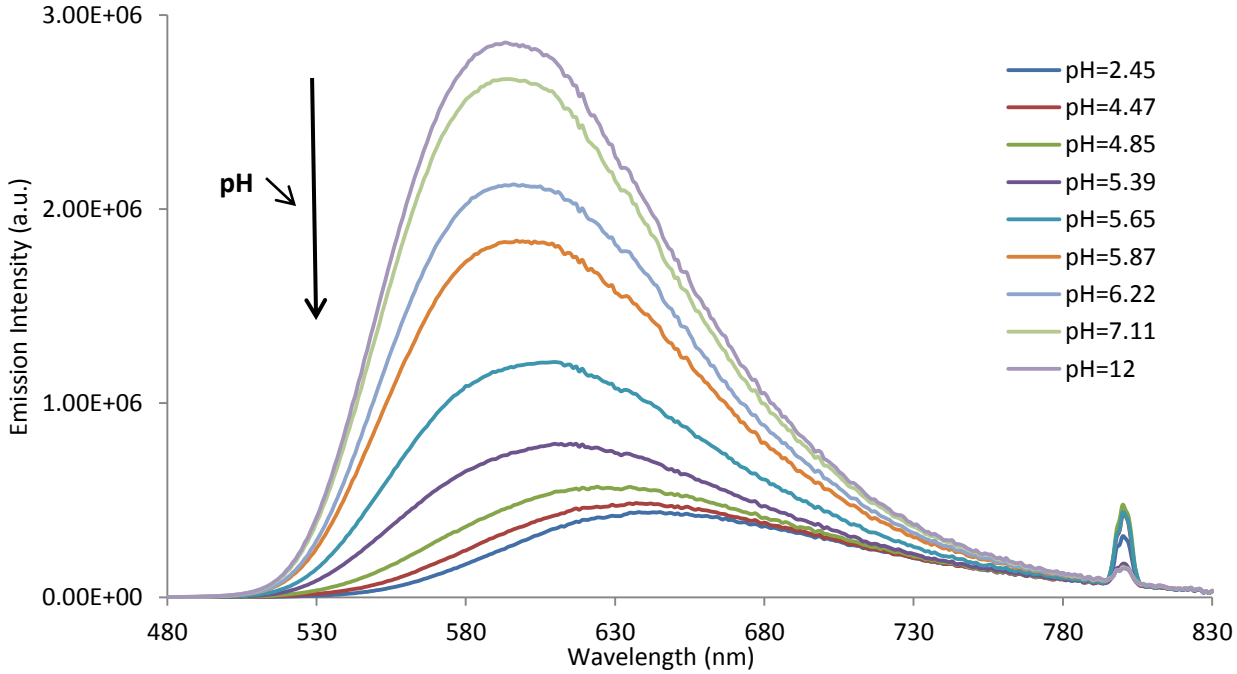

Figure 35. Variation of the emission intensity of complex **Ir(ppy)$_2$L^{10}** in DMSO / H_2O (1:1) as a function of pH. Trifluoroacetic acid and sodium hydroxide were used as acid and base respectively. The same profile was observed starting from the pre-formed sample of **[Ir(ppy)$_2$(L^{10}H)]PF$_6$**.

2.5.2. Ir(ppy)$_2$L^{11} and [Ir(ppy)$_2$(L^{11}H)]PF$_6$

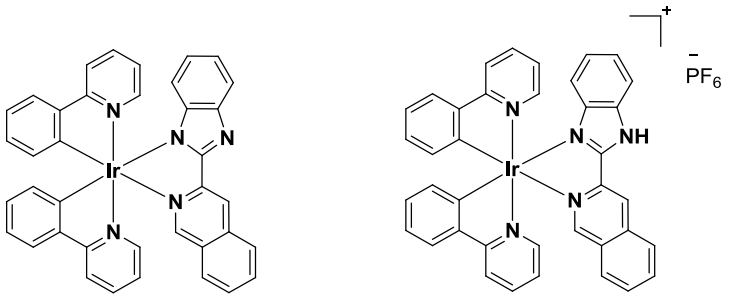

Ir(ppy)$_2$L^{11} **[Ir(ppy)$_2$(L^{11}H)]PF$_6$**

Figure 36. Representation of the neutral (left) and the cationic (right) iridium complexes

The absorption spectra of the titration and the variation of the absorption intensity at 400 nm were shown in **Figure 36** and **Table 9**. Behaviour was similar with one isosbestic point (namely, at 325 nm). In basic solution (from pH = 12 to pH = 7.9), the UV / Vis absorption spectrum of the neutral form was essentially composed of a broad band characterized by two maximum at 314 nm and 421 nm. The complex was in its neutral form. At pH around 5.0 until pH = 2, the spectrum shape of the cationic form was composed of maxima at λ = 316 and 356 nm. A pKa of 6.55 was found.

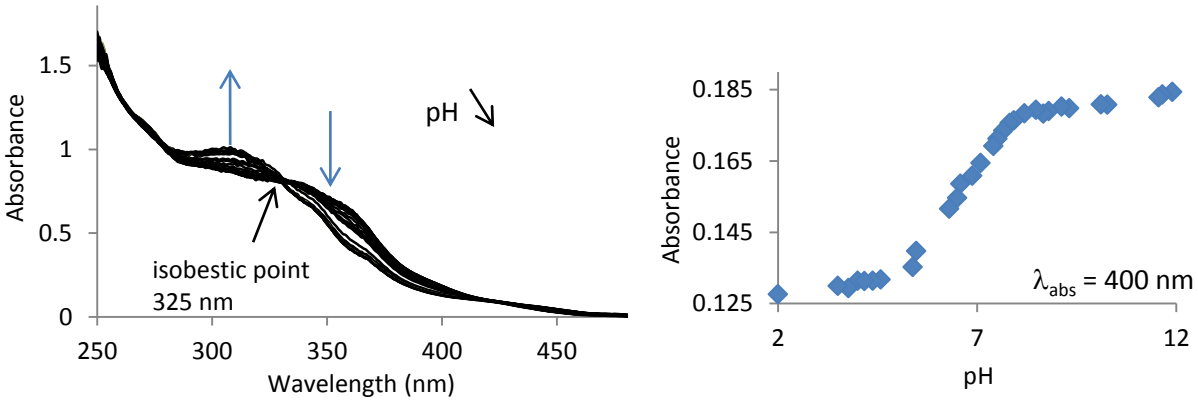

Figure 37. Variation of the absorption intensity of **Ir(ppy)$_2$L^{11}** in DMSO / H2O (1:1) as a function of pH. Trifluoroacetic acid and sodium hydroxide were used as acid and base respectively. The same profile was observed starting from the pre-formed sample of **[Ir(ppy)$_2$(L^{11}H)]PF$_6$**

The emission spectra always showed a single broad band (**Figure 37**). Emission and luminescence lifetime measurements at pH = 2 and pH = 14 were performed on degassed solutions by bubbling nitrogen for several minutes (**Table 7**). From pH = 12 to pH around 7.9, Neutral complex **Ir(ppy)$_2$L^{11}** was slightly emissive with a maximum at λ max = 602 nm. After pH = 7.8 the emission intensity increased with the protonation of the azole ring until pH around 5.3. After this pH, the protonation of the benzimidazole unit was complete. The emission band was characterized by a maximum at λ max = 623 nm. At pH = 12 and pH = 2 the protonated form **[Ir(ppy)$_2$(L^{11}H)]PF$_6$** had a shorter luminescence lifetime (τ = 14 μs) than the neutral form **Ir(ppy)$_2$L^{11}** (τ = 52 μs). A pKa* of 6.60 was found.

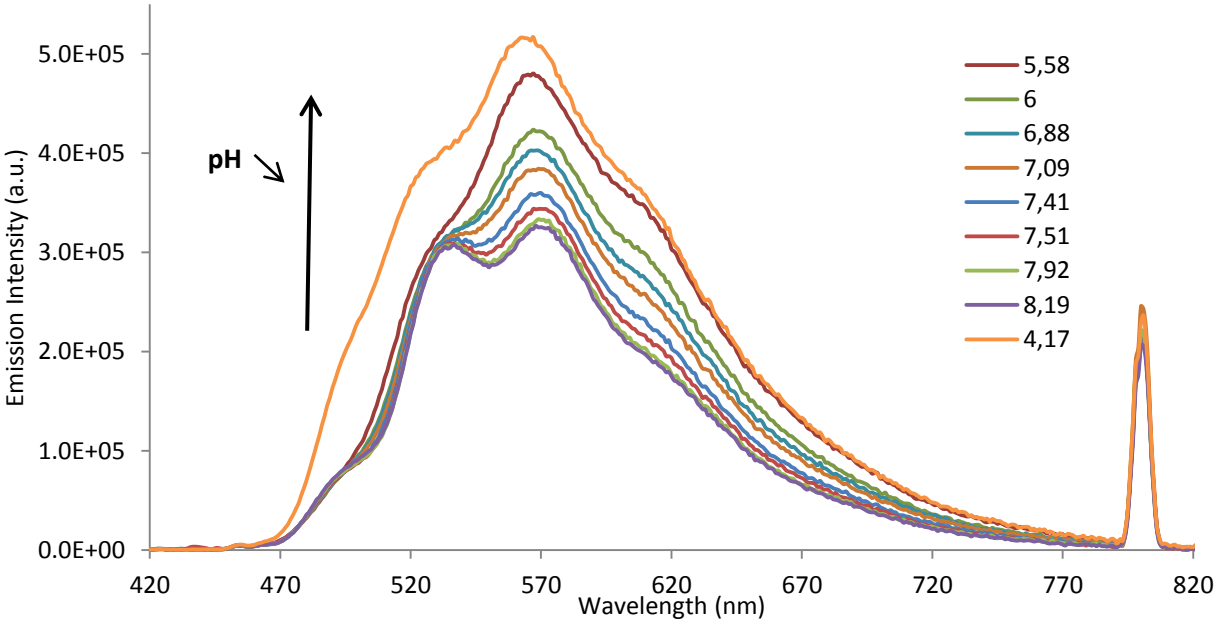

Figure 38. Variation of the emission intensity of complex **Ir(ppy)$_2$L^{11}** in DMSO / H_2O (1:1) as a function of pH. trifluoroacetic acid and sodium hydroxide were used as acid and base respectively. The same profile was observed starting from the pre-formed sample of **[Ir(ppy)$_2$(L^{11}H)]PF$_6$**

2.5.3. $Ir(ppy)_2L^{12}$ and $[Ir(ppy)_2(L^{12}H)]PF_6$

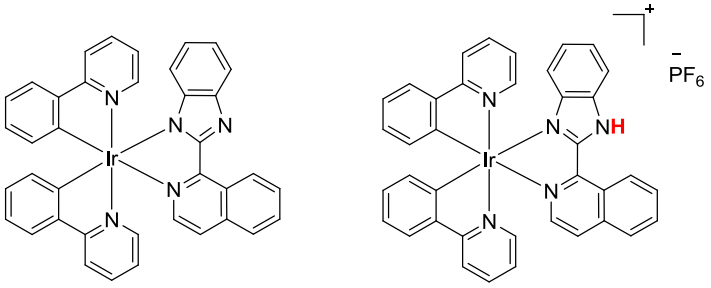

$Ir(ppy)_2L^{12}$ $[Ir(ppy)_2(L^{12}H)]PF_6$

Figure 39. Representation of the neutral (left) and the cationic (right) iridium complexes

The absorption spectra of the titration and the variation of the absorption intensity at 400 nm are shown in **Figure 40** and **Table 9**. In the pH range 12- 2, one isosbestic point at 376 nm was observed. In basic solution, the UV / Vis absorption spectrum was essentially composed of a broad band characterized by two maximum at 367 nm and 425 nm. From pH = 12 to pH = 6 the absorbance spectrum did not show any variations. After pH = 6, the absorbance bands were blue-shifted, the absorbance intensity at 400 nm decreased with the pH, whereas the shoulder at 303 nm and 367 nm became more pronounced. The protonation was complete and gave the cationic complex at pH = 5. A pKa of 5.52 was calculated.

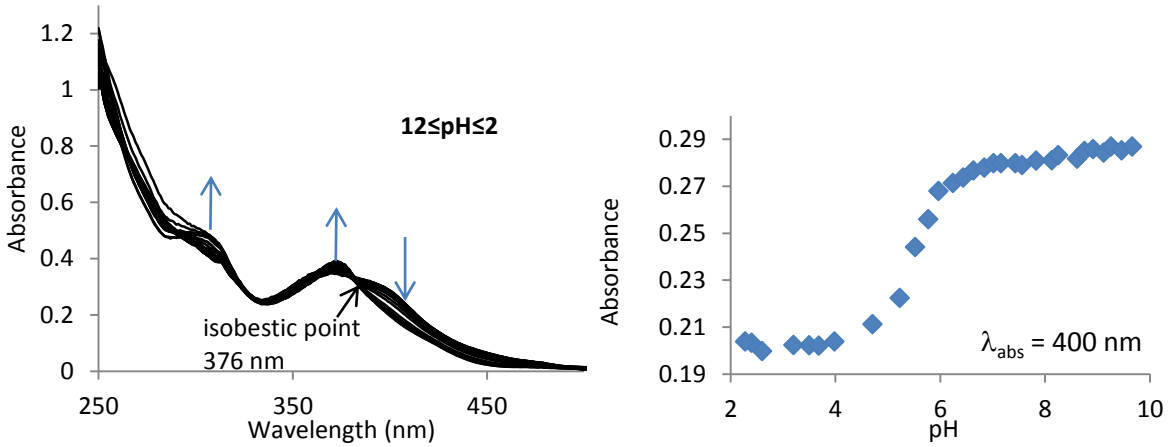

Figure 40. Variation of the absorption intensity of $Ir(ppy)_2L^{12}$ in DMSO / H_2O (1:1) as a function of pH. trifluoroacetic acid and sodium hydroxide were used as acid and base respectively. The same profile was observed starting from the pre-formed sample of $[Ir(ppy)_2(L^{12}H)]PF_6$

The emission spectra always showed a single broad band. From pH = 12 to pH around 6.5, the emissions of the neutral complex were highly emissive with a maximum at λ max = 620 nm. After pH = 6.5 the emission intensity decreased with the protonation of the azole ring until pH around 4.2. After this pH, the protonation of the benzimidazole unit was complete.

The weaker emission band was characterized by a maximum at λ max = 660 nm. At pH = 12 and pH = 2 the protonated form **[Ir(ppy)$_2$(L^{12}H)]PF$_6$** had a shorter luminescence lifetime (τ = 1 μs) than the neutral form **Ir(ppy)$_2$L^{12}** (τ = 4 μs). A pKa* of 5.37 was found.

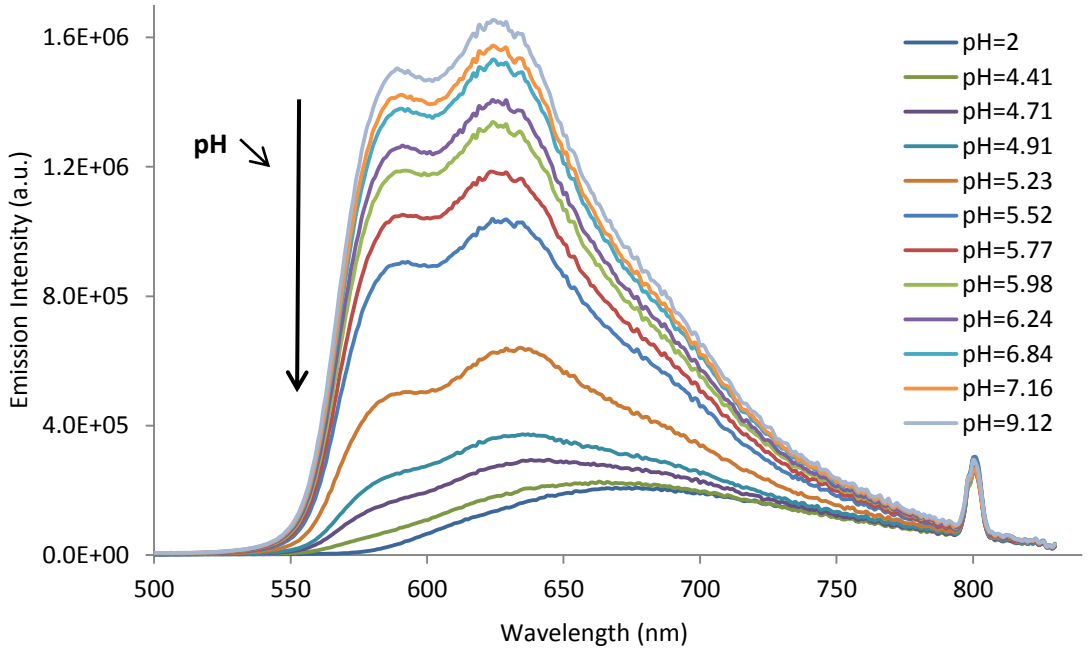

Figure 41. Variation of the emission intensity of complex **Ir(ppy)$_2$L^{12}** in DMSO / H_2O (1:1) as a function of pH. Trifluoroacetic acid and sodium hydroxide were used as acid and base respectively. The same profile was observed starting from the pre-formed sample of **[Ir(ppy)$_2$(L^{12}H)]PF$_6$**

2.5.4. [Ir(ppy)$_2$(L^{14}H$_2$)]PF$_6$, Ir(ppy)$_2$(L^{14}H) and [Ir(ppy)$_2$(L^{14})]Na

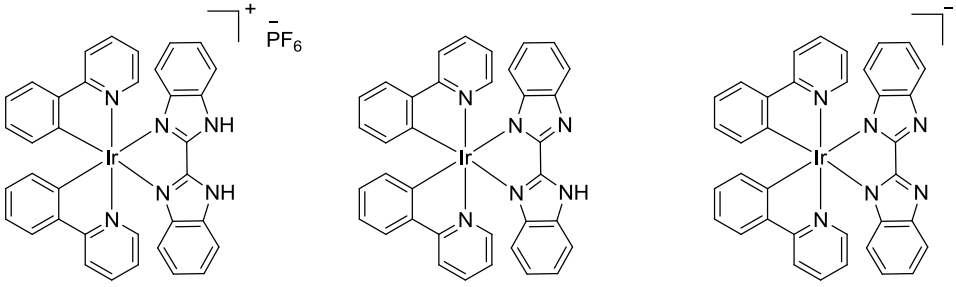

[Ir(ppy)$_2$(L^{14}H$_2$)]PF$_6$ **Ir(ppy)$_2$(L^{14}H)** **[Ir(ppy)$_2$(L^{14})]Na**

Figure 42. Three different forms of the *bis*-benzimidazole iridium complexes

The absorption spectra of the titration and the variation of the absorption intensity at 400 nm are shown in **Figure 43** and **Table 7**. In acid solution, the UV / Vis absorption spectrum was essentially composed of a broad band characterized by two maximum at 325 nm and 335 nm. From pH = 2 to pH = 6.9 the absorbance spectrum did not show any variations. The complex was in its cationic form. After pH = 6.9, the absorbance intensity at 325 and 335 nm decreased with the pH, whereas the shoulder at 360 nm became more

pronounced. The deprotonation of the first azolic ring started. At pH around 7 until pH = 10.5, the spectrum shape did not change anymore and was composed of maxima at 335 nm and a shoulder at 360 nm. After pH = 10.5, the absorbance intensity at 335 nm increase, which involves the formation of a new specie. Between pH = 10.5 until pH = 12, the spectrum shape did not change and was composed of a maxima at 335 nm and a shoulder at 360 nm. By comparison with the shape of the neutral form, the absorbance intensity at 370 nm decreased. As comparison with the previous titrations of **Ir(ppy)$_2$L^{10}**, **Ir(ppy)$_2$L^{11}**and **Ir(ppy)$_2$L^{12}**, where only two forms (neutral and cationic) are possible and observed, we distinguished three states (**Figure 44**). In fact, in the case of the *bis*-benzimidazole ligand, three species are possible: cationic **[Ir(ppy)$_2$(L^{14}H$_2$)]PF$_6$** neutral (**Ir(ppy)$_2$(L^{14}H)**) and anionic (**[Ir(ppy)$_2$(L^{14})]Na**). The deprotonation of the second azolic ring started to give the anionic form. The titration from pH = 12 to pH = 2 showed the same characteristics observed for the titration from pH= 2 to pH= 12.

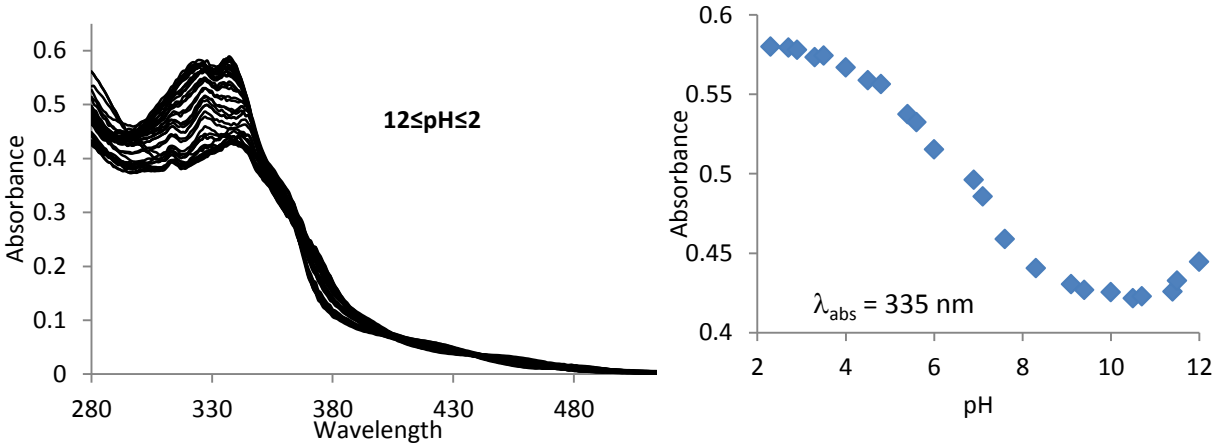

Figure 43. Variation of the absorption intensity of **Ir(ppy)$_2$(L^{15}H)** in DMSO / H_2O (1:1) as a function of pH. trifluoroacetic acid and sodium hydroxide were used as acid and base respectively

The emission spectra always showed a single broad band (**Figure 43** and **44**). From pH = 12 to pH around 10.5, the emission intensity of the neutral complex decreased and was characterized with a maximum at λ max = 508 nm. After pH = 10.5 the emission intensity increased with the protonation of the azole ring until pH around 6.9 and a maxima emission wavelength at λ max = 515 nm. At pH = 6.9 and pH = 2 the protonation of the second azolic ring was performed to give the cationic form **[Ir(ppy)$_2$(L^{10}H)]PF$_6$**. The protonation was characterized by a decrease of the emission intensity and a maximum at λ max = 555 nm. Surprisingly, the luminescence lifetime was constant for all the titration. Two pKa* were

calculated at 5.65 and 8.9. During the titration, the lifetime of degassed solution at pH 2, 6, 10 and 12 did not show any variation (τ = 1 μs).

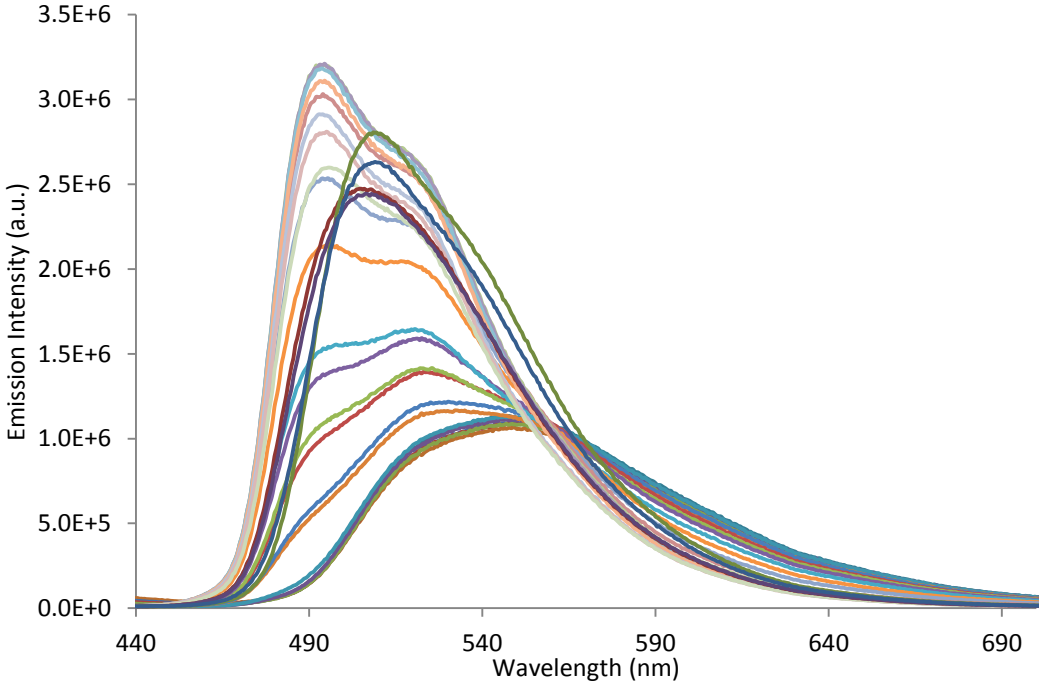

Figure 44. Variation of the emission intensity of complex **[Ir(ppy)$_2$(L^{14}H$_2$)]PF$_6$** in DMSO / H$_2$O (1:1) as a function of pH. trifluoroacetic acid and sodium hydroxide were used as acid and base respectively. The same profile was observed starting from the pre-formed sample of **Ir(ppy)$_2$(L^{14}H)**

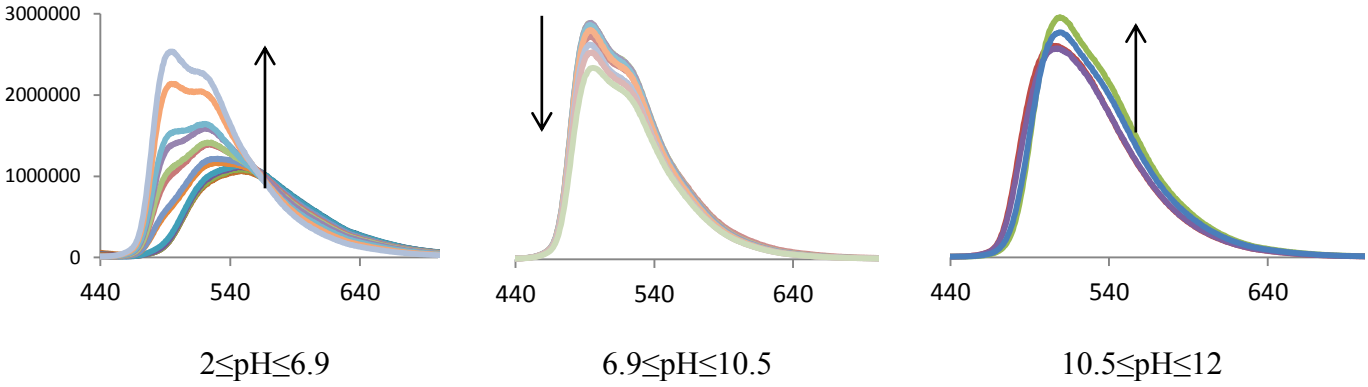

Figure 45. Variation of the absorption intensity of **Ir(ppy)$_2$(L^{14}H)** in DMSO / H2O (1:1) as a function of pH. trifluoroacetic acid and sodium hydroxide were used as acid and base respectively

Table 7. Photophysical data of cationic and neutral iridium complexes in a solution of DMSO / H_2O (1:1) at 298 K

Complex	λ_{abs} / nm	λ_{em} / nm	τ / μs	pK_a
$[Ir(ppy)_2(L^{10}H)]PF_6$	250, 290, 355, 418	646	0.2	5.45
$Ir(ppy)_2L^{10}$	250, 294, 361, 396, 446	590	2.8	
$[Ir(ppy)_2(L^{11}H)]PF_6$	314, 421	530, 556, 602	14	6.68
$Ir(ppy)_2L^{11}$	316, 356	528, 568, 623	52	
$[Ir(ppy)_2(L^{12}H)]PF_6$	301, 366, 425	660	1	5.37
$Ir(ppy)_2L^{12}$	301, 387, 367	585, 620	4	
$[Ir(ppy)_2(L^{14}H_2)]PF_6$	320, 334, 420, 469	555	1	
$Ir(ppy)_2(L^{14}H)$	309, 324, 340, 357, 449	489, 515	1	5.7; 8.8
$[Ir(ppy)_2L^{14}]Na$	309, 336, 357	508	1	

3. Concluding Remarks

We presented the synthesis of new pH sensitive iridium complexes containing iso-(quinolyl) or 2,2'- *bis*-benzimidazole unit. Two different routes were used to synthesize the neutral or the cationic complex. The deprotonation of the proligand **L^nH** (**n** = 10, 11, 12 and 14) leads to the neutral form as the ligand acted as a N^N cyclometallated ligand. This difference was shown with the NMR spectroscopy and a shift of the aromatic proton signals of the (iso)-quinolyl unit. DFT calculations made on the neutral complexes **$Ir(ppy)_2L^n$** and cationic complexes **$[Ir(ppy)_2(L^nH)](PF_6)$** (**n** = 10 to 12) showed that the HOMO was based on the ppy unit for the cationic iridium complexes and on the benzimidazole for the neutral complexes. Furthermore, the oxidation of neutral complexes is easier than the cationic complexes. Photophysical differences were observed between the three isomers **$Ir(ppy)_2L^{10}$**, **$Ir(ppy)_2L^{11}$**, **$Ir(ppy)_2L^{12}$**: the emission wavelength and the luminescence quantum yield of **$Ir(ppy)_2L^{10}$** and **$Ir(ppy)_2L^{12}$** are similar (λ_{em} = 579 nm and ϕ = 0.50 and 0.42, respectively) and red-shifted compared to **$Ir(ppy)_2L^{11}$**(λ_{em} = 535 nm and ϕ = 0.15). In contrast, **$Ir(ppy)_2L^{11}$** showed a longer lifetime (τ = 25 μs) than **$Ir(ppy)_2L^{10}$** and **$Ir(ppy)_2L^{12}$** (τ = 4.4 μs and 7.6 μs).

The photophysical properties showed a red shift of the emission for the cationic complexes compared to the neutral iridium complexes. The titration made on the (iso)-

quinoline iridium complexes **Ir(ppy)$_2$L^{10}**, **Ir(ppy)$_2$L^{11}** and **Ir(ppy)$_2$L^{12}** displayed pKa* of 5.45, 6.60 and 5.37 respectively. Furthermore, As the isomer iridium complexes **Ir(ppy)$_2$L^{11}** and **[Ir(ppy)$_2$L^{11}H](PF$_6$)** displayed a longer lifetime than the other complexes, it will be interesting to substitute the position 4 of the pyridyl ring by a phenyl or a biphenyl rings. The synthetic route was already choose and started (**Scheme 6**).

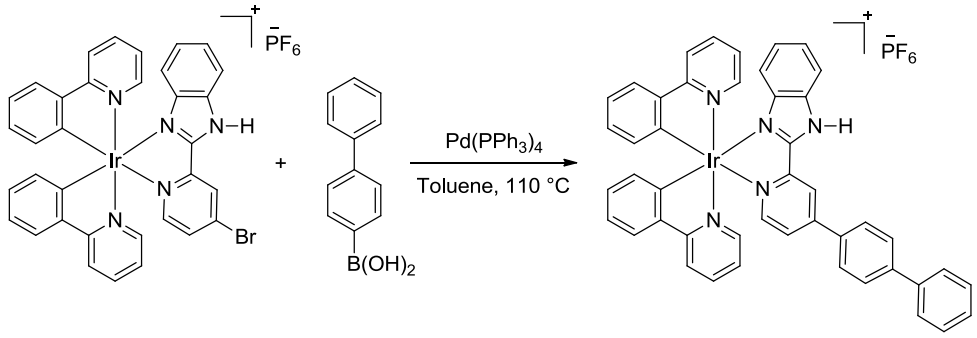

Scheme 6. Synthetic route of the formation of **[Ir(ppy)$_2$(pbzH-bph)]PF$_6$**

New iridium complexes incorporating a *bis*-benzimidazole ligand (bbz) were also synthesized and studied. In this case, *three* different forms may be anticipated in principle, namely a cationic, a neutral and an anionic form, according to the protonation state of the azole nitrogen atoms. The titration of the *bis*-benzimidazole iridium complexes displays of three different species: neutral, cationic and anionic forms. Their lifetime did not change for all the experiment in a mixture of DMSO / H_2O (1:1).

4. References

[1] R. Y. Tsien, *Angew. Chem. Int. Ed.*, 2009, **48**, 5612.

[2] R. P. Haughland, Handbook of fluorescent probes and research chemicals, *Molecular Probes Inc., Eugene, OR, 9th edn*, 1996.

[3] A. J. Amoroso, M. P. Coogan, J. E. Dunne, V. Fernandez-Moreira, J. B. Hess, A. J. Hayes, D. Lloyd, C. Millet, S. J. A. Pope, C. Williams, *Chem. Commun.*, 2007, 3066-3068.

[4] V. Fernandez-Moreira, F. L. Thorp-Greenwood, M. P. Coogan, *Chem.Commun.*, 2010, **46**, 186–202.

[5] S. W. Botchway, M. Charnley, J. W. Haycock, A. W. Parker, D. L. Rochester, J. A. Weinstein, J. A. G. Williams, *PNAS*, 2008, **105**, 16071-16076.

[6] C. P. Montgomery, B. S. Murray, E. J. New, R. Pal, D. Parker, *Acc. Chem. Res.*, 2009, **42**, 925-937.

[7] S. V. Eliseeva, J.-C. G. Bunzli, *Chem. Soc. Rev.*, 2010, **39**, 189-227.

[8] S. Faulkner, B. P. Burton-Pye, S. J. A. Pope, *Appl. Spectrosc. Rev.*, 2005, **40**, 1.

[9] B. Song, C. D. B. Vandevyver, A.-S. Chauvin, J.-C. G. Bunzli, *Org. Biomol. Chem.*, 2008, **6**, 4125.

[10] K. K.-W. Lo, S. P.-Y. Li, *RSC Adv*., 2014, **4**, 10560-10585.

[11] Y. You, W. Nam, *Chem. Soc. Rev.*, 2012, **41**, 7061-7084.

[12] Q. Liu, J. Peng, L. Sun, F. Li, *ACS Nano*, 2011, **5**, 8040-8048.

[13] Y. Wu, H. Jing, Z. Dong, Q. Zhao, H. Wu, F. Li, *Inorg.Chem*., 2011, **50**, 7412-7420.

[14] K. K.-W. Lo, K. H.-K. Tsang, K.-S. Sze, C.-K. Chung, T. K.-M. Lee, K. Y. Zhang, W.-K. Hui, C.-K. Li, J. S.-Y. Lau, D. C.-M. Ng, N. Zhu, *Coord. Chem. Rev.*, 2007, **251**, 2292-2310.

[15] W. Cheah, K.-C. Lau, Y.-Y. Yang, J.-C. Chen, M. H.-W. Lam, *Inorg. Chem.*, 2009, **48**, 872-878.

[16] K. K.-W. Lo, M.-W. Louie, K. Y. Zhang, *Coord. Chem.Rev*., 2010, **254**, 2603-2622.

[17] K. K.-W. Lo, M.-W. Louie, K.-S. Sze, J. S.-Y. Lau, *Inorg. Chem.*, 2008, **47**, 602-611.

[18] X. Chen, Y. Zhou, X. Peng, J. Yoon, *Chem. Soc. Rev.*, 2010, **39**, 2120-2135.

[19] L. Xiong, Q. Zhao, H. Chen, Y. Wu, Z. Dong, Z. Zhou, F. Li, *Inorg. Chem.*, 2010, **49**, 6402-6408.

[20] S. Ji, H. Guo, X. Yuan, X. Li, H. Ding, P. Gao, C. Zhao, W. Wu, W. Wu, J. Zhao, *Org. Lett.*, 2010, **12**, 2876-2879.

[21] M.-W. Louie, H.-W. Liu, M. H.-C. Lam, Y.-W. Lam, K. K.-W. Lo, *Chem. Eur. J.*, 2011, **17**, 8304.

[22] W. H.-T. Law, L. C.-C. Lee, M.-W. Louie, H.-W. Liu, T. W.-H. Ang, K. K.-W. Lo, *Inorg. Chem.*, 2013, **52**, 13029.

[23] K. Y. Zhang, K. K.-S. Tso, M.-W. Louie, H.-W. Liu, K. K.-W. Lo, *Organometallics*, 2013, **32**, 5098.

[24] Hua-Wei Liu, Kenneth Yin Zhang, Wendell Ho-Tin Law, and Kenneth Kam-Wing Lo, *Organometallics*, 2010, **29**, 3474-3476.

[25] L. S. Lerman, *J. Mol. Bio.*, 1961, **3**, 18.

[26] K. E. Erkkila, D. T. Odom, K. J. Barton, *Chem. Rev.*, 1999, **99**, 2777-2795.

[27] K. Y. Zhang, S. P.-Y. Li, N. Zhu, I. W.-S. Or, M. S.-H. Cheung, Y.-W. Lam, K. K.-W. Lo, *Inorg. Chem.*, 2010, **49**, 2530–2540.

[28] M.-W. Louie, H.-W. Liu, M. H.-C. Lam, T.-C. Lau, K. K.-W. Lo, *Organometallics*, 2009, **28**, 4297-4307.

[29] Y. You, S. Lee, T. Kim, K. Ohkubo, W.-S. Chae, S. Fukuzumi, G.-J. Jhon, W. Nam, S. J. Lippard, *J. Am. Chem. Soc.*, 2011, **133**, 18328-18342.

[30] Y. You, Y. Han, Y.-M. Lee, S. Y. Park, W. Nam, S. J. Lippard, *J. Am. Chem. Soc.*, 2011, **133**, 11488-11491.

[31] P.-K. Lee, W. H.-T. Law, H.-W. Liu, K. K.-W. Lo, *Inorg.Chem,*. 2011, **50**, 8570-8579.

[32] Y. You, S. Cho, W. Nam, *Inorg.Chem.*, 2014, **53**, 1804-1815.

[33] C. Y.-S. Chung, S. P.-Y. Li, M.-W. Louie, K. K.-W. Lo, V. W.-W. Yam, *Chem. Sci.*, 2013, **4**, 2453-2462.

[34] L. Murphy, A. Congreve, L.-O. Palsson, J. A. G. Williams, *Chem.Commun.*, 2010, **46**, 8743-8745.

[35] D. W. Hein, R. J. Alheim, J. J. Leavitt, *J. Am. Chem. Soc.*, 1957, **79**, 427-429.

[36] J. Kool, *J. Am. Chem. Soc*., 1953, **75**, 1891-1895.

[37] C. Bew, V. Otero de Joshi, J. Gray, P. T. Kaye, G. D. Meakins, *J. Chem. Soc.*, 1982, **4**, 945-948.

[38] W.-K. Huang, C.-W. Cheng, S.-M. Chang, Y.-P. Lee, D. E. Wei-Guang, *Chem. Comm*., 2010, **46**, 8992-8994.

[39] K. A. McGee, K. R. Mann, *Inorg. Chem.*, 2007, **46**, 7800-7809.

[40] Y. Chi, P.-T. Chou, *Chem. Soc. Rev.*, 2010, **39**, 638-655.

[41] P.-C. Wu, J.-K. Yu, Y.-H. Song, Y. Chi, P.-T. Chou, S.-M. Peng, G.-H. Lee, *Organometallics*, 2003, **22**, 4938-4946.

[42] C.-C. Cheng, W.-S. Yu, P.-T. Chou, S.-M. Peng, G.-H. Lee, P.-C. Wu, Y.-H. Song, Y. Chi, *Chem. Commun.*, 2003, 2628-2629.

[43] M.-A. Haga, *Inorg. Chim. Acta*, 1983, **75**, 29-35.

[44] K. J. Arm, J. A. G. Williams, *Chem. Commun.*, 2005, **2**, 230-232.

[45] J. Breu, P. Stössel, S. Schrader, A. Starukhin, W. J. Finkenzeller, H. Yersin, *Chem. Mater*., 2005, **17**, 1745-1752.

[46] G. E. Schneider, H. J. Bolink, E. C. Constable, C. D. Ertl, C. E. Housecroft, A. Pertegàs, J. A. Zampese, A. Kanitz, F. Kessler, S. B. Meier, *Dalton Trans.*, 2014, **43**, 1961.

[47] C. M. Cardona, W. Li, A. E.Kaifer, D. Stockdale, G. C. Bazan, *Adv. Mater.*, 2011, **23**, 2367-2370.

[48] A. P. Kulkarni, C. J. Tonzola, A. Babel, S. A. Jenekhe, *Chem. Mater.*, 2004, **16**, 4556-4573.

[49] Z. Wang, E. Turner, V. Mahoney, S. Madakuni, T. Groy, J. Li, *Inorg.Chem.*, 2010, **49**, 11276.

[50] V. Balzani, P. Ceroni, A. Juris, *Photochemistry and Photophysics: Concepts, Research, Applications*, Wiley-VCH, 2014.

[51] N. Kildahl, T. Varco-Shea, *Explorations in Chemistry*, New York, 1996.

CHAPTER FIVE:

Iridium and Platinum Complexes Containing Sulfur-based or Phosphine-based Ligands

1. Introduction

Homoleptic and heteroleptic cyclometallated Ir(III) complexes are well known to emit phosphorescence at ambient temperature with high quantum yield.[1,2] Numerous examples of cationic complexes incorporating a combination of two cyclometallated ligands and one diimine (*e.g.* bipyridine, phenanthroline or their derivatives) have been reported and the influence of the substitution of the diimine ligand on the electronic excited states described.[3] The emission energy of such heteroleptic complexes is readily fine-tuned by changing the nature of the C^N cyclometallated ligand and/or the N^N diimine ligand. For example, blue and green–blue phosphorescent Ir(III) complexes have been reported. The commonly used approaches to widen the HOMO–LUMO gap and shift emission further to the blue are either the use of electron-withdrawing substituents such as F or CF_3 in the metallated aryl ring, which lowers the HOMO, or the use of electron-donating substituents such as *tert*-butyl in the bipyridine rings which raise the LUMO (**Figure 1**).[4,5,6,7]

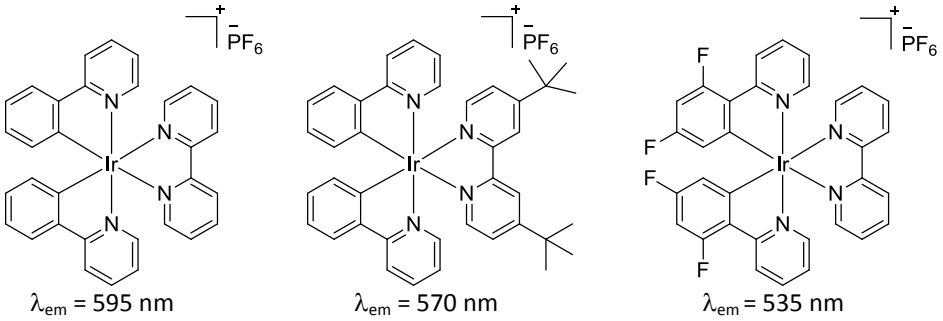

Figure 1. Example of tuning the emission of an heteroleptic iridium(III) complex. Left to right: **$[Ir(ppy)_2(bpy)]PF_6$**, **$[Ir(ppy)_2(^tBu\text{-}bpy)]PF_6$**, **$[Ir(2,6F_2ppy)_2(bpy)]PF_6$** with their emission wavelengths in degassed DCM at 298 K [4,5,6]

Another way to increase the energy gap is through the use of non-conjugated ancillary diarylphosphine chelates in place of the diimine.[8] Indeed, the π-accepting character of the PAr_2 group is expected to increase the metal to-ligand charge-transfer (MLCT) by increasing the LUMO energy level resulting in blue-shifted emission. Thus, blue shifts of the emission maxima have been obtained using neutral[9,10] or cationic[11] heteroleptic Ir(III) complexes combining C^N ligands with either P^C or P^N chelates.

Sulfur-based ligands have also been used in the generation of luminescent metal complexes. In a landmark study, Cummings and Eisenberg explored two series of Pt(diimine)(dithiolate) complexes in which the chelating ligands were systematically varied (**Figure 2**).[12] These complexes were obtained by replacement of the chloride ligands in complexes of the well-known form $PtCl_2$(*N^N*-diimine), which are normally not luminescent

in solution at room temperature. The first series consists of Pt(dbbpy)(dithiolate) complexes, with six different 1,1- or 1,2-dithiolates (S^S) of varying electron demand (dbbpy = 4,4'-di-*tert*-butyl-2,2'-bipyridine).[13,14,15,16,17,18] In the second series, electron-donating or withdrawing substituents were introduced into the N^N ligands, whilst the dithiolate was held constant as toluene-3,4-dithiolate (tdt).[19,20,21,22,23] These two series of complexes offer dramatic support for a charge-transfer-to-diimine formulation of the lowest-energy excited state. Thus, the lowest energy absorption band red-shifts in absorption by > 4000 cm^{-1} in Series II, on-going from the platinum(3,4,7,8-tetramethyl-1,10-phenanthroline) (toluene-3,4-dithiolate) (Pt(tmphen)(tdt)) through to the platinum(4,4'-*bis*(ethoxycarbonyl)-2,2'-bipyridine)(toluene-3,4-dithiolate) (Pt(4,4-($EtCO_2$)$_2$-bpy)(tdt)), as the electron accepting nature of the diimine increases. A good correlation with Hammett constants is observed for the substituted bipyridine ligands. There is a similar range of energies for Series I. The quantum yields of the complexes are of the order 10^{-3}-10^{-4}, and lifetimes are in the range 1–1000 ns in DCM at 298K.

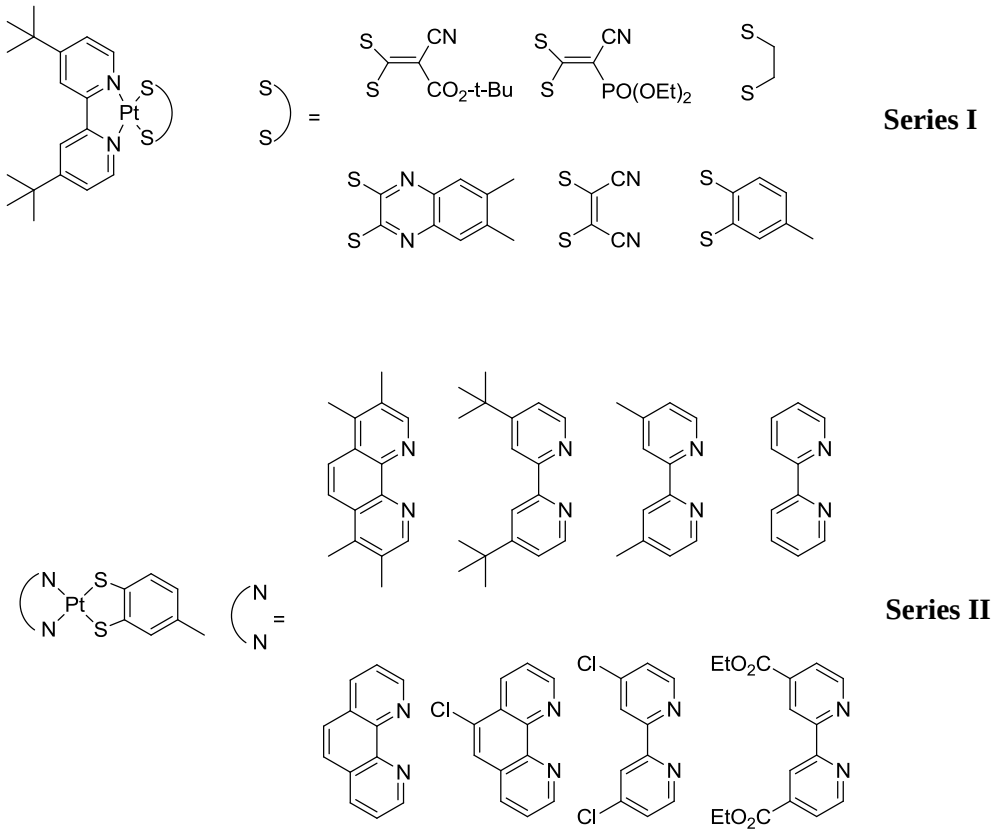

Figure 2. Platinum(II) diimine complexes (Series I and II) bearing S^S ligands[11]

In this Chapter, new platinum(II) and iridium(III) complexes are reported, incorporating one (Pt) or two (Ir) *N^C*-cyclometallating ligands, and with either an S^S or P^N-coordinating co-ligand to complete the coordination sphere of the metal ion. P^N ligands such as 8-(diphenylphosphino)quinoline (Ph_2Pqn), 2-(diphenylphosphino-amino)-pyridine (Ph_2PNHpy) and 8-(diphenylphosphinoamino)-pyrimidine ($Ph_2PNHpym$) represent an interesting class of heterobidentate ligands that had been applied previously at Université de Rennes for the palladium-catalyzed methoxy-carbonylation of olefins.[24] Having in hand these chelating ligands, we sought to use them for the preparation of luminescent cationic Ir(III) complexes. Meanwhile, an "inorganic analogue of acac" – well-established in the literature but never previously investigated in the context of luminescent metal complexes – has also been explored as an S^S-coordinating co-ligand.

2. Heteroleptic Iridium(III) and Platinum(II) Complexes bearing sulfur-based ligands

2.1. Synthesis

2.1.1. Ligand Synthesis

The transition metal chemistry of tetraphenyldithioimidodiphosphinic acid, $Ph_2P(S)NHP(S)Ph_2$ (SPNHPS) has been studied over recent years as its complexes have many applications as selective extraction agent for metals, as lanthanide NMR shift reagents and in catalysis.[25,26,27,28] The synthesis of the SPNHPS ligand consists of the reaction of *N*-(diphenylphosphino)-*P*,*P*-diphenyl-*N*-[(1*S*)-1-phenylethyl] with sulfur in THF at reflux for 8 h (**Scheme 1**).[29]

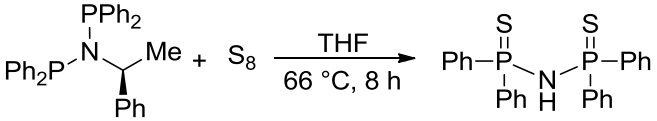

Scheme 1. Synthesis of the pro-ligand **SPNHPS**

2.1.2. Synthesis of metal complexes of the SPNPS ligand

The reaction of **SPNHPS** with metal ions usually involves the deprotonation of the NH group, which leads to the formation of the anionic tetraphenyldithioimidodiphosphinate ligand. The produced negative charge is delocalised throughout the SPNPS skeleton, just as in the deprotonation of 2,4-pentanedione to give the well-known $acac^-$ ligand.

2.1.2.1. Iridium complex

Ir(ppy)$_2$(SPNPS) was synthesized under mild conditions.[30] The iridium dimer complex [Ir(μ-Cl)(ppy)$_2$]$_2$ was reacted with the tetraphenyldithioimidodiphosphinic acid pro-ligand in a mixture of MeOH and DCM (1:1) at 52 °C for 24 h. After several washings with Et_2O, the product was obtained in 65 % yield (**Scheme 2**).

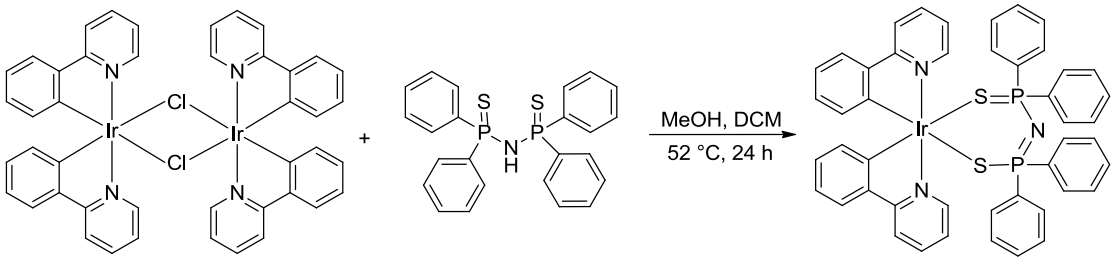

Scheme 2. Synthesis of **Ir(ppy)$_2$(SPNPS)**[29]

2.1.2.2. Platinum complexes

The synthesis of the platinum complexes showed that the temperature had a major impact on the reactivity and the formation of the complex. In the first instance, 1 equivalent of **[Pt(ppy)(μ-Cl)]$_2$** and 3 equivalents of phosphinothioic amide (*i.e.*, Pt : SPNPS ratio = 1:1.5) were reacted in 2-ethoxyethanol at 90 °C for 24 h, without addition of base. After purification by several washings with Et_2O, the homoleptic *bis*-phosphinothioic amide platinum complex **Pt(SPNPS)$_2$** was obtained in 46 % yield. There was no evidence for the anticipated heteroleptic product. Apparently, the platinum(II) centre is so thiophilic that the S^S ligand can displace the N^C ligand from the coordination sphere of platinum. When the reaction was performed at room temperature with the same stoichiometry, however, in a mixture of DCM and methanol (1:1), the heteroleptic **Pt(ppy)(SPNPS)** complex was isolated in 54 % yield (**Scheme 3**).

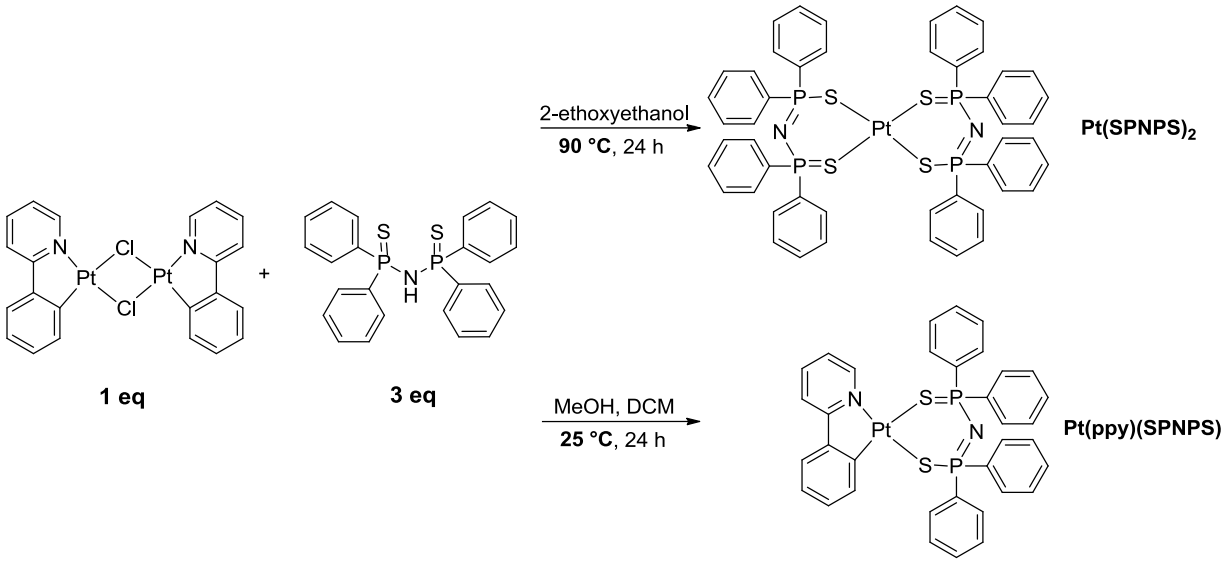

Scheme 3. Synthetic routes for the formation of **Pt(ppy)(SPNPS)** and **Pt(SPNPS)$_2$**

2.2. Characterisation

2.2.1. NMR spectroscopy

The NMR spectra of **Ir(ppy)$_2$(SPNPS), Pt(ppy)(SPNPS)** and **Pt(SPNPS)$_2$** complexes were recorded in $CDCl_3$ at 700 MHz. The ^{1}H NMR of **Pt(SPNPS)$_2$** showed only one set of three signals (*o*, *m*, *p* protons of the aromatic rings) due to its symmetry (**Figure 3**). On the other hand, the ^{1}H NMR spectrum of **Pt(ppy)(SPNPS)** displayed two characteristic signals at 9.4 ppm and 8.1 ppm corresponding to $H^{py\text{-}6}$ and $H^{3'}$ of the ppy ligand. Their localisation, close to the platinum metal centre, led to a clearly observable 3-bond ^{195}Pt–^{1}H coupling for both signals.

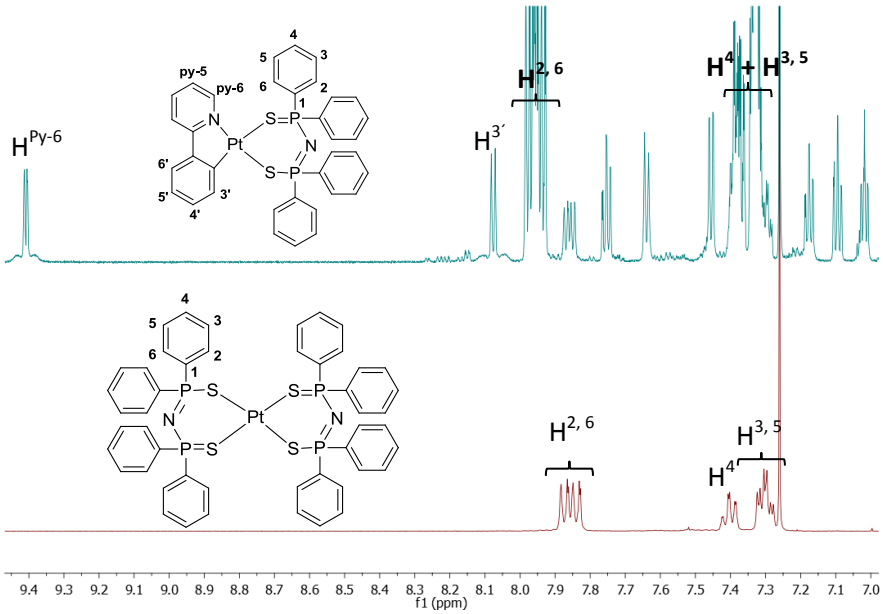

Figure 3. TOP: ^{1}H NMR spectrum of **Pt(ppy)(SPNPS)** complex and BOTTOM: ^{1}H NMR spectrum of **Pt(SPNPS)$_2$**. Both spectra were recorded in $CDCl_3$ at 298 K. Note the ^{195}Pt satellites around the peaks corresponding to H^{py-6} and $H^{3´}$ in the **Pt(ppy)(SPNPS)** complex

The ^{31}P NMR spectrum of **Pt(SPNPS)$_2$** showed only one phophorus signal at 32.6 ppm due to the equivalence of all four phosphorus atoms (**Figure 4**). Coupling to ^{195}Pt is evident from poorly-defined satellites on either side of the signal. By comparison, the ^{31}P signal of the free ligand is found at 57.6 ppm.[31] Furthermore, the ^{31}P NMR spectrum of **Pt(ppy)(SPNPS)** displayed two characteristic signals at 33.4 ppm and 36.7 ppm, the latter showing well-defined ^{195}Pt-coupling satellites.

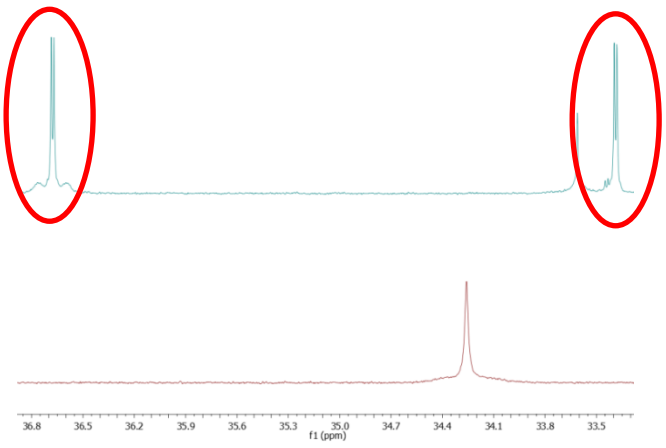

Figure 4. TOP: ^{31}P NMR of **Pt(ppy)(SPNPS)** complex and BOTTOM: ^{31}P NMR of **Pt(SPNPS)$_2$**. All spectra were recorded in $CDCl_3$ at 298 K. Note the ^{195}Pt satellites around peaks in **Pt(SPNPS)$_2$** and **Pt(ppy)(SPNPS)** complexes A third signal appeared, attributed to the ^{31}P of the free ligand.

2.2.2. Crystallography

The structures of the three complexes were confirmed by X-ray crystal structure analyses, as shown in **Figures 5** and **6**. Selected bond length and bond angle data are listed in **Table 1**. **Ir(ppy)$_2$(SPNPS)** crystallised in a mixture of DCM and hexane solution. The complex shows a distorted octahedral geometry around iridium, consisting of two cyclometallated C^N ligands and one S^S ligand. The ligand arrangement, where the two Ir–C bonds are in mutually *cis* positions, is similar to that of the parent phenylpyridine ligands in many heteroleptic Ir(III) complexes such as the diketonate complex **Ir(ppy)$_2$(acac)** and the cationic bipyridine derivatives. The N–Ir and C–Ir bond distances involving the cyclometallated ligand are in the same range as those reported for related Ir complexes.[14] The Ir–S bond distances of about 2.48 Å are significantly longer than those to the coordinated ppy ligand.

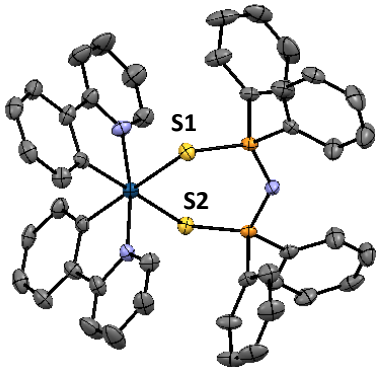

Figure 5. Molecular structure of **Ir(ppy)$_2$(SPNPS)**

Pt(ppy)(SPNPS) crystallised by slow evaporation from a chloroform solution (**Figure 9**). The molecule adopts a slightly distorted square-planar geometry: the angles *trans* S^1^Pt^N (174.9°) and S^2^Pt^C (172.2°) showed a deviation from the 180° of a pure square planar geometry. Furthermore, in this case, the Pt–S bond lengths (2.038 Å and 2.031 Å) are similar to those of Pt–C and Pt–N (2.010 Å and 2.048 Å respectively). Similar bond lengths were observed for ***cis*-Pt(ppy)$_2$**.

Pt(SPNPS)$_2$ was crystallised in DMSO solution (**Figure 6**). The crystal structure of this compound was previously reported.[32] The complex adopts a square planar geometry with angles *trans* S^1^Pt^S^{1*} and S^2^Pt^S^{2*} of 180°, angle *cis* S^1^Pt^S^2* and S^{1*}^Pt^S^2 of 86.8° and angle S^1^Pt^S^2 and S^{1*}^Pt^S^{2*} of 93.1°. These measurements are comparable with literature review. The differences between S^Pt^S are due to the six-membered metallo rings. The four Pt–S bond lengths are identical (Pt–S = 2.33 Å) and shorter than observed for

Pt(ppy)(SPNPS). The bond length P–S2 and P–S1 (2.0243 Å and 2.0309 Å respectively) are closer to single bond than double bond lengths. An angle of 60.6° was observed between the square planar S1^S2^Pt^S1*^S2* plane and the plane formed by the ligand S1^P1^P2^S2.

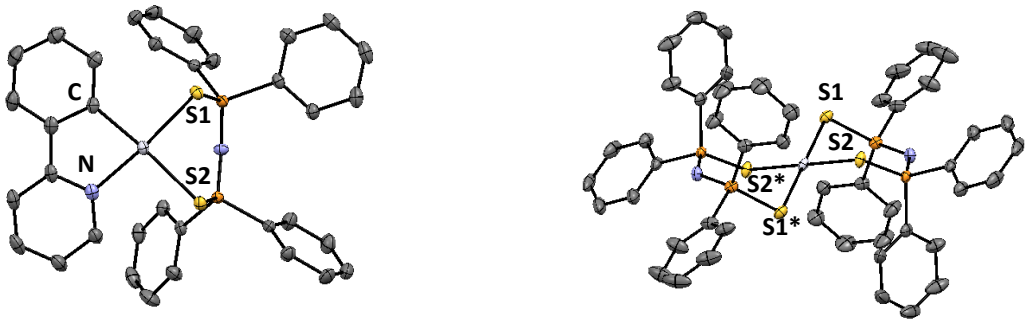

Figure 6. Molecular structure of **Pt(ppy)(SPNPS)** (left) and **Pt(SPNPS)$_2$** (right) (T = 120 K)

Table 1. Selected bond lengths (Å) and angles (°) of Pt(II) and Ir(III) complexes incorporating the SPNPS ligand. (All structures were acquired at 120 K). Data for the *cis*-Pt(ppy)$_2$ and *fac*-Ir(ppy)$_3$ are included for comparison.[33]

Complex	Bond angles / ° *trans* X^**Pt**^Y	Bond angles / ° *cis* X^**Pt**^Y	Bond angles / ° *cis* X^**Pt**^X and *cis* Y^**Pt**^Y
Pt(ppy)(SPNPS) (X = S^{1,2}, Y = N, C)	174.9(6), 172.2(6)	94.5(6), 94.9(6)	89.7(18), 81.0(8)
Pt(SPNPS)$_2$ (X = S^{1,2}, Y = S^{1*,2*})	180	86.8(3)	93.18(3)
***cis*-Pt(ppy)$_2$** (X = C, Y = N)	176.4(3), 176.8(3)	103.3(3), 101.9(3)	79.3(1), 79.3(1)

Complex	Bond lengths **M**–S^1	Bond lengths **M**–S^2	Bond lengths **M**–X	Bond lengths **M**–Y
Ir(ppy)$_2$(SPNPS) (X = C, Y = N)	2.492(14)	2.479(14)	2.030(6), 2.035(6)	2.059(5), 2.053(5)
***fac*-Ir(ppy)$_3$** (X = C, Y = N)	-	-	2.032, 2.034, 2.060	2.096, 2.095, 2.01
Pt(ppy)(SPNPS) (X = C, Y = N)	2.33(5)	2.41(5)	2.010(2)	2.048(19)
Pt(SPNPS)$_2$ (X = S, Y = S)	2.336(7)	2.337(7)	2.336(7)	2.337(7)
***cis*-Pt(ppy)$_2$** (X = C, Y = N)	-	-	1.993(4), 1.993(4)	2.127(3), 2.127(3)

2.2.3. Electrochemistry

Cyclic voltammetry was performed in DCM, with tetrabutylammonium hexafluorophosphate (0.1 M) as a supporting electrolyte, and the solutions were purged with nitrogen before each measurement. All data were measured at multiple scan rates (0.05, 0.1, 0.2, 0.3, 0.4 and 0.5 V.s-1) and are shown in **Table 2**. **Pt(ppy)(SPNPS)** displayed one irreversible oxidation wave with an oxidation potential of E_p^{ox} = 0.81 V, but no reduction waves within the investigated range. **Pt(SPNPS)$_2$** showed one irreversible oxidation wave at 1.00 V (E_p^{ox} = 0.94 V) and one irreversible reduction wave at E_p^{red} = –1.9 V. The cyclic voltammogram of **Ir(ppy)$_2$(SPNPS)** (**Figure 7**) displayed a reversible first oxidation wave ($E_{1/2}$ = 0.60 V) and a second, irreversible, second oxidation wave at around 1.1 V. No reduction was observable within the accessible window.

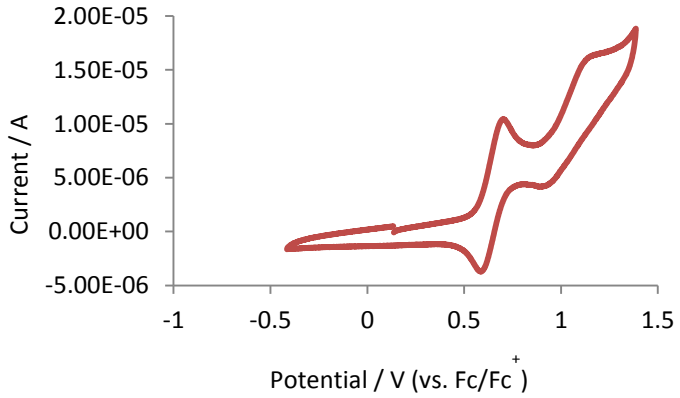

Figure 7. Cyclic voltammogram of **Ir(ppy)$_2$(SPNPS)** in 0.1 M NBu_4PF_6 at a glassy carbon electrode. Scan rate = 0.05 V s^{-1}.

Table 2. Electrochemical data of **Ir(ppy)$_2$(SPNPS)**, **Pt(ppy)(SPNPS)** and **Pt(SPNPS)$_2$** in DCM solution (0.1 M NBu_4PF_6)

Complex	E_p^{ox} / V	E_p^{red} / V	$E_{1/2}$ / V
Ir(ppy)$_2$(SPNPS)	0.47	-	0.60
Pt(ppy)(SPNPS)	0.81	-	-
Pt(SPNPS)$_2$	0.94	–1.9	-

2.2.4. Photophysics

The ground-state absorbance spectra of **Ir(ppy)$_2$(SPNPS)**, **Pt(ppy)(SPNPS)** and **Pt(SPNPS)$_2$** in dichloromethane solution are shown in **Figure 8**. They all showed intense bands in the UV region between 250 and 310 nm assigned to the $^1\pi$-π^* transitions of the

ligands. A weaker band at lower energy, extending into the visible region, is assigned to metal-to-ligand charge transfer transitions in each case. **Ir(ppy)$_2$(SPNPS)** shows lower energy MLCT band than **Pt(ppy)(SPNPS)** and **Pt(SPNPS)$_2$**. It is common for iridium complexes of a given N^C ligand to absorb at lower-energy than platinum complexes. As an example, **Ir(ppy)$_2$(acac)** absorbs at 476 nm whereas **Pt(ppy)(acac)** absorbs at 392 nm.[34,35]

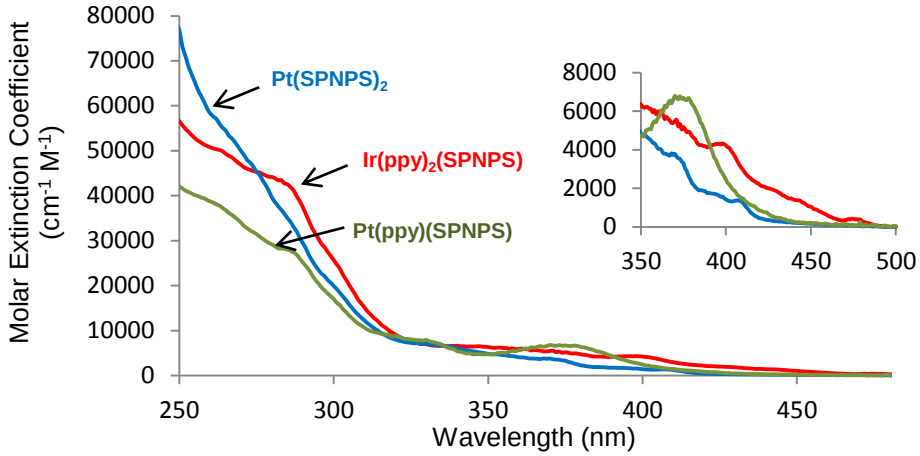

Figure 8. UV-visible absorption spectra of **Ir(ppy)$_2$(SPNPS)**, **Pt(ppy)(SPNPS)** and **Pt(SPNPS)$_2$** in DCM at 298 K

Table 3. Photophysical data of iridium(III) and platinum(II) complexes in degassed DCM at 298K and EPA solution at 77 K

Complex	λ_{abs} / nm (ε/ 10^3 L mol^{-1} cm^{-1})	λ_{em} / nm 298 K	ϕ	λ_{em} / nm 77 K
Ir(ppy)$_2$(SPNPS)	300 (35.3), 355 (6.07), 397 (4.58)	-	-	-
Pt(ppy)(SPNPS)	280 (18.5), 328 (6.37), 373 (6.19)	515, 546, 605 (sh)	0.001	475, 486, 500, 511, 538, 551, 592
Pt(SPNPS)$_2$	274 (30.2), 332 (44.1), 368 (3.96), 400 (1.67)	-	-	-

Luminescence data for **Ir(ppy)$_2$(SPNPS)**, **Pt(ppy)(SPNPS)** and **Pt(SPNPS)$_2$** are shown in **Table 3**. **Pt(ppy)(SPNPS)** was weakly emissive at room temperature, showing a broad band with a maximum at 515 nm (**Figure 9**). At 77 K, the emission spectrum shows pronounced vibrational structure, typical of Pt(N^C) complexes, with a maximum at 475 nm. Similar emission was observed for Pt(ppy)(acac) (λ_{em} = 481 nm).[35] The formation of an aggregate may be the cause of the broad, red shifted emission at 298 K. Neither Pt(SPNPS)$_2$ nor Ir(ppy)$_2$(SPNPS) displayed detectable emission at room temperature or at 77 K.

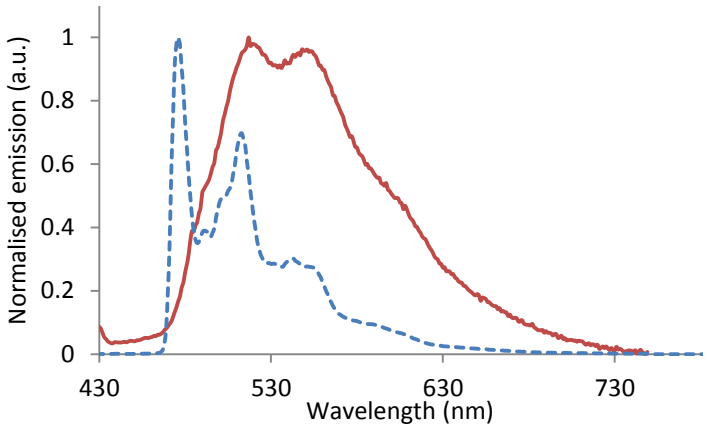

Figure 9. Emission spectra of **Pt(ppy)(SPNPS)** in degassed DCM at 298 K (red) and in EPA solution at 77 K (blue)

3. Heteroleptic iridium(III) complexes bearing phosphine-based ligands

P^N ligands such as 8-(diphenylphosphino)quinoline (Ph_2Pqn, $\mathbf{L^{16}}$), 2-(diphenylphosphinoamino)pyridine (Ph_2PNHpy, $\mathbf{L^{17}}$) and 8-(diphenylphosphinoamino)-pyrimidine ($Ph_2PNHpym$, $\mathbf{L^{18}}$) represent an interesting class of heterobidentate ligands that have been applied for the palladium catalyzed methoxy-carbonylation of olefins.[24] Having in hand these chelating ligands, we sought to use them for the preparation of luminescent cationic Ir(III) complexes (**Figure 10**). The three P^N ligands were prepared following previously reported procedures.[36,37] The cationic complexes $[Ir(ppyMe)_2\mathbf{L^n}]PF_6$ (L^n = $\mathbf{L^{16}}$, $\mathbf{L^{17}}$ and $\mathbf{L^{18}}$) in which $\mathbf{L^{16}}$ = 8-(diphenylphosphino)quinoline, $\mathbf{L^{17}}$ = 2-(diphenylphosphinoamino)pyridine and $\mathbf{L^{18}}$ = 8-(diphenylphosphinoamino)pyrimidine were readily accessible by treatment of the chloro-bridged dimer $[Ir(C^N\text{-}ppyMe)_2(\mu\text{-}Cl)]_2$ with 2 equivalents of the appropriate P^N ligand in the presence of excess $AgPF_6$ to facilitate the removal of the chloride ligands. The $AgPF_6$ also ensures that the complexes are isolated as their hexafluorophosphate salts, which offer better solubility over the chloride salts. All complexes were isolated in good yield after recrystallization from DCM/Et_2O. They were fully characterized by standard spectroscopic methods (^1H and ^{31}P NMR) and gave satisfactory analysis.

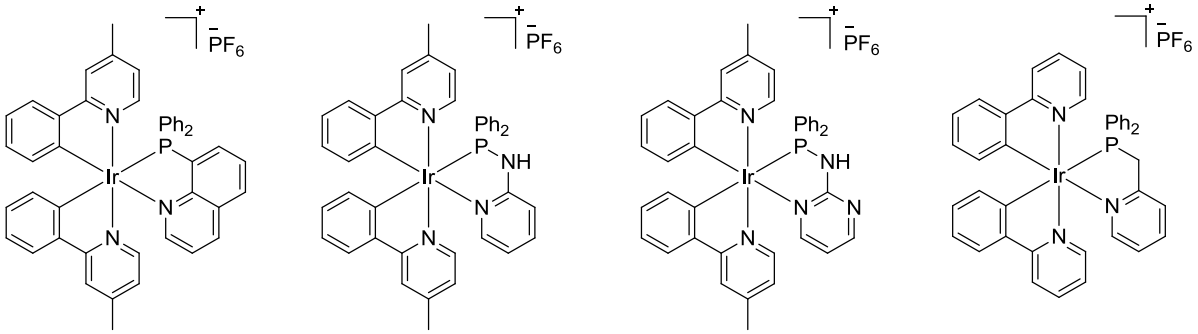

[Ir(ppyMe)$_2$L^{16}]PF$_6$ **[Ir(ppyMe)$_2$L^{17}]PF$_6$** **[Ir(ppyMe)$_2$L^{18}]PF$_6$** **[Ir(ppy)$_2$(dppmp)]PF$_6$**

Figure 10. Representation of iridium complexes **[Ir(ppyMe)$_2$L^{16}]PF$_6$**, **[Ir(ppyMe)$_2$L^{17}]PF$_6$** and **[Ir(ppyMe)$_2$L^{18}]PF$_6$**. **[Ir(ppy)$_2$(dppmp)]PF$_6$**, investigated in a study by another research group, has been included for comparison.[9]

3.1. Electrochemistry

Cyclic voltammetry was performed in DCM, with tetrabutylammonium hexafluorophosphate (0.1 M) as a supporting electrolyte, and the solutions were purged with nitrogen before each measurement. All data were shown in **Table 4**.

All complexes showed an irreversible oxidation and reduction. Determination of E_{onsets} was previously explained (**Chapter 3, Section. 2.3.4**). We can observe similar energy gap (2.71 eV) and optical gap (2.75 eV) for complex **[Ir(ppyMe)$_2$L^{16}]PF$_6$**. Furthermore, no significant difference of the electrochemical properties was observed for complexes **[Ir(ppyMe)$_2$L^{17}]PF$_6$** and **[Ir(ppyMe)$_2$L^{18}]PF$_6$** as we noticed before.

Table 4. Electrochemical data of **1**, **2** and **3** in DCM solution (0.1 M NBu_4PF_6)

Complex	Eonset-ox (V); HOMO (eV)	Eonset-red (V); LUMO (eV)	Energy gap E_g (eV)	Optical gap (eV)
[Ir(ppyMe)$_2$L^{16}]PF$_6$	0.77 ; -5.17	-1.94 ; -2.46	2.71	2.75
[Ir(ppyMe)$_2$L^{17}]PF$_6$	1.11 ; -5.51	-1.77 ; -2.63	2.88	3.02
[Ir(ppyMe)$_2$L^{17}]PF$_6$	1.22 ; -5.62	-1.61 ; -2.79	2.83	3.02

3.2. Photophysics

3.2.1. Absorption

The UV–Vis absorption data of complexes **[Ir(ppyMe)$_2$L^{16}]PF$_6$**, **[Ir(ppyMe)$_2$L^{17}]PF$_6$** and **[Ir(ppyMe)$_2$L^{18}]PF$_6$** in DCM are summarized in **Table 5**, and the corresponding spectra are shown in **Figure 11**. The spectra show intense absorption bands in the higher energy region (λ < 340 nm) which are dominated by intra-ligand ^{1}IL ($\pi \rightarrow \pi^*$)

transitions of the C^N and P^N ligands, and a moderately intense lower-energy absorption band at longer wavelength (around $\lambda \sim 360$ nm) assigned to the tail of the IL transitions overlapping with MLCT $d\pi$ (Ir)$\rightarrow \pi^*$ (C^N and P^N) transitions. The spectrum of complex **[Ir(ppyMe)$_2$L^{16}]PF$_6$** has a weak shoulder extending to longer wavelengths than for **[Ir(ppyMe)$_2$L^{17}]PF$_6$** and **[Ir(ppyMe)$_2$L^{18}]PF$_6$**, possibly reflecting the more extended π-conjugation of the chelated quinolylphosphine ligand. The spectra of **[Ir(ppyMe)$_2$L^{17}]PF$_6$** and **[Ir(ppyMe)$_2$L^{18}]PF$_6$** are very similar to those reported for the related complex **[Ir(ppy)(dppmp)]PF$_6$** having a P^N-coordinated 2-diphenylphosphinomethylpyridine (dppmp) ligand, which contains a saturated CH_2 bridge instead of NH.[9]

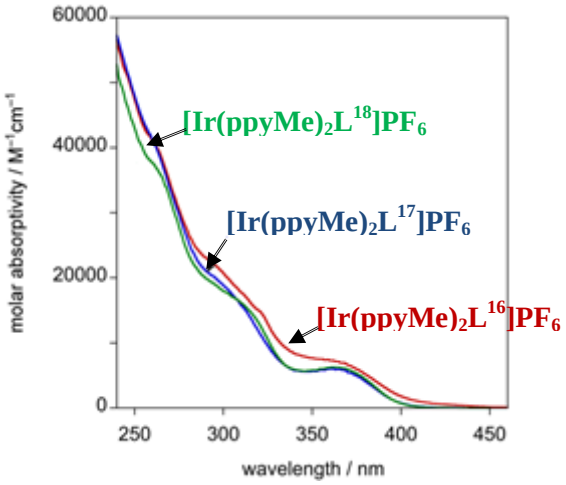

Figure 11. UV-visible absorption spectra of complexes **[Ir(ppyMe)$_2$L^{16}]PF$_6$**, **[Ir(ppyMe)$_2$L^{17}]PF$_6$** and **[Ir(ppyMe)$_2$L^{18}]PF$_6$** in DCM at 298 K

3.2.2. Emission

Upon irradiation, complexes **[Ir(ppyMe)$_2$L^{16}](PF$_6$)**, **[Ir(ppyMe)$_2$L^{17}](PF$_6$)** and **[Ir(ppyMe)$_2$L^{18}](PF$_6$)** are photoluminescent in DCM solution at 298 K but they display very different emission characteristics depending on the nature of the P^N ligand. The luminescence data are listed in **Table 5** and the emission spectra are shown in **Figure 12**. Complex **[Ir(ppyMe)$_2$L^{16}](PF$_6$)** displays a broad emission band centered in the orange region of the spectrum at $\lambda_{em} = 590$ nm with a lifetime of τ = 1800 ns. The emission is red-shifted compared to related well-known complexes such as Ir(C^N-ppy)$_2$(O^O-acac), which may be a reflection of a lower-lying LUMO, localized on the quinolyl group of the P^N ligand as opposed to the pyridyl of the C^N ligands. Complexes **[Ir(ppyMe)$_2$L^{17}](PF$_6$)** and **[Ir(ppyMe)$_2$L^{18}](PF$_6$)**, on the other hand, emit in the blue spectral region, and the spectra display well-resolved structure. The breaking of the conjugation of the P^N bridge has an essential impact in determining the nature of the emissive state. The blue emission could be

attributed to the π-accepting properties of the phosphorus, lowering the energy of the metal-based orbitals that contribute to the HOMO, whilst the LUMO remains localized on the pyridyl rings of the C^N ligands. As has frequently been found in other studies aimed at blue emitters, the quantum yield falls off and the lifetimes shorten on moving to the blue region, possibly due to quenching of the emissive state through close-lying d-d states. Replacement of a pyridine by a pyrimidine ring in **[Ir(ppyMe)$_2$L^{18}]PF$_6$** has little influence on the emission maxima, but it is striking that the lifetime decreases by an order of magnitude. This could be due to a greater degree of distortion in the excited state of **[Ir(ppyMe)$_2$L^{18}]PF$_6$**. Indeed, close inspection of the spectra of **[Ir(ppyMe)$_2$L^{17}]PF$_6$** and **[Ir(ppyMe)$_2$L^{18}]PF$_6$** reveals that, although the wavelengths of the emission maxima coincide, the relative intensity of the 0–0 vibrational band in the spectrum of **[Ir(ppyMe)$_2$L^{18}]PF$_6$** is substantially smaller than for **[Ir(ppyMe)$_2$L^{17}]PF$_6$**, consistent with a larger degree of excited state distortion in the former.

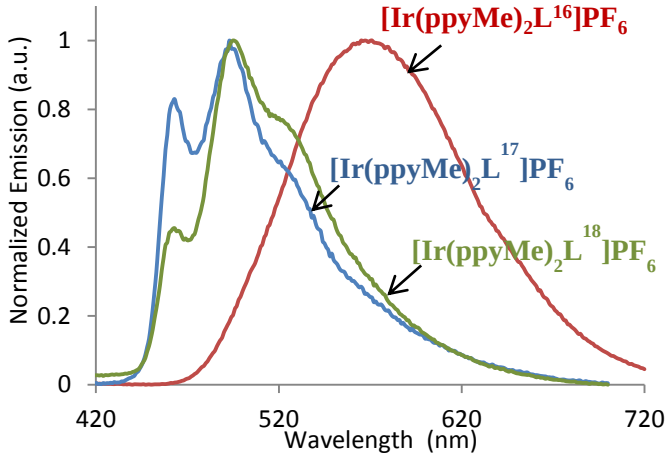

Figure 12. Normalized phosphorescence emission spectra of **complexes [Ir(ppyMe)$_2$L^{16}]PF$_6$**, **[Ir(ppyMe)$_2$L^{17}]PF$_6$** and **[Ir(ppyMe)$_2$L^{18}]PF$_6$** in degassed DCM solution at 298 K

At 77 K, on the other hand, such distortion will be impeded, and indeed the spectra of **[Ir(ppyMe)$_2$L^{17}]PF$_6$** and **[Ir(ppyMe)$_2$L^{18}]PF$_6$** under these conditions are essentially identical (**Figure 13**). The significant variation of emission wavelength between the use of ‘‘conjugated’’ and ‘‘non-conjugated’’ P^N ligands has been previously reported. For instance, when diphenylnaphthyl-phosphine (dpn) is used as ancillary ligand in Ir(III) complexes **[(C^N-Fppy)$_2$Ir(dpn)]**,[38] a broad emission in the orange region is observed λ_{em} = 580–630 nm (FppyH = 2-(2,4-difluoro-phenyl)pyridine) whereas the diphenylbenzyl phosphine analogue gives rise to blue-emitting species.[4a,b]

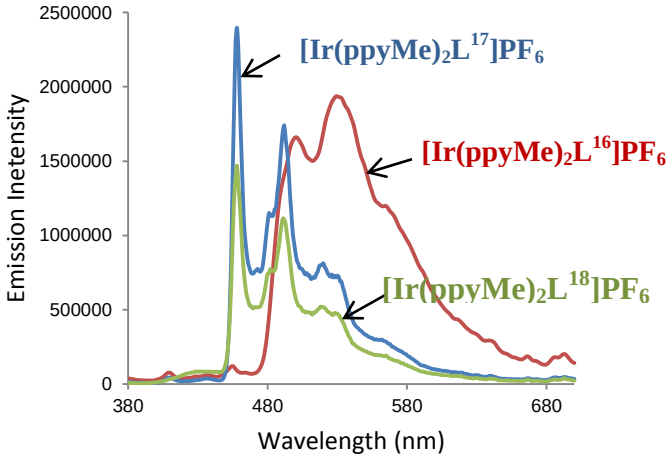

Figure 13. Normalized phosphorescence emission spectra of **[Ir(ppyMe)$_2$L^{16}]PF$_6$**, **[Ir(ppyMe)$_2$L^{17}]PF$_6$** and **[Ir(ppyMe)$_2$L^{18}]PF$_6$** complexes in EPA solution at 77 K

Table 5. Photophysical data of **[Ir(ppyMe)$_2$L^{16}]PF$_6$ (1), [Ir(ppyMe)$_2$L^{17}]PF$_6$ (2) and [Ir(ppyMe)$_2$L^{18}]PF$_6$ (3)** complexes in degassed DCM at 298 K and in EPA solution at 77 K

Complex	λ_{abs} / nm (ε / 10^3 L mol^{-1} cm^{-1})	λ_{em} / nm at 298K	τ / ns	λ_{em} / nm at 77K	ϕ at 298K
1	293sh (22.3), 359 (7.1)	580	1800	500, 530, 567	0.075
2	296 (20.1), 361 (5.9)	461, 491, 522	270	458, 481, 512	0.0068
3	306sh (16.8), 362 (6.3)	460, 493, 526	30	458, 481, 512	0.0004

4. Concluding Remarks

Two neutral cyclometallated platinum complexes, **Pt(SPNPS)$_2$** and **Pt(ppy)(SPNPS)** and one iridium complex **Ir(ppy)$_2$(SPNPS)** were prepared in moderate to good yields (46% 54% and 65%, respectively). The analysis of their properties was carried out by X-ray crystallography and by photoluminescence. **Pt(SPNPS)$_2$** and **Ir(ppy)$_2$(SPNPS)** did not show any emission at room temperature and at 77 K, while **Pt(ppy)(SPNPS)** is weakly emissive at room temperature (λ_{em} = 515 nm and ϕ = 0.001). Furthermore, we showed that the use of ‘‘non-conjugated’’ and π accepting phosphorus-based species as ancillary ligands allows the emission of cationic heteroleptic Ir(III) complexes (**1**, **2** and **3**) from yellow (complex **1**) to the blue region (complexes **2** and **3**).

5. References

[1] C.-H. Yang, M. Mauro, F. Polo, S. Watanabe, I. Muenster, R. Frohlich, L. De Cola, *Chem. Mater.*, 2012, **24**, 3684-3695.

[2] D. J. Stufkens, A. Vlcek, *Coord. Chem. Rev.*, 1998, **177**, 127.

[3] (a) Y. You, W. Nam, *Chem. Soc. Rev.*, 2012, **41**, 7061.

(b) S. Ladouceur, E. Zysman-Colman, *Eur. J. Inorg. Chem.*, 2013, 2985.

(c) C. Ulbricht, B. Beyer, C. Friebe, A. Winter, U.S. Schubert, *Adv. Mater.*, 2009, **21**, 4418.

[4] (a) To date, a large number of blue emissive iridium complexes has been reported. See *inter alia*: C. Adachi, M.A. Baldo, S.R. Forrest, M.E. Thompson, *Appl. Phys. Lett.*, 2000, **77**, 904.

(b) S. Stagni, S. Colella, A. Palazzi, G. Valenti, S. Zacchini, F. Paolucci, M. Marcaccio, R.Q. Albuquerque, L. De Cola, *Inorg. Chem.*, 2008, **47**, 10509.

(c) S. J. Lee, K.-M. Park, K. Yang, Y. Kang, *Inorg. Chem.*, 2009, **48**, 1030.

(d) J. M. Fernandez-Hernandez, J. I. Beltran, V. Lemaur, M.-D. Galvez-Lopez, C.-H. Chien, F. Polo, E. Orselli, R. Frolich, J. Cornil, L. de Cola, *Inorg. Chem.*, 2013, **52**, 1812.

(e) Y.-H. Song, Y.-C. Chiu, Y. Chi, Y.-M. Cheng, C.-H. Lai, P.-T. Chou, K.-T. Wong, M.-H. Tsai, C.-C. Wu, *Chem. Eur. J.*, 2008, **14**, 5423.

(f) M. Ashizawa, L. Yang, K. Kobayashi, H. Sato, A. Yamagishi, F. Okuda, T. Harada, R. Kuroda, M. Haga, *Dalton Trans.*, 2009, 1700.

(g) H. Oh, K.-M. Park, H. Hwang, S. Oh, J.H. Lee, J.-S. Lu, S. Wang, Y. Kang, *Organometallics* 2013, **32**, 6427.

(h) L. He, L. Duan, J. Qiao, R. Wang, P. Wei, L. Wang, Y. Qiu, *Adv. Funct. Mater.*, 2008, **18**, 2123.

(i) T. Sajoto, P. I. Djurovich, A. Tamayo, M. Yousufuddin, R. Bau, M. E. Thompson, R. J. Holmes, S. R. Forrest, *Inorg. Chem.*, 2005, **44**, 7992.

(j) C.-F. Chang, Y.-M. Cheng, Y. Chi, Y.-C. Chiu, C.-C. Lin, G.-H. Lee, P.-T. Chou, C.-C. Chen, C.-H. Chang, C.-C. Wu, *Angew. Chem. Int. Ed.*, 2008, **47**, 4542.

[5] D. L. Davies, M. P. Lowe, K. S. Ryder, K. Singh, S. Singh, *Dalton Trans*., 2011, **40**, 1028

[6] E. C. Constable, M. Neuburger, P. Rosel, G. E. Schneider, J. A. Zampese, C. E. Housecroft, F. Monti, N. Armaroli, R. D. Costa, E. Ortí, *Inorg. Chem.*, 2013, **52**, 885.

[7] Dong Ryeol Whang, Ken Sakai, and Soo Young Park, *Angew. Chem. Int. Ed.*, 2013, **52**, 11612.

[8] Y. Chi, P.-T. Chou, *Chem. Soc. Rev.*, 2010, **39**, 638.

[9] (a) J.-Y. Hung, Y. Chi, I.-H. Pai, Y.-C. Yu, G.-H. Lee, P.-T. Chou, K.-T. Wong, C.-C. Chen, C.-C. Wu, *J. Chem. Soc.*, Dalton Trans., 2009, 6472.

(b) Y.-C. Chiu, C.-H. Lin, J.-Y. Hung, Y. Chi, Y.-M. Cheng, K.-W. Wang, M.-W. Chung, G.-H. Lee, P.-T. Chou, *Inorg. Chem.*, 2009, **48**, 8164.

(c) C.-H. Lin, Y.-Y. Chang, J.-Y. Hung, C.-Y. Lin, Y. Chi, M.-W. Chung, C.-L. Lin, P.- T. Chou, G.-H. Lee, C.-H. Chang, W.-C. Lin, *Angew. Chem. Int. Ed.*, 2011, **50**, 3182.

(d) S. A. Moore, D. L. Davies, M.M. Karim, J. K. Nagle, M. O. Wolf, B. O. Patrick, *J. Chem. Soc*., *Dalton Trans.*, 2013, **42**, 12354.

[10] Y.-C. Chiu, Y. Chi, J.-H. Hung, Y.-M. Cheng, Y.-C. Yu, M.-W. Chung, G.-H. Lee, P.-T. Chou, C.-C. Chen, C.-C. Wu, H.-Y. Hsieh, *ACS Appl. Mater. Interfaces 1*, 2009, 433.

[11] A.-F. Ma, H.-J. Seo, S.-H. Jin, U.C. Yoon, M.H. Hyun, S.K. Kang, Y.-I. Kim, *Bull. Korean Chem. Soc.*, 2009, **30**, 2754.

[12] S. D. Cummings, R. J. Eisenberg, *J. Am. Chem. Soc.*, 1996, **118**, 1949.

[13] M. W. George, J. J. Turner, *Coord. Chem. Rev.*, 1998, **177**, 201.

[14] N. M. Shavaleev, L. P. Moorcraft, S. J. A. Pope, Z. R. Bell, S. Faulkner, M. D. Ward, *Chem. Eur. J.*, 2003, **9**, 5283.

[15] C. M. Che, K.-T. Wan, L.-Y. He, C.-K. Poon, V. W.-W. Yam, *J. Chem. Soc. Chem. Commun.*, 1989, 943.

[16] C. N. Pettijohn, E. B. Jochnowitz, B. Chuong, J. K. Nagle, A. Vogler, *Coord. Chem. Rev.*, 1998, **171**, 85.

[17] H. Kunkely, A. Vogler, *J. Am. Chem. Soc.*, 1990, **112**, 5625.

[18] K.-T. Wan, C.-M. Che, K.-C. Cho, *J. Chem. Soc. Dalton Trans*, 1991, 1077.

[19] M. Kato, C. Kosuge, K. Morii, J. S. Ahn, H. Kitagawa, T. Mitani, M. Matsushita, T. Kato, S. Yano, M. Kimura, *Inorg. Chem.*, 1999, **38**, 1638.

[20] T. J. Wadas, R. J. Lachicotte, R. Eisenberg, *Inorg. Chem.*, 2003, **42**, 3772.

[21] W. B. Connick, L. M. Henling, R. E. Marsh, *Acta Crystallogr.*, 1996.

[22] K.-T. Wan, C.-M. Che, K.-C. Cho, *J. Chem. Soc. Dalton Trans.*, 1991, 1077.

[23] M. Hissler, W. B. Connick, D. K. Geiger, J. E. McGarrah, D. Lipa, R. J. Lachicotte, R. Eisenberg, *Inorg. Chem.*, 2000, **39**, 447.

[24] P. A. Aguirre, C. A. Lagos, S. A. Moya, C. Zuniga, C. Vera-Oyarce, E. Sola, G. Peris, J. C. Bayon, *J. Chem. Soc. Dalton Trans.*, 2007, 5419.

[25] C. Silvestru, J. E. Drake, *Coord. Chem. Rev.*, 2001, **223**, 117.

[26] O. Navratil, E. Herrmann, G. Grossmann, J. Teply, J. Coll. Czech., *Chem. Commun.*, 1990, **55**, 364.

[27] L. Barkaoui, M. Charrouf, M. N. Rager, B. Denise, N. Platzer, H. Rudler, *Bull. Soc. Chim. France* 1997, **134**, 167.

[28] H. Rudler, B. Denise, J. R. Gregorio, J. Vaissermann, *Chem. Commun.*, 1997, 2290.

[29] S. T. Venkatakrishnan, S. S. Krishnamurthy, M. Nethaji, *J. Organomet. Chem.*, 2005, **690**, 4001.

[30] K. J. Arm, J. A. G. Williams, *Chem. Commun.*, 2005, **2**, 230.

[31] A. Singhal, D.P. Dutta, S.K. Kulshreshtha, S.M. Mobin, P. Mathur, *J. Organomet. Chem.*, 2006, **691**, 4320-4328.

[32] C. Güzelsoylu, S. Irişli O. Büyükgüngör, *Acta Cryst.*, 2011, **67**, 479.

[33] L. Chassot, E. Muller, A.Von Zelewsky, *Inorg. Chem.*, 1984, **23**, 4249-4253.

[34] S. Lamansky, P. Djurovich, D. Murphy, F. Abdel-Razzaq, R. Kwong, I. Tsyba, M. Bortz, B. Mui, R. Bau, M. E. Thompson, *Inorg. Chem.*, 2001, **40**, 1704-1711

[35] Z. He, Wai-Yeung Wong, X. Yu, H.-S. Kwok, Z. Lin, *Inorg. Chem.*, 2006, **45**, 10922-10937.

[36] P.A. Aguirre, C.A. Lagos, S.A. Moya, C. Zuniga, C. Vera-Oyarce, E. Sola, G. Peris, J.C. Bayon, *J. Chem. Soc., Dalton Trans.*, 2007, 5419.

[37] S. M. Aucott, A.M.Z. Slawin, J.D. Woolins, *J. Chem. Soc., Dalton Trans.*, 2000, 2559.

[38] B.-S. Du, C.-H. Lin, Y. Chi, J.-Y. Hung, M.-W. Chung, T.-Y. Lin, G.-H. Lee, K.-T. Wong, P.-T. Chou, W.-Y. Hung, H.-C. Chiu, *Inorg. Chem.*, 2010, **49**, 8713.

CHAPTER SIX

Experimental Methods

1. Materials and Methods

All solvents used were Analar® quality (with the exception of acetonitrile which was HPLC grade) and were used without further purification. Dry, oxygen-free solvents were obtained by passing the HPLC grade solvent through a Pure Solv 400 solvent purification system. Water was purified using the PuriteSTILL Plus^{TM} system and had a conductivity of ≤ 0.04 μS cm^{-1}. Unless stated otherwise, all reagents were used as supplied from commercial sources. Reactions requiring an inert atmosphere were carried out using Schlenk line techniques under an atmosphere of dry nitrogen.

Thin layer chromatography (TLC) was carried out on silica plates (Merck Art 5554) which are fluorescent upon irradiation at 254 nm. Column chromatography was carried out using silica (Merck Silica Gel 60, 230-400 mesh).

2. Characterization Techniques

^{1}H NMR spectra were recorded in the appropriate solvents on Mercury-400, Varian-200, Varian-500 or VNMRS-700 MHz instruments. ^{13}C NMR spectra were recorded at 126 MHz on the Varian Inova-500 or at 176 MHz on the VNMRS-700 MHz. Chemical shifts are quoted relative to the appropriate protio-solvent resonances, and all *J* values are given in Hz.

Low-resolution electrospray mass spectra (ES) were recorded using a Thermo Finnigan LTQ FT mass spectrometer, with methanol or acetonitrile as the carrier solvent. Accurate ES mass spectra were obtained using either a LCT Premier XE mass spectrometer (Waters Ltd, UK) or a LTQ FT mass spectrometer (Thermo-Finnigan Corporation). Solid state mass spectroscopy was performed on a Waters Xevo quadrupole time-of-flight (QToF) machine fitted with an atmospheric solids analysis probe (ASAP). High resolution mass spectrometry was performed on a Waters Xevo QToF (ASAP) spectrometer.

Elemental analysis was performed using an Exeter Analytical E-440 elemental analyser. Melting points were determined on a Gallenkamp 8893 39 capillary melting point apparatus.

X-Ray diffractions were collected by Dr Dmitry S. Yufit at Durham University. Crystallographic data for all reported structures were collected at 120 K. X-Ray diffraction data for all complexes were collected on an Oxford Diffraction Gemini S Ultra diffractometer using graphite monochromated Mo Kα radiation (λ = 0.71073 Å). The data were collected and integrated using Oxford Diffraction CrysAlis software.[1] X-ray diffraction data for $PtL^{11}Cl$ were collected at 120 K on a Nonius Kappa CCD diffractometer using graphite monochromated Mo Kα radiation (λ = 0.71073 Å); data were collected using the strategy calculated by the COLLECT software (Nonius, 1999)[2] and integrated using HKL Scalepack.[3] The remaining X-ray diffraction data were collected at 120 K on a Bruker APEX CCD diffractometer. These data were collected using the SMART software, with subsequent data processing carried out in SAINT.[4] All of the structures were solved by direct methods in SHELXS-97 and refined by full matrix least squares on F2 in SHELXL-97.[5]

3. Photophysical Characterization

UV/Vis absorption spectra were measured using a Biotek Instruments UVIKON XS spectrometer operating with LabPower software. The sample was held in a quartz cuvette of 1 cm path length, and spectra were recorded against a reference of pure solvent held in a matched cuvette. Extinction coefficients were determined using a dilution method, and graphical application of the Beer-Lambert law:

$$A = \varepsilon l c$$

Equation 1: where A is absorbance, ε is molar absorptivity, l is the path length and c is the concentration.

Solution-based emission and excitation spectra were acquired on a Jobin-Yvon Spex Fluoromax-2 spectrometer. All samples were contained within quartz cuvettes of 1 cm path length. Samples that were to be measured in the absence of air were placed in quartz cuvettes that were modified with appropriate glassware to allow connection to a high vacuum line. To remove air prior to the measurement, the sample was degassed within the cuvette by three freeze-pump-thaw cycles. Emission was recorded at 90 ° to the excitation source, and appropriate filters were used when required to remove second order peaks. All emission spectra were corrected after acquisition for dark count and for the spectral response of the detector. Excitation spectra were automatically corrected upon measurement for lamp output,

through use of a beam splitter which directs 8% of the excitation light to a reference photodiode.

The quantum yields were determined relative to a reference solution containing $[Ru(bpy)_3]Cl_2$. The quantum yield of this complex is well established in air-equilibrated H_2O to be 0.028.[11] To measure the quantum yield, a sample of the complex in DCM was prepared so that the absorbance at the chosen excitation wavelength was below 0.1, to minimize inner filter effects. A solution containing $[Ru(bpy)_3]Cl_2$ with similar absorbance was prepared, and the emission spectra of the complex and reference were measured under identical conditions (i.e. same excitation wavelength, same slit size). The quantum yield was determined from the absorbance and emission data by use of equation 1:

$$\Phi = \Phi_{ST} [I / I_{ST}] [A_{ST} / A] [n^2 / n_{ST}^2]$$

Equation 2: where Φ is the quantum yield of the sample, Φ_{ST} is the quantum yield of the standard, I and I_{ST} are the overall intensities of the sample and standard respectively (obtained from integration of the respective emission spectrum), A and A_{ST} are the absorbance of the sample and standard at the chosen excitation wavelength, and n and n_{ST} are the refractive indices of the solvents.

Lifetimes were determined using an Edinburgh Instruments OB 920 fluorimeter. Luminescence lifetimes of the complexes up to approximately 10 μs were measured by time-correlated single-photon counting (TCSPC), using an EPL-375 pulsed-diode laser as the excitation source (374 nm excitation pulse length of 60 ps). The laser repetition rate was selected such that the pulse period was at least 5-10 times longer than the luminescence lifetime being measured. The emission was detected at 90 ˚ to the excitation source, after passage through a monochromator using a Peltier-cooled R928. Lifetimes in excess of 10 μs were measured by multichannel scaling, and a xenon flash lamp was used as the excitation source (excitation wavelength matched to a suitable absorption band of the complex, pulse length of approximately 2 μs).

The lifetimes were obtained by least-squares fitting to a mono-exponential decay and goodness-of-fit was assessed from the residuals. Low temperature (77 K) experiments were performed using a glass vacuum cold finger apparatus built in-house. A small amount of sample was dissolved in a mixture of ether/isopentane/ethanol (2:2:1 by volume and referred to in this thesis as EPA), and placed into a glass tube. The cold finger was filled with liquid

nitrogen and the tube containing the sample was inserted (see right). EPA forms an amorphous glass upon freezing, which has a very low propensity for cracking.

4. Electrochemical Measurements

Cyclic voltammetry was carried out in a background electrolyte of tetrabutylammonium tetrafluoroborate (0.1 M) in CH_2Cl_2. A μAutolab type III potentiostat was used with computer control and data storage *via* GPES Manager. A three-electrode assembly was employed, consisting of a platinum wire counter electrode, platinum flag reference electrode and a platinum working electrode. The measurements were carried out in a glass cell charged with 2 mg of complex in 2 mL of electectrolyte and purged with nitrogen.

5. General Procedures

5.1. General Procedures for Chapter Three

5.1.1. Synthesis of Tetradentate Ligands

General Stille Cross Coupling Procedure

Precursor **1**, a stannane derivative and LiCl were placed into a Schlenk tube. Toluene was added and a condenser was fitted. The mixture was degassed by three freeze-pump-thaw cycles, and *bis*(triphenylphosphine) palladium dichloride $PdCl_2(PPh_3)_2$ was added to the mixture. The reaction was heated at 110 °C for 48 h under nitrogen. After cooling to room temperature, water (5 mL) was poured into the reaction mixture. The organic phase was extracted with dichloromethane (2 × 10 mL), and washed with water (2 × 10 mL). The organic layer was dried with $MgSO_4$, filtered, and the solvent was removed under reduced pressure. The crude product was purified by column chromatography on silica gel.

General Suzuki-Miyaura Cross Coupling Procedure

Precursor **IV**, a boronic acid derivative and sodium carbonate were suspended in a mixture of DME and water (5:1) or in toluene. The reaction mixture was degassed by three freeze-pump-thaw cycles and put under a nitrogen atmosphere. The catalyst, *tetrakis*(*tri*phenylphosphine) palladium, $Pd(PPh_3)_4$ was added to the solution, and the mixture was heated at 80 °C for 24 h. After cooling to room temperature, the solution was poured into water, and the organic layer

was extracted with DCM (2 × 10 mL) and washed with water (2 × 10 mL). The organic layer was dried with $MgSO_4$, filtered, and the solvent was removed in *vacuo*. The crude product was purified by column chromatography on silica gel.

5.1.2. Synthesis of tetradentate complexes

General platinum complexation procedure 1

Ligand $\mathbf{L^nH_2}$ (0.66 mmol), K_2PtCl_4 (0.30 g, 0.72 mmol), and acetic acid (3 mL) were introduced into a Schlenk. The reaction mixture was degassed with three freeze-pump-thaw cycles, and heated at 90 °C for 24 to 48 h. The reaction was quenched with water (5 mL), and the precipitate was collected by centrifugation and washed with EtOH (1 × 5 mL) and Et_2O (5 × 5 mL).

General palladium complexation procedure 2

Ligand $\mathbf{L^nH_2}$ (0.20 mmol), $Pd(OAc)_2$ (0.05 g, 0.22 mmol), and acetic acid (3 mL) were introduced into a Schlenk. The reaction mixture was degassed with three freeze-pump-thaw cycles, and heated at 90 °C for 24 h. The reaction was quenched with water (5 mL), and the precipitate was collected by centrifugation and washed with EtOH (1 × 5 mL) and Et_2O (5 × 5 mL). The product was dissolved in a minimum of DMF and crystallized by slow diffusion of DCM into the DMF.

General mercuric complexation procedure 3

Ligand $\mathbf{L^nH_2}$ (0.062 mmol), $Hg(OAc)_2$ (0.31 mmol, 5 equiv.), and EtOH (3 mL) were introduced into a Schlenk. The reaction mixture was heated at 78 °C for 24 h. The reaction was quenched with water (5 mL), and the precipitate was collected by Büchner filtration and washed with EtOH (1 × 5 mL) and Et_2O (5 × 5 mL)

5.2. General Procedures for Chapter Four

5.2.1. Ligands Synthesis

Method A: General procedure for the synthesis of benzimidazol-(iso)-quinolines:

Under an atmosphere of nitrogen, the heterocyclic carboxylic acid derivative (1 eq), 1,2-benzenediamine (1 eq) and an excess of polyphosphoric acid (PPA) were heated to 150 °C for 2 h. After cooling to room temperature, the solution was poured into cold water with stirring. The pH was adjusted to 7-8 by addition of 1 M NaOH aqueous solution and the resulting beige precipitate was filtered, washed with water, and dried under vacuum.

5.2.2. Complexes Synthesis

Method B: General procedure for the synthesis of cationic, *bis*-cyclometallated iridium complexes:

A suspension of $[Ir(\mu\text{-}Cl)(ppy)_2]_2$ (1 eq) and ligand (2.2 eq) in a mixture of MeOH and DCM (1:1) was heated at 52 °C for 24 h under a positive pressure of N_2. After cooling to room temperature, the solvent was removed under reduced pressure and the resulting solid was dissolved in a mixture of water and acetonitrile (1:1). The solution was added dropwise to an aqueous solution of KPF_6, and the resulting precipitate was collected by centrifuge and washed with water. The product was dried under vacuum to give a red, yellow or orange solid.

Method C: General procedure for the synthesis of neutral iridium complexes:

A mixture of ligand (2 eq), $[Ir(\mu\text{-}Cl)(ppy)_2]_2$ (1 eq), and potassium carbonate (10 eq) in DMF (3 mL) was degassed prior to being refluxed under an atmosphere of nitrogen for 24 h. After allowing to cool to ambient temperature, water (10 mL) was added, and the resulting precipitate was separated by centrifugation, and washed with water (3 x 5 mL). The yellow solid was dissolved in CH_2Cl_2, the solution dried over $MgSO_4$, filtered, and the solvent removed under reduced pressure. Recrystallisation from THF gave the title complex.

6. Experimental Details for Chapter Two

$[Ir(C^N\text{-}thpy)_2(\mu\text{-}Cl)]_2$

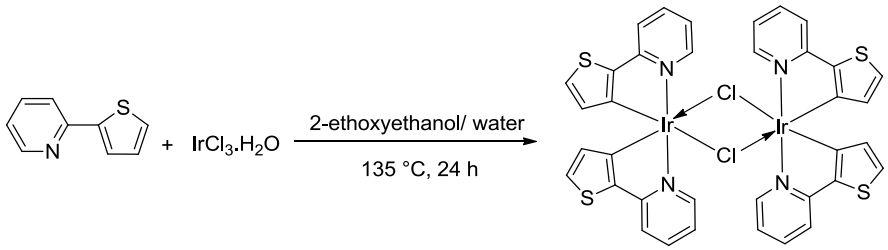

In a Schlenk tube, under argon atmosphere, 2,2'-thienylpyridine (0.94 g, 5.81 mmol) and iridium chloride (0.5 mg, 1.67 mmol) were dissolved in a mixture of 2-ethoxyethanol (12 mL) and water (4 mL). The reaction mixture was stirred for 24 h at 135 °C, quenched by addition of distilled water (15 mL) and the precipitate was decanted by centrifugation. The product was washed with ethanol and diethyl ether. An orange powder was obtained in 80 % yield (0.73 g). **^{1}H NMR** (400 MHz, CD_2Cl_2): 9.04 (ddd, *J* = 5.8 Hz, *J* = 1.5 Hz, *J* = 0.8 Hz, 1H, H^6-py), 7.71 (ddd, *J* = 8.1 Hz, *J* = 7.4 Hz, *J* = 1.6 Hz, 1H, H^4-py), 7.60 (ddd, *J* = 8.1 Hz, *J* = 1.5 Hz, *J* = 0.8 Hz, 1H, H^3-py), 7.16 (d, *J* = 4.8 Hz, 1H, H^5-thio), 6.71 (ddd, *J* = 7.4 Hz, *J* = 5.8 Hz, *J* = 1.5 Hz, 1H, H^5-py), 5.93 (d, *J* = 4.8 Hz, 1H, H^4-thio).**^{13}C {^{1}H} NMR** (101 MHz, CD_2Cl_2): 164.6 (C^2-py), 151.5 (C^6-py), 145.0 (C^3-thio), 137.2 (C^4-py), 135.4 (C^2-thio), 129.2 (C^4-thio), 127.6 (C^5-thio), 119.5 (C^5-py), 117.4 (C^3-py).

fac-$Ir(C^N\text{-}thpy)_3$

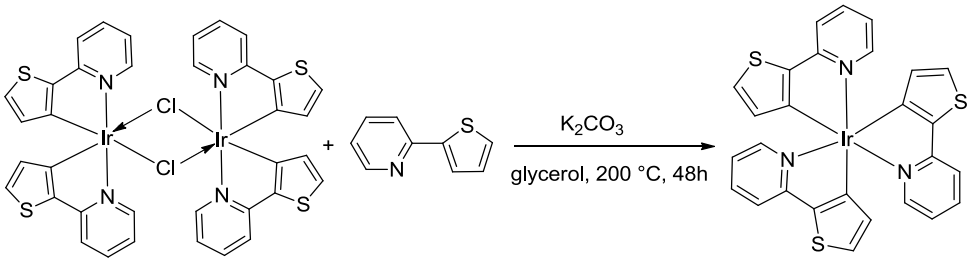

The $[Ir(C^N\text{-}thpy)_2(\mu\text{-}Cl)]_2$ (0.73 g, 0.66 mmol) was added to a mixture of 2,2'-thienylpyridine (0.27 g, 1.65 mmol) and K_2CO_3 (0.91 g, 6.62 mmol) in 20 mL of glycerol. The solution was stirred for 48 h at 200 °C, quenched by addition of 20 mL of distilled water and the resulting precipitate separated by centrifugation. The product was washed with ethanol and diethyl ether. An orange powder was obtained after purification by column

chromatography on silica gel (eluant = CH_2Cl_2, R_f = 0.61). (0.51 g, 58 %). ^{1}H NMR (400 MHz, CD_2Cl_2): 7.58 (d, *J* = 5.4 Hz, 1 H), 7.54 (d, *J* = 7.5 Hz, 1 H), 7.49 (d, *J* = 7.5 Hz, 1 H),7.21 (d, *J* = 4.6 Hz, 1 H), 6.79 (t, *J* = 5.6 Hz, 1 H) ,6.35 (d, *J* = 4.7 Hz, 1 H). ^{13}C {^{1}H} NMR (100 MHz, CD_2Cl_2): 162.4, 159.2, 147.9, 136.7, 135.3, 134.8, 127.4, 119.2, 117.4.

N-butyl-4-bromonaphtalimide, NI-Br [1]

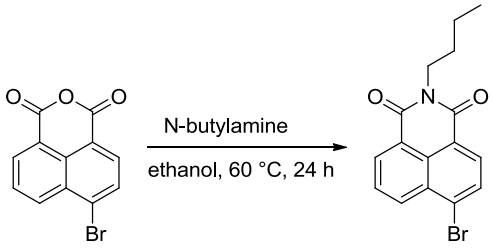

In a round bottom flask, 4-bromonaphthalene (2 g, 7.2 mmol) and *n*-butylamine (0.64 g, 8.6 mmol) were dissolved in EtOH (150 mL). After 18 h of stirring at 60 °C, the solution was hydrolysed with water (20 mL), and the compound was extracted with DCM (40 mL). The organic phase was dried with $MgSO_4$. A light brown powder was obtained. Yield 1.5 g (64%). ^{1}H NMR (400 MHz, $CDCl_3$): 8.68 (d, *J* = 7.2 Hz, 1 H) 8.57 (d, *J* = 8.5 Hz, 1 H), 8.41 (d, *J* = 7.9 Hz, 1 H), 8.02 (d, *J* = 7.9 Hz, 1 H), 7.84 (t, *J* = 7.9 Hz, 1 H), 4.17 (t, *J* = 7.5 Hz, 2 H), 1.71 (m, 2 H), 1.45 (m, 2 H), 0.98 (t, *J* = 7.3 Hz, 3 H). ^{13}C {^{1}H} NMR (100 MHz, $CDCl_3$): 163.5, 163.4, 133.1, 131.9, 131.1, 131.0, 130.5, 130.1, 128.9, 128.0, 123.1, 122.2, 40.4, 30.1, 20.4, 13.9.

1-Bromopyrene, Pyr-Br [2]

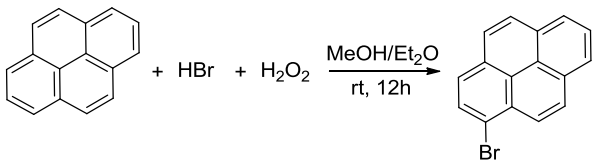

In a round bottom flask, pyrene (2 g, 10 mmol) and HBr (1.7 mL, 11 mmol) were added to a mixture of MeOH and Et_2O (20 mL : 20 mL). An excess of H_2O_2 was added dropwise to the reaction mixture. After 24 h of stirring at room temperature, the precipitate was washed with Et_2O (20 mL) followed by acetone (20 mL). 1-Bromopyrene was obtained without further purification in 98 % yield. ^{1}H NMR (400 MHz, $CDCl_3$): 8.45 (d, *J* = 8.2 Hz, 1H), 8.21 (m, 4 H), 8.05 (m, 4 H).

3-bromoperylene, Per-Br [3]

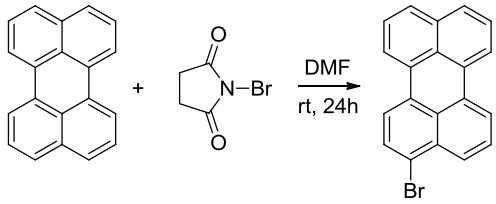

In a round bottom flask, perylene (0.20 g, 0.79 mmol) was dissolved in distilled DMF (36 mL). NBS (0.14 g, 0.79 mmol) was added dropwise to the solution. After 24 h of stirring at room temperature, the reaction was quenched with 50 mL of water. The precipitate formed was extracted into CH_2Cl_2 (3 × 50 mL) of and the solution was washed with distilled water (10 mL). The yellow powder was obtained in 78 % yield. ^{1}H NMR (400 MHz, $CDCl_3$): 8.22 (d, *J* = 7.5 Hz, 1 H), 8.19 (m, 1 H), 8.15 (d, *J* = 7.4 Hz, 1 H), 8.08 (d, *J* = 8.3 Hz, 1 H), 7.98 (d, *J* = 8.0 Hz, 1 H), 7.76 (d, *J* = 8.1 Hz, 1 H), 7.70 (m, 2 H), 7.58 (t, *J* = 8.0 Hz, 1 H), 7.48 (m, 2 H).

7-diethylamino-2-oxo-chromene-3-carboxylic acid ethyl ester [4]

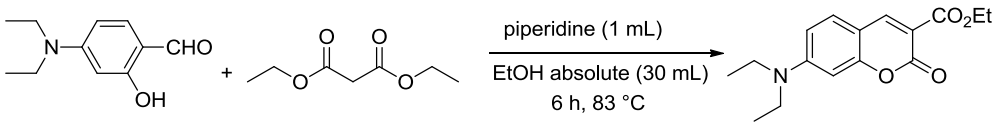

4-Diethylaminosalicylaldehyde (1.93 g, 10 mmol), diethylmalonate (3.2 g, 20 mmol) and piperidine (1 mL) were combined inabsolute ethanol (40 mL). The reaction mixture was heated at 78 °C for 6 h. The solvent was evaporated and the product was extracted with CH_2Cl_2 (30 mL) and purified by chromatography on silica gel (petroleum ether / ethyl acetate, 3:1). A yellow crystalline solid was isolated in 70 % yield. ^{1}H NMR (400 MHz, CD_2Cl_2): 8.39 (s, 1 H), 7.37 (d, *J* = 8.9 Hz, 1 H), 6.63 (dd, J = 8.9 Hz, *J* = 2.4 Hz, 1 H), 6.45 (d, *J* = 2.2 Hz, 1 H), 4.30 (q, *J* = Hz, 2 H), 3.45 (q, *J* = 7.1 Hz, 4H), 1.36 (t, *J* = Hz, 3 H), 1.22 (t, *J* = 7.1 Hz, 6H).

7-(diethylamino)chromen-2-one [4]

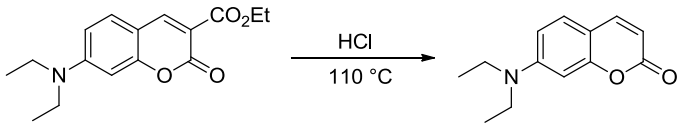

7-Diethylamino-2-oxo-chromene-3-carboxylic acid ethyl ester (1 g, 3.46 mmol) was added to a solution of HCl (60 mL). The reaction mixture was heated at 110 °C for 5 h. After cooling, saturated sodium acetate solution (30 mL) was added and the pH was adjusted to 4-5 with a saturated solution of sodium hydroxide. The precipitate was filtered and dried under vacuum at 50 °C. The white solid was obtained with 80 % yield. ^{1}H NMR (400 MHz, CD_2Cl_2): 7.54 (d, *J* = 9.3 Hz, 1 H), 7.26 (d, *J* = 8.9 Hz, 1 H), 6.58 (dd, *J* = 8.7 Hz, *J* = 2.4 Hz, 1 H), 6.48 (d, *J* = 2.2 Hz, 1 H), 5.96 (d, *J* = 9.3 Hz, 1 H), 3.42 (q, *J* = 7.1 Hz, 4 H), 1.20 (t, *J* = 7.1 Hz, 6 H).

3-bromo-7-(diethylamino)chromen-2-one [4]

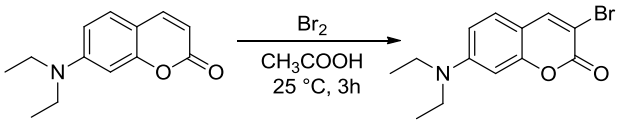

In a round bottom flask, Br_2 (0.89 g, 5.57 mmol) was added dropwise to a solution of 7-diethylaminocoumarin (1.21 g, 5.57 mmol) in acetic acid (30 mL). The reaction mixture was stirred for 2 h 30 at room temperature. The white precipitate was washed with distilled water (3 × 20 mL) and extracted with CH_2Cl_2 (40 mL). After evaporation, the solid was recrystallized from acetonitrile in 78 % yield. ^{1}H NMR (400 MHz, CD_2Cl_2): 8.18 (s, 1 H), 7.92 (d, *J* = 8.9 Hz, 1 H), 7.67 (s, 1 H), 7.67 (d, 1 H), 3.37 (d large, 4H), 1.29 (t, *J* = 7.1 Hz, 6H).

2-methyl-5-(N-butylnaphatalenyl)thiophene

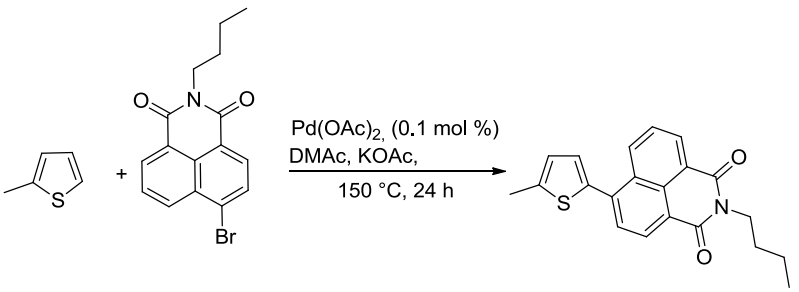

In a Schlenk tube, *N*-butyl-4-bromonaphthalimide (0.166 g, 0.5 mmol), 2-methylthiophene (0.075 g, 0.75 mmol), and KOAc (0.098 g, 1 mmol) were mixed with $Pd(OAc)_2$ (0.001 mg,

0.005 mmol) in DMAc (5mL) at 150 °C. After 48 h of stirring, the 2-methyl-5-(N-butylnaphthalenyl)thiophene was purified by chromatographic silica gel (pentane). A yellow powder was obtained in 65 % yield. ^{1}H NMR (400 MHz, CD_2Cl_2): 8.67 (dd, *J* = 8.5 Hz, J = 1.12 Hz), 8.58 (d, *J* = 7.3 Hz, *J* = 1.12 Hz), 8.52 (d, *J* = 7.6 Hz), 7.83 (d, *J* = 7.6 Hz), 7.81 (t, *J* = 7.9 Hz), 7.16 (d, *J* = 3.7 Hz), 6.91 (d, *J* = 6.7 Hz), 4.13 (t, *J* = 12 Hz), 1.68 (m), 1.43 (m), 0.96 (t, *J* = 10 Hz). ^{13}C {^{1}H} NMR (100 MHz, CD_2Cl_2): 164.1, 163.8, 142.8, 139.3, 137.4, 132.2, 130.9, 130.4, 129.8, 129.0, 128.2, 127.0, 126.3, 123.1, 121.7, 40.1, 30.2, 20.4, 15.11, 13.6. **HRMS** [M + H^{+}] for $C_{21}H_{19}N_2O_2S$ m/z theoretical: 349.45. Found: 350.01.

2-methyl-5-(pyrene)thiophene

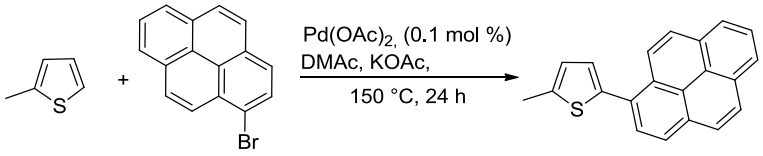

In a Schlenk tube, 1-bromopyrene (0.141 g, 0.5 mmol), 2-methylthiophene (0.075 g, 0.75 mmol), and KOAc (0.098 g, 1 mmol) were mixed with $Pd(OAc)_2$ (0.001 mg, 0.005 mmol) in DMAc (5mL) at 150 °C for 48 h. After evaporation of the solvent, the 2-methyl-5-(pyrene)thiophene was purified by column chromatography on silica gel (pentane). ^{1}H NMR (400 MHz, CD_2Cl_2): 8.56 (d, *J* = 9.3, 1 H), 8.17 (m, 3 H), 8.05 (m, 5H), 7.19 (d, *J* = 3.4 Hz, 1H), 6.94 (m, 1H), 2.64 (s, 1H). **HRMS** [M + H^{+}] for $C_{21}H_{14}S$ m/z theoretical: 298.08. Found: 299.97.

2-methyl-5-(perylene)thiophene

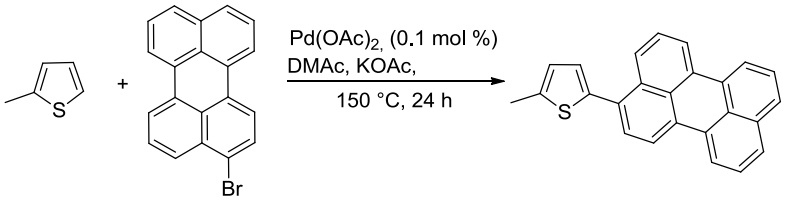

In a Schlenk tube, 3-bromoperylene (0.166 g, 0.5 mmol), 2-methylthiophene (0.075 g, 0.75 mmol), and KOAc (0.098 g, 1 mmol) were mixed with $Pd(OAc)_2$ (0.001 mg, 0.005 mmol) in DMAc (5mL) at 150 °C. After 48 h of stirring, the 2-methyl-5-(perylene)thiophene was purified by column chromatography on silica gel (pentane). ^{1}H NMR (400 MHz, CD_2Cl_2): 8.22 (m, 1 H), 7.71 (m, 3 H), 7.50 (m, 5H), 7.08 (d, *J* = 3.4 Hz, 1H), 6.87 (d, *J* = 3.5 Hz, 1H),

2.64 (s, 3H). ^{13}C {^{1}H} NMR (100 MHz, CD_2Cl_2):140.5, 139.3, 134.6, 133.0, 132.5, 131.2, 131.1, 130.9, 130.7, 128.6, 128.6, 128.4, 127.8, 127.7, 127.4, 126.8, 126.8, 126.6, 125.8, 125.6, 120.6, 120.5, 120.4, 120.3, 119.8, 29.6. **HRMS** [M + H^+] for $C_{25}H_{16}S$ m/z theoretical: 348.10. Found: 349.76.

2-methyl-5-(7-(diethylamino)chromen-2-one)thiophene

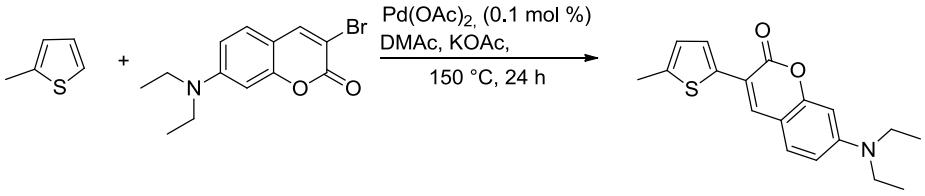

In a Schlenk tube, 3-bromo-7-(diethylamino)chromen-2-one (0.166 g, 0.5 mmol), 2-methylthiophene (0.075 g, 0.75 mmol), and KOAc (0.098 g, 1 mmol) were mixed with $Pd(OAc)_2$ (0.001 mg, 0.005 mmol) in DMAc (5 mL) at 150 °C. After 48 h of stirring, the 2-methyl-5-(N-butylnaphatlenyl)thiophene was purified by column chromatography on silica gel (CH_2Cl_2). A yellow powder was obtained in 15 % yield. ^{1}H NMR (400 MHz, $CDCl_3$): 7.62 (s, 1 H), 7.29 (d, *J* = 8.8 Hz, 1 H), 7.26 (d, *J* = 6.1 Hz, 1 H), 6.91 (d, *J* = 5.11 Hz, 1 H), 6.61 (dd, *J* = 8.8 Hz, *J* = 2.4 Hz, 1 H), 6.54 (d, *J* = 2.2 Hz, 1 H), 3.44 (q, 4H), 2.30 (s, 3H), 1.22 (t, 6H). **HRMS** [M + H^+] for $C_{18}H_{19}N_2O_2S$ m/z theoretical: 313.11. Found: 314.23.

4-methyl-2-phenylpyridine

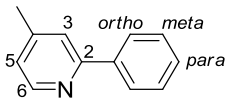

Preparation of the phenyllithium

An excess of lithium (2.89 g, 430 mmol) was ground, activated in ethanol, deactivated in *n*-heptane and suspended in 70 mL of diethyl ether. The suspension was cooled to 0 ^{o}C and bromobenzene (22.6 mL, 215 mmol) in diethyl ether (70 mL) was added dropwise during 20 min. The reaction mixture was stirred for six hours at room temperature.

Preparation of 4-methyl-2-phenylpyridine

The freshly-prepared phenyllithium was added dropwise to a solution of 4-picoline (5 g, 53.8 mmol) in 70 mL toluene at 0 ^{o}C. The reaction was stirred for 24 h at room temperature,

cooled down to 0 °C and distilled water was added dropwise to hydrolyze the excess phenyllithium. The residue was extracted in dichloromethane, washed with water and dried over $MgSO_4$. The product was purified by column chromatography on silica gel (100% *n*-heptane to *n*-heptane/ethylacetate 8:2) to afford an orange powder (m = 5 g, 55%). **^{1}H NMR** (200 MHz, $CDCl_3$): 8.55 (d, *J* = 4.8 Hz, 1H, H^6-py), 7.98 (m, 2H, *H-ortho*), 7.55 (s, 1H, H^3-py), 7.43 (m, 3H, *H-meta, H-para*), 7.05 (dd, *J* = 4.8 Hz, *J* = 1 Hz, 1H, H^5-py), 2.41 (s, 3H, CH_3). **^{13}C{^{1}H} NMR** (75 MHz, $CDCl_3$) δ = 157.2 (C^4-py), 149.4 (C^6-py), 147.7 (C^2-py), 139.5 (*C*-ipso Ph), 128.8 (*C-para*), 128.7 (*C-meta*), 126.9 (*C-ortho*), 123.1 (C^5py), 121.1 (C^3-py), 21.1 (CH_3).

Ir(C^N-thpy-NI)$_3$, 39a and Ir(C^N-thpy)(C^N-thpy-NI)$_2$, 39b

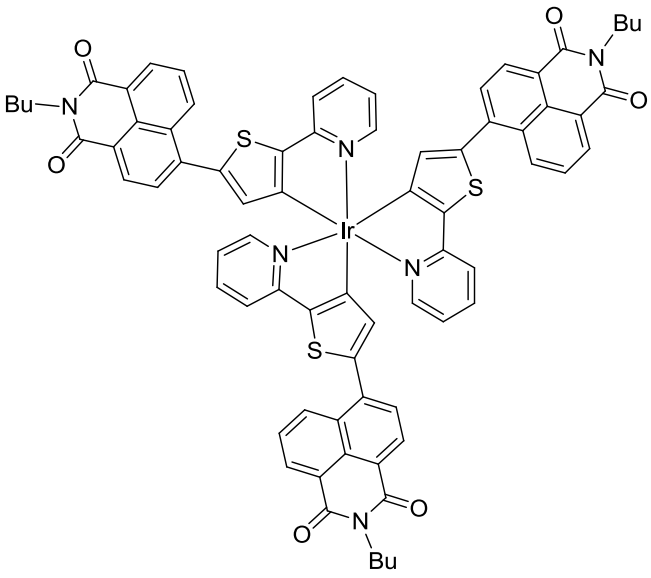

39a **39b**

N-butyl-4-bromonaphthalimide (498 mg, 1.50 mmol), *fac*-Ir(thpy)$_3$ (168 mg, 0.25 mmol), and KOAc (147 mg, 1.5 mmol) with $Pd(OAc)_2$ (2.80 mg, 0.0125 mmol) were combined in DMAc (5mL) at 150 °C during 48 h. The solvent was evaporated and the reaction mixture was purified by column chromatography on silica gel (pentane/Et_2O, 6:4). Two products were collected, **39a** in 40 % yield and **39b** in less than 5 % yield. **HRMS** [M + H^+] for $C_{75}H_{57}IrN_6O_6S_3$ m/z theoretical: 1426.70. Found: 1427.87.

Characterisations for **39a:**

^{1}H NMR (400 MHz, CD_2Cl_2): 9.18 (d, *J* = 8.2 Hz, 1 H), 8.77 (t, *J* = 6.9 Hz, 1 H), 8.71 (d, *J* = 7.2 Hz, 1 H), 8.65 (d, *J* = 8.5 Hz, 1 H), 8.61 (d, *J* = 7.3 Hz, 1 H), 8.57 (m, 1 H), 8.59 (s, 1 H),

8.48 (m, 2 H), 8.11 (t, *J* = 8.0 Hz, 1 H), 7.93 (d, *J* = 7.6 Hz, 1 H), 7.89 (d, *J* = 7.9 Hz, 1 H), 7.86 (t, *J* = 7.5 Hz, 1 H), 7.82 (m, 1 H), 7.67 (m, 6 H), 7.31 (d, *J* = 4.6 Hz, 1 H), 7.24 (d, *J* = 8.2 Hz, 1 H), 7.00 (t, *J* = 6.5 Hz, 1 H), 6.93 (m, 1 H), 6.74 (d, *J* = 6.7 Hz, 1 H), 6.69 (d, *J* = 6.7 Hz, 1 H), 4.12 (t, *J* = 7.4 Hz, 2H), 1.42 (m, 2H), 1.67 (m, 2H), 0.96 (t, *J* = 4.6 Hz, 3H). **HRMS** [M + H^+] for $C_{59}H_{44}IrN_5O_4S_3$ m/z theoretical: 1175.42. Found: 1176.56.

Characterisations for **39b:**

^{1}H NMR (400 MHz, CD_2Cl_2): 9.47 (d, *J* = 5.3 Hz, 1 H), 8.53 (dd, *J* = 7.3 Hz, *J* = 1.1 Hz, 1 H), 8.46 (dt, *J* = 7.7 Hz, *J* = 1.7 Hz, 1 H), 8.42 (dd, *J* = 8.6 Hz, *J* = 1.1 Hz, 1 H), 7.64-7.79 (m, 4 H), 6.85 (t, *J* = 6.6 Hz, J = 1.4 Hz), 6.28 (t, *J* = 13.6 Hz), 4.12 (t, *J* = 7.4 Hz, 2H), 1.42 (m, 2H), 1.67 (m, 2H), 0.96 (t, *J* = 4.6 Hz, 3H). ^{13}C {^{1}H} NMR (100 MHz, CD_2Cl_2): 163.8, 163.8, 163.6, 153.4, 147.1, 142.6, 138.7, 138.4, 137.7, 131.9, 131.1, 130.9, 130.1, 129.68 128.7, 127.9, 127.0, 123.0, 122.0, 120.7, 118.1, 0.74, 13.6, 15.0, 20.3, 40.0. **HRMS** [M + H^+] for $C_{40}H_{31}IrN_4O_2S_3$ m/z theoretical: 888.11. Found: 889.16.

Ir(C^N-thpy-pyr)$_3$, 40a and Ir(C^N-thpy)(C^N-thpy-pyr)$_2$, 40b

1-Bromopyrene (336 mg, 1.19 mmol), *fac*-Ir(thpy)$_3$ (115 mg, 0.17 mmol), KOAc (117.4 mg, 1.19 mmol) and $Pd(OAc)_2$ (1.92 mg, 0.0085 mmol) were combined in DMAc (5 mL) and the mixture heated at 150 °C for 48 h. The solvent was evaporated and the reaction mixture was purified by column chromatography on silica gel (pentane/Et_2O, 6:4). Two products were collected, **40a** in 23 % yield and **40b** in less than 5 % yield.

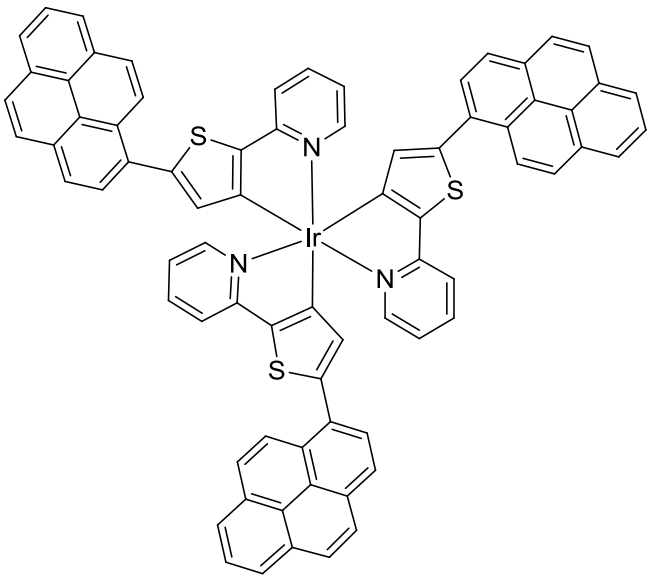

40a

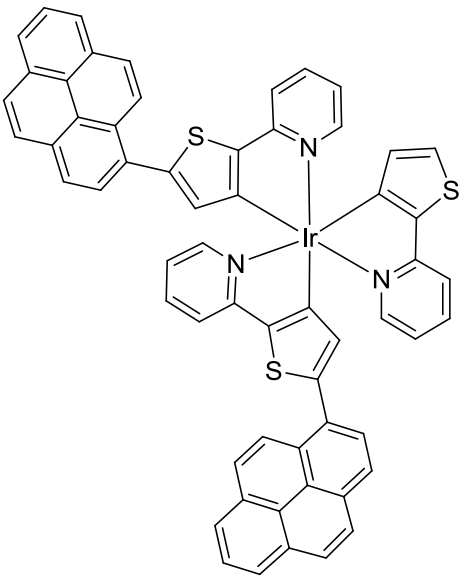

40b

Due to the poor solubility of **40a** and **40b**, analysis by ^{1}H NMR spectroscopy was possible.
40a: **HRMS** [M + H^{+}] for $C_{75}H_{49}IrN_3S_3$ m/z theoretical: 1273.22. Found: 1274.78.
40b: **HRMS** [M + H^{+}] for $C_{59}H_{34}IrN_3S_3$ m/z theoretical: 1073.33. Found: 1074.09.

Synthesis of Complex 41

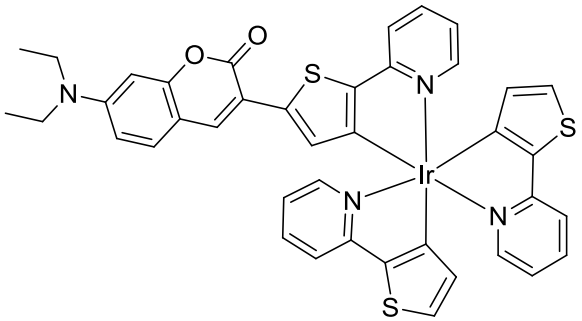

3-Bromo-7-(diethylamino)chromen-2-one (296.06 mg, 0.90 mmol), *fac*-Ir(thpy)$_3$ (100 mg, 0.15 mmol), and KOAc (87.5 mg, 0.9 mmol) with $Pd(OAc)_2$ (1.70 mg, 0.0075 mmol) were combined in DMAc (5mL) at 150 °C during 48 h. The solvent was evaporated and the reaction mixture was purified by column chromatography on silica gel (CH_2Cl_2) An orange powder was collected. ^{1}H NMR (400 MHz, CD_2Cl_2): 7.88 (s, 1 H), 7.65 (m, 1 H), 7.58 (m, 8 H), 7.33 (d, *J* = 8.9 Hz, 1 H), 7.31 (d, *J* = 4.6 Hz, 1 H), 7.27 (d, *J* = 4.7 Hz, 1 H), 6.86 (s, 1 H), 6.83 (d, *J* = 5.4 Hz, 1 H), 6.83 (m, 2 H), 6.64 (dd, *J* = 8.9 Hz, *J* = 2.5 Hz, 1 H), 6.54 (d, *J* = 3.3 Hz, 1 H), 6.53 (d, *J* = 4.7 Hz, 1H), 6.43 (d, *J* = 4.6 Hz, 1H), 3.46 (q, *J* = 7.1 Hz, 4H), 1.26 (t, *J* = 7.1 Hz, 6H). **HRMS** [M + H^{+}] for $C_{40}H_{31}IrN_4O_2S_3$ m/z theoretical: 888.11. Found: 889.16.

Ir(*C*^*N*-ppy)$_2$(tta)

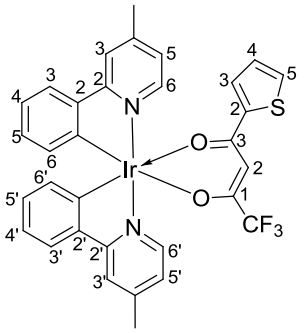

In a Schlenk tube, under argon atmosphere, the chloro-bridged dimer Ir(*C*^*N*-2-ppy)$_2$(μ-Cl)]$_2$ (289 mg, 0.27 mmol), 1-(2-thienyl)-3,3,3-trifluoroacetone (155 mg, 0.70 mmol), and K_2CO_3 (386 mg, 2.80 mmol) were introduced into 10 mL of 2-ethoxyethanol. The reaction mixture

was heated at 80 °C for 24 h, quenched by 10 mL of distilled water and the precipitate was decanted by centrifugation. The product was then washed with water, ethanol, and diethyl ether to afford an orange powder (m = 301 mg, 72 %).**^{1}H NMR** (400 MHz, CD_2Cl_2) δ = 8.55 (ddd, *J* = 5.8 Hz, *J* = 1.6 Hz, *J* = 0.8 Hz, 1H, H^6 or $H^{6'}$-py), 8.52 (ddd, *J* = 5.7 Hz, *J* = 1.6 Hz, *J* = 0.8 Hz, 1H, H^6-py or $H^{6'}$-py), 7.95 (s, 2H, H^3-py, $H^{3'}$-py), 7.71 (dd, *J* = 3.9 Hz, *J* = 1.2 Hz, 1H, H^5-thio), 7.68–7.66 (m, 1H, H^3-Ph or $H^{3'}$-Ph), 7.66–7.64 (m, 1H, H^3-Ph or $H^{3'}$-Ph), 7.59 (dd, *J* = 5.0 Hz, *J* = 1.1 Hz, 1H, H^3-thio), 7.25 (ddd, *J* = 7.3 Hz, *J* = 5.8 Hz, *J* = 1.4 Hz, 1H, H^5-py or $H^{5'}$-py), 7.20 (ddd, *J* = 7.3 Hz, *J* = 5.8 Hz, *J* = 1.4 Hz, 1H, H^5-py or $H^{5'}$-py), 7.08 (dd, *J* = 5.0 Hz, *J* = 3.8 Hz, 1H, H^4-thio), 6.94 (m, 2H, H^4-Ph, $H^{4'}$-Ph), 6.82 – 6.74 (m, 2H, H^5-Ph, $H^{5'}$-Ph), 6.32 (ddd, *J* = 7.6, 1.2, 0.5 Hz, 1H, H^6-Ph or $H^{6'}$-Ph), 6.29 (s, 1H, *H*-metine), 6.27 (ddd, *J* = 7.7, 1.2, 0.5 Hz, 1H, H^6-Ph or $H^{6'}$-Ph), 2.61 (s, H^{-CH3}) **^{13}C{^{1}H} NMR** (101 MHz, CD_2Cl_2 δ = 176.37 (O=*C*), 168.0 (C^2-py or $C^{2'}$-py), 167.91(C^2-py or $C^{2'}$-py), 147.92 (C^6-py , $C^{6'}$-py), 145.7 (C^2-thio), 144.98 (C^2-Ph, $C^{2'}$Ph), 144.48(C^1-Ph, $C^{1'}$Ph) , 143.90 (C^2-Ph or $C^{2'}$-Ph), 137.73 (C^4-py, $C^{4'}$-py), 133.10 (C^6-Ph, $C^{6'}$-Ph), 131.6 (C^3-thio), 128.97 (C^5-thio), 128.89(C^5-Ph, $C^{5'}$-Ph), 128.4 (C^4-thio), 123.98 (C^3-Ph or $C^{3'}$-Ph), 123.83 (C^3-Ph or $C^{3'}$-Ph), 122.15 (C^5-py or $C^{5'}$-py), 122.11 (C^5-py or $C^{5'}$-py), 121.39 (C^4-Ph or $C^{4'}$-Ph), 121.29 (C^4-Ph or $C^{4'}$-Ph), 118.85 (C^3-py or $C^{3'}$-py), 118.72 (C^3-Ph or $C^{3'}$-Ph), 92.69 (*C*-methine). **HRMS** [M^+] for $C_{30}H_{22}F_3N_2O_2F_3SIr$ m/z theoretical: 722.08215. Found: 722.0809.

Ir(ppy-Me)$_2$(tta-NI)

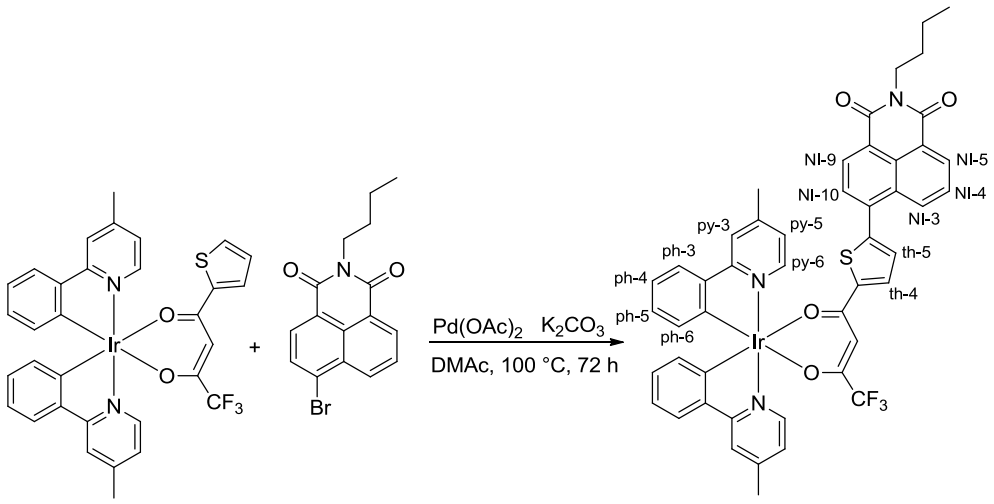

DMAc (4 mL) was added to a Schlenk charged with *N*-butyl-4-bromonaphthalimide (26 mg, 0.080 mmol), Ir(ppy-Me$_2$)$_2$(tta) (50 mg, 0.067 mmol), KOAc (10 mg, 0.1 mmol) and $Pd(OAc)_2$ (0.2 mg, 0.0066 mmol). Then the mixture was heated at 100 °C for 72 h. After

cooling at room temperature, 10 mL of water was added and the resulting precipitate was washed several times with ethanol and diethyl ether. The resulting mixture was purified by column chromatography on silica gel (Eluent: hexane / diethyl ether, 9:1 and then 7:3). The solvent was removed under reduced pressure to afford a red solid (11 mg, 16.5 %). ^{1}H NMR (600 MHz, $CDCl_3$) δ 8.65 (d, 1 H, *J* = 7.64 Hz, H^{NI-3}), 8.56 (d, 1 H, *J* = 8.50 Hz, H^{NI-9}), 8.50 (d, 1 H, *J* = 7.64 Hz, H^{NI-5}), 8.37 (d, 1 H, *J* = 5.85 Hz, $H^{py-6\ or\ py-6'}$), 8.34 (d, 1 H, *J* = 5.85 Hz, $H^{py-6\ or\ py-6'}$), 7.75 (d, 1 H, *J* = 8.50 Hz, H^{NI-10}), 7.74 (s, 1 H, $H^{py-3\ or\ py-3'}$), 7.73 (d, 1 H, *J* = 4.23 Hz, H^{th-5}), 7.72 (s, 1 H, $H^{py-3\ or\ py-3'}$), 7.69 (t, 1 H, *J* = 7.64 Hz, H^{NI-4}), 7.56 (d, 2 H, *J* = 7.60 Hz, $H^{ph-3\ and\ ph-3'}$), 7.24 (d, 1 H, *J* = 4.23 Hz, H^{th-4}), 7.03 (d, 1 H, *J* = 5.85 Hz, $H^{py-5\ or\ py-5'}$), 7.00 (d, 1 H, *J* = 5.85 Hz, $H^{py-5\ or\ py-5'}$), 6.85 (t, 2 H, *J* = 7.60 Hz, $H^{ph-4\ and\ ph-4'}$), 6.72 (t, 2 H, *J* = 7.60 Hz, $H^{ph-5\ and\ ph-5'}$), 6.31 (d, 1 H, *J* = 7.60 Hz, $H^{ph-6\ or\ ph-6'}$), 6.25(d, 1 H, *J* = 7.60 Hz, $H^{ph-6\ or\ ph-6'}$), 6.21 (s, 1 H, -CH), 4.21 (t, 2 H, $-CH_2$), 2.62 (s, 3 H, $-CH_3$), 2.60 (s, 3 H, $-CH_3$), 1.74 (m, 2 H, $-CH_2$), 1.47 (m, 2 H, $-CH_2$), 1.00 (t, 3 H, $-CH_3$). ^{13}C{^{1}H} (101 MHz, $CDCl_3$) δ 174.9, 167.9, 164.2, 163.9, 149.2, 148.0, 147.4, 147.3, 145.1, 145.0, 144.9, 144.9, 144.3, 138.4, 133.5, 133.4, 131.9, 131.6, 130.5, 129.9, 129.6, 128.9, 128.9, 128.8, 128.6, 127.6, 123.7, 123.5, 123.2, 123.1, 122.9, 122.7, 121.2, 121.1, 119.6, 119.4, 40.5, 30.5, 30.3, 21.6, 21.6, 20.5. HRMS: m/z = 999.2083 ($M + 2\ H^+$) calcd for $C_{17}H_{13}Br_2N_3O$ m/z = 999.2063.

7. Experimental details for Chapter Three

[Pt(Mabiq)]PF_6

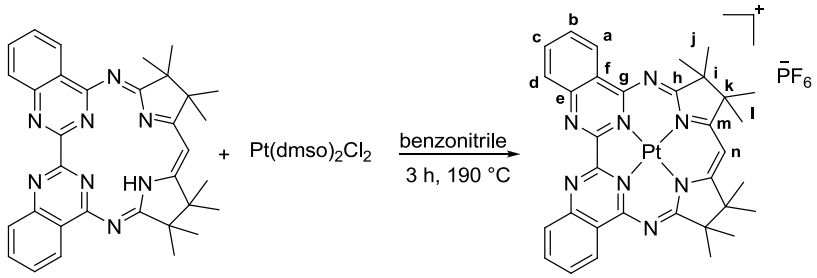

MabiqH (28 mg, 0.0516 mmol) and $PtCl_2(dmso)_2$ (21.7 mg, 0.0516 mmol) were placed in a schlenk tube. Benzonitrile (2 mL) was added. After degasing using freeze and pump thaw method (3 times), the solution was heated at 190 °C for 3 h. After cooling to room temperature, 3 mL of distilled water was added. The orange precipitate was washed with EtOH (3 × 5 mL) and Et_2O (3 × 5 mL) by centrifugation. The crude solid was recrystallized in CH_3CN/ Et_2O. ^{1}H NMR (700 MHz, CD_3CN) δ = 9.26 (d, *J* = 8.0 Hz, 2H, H^{d}), 8.39 (d, *J* = 8.0

Hz, 2H, H^a), 8.30 (t, *J* = 8.0 Hz, 2H, H^b), 8.05 (t, *J* = 8.0 Hz, 2H, H^c), 7.13 (s, 1H, H^n), 1.60 (s, 6H, H^j), 1.59 (s, 6H, H^l). $^{13}C\{^1H\}$ NMR (176 MHz, CD_3CN) δ = 180.5 (C^m), 175.5 (C^h), 155.1 (C^g), 150.4 (C^e), 137.4 (C^b), 132.2 (C^c), 130.3 (C^a), 127.6 (C^d), 123.8 (C^f), 98.9 (C^n), 53.2 (C^{i+k}), 52.7 (C^{i+k}), 24.8 (C^j), 24.3 (C^l). HRMS (ES+) *m/z* = 735.2471 (M) calcd for $C_{33}H_{33}N_8Pt$ *m/z* = 735.2455.

[Au(Mabiq)]PF_6

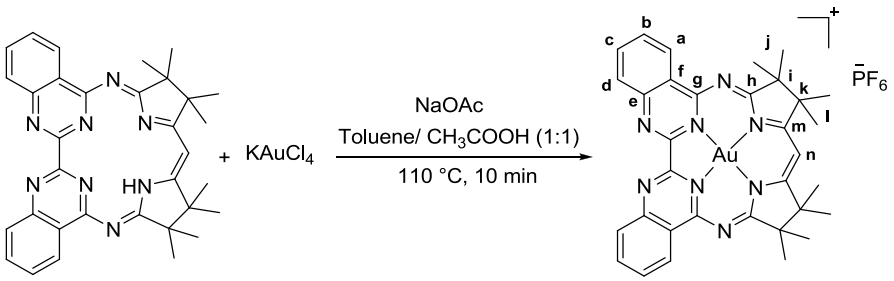

(H)Mabiq (20.0 mg, 0.0316 mmol), potassium tetrachloroaurate(III) (37.0 mg, 0.0979 mmol), and sodium acetate (61.0 mg, 0.744 mmol) were dissolved in a solution of toluene (12 mL) and glacial acetic acid (12 mL). The reaction mixture was heated at reflux for 10 min. The mixture was then diluted in dichloromethane (30 mL) and washed with water (2 × 100 mL). After evaporation of the organic layer, the residue was dissolved in chloroform (12 mL) and stirred with a saturated solution of potassium hexafluorophosphate (0.600 g, 0.326 mmol) in water (12 mL) for 18 h. The solution was evaporated and the yellow solid was washed with Et_2O (3 × 5 mL) using centrifugation method. A yellow solid was obtained in 67 % yield. ^1H NMR (700 MHz, dmso-d_6) δ = 9.02 (d, *J* = 7.8 Hz, 2H, H^d), 8.30 (m, 4H, $H^{a,b}$), 8.03 (m, 2H, H^c), 6.99 (s, 3H), 1.57 (s, 3H), 1.40 (s, 3H), 1.36 (s, 6H), 1.28 (s, 3H), 1.15 (s, 3H), 1.01 (s, 3H). $^{13}C\{^1H\}$ NMR (176 MHz, DMSO-d_6) δ = 181.3, 180.7, 170.0, 168.9, 151.5, 151.3, 148.8, 148.7, 148.2, 147.7, 147.5, 136.9, 136.6, 131.1, 131.0, 129.0, 128.9, 126.9, 122.4, 122.1, 107.8, 90.3, 62.4, 51.7, 51.3, 50.8, 49.1, 47.8.

6-bromo-N-(6-bromopyridin-2-yl)-N-(4-methoxyphenyl)pyridin-2-amine, IV [5]

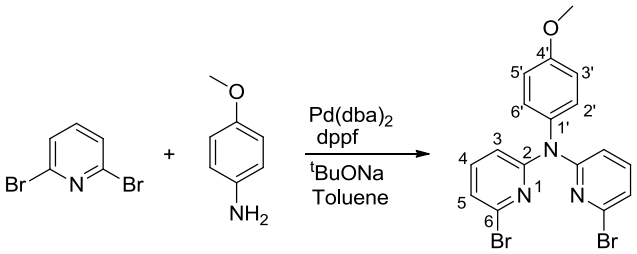

A mixture of *p*-Anisidine (0.49 g, 4 mmol), 2,6-dibromopyridine (2,37 g, 10 mmol), sodium tert-butoxide (0.96 g, 10 mmol), $Pd(dba)_2$ (0.05 g, 0.08 mmol) and dppf (0.09 g, 0.16 mmol) were poured in dry toluene (40 mL). The reaction mixture was heated at 110 °C for 48 h under a nitrogen atmosphere. After cooling to room temperature, water (10 mL) was added to the reaction mixture. The organic phase was extracted with ethyl acetate (3 × 20 mL), and washed with water (3 × 20 mL). The organic layer was dried with $MgSO_4$, and the solvent was reduced under vacuum. The crude oil was purified with column chromatography on silica gel (hexane / ethyl acetate, 100:0 and then 80:20), to give a white powder (1.04 g, 60 %). R_f = 0.66 (silica, 100 % DCM). ^{1}H NMR (700 MHz, $CDCl_3$) δ = 7.36 (t, *J* = 7.8 Hz, 2 H, H^4), 7.13 (d, *J* = 8.9, 2 H, $H^{3', 5'}$), 7.06 (d, *J* = 7.8 Hz, 2 H, H^3), 6.94 (d, *J* = 8.9 Hz, 2 H, $H^{2', 6'}$), 6.92 (d, *J* = 7.8 Hz, 2 H, H^5), 3.84 (s, 3 H, H^{-Me}). ^{13}C {^{1}H} NMR (175 MHz, $CDCl_3$) δ = 157.5 ($C^{4'}$), 156.3 (C^2), 138.6 (C^6), 138.4 (C^4), 135.1 ($C^{1'}$), 128.8 ($C^{3', 5'}$), 120.7 (C^3), 114.3 ($C^{2', 6'}$), 113.4 (C^5), 54.6 (C^{-Me}). HRMS (ES+) *m/z* = 433.9509 ($M+H^+$) calcd for $C_{17}H_{14}Br_2N_3O$ *m/z* = 433.9504. Mp ≥ 125 °C.

2-iodobenzoquinoline V [6]

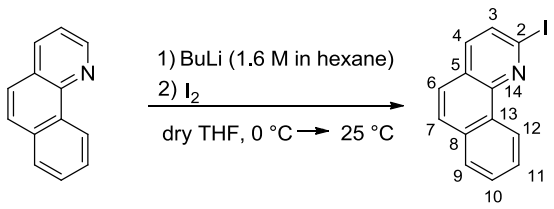

A solution of BuLi (1.6 M in hexanes solution, 6.0 mmol) was added to a solution of 2,2,6,6-tetramethylpiperidine (0.85 g, 6.0 mmol) in THF (5 mL) at 0 °C. After 5 min, $ZnCl_2$.TMEDA (0.51 g, 2.0 mmol) was added to the solution. The mixture was stirred for 15 min at 0 °C before introduction of the benzoquinoline (0.72 g, 4.0 mmol). After 2 h at 25 °C, a solution of

I_2 (1.52 g, 6.0 mmol) in THF (10 mL) was added. The mixture was stirred overnight before addition of an aqueous saturated solution of $Na_2S_2O_3$ (4 mL) and extraction with EtOAc (3 × 20 mL). The combined organic layers were dried over $MgSO_4$, filtered, and concentrated under reduced pressure. The crude product was purified by column chromatography on silica gel (hexane/ ethyl acetate, 70:30) to give a white powder (0.96 g, 79 %). R_f = 0.59 (silica, 30 % Et_2O, 70 % hexane). ^{1}H NMR (600 MHz, $CDCl_3$) δ = 9.21 (d, *J* = 7.4 Hz, 1 H, H^3), 7.90 (d, *J* = 7.6 Hz, 1 H, H^{12}), 7.87 (d, *J* = 8.2, 1 H, H^9), 7.84 (d, *J* = 8.6 Hz, 1 H, H^7), 7.79 – 7.69 (m, 3 H, $H^{4+10+11}$), 7.63 (d, *J* = 8.8, 1 H, H^6). ^{13}C{^{1}H} NMR (175 MHz, $CDCl_3$) δ = 148.2 (C^{14}), 137.0 (C^4), 133.7 (C^5), 132.7 (C^9), 130.7 (C^{13}), 128.9 (C^{11}) 128.5 (C^7), 127.8 (C^{12}), 127.5 (C^{10}), 125.5 (C^8), 124.9 (C^3), 124.8 (C^6), 117.5 (C^2). HRMS (ES+) *m/z* = 305.978 ($M+H^+$) calcd for $C_{13}H_8IN$ *m/z* = 305.980. Mp ≥ 121 °C.

N-(4-methoxyphenyl)-6-phenyl-N-(6-phenylpyridin-2-yl)pyridin-2-amine, L^1H_2

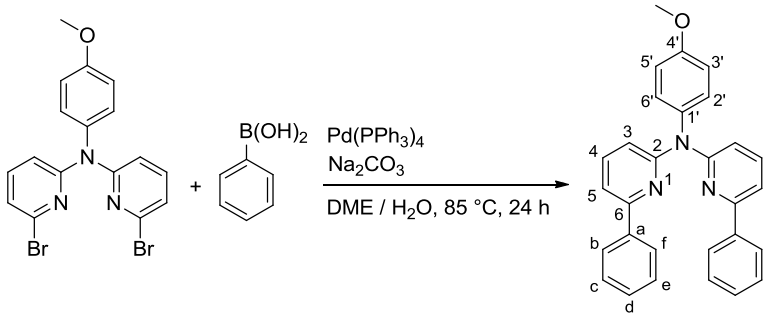

Ligand **L^1H_2** was prepared *via* the Suzuki-Miyaura cross-coupling methodology using precursor **1** (0.41 g, 0.931 mmol), phenyl boronic acid (0.34 g, 2.79 mmol), sodium carbonate (0.99 g, 9.31 mmol) and *tetrakis*(*tri*phenylphosphine) palladium, $Pd(PPh_3)_4$ (0.08 g, 0.07 mmol). The crude product was purified with column chromatography on silica gel (hexane/ ethyle acetate 7:3) to give a white powder (0.12 g, 30 %). R_f = 0.37 (silica, 100 % DCM). ^{1}H NMR (700 MHz, $CDCl_3$) δ = 7.88 (d, *J* = 7.1 Hz, 4 H, $H^{b, f}$), 7.61 (t, *J* = 7.9 Hz, 2 H, H^4), 7.41 – 7.30 (m, 8 H, $H^{5, c, d, e}$), 7.28 (d, *J* = 8.8 Hz, 2 H, $H^{2', 6'}$), 7.04 (d, *J* = 8.2 Hz, 2 H, H^3), 6.98 (d, *J* = 8.8 Hz, 2 H, $H^{3', 5'}$), 3.87 (s, 3 H, H^{-Me}). ^{13}C{^{1}H} NMR (175 MHz, $CDCl_3$) δ = 157.8(C^2), 157.7 (C^6), 155.3 (C^a), 139.4 ($C^{1'}$), 137.9 (C^4), 129.9 ($C^{2', 6'}$), 128.8 (C^d), 128.7 ($C^{c, e}$), 126.8 ($C^{b, f}$), 114.9 ($C^{3', 5'}$), 114.7 (C^3), 113.7 (C^5), 55.7 (C^{-Me}). HRMS (ES+) *m/z* = 430.1907 ($M+H^+$) calcd for $C_{29}H_{24}N_3O$ *m/z* = 430.1919. Mp ≥ 188 °C.

N,6-bis(4-methoxyphenyl)-N-(6-(4-methoxyphenyl)pyridin-2-yl)pyridin-2-amine, L^2H_2

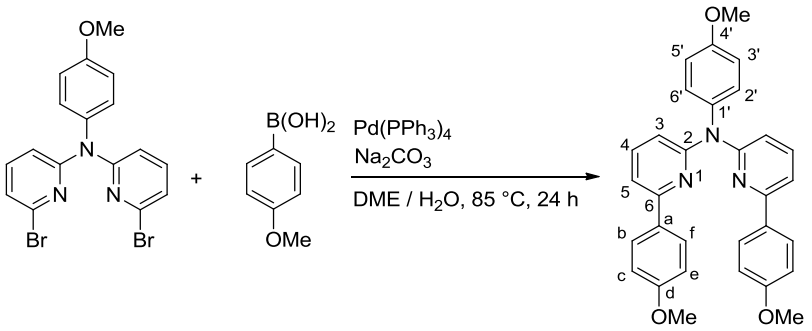

Ligand $\mathbf{L^2H_2}$ was prepared *via* the Suzuki-Miyaura cross-coupling methodology from precursor **1** (0.54 g, 1.25 mmol) 2-naphthaleneboronic acid (0.57 g, 3.75 mmol) sodium carbonate (1.32, 12.5 mmol) and *tetrakis*(*tri*phenylphosphine) palladium, $Pd(PPh_3)_4$ (0.12 g, 0.1 mmol). The crude product was purified with column chromatography on silica gel (hexane/ ethyl acetate 7:3) to give a white powder (0.48 g, 79 %). R_f = 0.81 (silica, 100 % DCM). ^{1}H NMR (700 MHz, $CDCl_3$) δ = 7.84 (d, *J* = 8.8 Hz, 4H, $H^{b, f}$), 7.57 (t, *J* = 7.9 Hz, 2H, H^4), 7.31 (d, *J* = 7.9 Hz, 2H, H^5), 7.28 (d, *J* = 7.9 Hz, 2H, $H^{2',6'}$), 6.98 (d, *J* = 7.9 Hz, 4H, $H^{3',5',3}$), 6.90 (d, *J* = 8.8 Hz, 4H, $H^{c,e}$), 3.88 (s, 3H, H^{-Me}), 3.83 (s, 6H, H^{-Me}). ^{13}C{^{1}H} NMR (176 MHz, $CDCl_3$) δ = 160.3, 157.7, 154.9, 138.0, 137.7, 132.1, 129.9, 128.0, 114.8, 114.0, 113.9, 112.8, 55.6, 55.4. HRMS (ES+) *m/z* = 490.2136 ($M+H^+$) calcd for $C_{31}H_{28}N_3O_3$ *m/z* = 490.2131. Mp ≥ 162 °C.

N-(4-methoxyphenyl)-6-(naphthalen-1-yl)-N-(6-(naphthalen-1-yl)pyridin-2 yl)pyridin-2-amine, L^3H_2

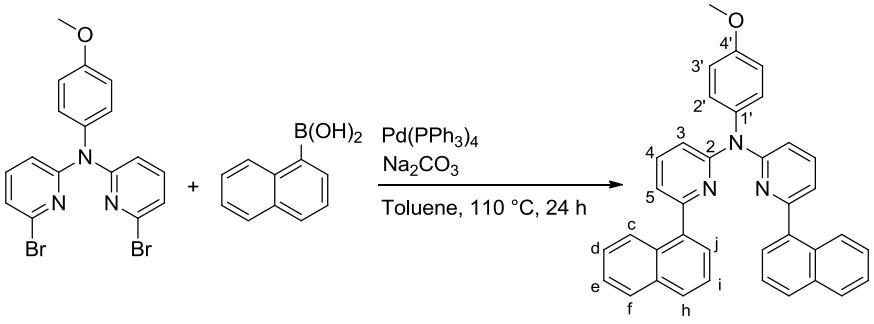

Ligand $\mathbf{L^3H_2}$ was prepared *via* the Suzuki-Miyaura cross-coupling methodology. Precursor **1** (0.23 g, 0.535 mmol) 1-naphthaleneboronic acid (0.28 g, 1.60 mmol), sodium carbonate (0.57 g, 5.35 mmol) and *tetrakis*(*tri*phenylphosphine) palladium, $Pd(PPh_3)_4$ (0.05, 0.043 mmol).

The crude product was purified with column chromatography on silica gel (hexane/ DCM, 5:5) to give a white powder (0.13 g, 47 %). R_f = 0.28 (silica, 100 % DCM). ^{1}H NMR (700 MHz, $CDCl_3$) δ = 8.13 (d, *J* = 8.6 Hz, 2H, H^c), 7.83 (d, *J* = 8.2 Hz, 4H, $H^{f,h}$), 7.65 (t, *J* = 8.2 Hz, 2H, H^4), 7.58 (d, *J* = 7.2 Hz, 2H, H^j), 7.46 (t, *J* = 7.2 Hz, 2H, H^i), 7.37 (t, *J* = 8.6 Hz, 2H, H^e), 7.33 (d, *J* = 8.8 Hz, 2H, $H^{2'}$), 7.22 – 7.17 (m, 4H, $H^{5,d}$), 7.14 (d, *J* = 8.3 Hz, 2H, H^3), 6.98 (d, *J* = 8.6 Hz, 2H, $H^{3'}$), 3.86 (s, 3H, H^{-Me}). ^{13}C{^{1}H} NMR (175 MHz, $CDCl_3$) δ = 157.8, 157.8, 157.7, 138.4, 138.1, 137.7, 134.0, 131.2, 129.9, 128.8, 128.1, 127.7, 126.3, 126.0, 125.7, 125.3, 118.9, 115.1, 114.7, 55.6. HRMS (ES+) *m/z* = 530.2226 ($M+H^+$) calcd for $C_{37}H_{28}N_3O$ *m/z* = 530.2232. Mp ≥ 113 °C.

N-(4-methoxyphenyl)-6-(naphthalen-2-yl)-N-(6-(naphthalen-2-yl)pyridin-2 yl)pyridin-2-amine, L^4H_2

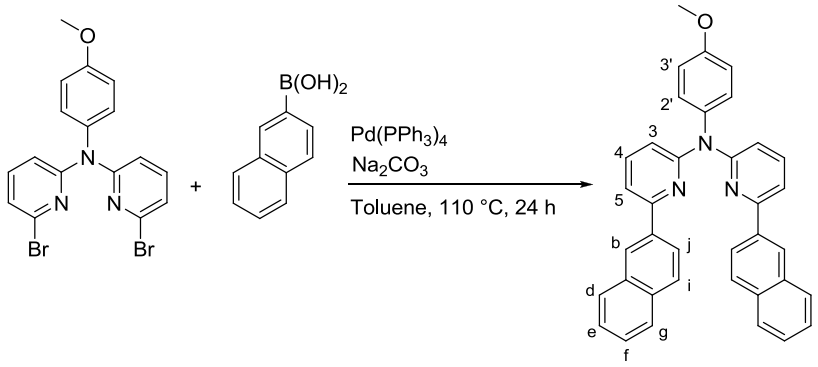

Ligand **L^4H_2** was prepared *via* the Suzuki-Miyaura cross-coupling methodology. Precursor **1** (0.23 g, 0.535 mmol) 2-naphthaleneboronic acid (0.28 g, 1.60 mmol), sodium carbonate (0.57 g, 5.35 mmol) and tetrakis(triphenylphosphine) palladium, $Pd(PPh_3)_4$ (0.05 g, 0.043 mmol). The crude product was purified with column chromatography on silica gel (hexane/ ethyle acetate 7:3) to give a white powder (0.16 g, 55 %). R_f = 0.81 (silica, 100 % DCM). ^{1}H NMR (700 MHz, $CDCl_3$) δ = 8.40 (s, 2H, H^b), 8.04 (d, *J* = 8.5 Hz, 2H, H^j), 7.81 (m, 6H, $H^{d,g,i}$), 7.68 (t, *J* = 7.9 Hz, 2H, H^4), 7.55 (d, *J* = 7.9 Hz, 2H, H^5), 7.45 (m, 4H, $H^{e,f}$), 7.35 (d, *J* = 9.1 Hz, 2H, $H^{2'}$), 7.10 (d, *J* = 8.0 Hz, 2H, H^3), 7.02 (d, *J* = 9.1 Hz, 2H, $H^{3'}$), 3.90 (s, 3H, H^{-Me}). ^{13}C{^{1}H} NMR (175 MHz, $CDCl_3$) δ = 132.7, 132.5, 129.1, 127.7, 127.3, 126.7, 125.2, 123.6, 113.6, 54.7. HRMS (ES+) *m/z* = 530.2238 ($M+H^+$) calcd for $C_{37}H_{28}N_3O$ *m/z* = 530.2232. Mp ≥ 151 °C.

6-(3,5-bis(trifluoromethyl)phenyl)-N-(6-(3,5-bis(trifluoromethyl) phenyl)pyridin-2-yl)-N-(4-methoxyphenyl)pyridin-2-amine, L^5H_2

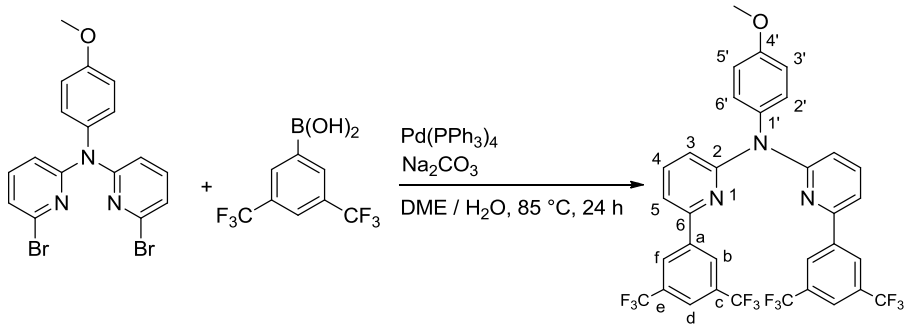

Ligand $\mathbf{L^5H_2}$ was prepared *via* the Suzuki-Miyaura cross-coupling methodology. Precursor **1** (0.23 g, 0.535 mmol), 3,5-*bis*(*tri*fluoromethyl)phenylboronic acid (0.41 g, 1.60 mmol), sodium carbonate (0.57 g, 5.35 mmol) and tetrakis(triphenylphosphine) palladium, $Pd(PPh_3)_4$ (0.05 g, 0.043 mmol). The crude product was purified with column chromatography on silica gel (hexane/ DCM 7:2) to give a white powder (0.19 g, 51 %). R_f = 0.66 (silica, 50 % DCM, 50 % hexane). ^{1}H NMR (700 MHz, $CDCl_3$) δ = 8.32 (s, 4 H, $H^{f,\,b}$), 7.82 (s, 2 H, H^d), 7.68 (m, 2 H, H^4), 7.48 (d, *J* = 8.3 Hz, 2 H, H^5), 7.30 (d, *J* = 8.9 Hz, 2 H, $H^{2',6'}$), 7.22 (d, *J* = 8.3 Hz, 2 H, H^3), 7.05 (d, *J* = 8.9 Hz, 2 H, $H^{3',5'}$), 3.89 (s, 3 H, H^{-Me}). $^{13}C\{^1H\}$ NMR (175 MHz, $CDCl_3$) δ = 158.8 ($C^{4'}$), 157.4 (C^2), 151.5 (C^a), 141.1, 138.4 (C^4), 136.5, 132.0 (C^{CF_3}), 131.9 (C^{CF_3}), 130.4 ($C^{2',\,6'}$), 126.7 ($C^{f,b}$), 124.3 (C^e), 122.7 (C^c), 122.2 (C^d), 115.9 (C^5), 115.3 ($C^{3',5'}$), 113.9 (C^3), 55.7 (C^{-Me}). HRMS (ES+) *m/z* = 702.1414 ($M+H^+$) calcd for $C_{33}H_{20}F_{12}N_3O$ *m/z* = 702.1415. Mp ≥ 198 °C.

6-(2,4-difluorophenyl)-N-(6-(2,4-difluorophenyl)pyridin-2-yl)-N-(4-methoxyphenyl)pyridin-2-amine, L^6H_2

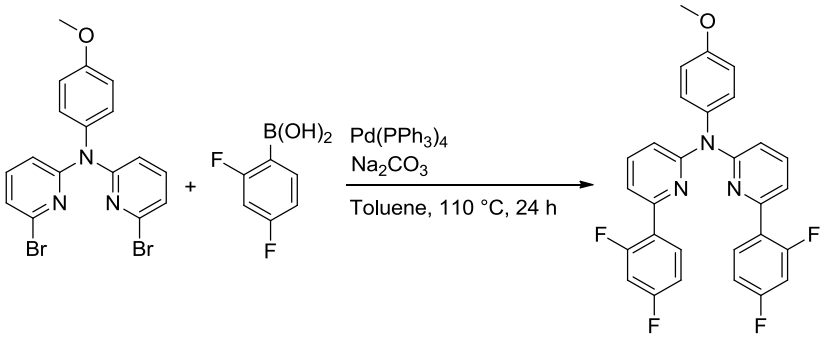

Ligand $\mathbf{L^6H_2}$ was prepared *via* the Suzuki-Miyaura cross-coupling methodology. Precursor **1** (0.35 g, 0.795 mmol) 3,5-*bis*(*tri*fluoromethyl)phenylboronic acid (0.38 g, 2.38 mmol), sodium carbonate (0.84 g, 7.95 mmol) and tetrakis(triphenylphosphine) palladium, $Pd(PPh_3)_4$ (0.07 g, 0.06 mmol). The crude product was purified with column chromatography on silica gel (dichloromethane) to give a yellow powder (0.30 g, 75 %). R_f = 0.5 (silica, 100 % DCM). ^{1}H NMR (400 MHz, $CDCl_3$) δ = 7.79 (td, *J* = 9.1, 6.8 Hz, 1H), 7.66 – 7.58 (m, 1H), 7.47 – 7.41 (m, 1H), 7.27 – 7.22 (m, 1H), 7.02 (dd, *J* = 8.2, 0.5 Hz, 1H), 7.00 – 6.94 (m, 1H), 6.90 – 6.80 (m, 2H). $^{13}C\{^1H\}$ NMR (101 MHz, $CDCl_3$) δ = 157.8, 157.5, 150.1, 137.7, 137.4, 132.1, 132.0, 129.6, 117.8, 117.7, 114.9, 114.8, 111.7, 111.5, 104.4, 104.2, 103.9. HRMS (ES+) *m/z* = 502.1530 ($M+H^+$) calcd for $C_{29}H_{19}F_4N_3O$ *m/z* = 502.1543. Mp ≥ 127 °C.

N-(4-methoxyphenyl)-6-(thiophen-2-yl)-N-(6-(thiophen-2-yl)pyridin-2-yl)pyridin-2-amine, L^7H_2

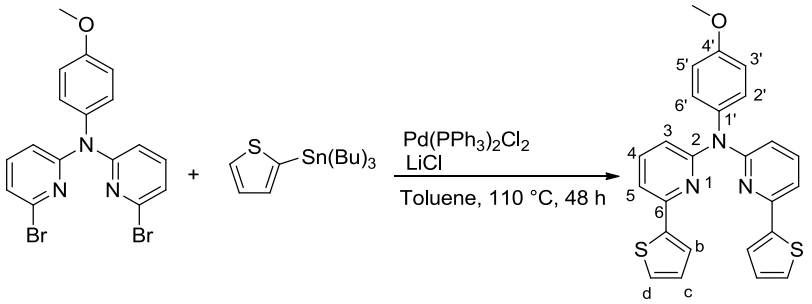

Ligand $\mathbf{L^7H_2}$ was prepared *via* the Stille cross-coupling methodology. Reagents: Precursor **1** (0.25 g, 0.57 mmol), 2-*tri*-n-butylstannylthiophene (0.54 g, 1.44 mmol) and *bis*(*tri*phenylphosphine)palladium dichloride {$Pd(PPh_3)_2Cl_2$} (0.03 g, 0.04 mmol). Purification: The crude product was purified with column chromatography on silica gel (hexane/ ethyl acetate, 70:30) to give a white powder (0.16 g, 63 %). R_f = 0.59 (silica, 100 % DCM). ^{1}H NMR (700 MHz, $CDCl_3$) δ = 7.54 (t, *J* = 7.9 Hz, 2H, H^4), 7.47 (d, *J* = 3.4 Hz, 2H, H^b), 7.27 (m, 4H, $H^{2',6',d}$), 7.23 (d, *J* = 7.9 Hz, 2H, H^5), 7.03 (m, 4H, $H^{3,c}$), 6.99 (d, *J* = 8.7 Hz, 2H, $H^{3',5'}$), 3.87 (s, 3H, H^{-Me}). ^{13}C{^{1}H} NMR (175 MHz, $CDCl_3$) δ = 158.1 ($C^{4'}$), 157.0 (C^6), 150.5 (C^2), 145.7 (C^a), 137.7 (C^4), 137.1 ($C^{1'}$), 130.5 (C^d), 127.9 (C^3), 127.2 ($C^{2',6'}$), 124.2 (C^b), 114.8 ($C^{3',5'}$), 114.1 (C^c), 111.9 (C^5), 55.6 (C^{-Me}). HRMS (ES+) *m/z* = 442.1033 ($M+H^+$) calcd for $C_{25}H_{19}N_3OS_2$ *m/z* = 442.1040.1920 Mp ≥ 137 °C.

6-(benzo[b]thiophen-2-yl)-N-(6-(benzo[b]thiophen-2-yl)pyridin-2-yl)-N-(4 methoxyphenyl)pyridin-2-amine, L^8H_2

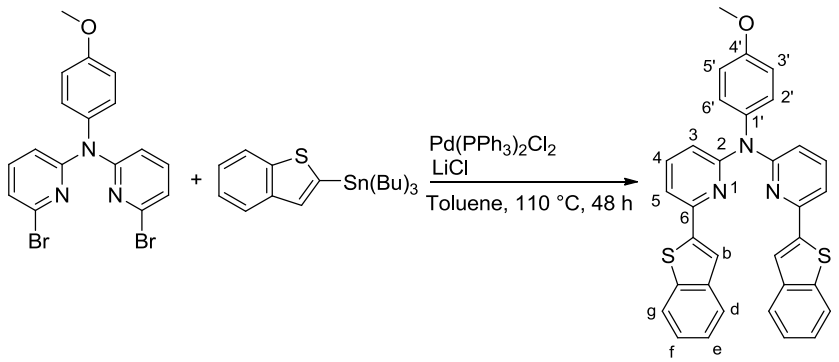

Ligand $\mathbf{L^8H_2}$ was prepared *via* the Stille cross-coupling methodology. Reagents: Precursor **1** (0.25 g, 0.57 mmol), 2-*tri*-n-butylstannylbenzothiophene (0.61 g, 1.44 mmol) and *bis*(*tri*phenylphosphine)palladium dichloride {$Pd(PPh_3)_2Cl_2$} (0.03 g, 0.04 mmol). Purification: The crude product was purified with column chromatography on silica gel (hexane/ ethyl acetate, 70:30) to give a white powder (0.24 g, 79 %). R_f = 0.34 (silica, 50 % DCM, 50 % hexane). ^{1}H NMR (700 MHz, $CDCl_3$) δ = 7.78 (d, *J* = 8.3 Hz, 2H, H^d), 7.74 (m, 4H, $H^{b,g}$), 7.63 (t, *J* = 7.9 Hz, 2H, H^4), 7.41 (d, *J* = 7.9 Hz, 2 H, H^5), 7.33-7.28 (m, 6H, $H^{e,f,2',6'}$), 7.13 (d, *J* = 7.9 Hz, 2 H, H^3), 7.04 (d, *J* = 8.7 Hz, 2 H, $H^{3',5'}$), 3.91 (s, 3 H, H^{-Me}). ^{13}C {^{1}H} NMR (175 MHz, $CDCl_3$) δ = 158.3, 157.0, 150.4, 145.6, 140.9, 140.7, 137.8, 136.8, 130.6, 124.8, 124.4, 124.1, 122.6, 120.8, 115.0, 114.9, 113.0, 55.7 (C^{-Me}). HRMS (ES+) *m/z* = 542.1361 ($M+H^+$) calcd for $C_{33}H_{24}N_3OS_2$ *m/z* = 542.1354. Mp ≥ 201 °C.

N-(benzo[h]quinolin-2-yl)-N-(4-methoxyphenyl)benzo[h]quinolin-2-amine, L^9H_2

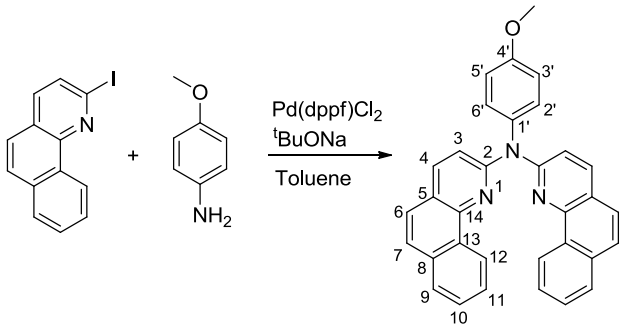

Ligand $\mathbf{L^9H_2}$ was prepared *via* the Buchwald-Hartwig Amination methodology. Reagents: *p*-anisidine (0.07 g, 0.584 mmol), 2-iodobenzoquinolone (0.39 g, 1.28 mmol), sodium *tert*-

butoxide (0.13 g, 1.35 mmol), and Pd(dppf)Cl_2 (0.02 g, 0.0292 mmol). Purification: The crude oil was purified with column chromatography on silica gel (hexane / dichloromethane, 5:5), to give a white powder (0.09 g, 31 %). R_f = 0.62 (silica, 100 % DCM).^{1}H NMR (700 MHz, $CDCl_3$) δ = 8.83 (d, *J* = 8.3 Hz, 2 H, H^{12}), 8.07 (d, *J* = 8.6 Hz, 2 H, H^4), 7.86 (d, *J* = 8.3 Hz, 2 H, H^9), 7.71 (d, *J* = 8.7 Hz, 2 H, H^6), 7.67 (d, *J* = 8.7 Hz, 2 H, H^7), 7.60 (t, *J* = 8.3 Hz, 2 H, H^{10}), 7.50 (m, 4 H, $H^{11,3}$), 7.41 (d, *J* = 8.9 Hz, 2 H, $H^{2',6'}$), 7.07 (d, *J* = 8.9 Hz, 2 H, $C^{3',5'}$), 3.93 (s, 3 H, C^{-Me}). ^{13}C {^{1}H} NMR (175 MHz, $CDCl_3$) δ = 158.3, 156.0, 144.9, 137.0, 134.0, 131.0, 130.4, 127.9, 127.6, 126.6, 125.5, 125.0, 124.7, 122.6, 116.5, 115.0, 55.7. HRMS (ES+) *m/z* = 478.1930 ($M+H^+$) calcd for $C_{33}H_{24}N_3O$ *m/z* = 478.1920. Mp ≥ 250 °C.

SYNTHESIS OF TETRADENTATE PLATINUM COMPLEXES

PtL^1

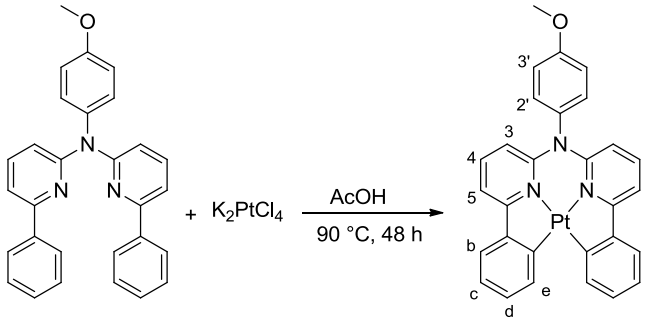

The complex was prepared *via* procedure **1**. **L^1H_2** (0.28 g) (Crystallization was performed by slow diffusion of DCM into DMF. (0.14 g, 33 %). ^{1}H NMR (600 MHz, $CDCl_3$) δ = 8.42 (d, *J* = 7.4 Hz, 2H, H^e), 7.80 (d, *J* = 7.4 Hz, 2H, H^b), 7.71 (t, *J* = 8.7 Hz, 2H, H^4), 7.61 (d, *J* = 8.7 Hz, 2H, H^5), 7.46 (t, *J* = 7.4 Hz, 2H, H^d), 7.31 (d, J = 8.7 Hz, 2H, $H^{2'}$), 7.23 (t, J = 7.4 Hz, 2H, H^c), 7.18 (d, J = 8.7 Hz, 2H, $H^{3'}$), 6.53 (d, *J* = 8.7 Hz, 2H, H^3), 3.96 (s, 3H, H^{-Me}). ^{13}C {^{1}H} NMR (151 MHz, $CDCl_3$) δ = 164.3 (C^2), 160.2 ($C^{4'}$), 149.1 (C^6), 148.8 (C^f), 147.0 (C^a), 136.9 (H^4), 136.1 (H^e), 136.0 ($C^{1'}$), 131.5 ($H^{2'}$), 129.5 (H^d), 123.9 (H^b), 123.4 (H^c), 116.7 ($H^{3'}$), 113.9 (H^3), 111.8 (H^5), 55.8 (C^{-Me}). HRMS (AP+) *m/z* = 622.100 (M) calcd for $C_{29}H_{21}N_3OPt$ *m/z* = 622.130. Mp ≥ 250 °C.

PtL^1ClCN

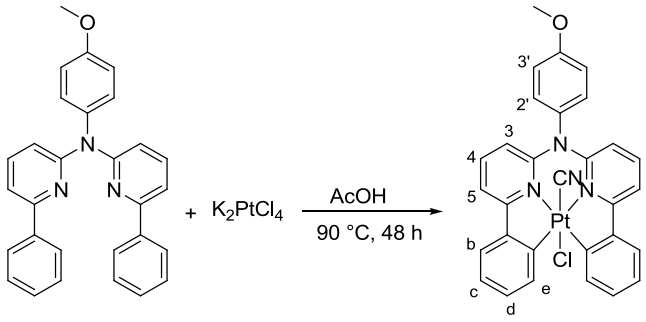

The complex was prepared *via* procedure **1**. $\mathbf{L^1H_2}$ (0.28 g) Crystallization was performed by slow diffusion of hexane into DCM unexpectedly yielding the Pt(IV) complex (0.056 g, 20 %). ^{1}H NMR (700 MHz, DMSO-d6) δ = 8.29 (d, *J* = 7.9 Hz, 2H, H^e), 8.12 (d, *J* = 7.9 Hz, 2H, H^b), 8.11 (d, *J* = 8.6 Hz, 4H, H^5), 7.98 (t, *J* = 7.9 Hz, 2H, H^d), 7.62 (d, *J* = 8.5 Hz, 2H, $H^{2'}$), 7.44 (t, *J* =, 2H, H^5), 7.33 – 7.23 (m, 4H, H^c), 6.86 (d, *J* = 8.6 Hz, 2H, H^3), 3.89 (s, 3H, H^{-Me}). ^{13}C{^{1}H} NMR (176 MHz, DMSO-d6) δ = 163.4, 159.6, 151.4, 146.4, 139.9, 138.7, 135.7, 135.3, 131.7, 129.6, 125.5, 124.1, 116.4, 114.9, 114.1, 55.6.

PtL^2Cl_2

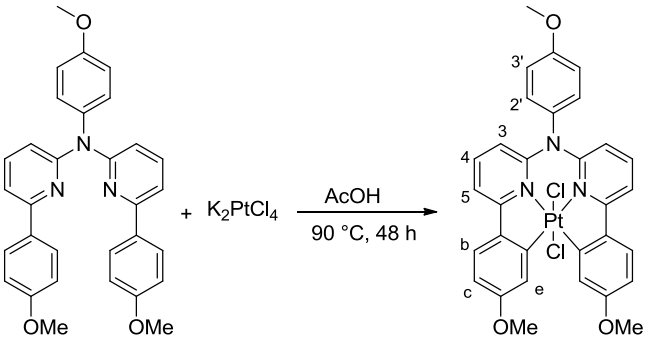

The complex was prepared via procedure **1**. $\mathbf{L^2H_2}$ (0.32 g) The product was dissolved in DCM for crystallization by slow diffusion of hexane into DCM (0.11 g, 22 %). ^{1}H NMR (700 MHz, $CDCl_3$) δ = 7.79 (d, *J* = 8.7 Hz, 2H, H^b), 7.71 (d, *J* = 2.4 Hz, 2H, H^e), 7.69 – 7.62 (m, 4H, $H^{4,5}$), 7.42 (d, *J* = 8.8 Hz, 2H, $H^{2'}$), 7.19 (d, *J* = 8.8 Hz, 2H, $H^{3'}$), 6.89 – 6.85 (dd, *J* = 8.7, 2.4, 2H, H^c), 6.57 (d, *J* = 8.0 Hz, 2H), 4.03 (s, 6H), 3.95 (s, 3H, H^3). HRMS (AP+) *m/z* = 751.0910 (M) calcd for $C_{31}H_{25}Cl_2N_3O_3Pt$ *m/z* = 751.0900. Mp ≥ 250 °C.

Attempted complexation of Pt(II) to L^5H_2, VI

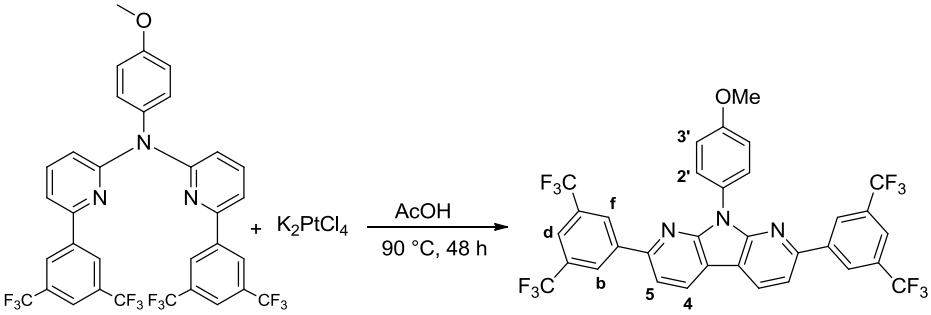

The attempted complexation of platinum(II) to L^5H_2 (0.46 g) using procedure **1** led to the unexpected organic product shown above, as a green solid (0.39 g, 85 %).^{1}H NMR (700 MHz, $CDCl_3$) δ = 8.61 (s, 4H, $H^{f,b}$), 8.54 (d, *J* = 8.0 Hz, 2H, H^5), 7.94 (d, *J* = 8.9 Hz , 2H, $H^{2'}$), 7.87 (m, 4H, $H^{d,4}$), 7.21 (d, *J* = 8.9 Hz, 2H, $H^{3'}$), 3.98 (s, 3H, H^{-Me}). ^{13}C {^{1}H} NMR (176 MHz, $CDCl_3$) δ = 158.8, 152.0, 151.8, 141.4, 132.5, 132.3, 132.1, 131.9, 130.3, 128.3, 128.1, 127.5, 127.2, 125.8, 124.3, 122.7, 122.5, 121.2, 115.7, 114.2, 114.1, 114.1, 55.7. HRMS (ES+) *m/z* = 700.1239 ($M+H^+$) calcd for $C_{33}H_{18}N_3OF_{12}$ *m/z* = 700.1258.

PtL^3Cl_2

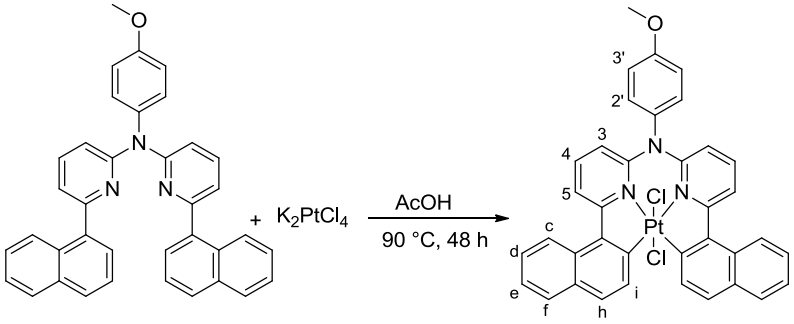

The complex was prepared *via* procedure **1**. **L^3H_2** (0.35 g) The yellow solid was dried under reduced pressure. Crystallization was performed by slow diffusion of hexane into DCM (0.16 g, 31 %). ^{1}H NMR (700 MHz, $CDCl_3$) δ = 8.57 (d, *J* = 8.7 Hz, 2H, H^c), 8.48 (d, *J* = 8.5 Hz, 2H, H^i), 8.22 (d, *J* = 8.1 Hz, 2H, H^5), 8.06 – 7.99 (m, 4H, $H^{f,\ h}$), 7.80 (t, J = 8.1 Hz, 2H, H^4), 7.59 (t, *J* = 7.2 Hz, 2H, H^d), 7.49-7.44 (m, 4H, $H^{2',\ e}$), 7.23 (d, *J* = 8.8 Hz, 2H, $H^{3'}$), 6.73 (d, *J* = 8.6 Hz, 2H, H^3), 3.98 (s, 3H, H^{-Me}). ^{13}C{^{1}H} NMR (176 MHz, $CDCl_3$) δ = 162.3 (C^2), 160.5 ($C^{4'}$), 152.4 (C^6), 139.8 (C^4), 137.9 (C^a), 137.4 (C^j), 136.1 ($C^{1'}$), 133.4 (C^i), 131.5($C^{2'}$), 131.2 (C^h), 130.5 (C^b), 129.6 (C^f), 127.1 (C^g), 126.2 (C^d), 124.9 (C^e), 123.7 (C^c), 119.8 (C^5), 116.9

($C^{3'}$), 114.6 (C^{3}), 55.9 (C^{-Me}). HRMS (AP+) *m/z* = 722.1702 ($M-2Cl^-$) calcd for $C_{37}H_{26}N_3OPt$ *m/z* = 722.1703. Mp ≥ 250 °C.

PtL^4

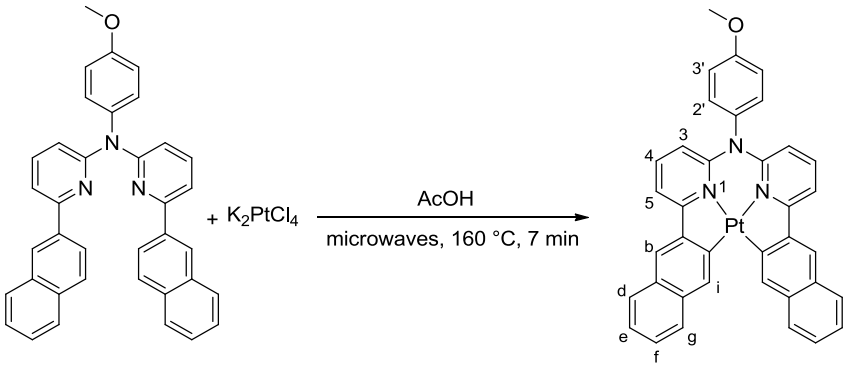

Ligand $\mathbf{L^4H_2}$ (0.35 g, 0.66 mmol), K_2PtCl_4 (0.30 g, 0.72 mmol), and acetic acid (3 mL) were introduced to a microwave cell. The reaction mixture was degassed with three freeze-pump-thraw, and heated at 160 °C for 30 min in a microwave. The reaction was quenched with water (5 mL), and the precipitate was collected and washed with Et_2O (5 × 5 mL) by centrifugation. The red solid was dried under reduced pressure and crystallized by slow diffusion of hexane into DCM (0.36 g, 75 %). NMR (700 MHz, $CDCl_3$) δ = 8.78 (s, 2H, H^i), 8.21 (s, 2H, H^b), 8.02 (d, *J* = 7.9 Hz, 2H, H^d), 7.88 (d, *J* = 7.9 Hz, 2H, H^g), 7.72 (d, *J* = 7.7 Hz, 2H, H^5), 7.64 (t, *J* = 7.7 Hz, 2H, H^4), 7.52 (t, *J* = 7.5 Hz, 2H, H^e), 7.40 (t, *J* = 7.5 Hz, 2H, H^f), 7.24 (d, *J* = 8.6, 2H, $H^{2'}$), 7.09 (d, *J* = 8.6, 2H, $H^{3'}$), 6.43 (d, *J* = 7.7 Hz, 2H, H^3), 3.92 (s, 3H, H^{-Me}). ^{13}C {^1H} NMR (175 MHz, $CDCl_3$) δ = 163.6, 149.5, 146.9, 143.3, 135.2, 133.9, 133.8, 131.2, 130.0, 127.0, 127.4, 122.9, 122.8, 116.8, 116.3, 114.3, 114.0, 55.6. HRMS (AP+) *m/z* 722.1701 ($M+H^+$) calcd for $C_{37}H_{26}N_3OPt$ *m/z* = 722.1703. Mp ≥ 250 °C.

PtL^7

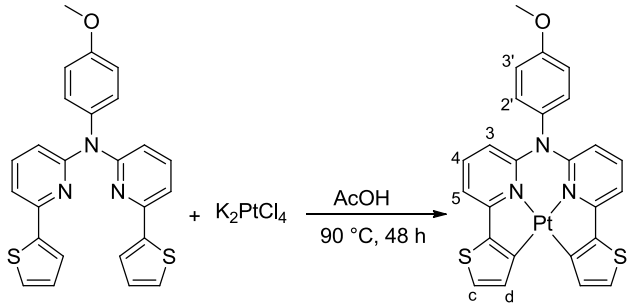

The complex was prepared via procedure **1**. $\mathbf{L^7H_2}$ (0.29 g) Crystallization was performed by slow diffusion of hexane into DCM. (0.22 g, 52 %). NMR (700 MHz, CD_2Cl_2) δ = 7.72 (m, 4H, $H^{4,d}$), 7.60 (d, *J* = 4.6 Hz, 2H, H^c), 7.35 (m, 4H, $H^{2',5}$), 7.21 (d, *J* = 8.7 Hz, 2H, $H^{3'}$), 6.46 (d, *J* = 8.5 Hz, 2H, H^3), 3.95 (s, 3H, H^{-Me}). ^{13}C {^1H} NMR (176 MHz, CD_2Cl_2) δ = 160.7 ($C^{4'}$), 158.9 (C^2), 152.8 (C^a), 148.6 (C^6), 142.3 (C^e), 137.6 (C^d), 135.7 (C^4), 135.6 ($C^{1'}$), 131.7 ($C^{2'}$), 128.5 (C^c), 116.8 ($C^{3'}$), 112.7 (C^3), 111.1 (C^5), 56.1 (C^{-Me}). HRMS (AP+) *m/z*= 634.0526 ($M+H^+$) calcd for $C_{25}H_{18}N_3OPtS_2$ *m/z* = 634.0518. Mp ≥ 250 °C.

PtL^7Cl_2

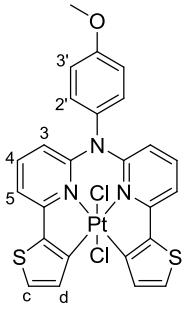

$\mathbf{PtL^7Cl_2}$ was obtained by irradiation of $\mathbf{PtL^7}$ with light at 298 K in $CDCl_3$. ^1H NMR (400 MHz, $CDCl_3$) δ = 7.75 – 7.57 (m, 6H, $H^{c,d,4}$), 7.44 (m, 4H, $H^{2',5}$), 7.21 (d, *J* = 9.0 Hz, 2H, $H^{3'}$), 6.45 (d, 2H, H^3), 3.97 (s, 3H, H^{-Me}).

PtL^8

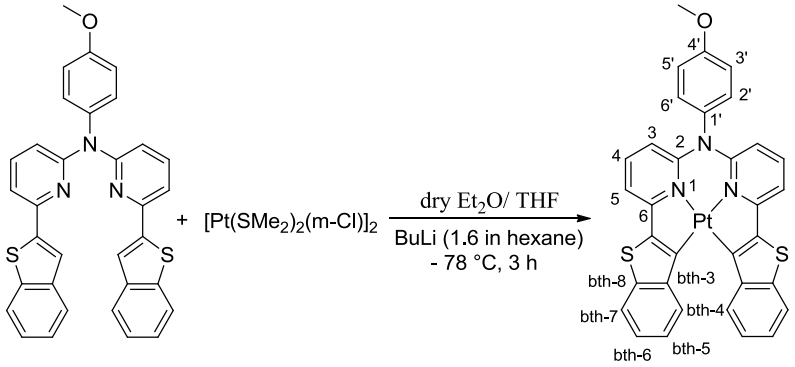

A mixture of dry Et_2O and THF (2 mL of each) was added to a mixture of $\mathbf{L^8H_2}$ (0.03 g, 0.0564 mmol) and $[Pt(\mu\text{-}Cl)(SMe_2)_2]_2$ (0.02 g, 0.0282 mmol). The reaction was cooled to –10 °C under nitrogen pressure. BuLi (1.6 M in hexane, 4 eq) was added dropwise to the solution and the reaction was allowed to warm to room temperature after 30 min at -10 °C. The reaction mixture was quenched with water (5 mL), and the precipitate was collected by centrifugation. Crystallization was performed by slow diffusion of hexane into DCM. (0.01 g, 20 %). ^{1}H NMR (700 MHz, $CDCl_3$) δ = 8.10 (d, *J* = Hz, 2H), 7.89 (d, *J* = Hz, 2H), 7.74 (t, *J* = Hz, 2H), 7.41 (d, *J* = Hz, 2H), 7.29 (m, *J* = 8.0 Hz, 4H, H-ph), 7.19 (t, *J* = Hz, 2H), 7.09 (t, *J* = Hz, 2H), 7.44 (d, 2H), 3.96 (s, 2H, -CH_3). ^{13}C{^{1}H} NMR (175 MHz, $CDCl_3$) δ = 158.3, 156.9, 150.4, 145.4, 140.9, 140.7, 137.8, 136.8, 130.6, 124.8, 124.4, 124.1, 122.6, 120.8, 115.0, 114.9, 113.0, 55.7 (C^{-Me}). HRMS (ES+) *m/z* = 542.1361 ($M+H^+$) calcd for $C_{33}H_{24}N_3OS_2$ *m/z* = 542.1354. Mp ≥ 250 °C.

PtL^8Cl_2

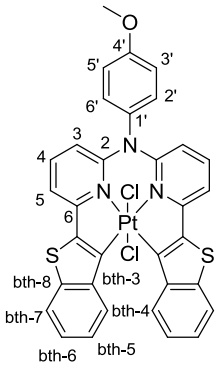

Irradiation of $\mathbf{PtL^8}$ with light at 298 K in $CDCl_3$. ^{1}H NMR (700 MHz, $CDCl_3$) δ = 7.68 (d, J = Hz, 2 H, H-), 7.61-7.66 (m, 2 H, H-), 7.42 (m, 2 H, H-), 7.20 (d, J = Hz, 2 H, H-), 6.44 (d, J = 8.0 Hz, 4 H, H-ph), 3.96 (s, 3H, H^{-Me}). Mp ≥ 250 °C.

PtL[9]

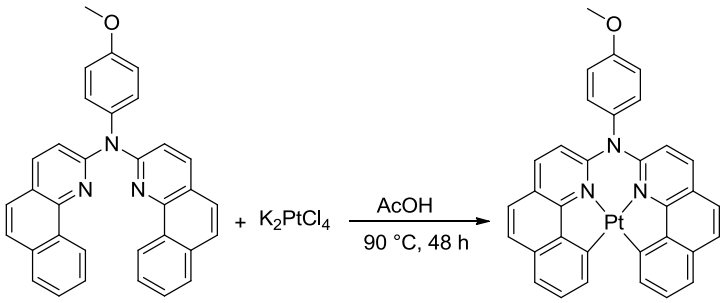

Ligand **L[9]H$_2$** (0.32 g, 0.66 mmol), K_2PtCl_4 (0.30 g, 0.72 mmol), and acetic acid (3 mL) were introduced to a microwave cell. The reaction mixture was degassed with three freeze-pump-thaw cycles, and heated at 160 °C for 30 min in a microwave. The reaction was quenched with water (5 mL), and the precipitate was collected and washed with Et_2O (5 x 5 mL) by centrifugation. The brown solid was dried under reduced pressure. Crystallization was performed by slow diffusion of DCM into DMF. (0.13 g, 30 %). HRMS (AP+) *m/z*= 668.1363 ($M+H^+$) calcd for $C_{33}H_{22}N_3OPt$ *m/z* = 668.1373. Mp ≥ 250 °C. The product was too insoluble to have correct NMR spectroscopies.

SYNTHESIS OF TETRADENTATE PALLADIUM COMPLEXES

PdL[1]

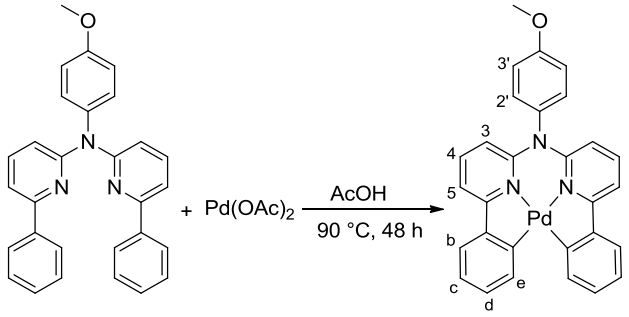

The complex was prepared *via* procedure **2**. **L[1]H$_2$** (0.09 g) Crystallization was performed by slow diffusion of DCM into DMF. (0.06 g, 60 %). ^{1}H NMR (400 MHz, $CDCl_3$) δ = 8.26 (d, *J*

= 7.6 Hz, 2H, H^e), 7.75 (d, *J* = 7.6 Hz, 2H, H^b), 7.60 – 7.55 (m, 4H, $H^{4, 5}$), 7.41 (td, *J* = 7.6, 1.1 Hz, 2H, H^d), 7.27 (m, 2H, $H^{2'}$), 7.21 (t, *J* = 7.6 Hz, 2H, H^c), 7.15 (d, *J* = 8.7 Hz, 2H, $H^{3'}$), 6.36 (d, *J* = 7.5 Hz, 2H, H^3), 3.93 (s, 3H, H^{-Me}).$^{13}C\{^1H\}$ NMR (101 MHz, $CDCl_3$) δ = 163.3 (C^2), 160.6 ($C^{4'}$), 160.1 (C^6), 151.6 (C^f), 147.8 (C^a), 138.0 (C^4), 136.3 (C^e), 135.9 ($C^{1'}$), 131.5 ($C^{2'}$), 129.3 (C^d), 123.9 (C^b), 123.9 (C^c), 116.6 ($C^{3'}$), 113.6 (C^3), 111.7 (C^5), 55.84 (C^{-Me}). HRMS (AP+) *m/z* =532.0803 ($M+H^+$) calcd for $C_{29}H_{21}N_3OPd$ *m/z* = 532.0803. Mp ≥ 250 °C.

PdL^6

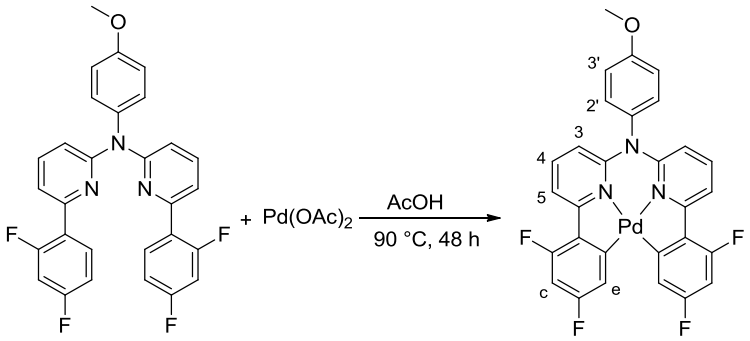

The complex was prepared via procedure **2**. $\mathbf{L^6H_2}$ (0.10 g) Crystallization was performed by slow diffusion of DCM into DMF. (0.08 g, 67 %). ^1H NMR (700 MHz, CD_2Cl_2) δ = 7.91 (d, *J* = 8.5 Hz, 2 H, H^5), 7.68 (t, *J* = 8.5 Hz, 2 H, H^4), 7.55 (dd, *J* = 8.2, 2.4 Hz, 2 H, H^e), 7.29 (d, *J* = 8.7 Hz, 2 H, $H^{2'}$), 7.19 (d, *J* = 8.7 Hz 2 H, $H^{3'}$), 6.71 – 6.62 (m, 2 H, H^c), 6.50 (d, *J* = 8.5 Hz, 2 H, H^3), 3.94 (s, 3 H, H^{Me}). $^{13}C\{^1H\}$ NMR (176 MHz, CD_2Cl_2) δ = 166.9 (C^f), 160.7 ($C^{4'}$), 159.5 (C^6), 151.8 (C^2), 139.1 (C^4), 135.9 ($C^{1'}$), 131.6 ($C^{2'}$), 130.5 (C^a), 117.8 (d, *J* = 16.2 Hz, C^e), 117.0 ($C^{3'}$), 116.1 (d, *J* = 21.8 Hz, C^5), 114.6 (C^3), 100.4 (t, *J* = 27.2 Hz, C^c), 56.1 (C^{-Me}). HRMS (AP+) *m/z* = 603.0366 (M) calcd for $C_{29}H_{17}F_4N_3OPd$ *m/z* = 603.0348. Mp ≥ 250 °C.

PdL^7

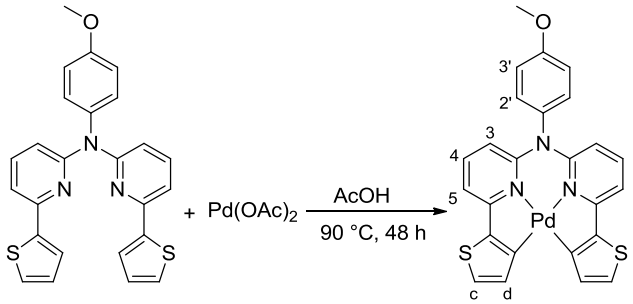

The complex was prepared *via* procedure **2**. $\mathbf{L^7H_2}$ (0.09 g) Crystallization was performed by slow diffusion of DCM into DMF. (0.06 g, 52 %). ^{1}H NMR (700 MHz, CD_2Cl_2) δ = 7.64 (d, *J* = 4.7 Hz, 2H, H^d), 7.59 (td, *J* = 8.7, 7.6 Hz, 2H, H^4), 7.53 (d, *J* = 4.7 Hz, 2 H, H^c), 7.32 (d, *J* = 8.7 Hz, 2 H, $H^{2'}$), 7.28 (d, *J* = 7.6 Hz, 2 H, H^5), 7.19 (d, *J* = 8.7 Hz, 2 H, $H^{3'}$), 6.29 (d, *J* = 8.7 Hz, 2 H, H^3), 3.94 (s, 3 H, H^{-Me}). $^{13}C\{^1H\}$ NMR (176 MHz, CD_2Cl_2) δ = 162.9 (C^e), 160.6 ($C^{4'}$), 158.4 (C^6), 151.2 (C^2), 141.6 (C^a), 138.7 (C^4), 135.4 (C^d), 135.3 ($C^{1'}$), 131.7 ($C^{2'}$), 127.0 (C^c), 116.8 ($C^{3'}$), 112.2 (C^3), 111.1 (C^5), 56.1 (C^{-Me}). HRMS (ES+) *m/z* = 541.9947 ($M+H^+$) calcd for $C_{25}H_{18}N_3OS_2Pd$ *m/z* = 541.9968. Mp ≥ 250 °C.

PdL^9

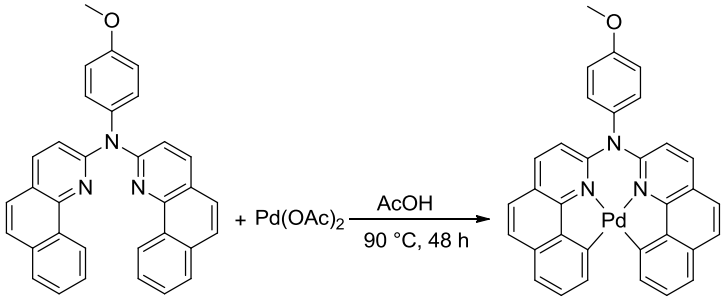

The complex was prepared *via* procedure **2**. $\mathbf{L^9H_2}$ (0.10 g) Crystallization was performed by slow diffusion of DCM into DMF. (0.02 g, 15 %). HRMS (AP+) *m/z* = 580.0820 ($M+H^+$) calcd for $C_{33}H_{22}N_3OPd$ *m/z* = 580.0803. Mp ≥ 250 °C.

SYNTHESIS OF TETRADENTATE MERCURIC COMPLEXES

HgL^7

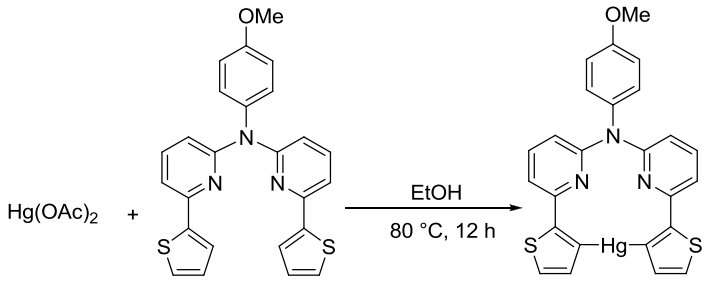

The complex was prepared *via* procedure **3**. Yellow powder (Yield = 45 %). ^{1}H NMR (400 MHz, DMSO) δ = 7.81 (d, *J* = 3.6 Hz, 2 H), 7.69 (t, *J* = 7.9 Hz, 2 H), 7.43 (d, *J* = 7.6 Hz, 2 H), 7.21 (d, *J* = 8.9 Hz, 2 H), 7.04 (dd, *J* = 10.7, 6.3 Hz, 4 H), 6.89 (d, *J* = 8.2 Hz, 2 H), 3.81 (s, 3 H). ^{13}C{^{1}H} NMR (176 MHz, dmso-d_6) δ = 157.3, 156.7, 156.6, 150.8, 150.4, 147.7, 138.3, 136.6, 136.5, 135.5, 129.6, 124.6, 114.7, 113.8, 112.2, 55.2. HRMS (AP+) *m/z* = 637(M) calcd for $C_{29}H_{17}F_4N_3OPd$ *m/z* = 603.0348. Mp ≥ 250 °C.

8. Experimental details for Chapter Four

$[Ir(\mu\text{-}Cl)(ppy)_2]_2$

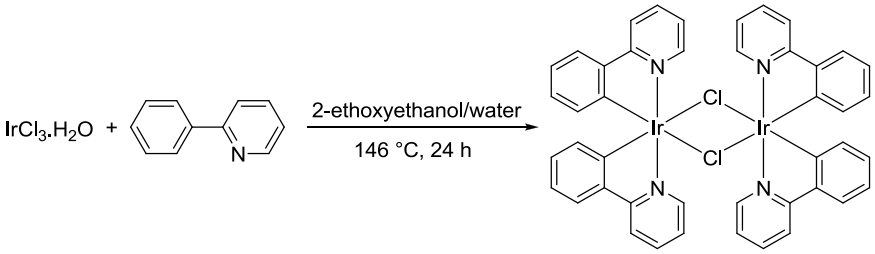

In a Schlenk tube, a suspension of 2-phenylpyridine (0.65 g, 4.18 mmol) and iridium trichloride hydrate (0.50 g, 1.67 mmol) in a mixture of 2-ethoxyethanol (12 mL) and water (4 mL) was heated for 24 h at 146 °C. After cooling to room temperature, the precipitate was collected via centrifugation and washed with EtOH (2 × 10 mL) and Et_2O (2 × 10 mL). The product was dried under vacuum to give a yellow powder (0.71 g, 79 %).

$[Pt(\mu\text{-}Cl)(ppy)]_2$

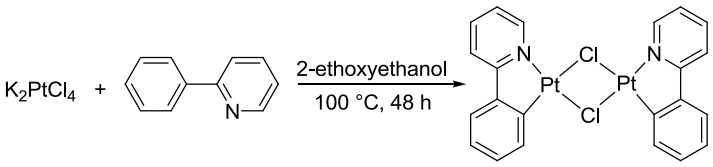

In a Schlenk tube, a suspension of 2-phenylpyridine (0.65 g, 4.18 mmol) and potassium tetrachloroplatinate (0.50 g, 1.67 mmol) in a mixture of 2-ethoxyethanol (12 mL) and water (4 mL) was heated for 24 h at 146 °C. After cooling to room temperature, the precipitate was collected via centrifugation and washed with EtOH (2 × 10 mL) and Et_2O (2 × 10 mL). The product was dried under vacuum to give a yellow powder (0.71 g, 79 %).

2-(2-quinolyl)benzimidazole, $L^{10}H$

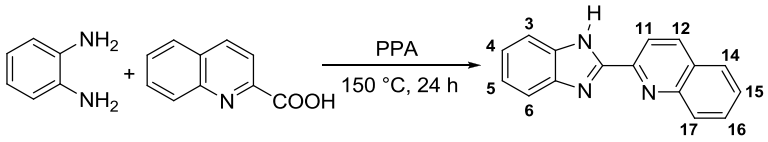

$L^{10}H$ was prepared following method A, starting from 1,2-phenylenediamine (156 mg, 1.02 mmol) and quinoline-2-carboxylic acid (250 mg, 1.44 mmol), giving the product as a white powder (205 mg, 58 %). ^{1}H NMR (700 MHz, $CDCl_3$) δ = 8.59 (d, *J* = 8.5 Hz, 1 H, H^9), 8.33 (d, *J* = 8.6 Hz, 1 H, H^{10}), 8.12 (d, *J* = 8.5 Hz, 1 H, H^{12}), 7.88 (d, *J* = 8.0 Hz, 1 H, H^{15}), 7.76 (t, *J* = 7.6 Hz, 1 H, H^{14}), 7.71 (s, 2 H, H^{2+5}), 7.59 (t, *J* = 7.4 Hz, 1 H, H^{13}), 7.36 – 7.30 (m, 2 H, H^{3+4}). $^{13}C\{^1H\}$ NMR (176 MHz, $CDCl_3$) δ = 150.8 (C^7), 148.0 (C^8), 147.6 (C^{18}), 137.6 (C^{10}), 130.4 (C^{14}), 129.2 (C^{15}), 128.7 (C^{11}), 128.0 (C^{12}), 127.5 (C^{13}), 123.8 ($C^{3,4,2,5}$), 119.3 (C^9). HRMS (ES+) *m/z* = 246.1034 ($M+H^+$) calcd for $C_{16}H_{12}N_3$ *m/z* = 246.1031. Mp ≥ 223 °C.

2-(3-isoquinolyl)benzimidazole, $L^{11}H$

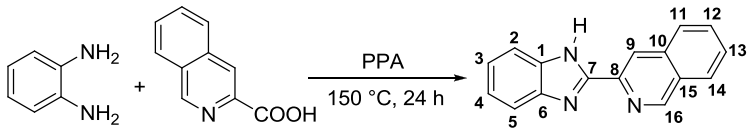

$L^{11}H$ was prepared following method A, from 1,2-phenylenediamine (62.5 mg, 0.58 mmol), and isoquinoline-3-carboxylic acid (100 mg, 0.58 mmol), giving the product as a white powder (142 mg, 47 %). ^{1}H NMR (700 MHz, $CDCl_3$) δ = 8.59 (d, *J* = 8.5 Hz, 1 H, H^{16}), 8.32 (d, *J* = 8.6 Hz, 1 H, H^{9}), 8.12 (d, *J* = 8.5 Hz, 1 H), 7.88 (d, *J* = 8.0 Hz, 1 H), 7.75 (t, *J* = 7.6 Hz, 2 H), 7.71 (s, 1 H), 7.59 (t, *J* = 7.4 Hz, 1 H), 7.35 – 7.30 (m, 2 H). $^{13}C\{^{1}H\}$ NMR (176 MHz, $CDCl_3$) δ = 152.3, 151.5, 141.9, 136.4, 134.8, 131.3, 129.1, 128.4, 127.8, 127.7, 120.4, 118.7, 116.8. HRMS (ES+) *m/z* = 246.1027 ($M+H^+$) calcd for $C_{16}H_{12}N_3$ *m/z* = 246.1031. Mp = 152 °C.

2-(1-isoquinolyl)benzimidazole, $L^{12}H$

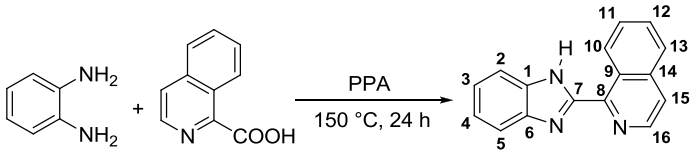

Ligand **$L^{12}H$** was prepared following method A from 1,2-phenylenediamine (156 mg, 1.02 mmol) and 4-isoquinoline-1-carboxylic acid (250 mg, 1.44 mmol), giving the product as a white powder (216 mg, 61 %). ^{1}H NMR (700 MHz, $CDCl_3$) δ = 10.92 (s, 1 H, N-H), 10.22 (d, *J* = 8.6 Hz, 1 H, H^{16}), 8.58 (d, *J* = 5.5 Hz, 1 H, H^{10}), 7.97 (d, *J* = 7.7 Hz, 1 H, H^{2}), 7.89 (d, *J* = 8.1 Hz, 1 H, H^{13}), 7.78 (m, 3 H, $H^{11+12+15}$), 7.55 (d, *J* = 7.7 Hz, 1 H, H^{5}), 7.34 (m, 2 H, H^{3+4}). $^{13}C\{^{1}H\}$ NMR (176 MHz, $CDCl_3$) δ = 151.6 (C^{8}), 146.7 (C^{9}), 145.1 (C^{7}), 141.5 (C^{10}), 137.3 (C^{14}), 133.1 (C^{1}), 130.7 (C^{15}), 128.9 (C^{12}), 128.6 (C^{16}), 126.9 (C^{13}), 126.8 (C^{6}), 124.4 (C^{3}), 122.7 (C^{11}), 122.6 (C^{4}), 120.8 (C^{2}), 111.2 (C^{5}). HRMS (ES+) *m/z* = 246.1053 (M+H) calcd for $C_{16}H_{12}N_3$ *m/z* = 246.1031. Mp ≥ 211 °C.

2-(4-bromopyrid-2-yl)benzimidazole, $L^{13}H$

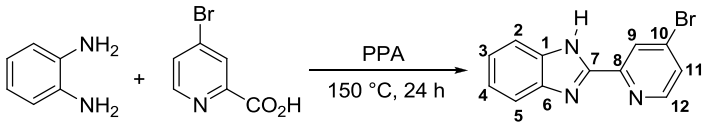

$L^{13}H$ was prepared following method A from 1,2-phenylenediamine (268 mg, 2.47 mmol) and 4-bromopicolinic acid (500 mg, 2.47 mmol), giving the product as a white powder (0.34 mg, 51 %). ^{1}H NMR (700 MHz, $(CD_3)_2CO$) δ = 8.56 (d, *J* = 2.6 Hz, 1 H, H^{12}), 8.55 (s, 1 H, H^{9}), 7.70 (dd, *J* = 5.3, 1.8 Hz, 3 H, $H^{2,5,11}$), 7.28 (dd, *J* = 6.0, 3.1 Hz, 2 H, $H^{3,4}$). ^{13}C {^{1}H} NMR (176 MHz $(CD_3)_2CO$) δ = 232.6 (C^{7}), 150.4 (C^{12}), 150.2 ($C^{1,6}$), 149.3 (C^{8}), 132.9 (C^{10}), 127.3 ($C^{2,5,11}$), 124.1 (C^{9}), 122.9 ($C^{3,4}$). HRMS (ES+) *m/z* = 273.9988 ($M+H^{+}$) calcd for $C_{12}H_8BrN_3$ *m/z* = 273.9980. Mp ≥ 185 °C.

2,2'-Bisbenzimidazole, $L^{14}H_2$ [7]

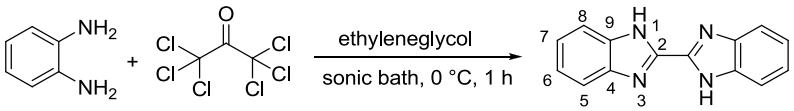

A solution of hexachloropropanone (1.06 g, 0.002 mol) was added dropwise to 1,2-benzenediamine (5.32 g, 0.02 mol) in ethylene glycol (5 mL) at 0 °C. The reaction mixture was sonicated for 1 h at 0 °C. The gray-white precipitates were isolated from the solution by filtration on a Büchner funnel. The solid was washed with Et_2O (3 × 20 mL) and acetone (2 x 10 mL), and dried under reduced pressure to give a white solid (2.5 g, 53 %). ^{1}H NMR (600 MHz, $(CD_3)_2SO$) δ = 13.52 (s, 2 H, -NH), 7.75 (d, *J* = 8.0 Hz, 2 H, H^{8}), 7.55 (d, *J* = 7.8 Hz, 2 H, H^{5}), 7.44 (m, 4 H, $H^{6, 7}$). ^{13}C{^{1}H} NMR (150 MHz, $(CD_3)_2SO$) δ = 143.9 (C^{2}), 134.6 (C^{4}), 134.9 (C^{9}), 123.7 (C^{6}), 122.3 (C^{7}), 119.3 (C^{8}), 112.2 (C^{5}). HRMS (ES+) *m/z* = 235.1017 (M+H) calcd for $C_{14}H_{10}N_4$ *m/z* = 235.0984. Mp ≥ 250 °C.

1,1'-Dimethyl-2,2'-bisbenzimidazole, L^{15} [9]

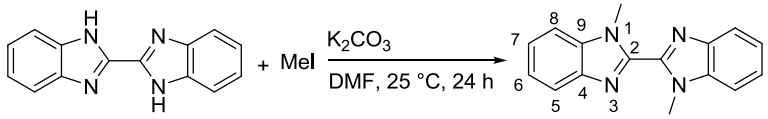

2,2'-Bisbenzimidazole (50 mg, 0.213 mmol) and potassium carbonate (74 mg, 0.533 mmol) were dissolved in DMF (5 mL) at 298 K. After 30 min, iodomethane (181 mg, 1.28 mmol) was added dropwise to the solution. The reaction mixture was stirred for 12 h at 298 K. The beige precipitate formed was centrifuged and washed with Et_2O (3 × 10 mL) and acetone (2 × 10 mL). The product was dried under reduced pressure to give a white solid. (42 mg, 75 %).^{1}H NMR (600 MHz, $(CD_3)_2SO$) δ = 7.81 (d, *J* = 8.1 Hz, 2 H, H^8), 7.72 (d, *J* = 8.1 Hz, 2 H, H^5), 7.41 (t, *J* = 8.1 Hz, 2 H, H^7), 7.34 (t, *J* = 8.1 Hz, 2 H, H^6), 4.27 (s, 6 H, H^{-CH_3}). ^{13}C{^{1}H} NMR (151 MHz, $(CD_3)_2SO$) δ = 142.9, 141.8, 135.9, 123.7, 122.6, 119.6, 110.9, 54.3. HRMS (ES+) *m/z* = 263.1303 ($M+H^+$) calcd for $C_{16}H_{14}N_4$ *m/z* = 263.1297. Mp ≥ 250 °C.

$[Ir(ppy)_2(L^{10}H)]PF_6$

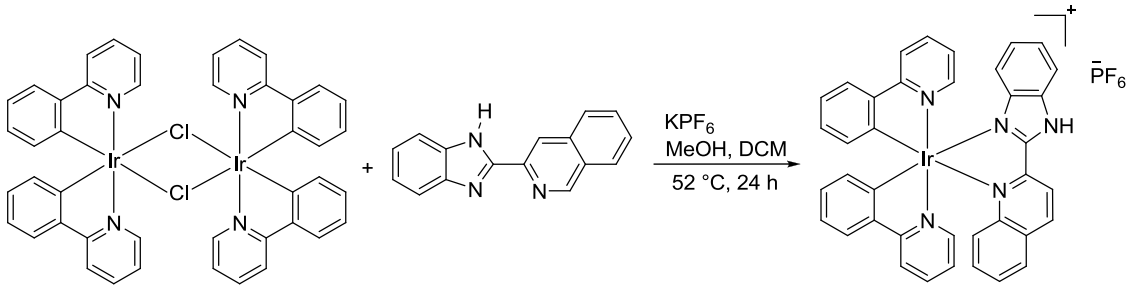

$[Ir(ppy)_2(L^{10}H)]PF_6$ was prepared following **method B** from $[Ir(\mu\text{-}Cl)(ppy)_2]_2$ (50 mg, 0.046 mmol), and **$L^{10}H$** (25 mg, 0.103 mmol), leading to the product as a red powder (54 mg, 78 %). ^{1}H NMR (600 MHz, $CDCl_3$) δ = 12.19 (s, 1 H, NH), 8.74 (1 H, d, *J* = Hz,), 8.61 (1 H, d, *J* = Hz,), 8.12 (1 H, d, *J* = Hz,), 7.91 (3 H, d, *J* = Hz,), 7.84 (1 H, d, *J* = Hz,), 7.74-7.63 (5 H, m,), 7.55 (1 H, t, *J* = Hz,), 7.48 (1 H, d, *J* = Hz), 7.35 (1 H, t, *J* = Hz,), 7.27 (1 H, t, *J* = Hz,), 7.13 (1 H, t, = Hz,), 7.06 (1 H, t, *J* = Hz), 7.02-6.86 (5 H, m,), 6.46 (1 H, d, *J* = Hz,), 6.24 (1 H, d, *J* = Hz,), 5.96 (1 H, d, *J* = Hz,). ^{13}C{^{1}H} NMR (176 MHz, $CDCl_3$) δ = 168.1, 167.9, 152.4, 149.5, 148.5, 143.9, 143.8, 141.9, 137.6, 137.5, 136.5, 133.2, 132.3, 131.6,

130.8, 130.1, 128.0, 127.7, 126.6, 126.1, 125.4, 124.8, 124.5, 123.9, 123.2, 122.8, 122.5, 122.4, 119.7, 119.2, 118.5, 117.3, 115.0. HRMS (ES+) *m/z* = 743.1788 (M) calcd for $C_{38}H_{26}IrN_5$ *m/z* = 743.1794. Mp ≥ 250 °C.

$Ir(ppy)_2L^{10}$

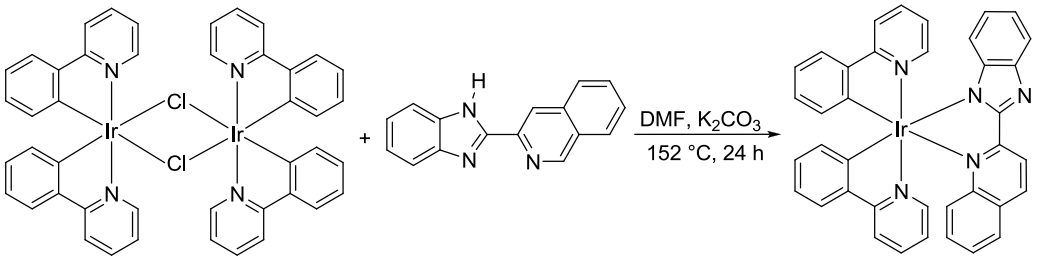

$Ir(ppy)_2L^{10}$ was prepared following **method C** from $[Ir(\mu\text{-}Cl)(ppy)_2]_2$ (50 mg, 0.046 mmol), and **$L^{10}H$** (25 mg, 0.103 mmol), giving the product as an orange powder (44 mg, 63 %). ^{1}H NMR (700 MHz, $CDCl_3$) δ = 8.78 (d, *J* = 8.6 Hz, 1 H,), 8.38 (d, *J* = 8.6 Hz, 1H), 8.11 (d, *J* = 8.9 Hz, 1H), 7.84 (ddd, *J* = 4.0, 2.8, 2.2 Hz, 2H), 7.81 (d, *J* = 8.2 Hz, 1H), 7.79 (dd, *J* = 8.1, 1.3 Hz, 1H), 7.76 (d, *J* = 8.0 Hz, 1H), 7.67 (dd, *J* = 7.9, 1.1 Hz, 1H), 7.64 (dd, *J* = 7.7, 1.1 Hz, 1H), 7.63 – 7.58 (m, 1H), 7.54 (td, *J* = 8.2, 1.6 Hz, 1H), 7.42 (td, *J* = 6.9, 1.3 Hz, 2H), 7.19 – 7.13 (m, 2H), 7.09 – 7.05 (m, 1H), 7.00 (td, *J* = 7.5, 1.3 Hz, 1H), 6.96 (td, *J* = 7.4, 1.4 Hz, 1H), 6.87 (td, *J* = 7.5, 1.3 Hz, 1H), 6.82 – 6.74 (m, 3H), 6.52 (dd, *J* = 7.5, 0.9 Hz, 1H), 6.25 (dd, *J* = 7.7, 0.7 Hz, 1H), 5.90 (d, *J* = 8.3 Hz, 1H). $^{13}C\{^1H\}$ NMR (176 MHz, $CDCl_3$) δ = 168.7, 167.9, 158.9, 155.4, 150.2, 149.1, 148.0, 145.3, 144.2, 143.9, 143.5, 139.8, 137.0, 136.8, 132.2, 131.8, 131.1, 130.5, 130.0, 129.3, 128.5, 128.3, 127.5, 124.7, 124.2, 122.9, 122.7, 122.4, 122.2, 121.7, 120.7, 119.2, 118.9, 117.6, 116.8. HRMS (AP+) *m/z* = 743.1783 (M) calcd for $C_{38}H_{26}N_5Ir$ *m/z* = 743.1794. Mp ≥ 250 °C. Anal. Calcd for $C_{38}H_{26}IrN_5$: C 61.27, H 3.52, N 9.4; found C 61.25, H 3.51, N 9.45.

$[Ir(ppy)_2(L^{11}H)]PF_6$

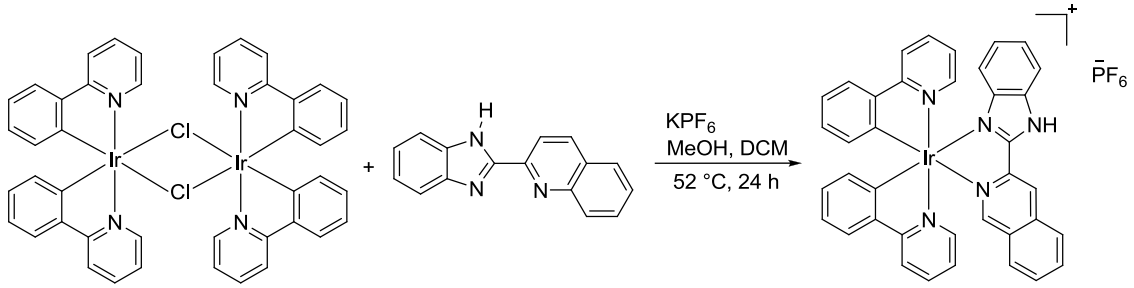

$[Ir(ppy)_2(L^{11}H)]PF_6$ was prepared following **method B** from $[Ir(\mu\text{-}Cl)(ppy)_2]_2$ (50 mg, 0.046 mmol), and **$L^{11}H$** (25 mg, 0.103 mmol), as an orange powder (39 mg, 56 %). ^{1}H NMR (700 MHz, $CDCl_3$) δ = 9.27 (s, 1H), 8.44 (s, 1H), 8.30 (d, *J* = 7.6 Hz, 1H), 7.94 – 7.85 (m, 3H), 7.82 (d, *J* = 8.2 Hz, 1H), 7.77 (m, 2H), 7.70 (m, 5H), 7.51 (d, *J* = 5.3 Hz, 1H), 7.33 (t, *J* = 7.3 Hz, 1H), 7.10 (m, 2H), 6.98 (t, 7.6 Hz, 2H), 6.96 (t, *J* = 7.3 Hz, 1 H), 6.93 (t, *J* = 6.6 Hz, 1 H), 6.89 (t, *J* = 6.8 Hz, 1 H), 6.46 (d, *J* = 7.6 Hz, 2H), 6.43 (d, *J* = 7.6 Hz, 2H), 6.23 (d, *J* = 8.1 Hz, 1H). ^{13}C{^{1}H} NMR (175 MHz, $CDCl_3$) δ = 168.3, 167.9, 154.3, 149.5, 148.2, 144.1, 137.7, 137.5, 133.7, 132.6, 132.4, 131.8, 131.4, 130.8, 130.1, 130.0, 129.5, 129.2, 128.0, 125.7, 124.8, 124.5, 123.2, 122.8, 122.5, 122.3, 119.5, 119.2, 117.1, 114.1. HRMS (ES+) *m/z* = 744.1837 (M+H) calcd for $C_{38}H_{27}IrN_5$ *m/z* = 744.1872. Mp ≥ 250 °C.

$Ir(ppy)_2L^{11}$

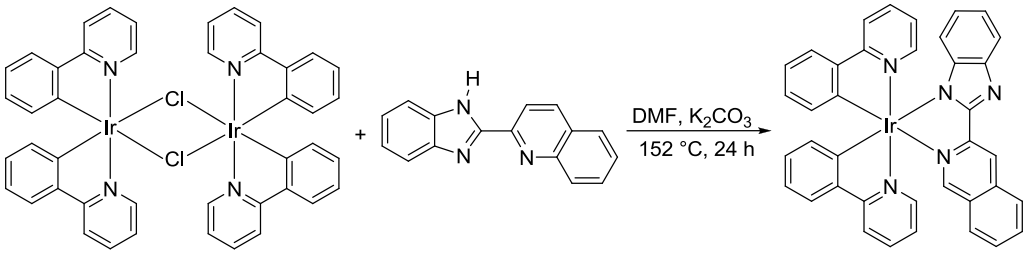

$Ir(ppy)_2L^{11}$ was prepared following **method C** from $[Ir(\mu\text{-}Cl)(ppy)_2]_2$ (50 mg, 0.046 mmol), and **$L^{11}H$** (25 mg, 0.103 mmol), which gave the product as a yellow powder (31 mg, 45 %). ^{1}H NMR (700 MHz, $CDCl_3$) δ = 8.40 (s, 1H), 7.99 (d, *J* = 7.7 Hz, 1H), 7.84 – 7.75 (m, 4H), 7.72 (t, *J* = 7.5 Hz, 1H), 7.68 (t, *J* = 8.4 Hz, 3H), 7.61 – 7.49 (m, 4H), 7.07 (t, *J* = 7.6 Hz, 1H), 7.05 – 7.00 (m, 2H), 6.95 (td, *J* = 7.4, 1.3 Hz, 1H), 6.90 (td, *J* = 7.5, 1.3 Hz, 1H), 6.75 (dt, *J* =

17.3, 6.1 Hz, 3H), 6.53 – 6.45 (m, 2H), 6.16 (d, *J* = 8.1 Hz, 1H). $^{13}C\{^{1}H\}$ NMR (176 MHz, $CDCl_3$) δ = 168.7, 168.5, 153.5, 150.2, 148.5, 144.8, 144.3, 137.0, 136.7, 136.4, 132.6, 132.5, 132.4, 130.5, 129.8, 129.0, 128.1, 124.6, 124.3, 122.7, 122.2, 121.8, 121.6, 118.9, 118.8, 115.8. HRMS (AP+) *m/z* = 743.1790 (M) calcd for $C_{38}H_{26}N_5Ir$ *m/z* = 743.1794. Mp ≥ 250 °C. Anal. Calcd for $C_{38}H_{26}IrN_5$: C 61.27, H 3.52, N 9.4; found C 61.25, H 3.51, N 9.45.

$[Ir(ppy)_2(L^{12}H)]PF_6$

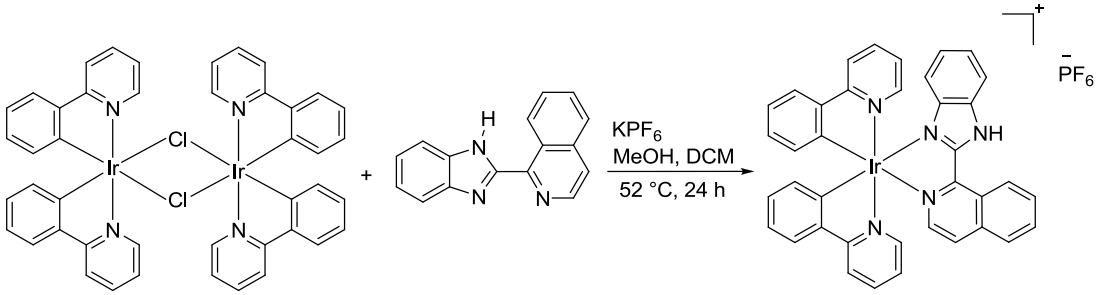

$[Ir(ppy)_2(L^{12}H)]PF_6$ was prepared following **method B** from $[Ir(\mu\text{-}Cl)(ppy)_2]_2$ (50 mg, 0.046 mmol), and **$L^{12}H$** (25 mg, 0.103 mmol), yielding the product as a red powder (53 mg, 77 %). ^{1}H NMR (400 MHz, $CDCl_3$) δ = 13.43 (s, 1 H, NH), 9.17 (d, *J* = 9.15 Hz, 1 H), 8.14 (m, 1 H), 8.03 (d, *J* = 8.90 Hz, 1 H), 7.95-7.87 (m, 5 H), 7.73-7.66 (m, 5 H), 7.44 (d, *J* = 6.25 Hz, 1 H,), 7.39 (t, *J* = 7.70 Hz, 1 H), 7.12-7.07 (m, 3 H), 7.02 (t, *J* = 7.70 Hz, 2 H,), 6.98 (m, 2 H), 6.91 (t, *J* = 6.40 Hz,), 6.87 (t, *J* = 6.90 Hz,), 6.44 (d, *J* = 7.30 Hz, 1 H,), 6.39 (d, *J* = 7.60 Hz, 1 H,), 6.32 (d, *J* = 8.70 Hz, 1 H,). $^{13}C\{^{1}H\}$ NMR (150 MHz, ($CDCl_3$)) δ = 167.4, 167.1, 151.6, 148.7, 147.7, 143.2, 143.0, 141.2, 136.9, 136.7, 135.7, 132.5, 131.5, 130.8, 130.0, 129.3, 127.2, 126.9, 125.9, 125.3, 124.6, 124.0, 123.7, 122.4, 122.1, 121.7, 121.6. HRMS (ES+) m/z = 744.1870 (M) calcd for $C_{38}H_{27}IrN_5$ m/z = 744.1849. Mp ≥ 250 °C.

$Ir(ppy)_2L^{12}$

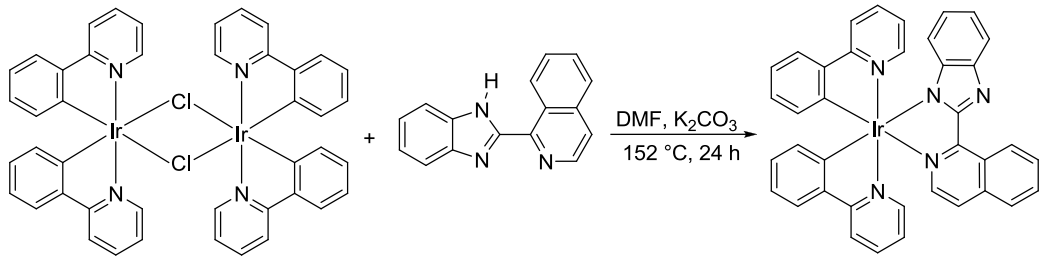

$Ir(ppy)_2L^{12}$ was prepared following **method B** from $[Ir(\mu\text{-}Cl)(ppy)_2]_2$ (50 mg, 0.046 mmol), and **$L^{12}H$** (25 mg, 0.103 mmol), giving the product as anorange powder (43 mg ,62 %). ^{1}H NMR (600 MHz, $CDCl_3$) δ = 8.80 (d, *J* = Hz, 1 H), 8.27(d, *J* = Hz, 1 H), 8.12 (d, *J* = Hz, 1 H), 7.91 (d, *J* = Hz, 1 H), 7.85 (d, *J* = Hz, 1 H), 7.79 (d, *J* = Hz, 1 H), 7.74 (d, *J* = Hz, 1 H), 7.67 (d, *J* = Hz, 1 H), 7.63 (d, *J* = Hz, 1 H), 7.58 (t, *J* = Hz, 1 H), 7.51 (t, *J* = Hz, 1 H), 7.40 (d, *J* = Hz, 1 H), 7.37 (t, *J* = Hz, 1 H), 7.14 (t), 7.08 (t, *J* = Hz, 1 H), 6.98 (m, 1 H), 6.86 (t, *J* = Hz, 1 H), 6.72 (t, *J* = Hz, 1 H), 6.57 (d, *J* = Hz, 1 H), 6.26 (d, *J* = Hz, 1 H), 5.87 (d, *J* = Hz, 1 H). HRMS (AP+) *m/z* = 743.1791 (M) calcd for $C_{38}H_{26}N_5Ir$ *m/z* = 743.1794. Mp ≥ 250 °C. Anal. Calcd for $C_{38}H_{26}IrN_5$: C 61.27, H 3.52, N 9.40; found C 61.26, H 3.51, N 9.45.

$[Ir(ppy)_2L^{13}H]PF_6$

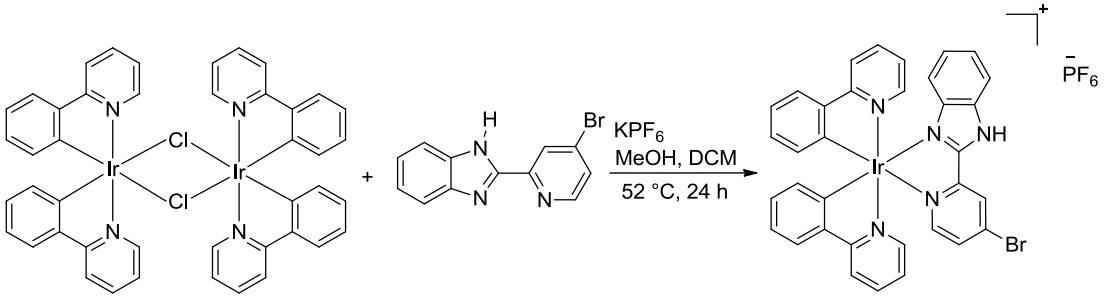

$[Ir(ppy)_2L^{13}H]PF_6$ was prepared following **method B** from $[Ir(\mu\text{-}Cl)(ppy)_2]_2$ (50 mg, 0.046 mmol), and 2-(4-bromo-pyrid-2-yl)benzimidazole (28 mg, 0.103 mmol), leading to the product as a brown powder (71 mg, 40 %). ^{1}H NMR (700 MHz, $CDCl_3$) δ = 11.92 (s, 1 H), 8.79 (s, 1 H), 7.91 (d, *J* = 8.5 Hz, 1 H), 7.87 (d, *J* = 8.5 Hz, 1 H), 7.82 (d, *J* = 8.3 Hz, 1 H), 7.76 (t, *J* = 8.0 Hz, 1 H), 7.74 – 7.67 (m, 4 H), 7.62 (d, *J* = 5.8 Hz, 1 H), 7.54 – 7.49 (m, 2 H), 7.35 (t, *J* = 8.0 Hz, 1H), 7.10 (t, *J* = 7.4 Hz, 1 H), 7.06 (t, *J* = 7.3 Hz, 1 H), 7.01 (t, *J* = 7.6 Hz, 2 H), 6.95 (m, 3 H), 6.41 (d, *J* = 7.9 Hz, 1 H), 6.35 (d, *J* = 7.4 Hz, 1 H), 6.23 (d, *J* = 8.0 Hz, 1 H). $^{13}C\{^1H\}$ NMR (176 MHz, $CDCl_3$) δ = 168.3, 167.9, 150.9, 150.4, 149.6, 148.7, 148.5, 146.2, 144.1, 144.0, 140.3, 138.1, 137.9, 137.1, 134.6, 132.4, 131.9, 131.3, 131.0, 130.4,

127.9, 126.9, 125.6, 124.9, 124.7, 123.6, 123.2, 122.8, 122.7, 119.6, 119.5, 117.7, 114.8 . HRMS (ES+) *m/z* = 772.0830 (M) calcd for $C_{34}H_{24}BrIrN_5$ *m/z* = 772.0821. Mp ≥ 250 °C.

$[Ir(ppy)_2L^{14}H_2]PF_6$

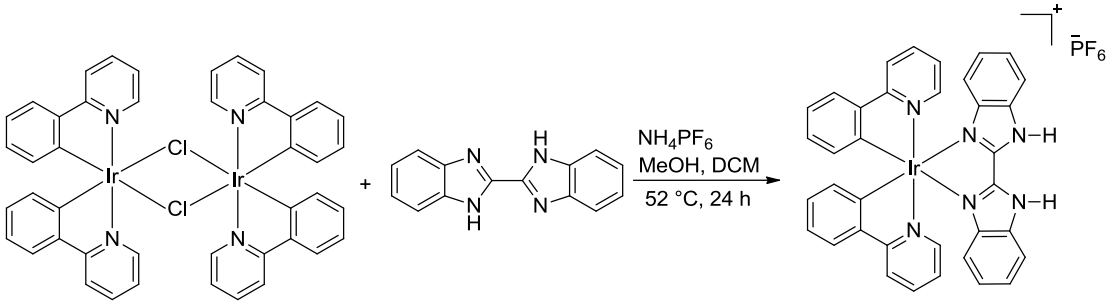

$[Ir(ppy)_2L^{14}H_2]PF_6$ was prepared following **method B** from $[Ir(\mu\text{-}Cl)(ppy)_2]_2$ (50 mg, 0.046 mmol) and 2,2'-bisbenzimidazole (25 mg , 0.103 mmol), which gave the product as ayellow solid (128 mg, 75 %). ^{1}H NMR (700 MHz, $CDCl_3$) δ = 12.10 (s, 2 H, NH), 7.84 (d, *J* = 8.20 Hz, 2 H), 7.69 (m, 6 H), 7.65 (t, *J* = 6.80 Hz, 2 H), 7.32 (t, *J* = 7.7 Hz, 2 H), 7.10 (t, *J* = 7.6 Hz, 2 H), 7.01 (t, *J* = 7.7 Hz, 2 H), 6.96 (t, *J* = 7.6 Hz, 2 H), 6.88 (t, *J* = 6.80 Hz, 2 H), 6.52 (d, *J* = 7.60 Hz, 2 H), 6.20 (d, *J* = 8.30 Hz, 2 H). ^{13}C{^{1}H} NMR (176 MHz, $CDCl_3$) δ = 168.2, 149.4, 147.7, 144.7, 140.5, 137.2, 134.4, 132.5, 129.9, 125.5, 124.7, 124.3, 122.7, 122.1, 118.9, 117.5, 114.1. HRMS (ES+): *m/z* = 733.1846 (M) calcd for $C_{36}H_{26}IrN_6$ *m/z* = 733.1825. Mp ≥ 250 °C.

$Ir(ppy)_2(L^{14}H)$

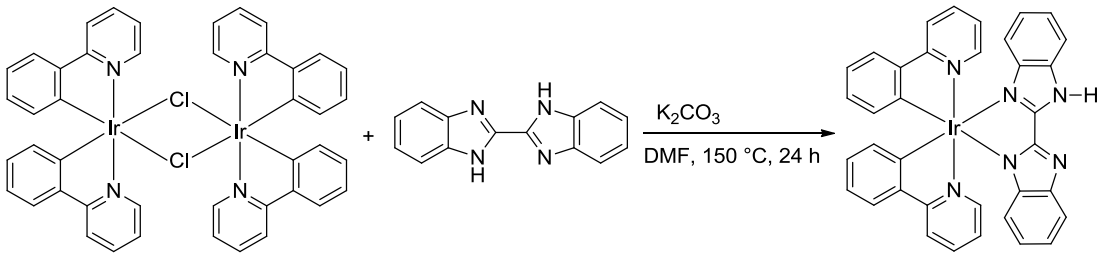

$Ir(ppy)_2(L^{14}H)$ was prepared following **method C** from $[Ir(\mu\text{-}Cl)(ppy)_2]_2$ (50 mg, 0.046 mmol), and 2,2'-bisbenzimidazole (25 mg , 0.103 mmol), giving a yellow powder (90 mg, 53 %). ^{1}H NMR (700 MHz, $CDCl_3$) δ = 7.84 (d, *J* = 8.20 Hz, 2 H), 7.69 (m, 6 H), 7.65 (t, *J* = 6.80 Hz, 2 H), 7.32 (t, *J* = 7.7 Hz, 2 H), 7.10 (t, *J* = 7.6 Hz, 2 H), 7.01 (t, *J* = 7.7 Hz, 2 H), 6.96 (t, *J* = 7.6 Hz, 2 H), 6.88 (t, *J* = 6.80 Hz, 2 H), 6.52 (d, *J* = 7.60 Hz, 2 H), 6.20 (d, *J* = 8.30 Hz, 2 H). ^{13}C{^{1}H} NMR (176 MHz, $CDCl_3$) δ = 168.2, 149.4, 147.7, 144.7, 140.5, 137.2

, 134.4, 132.5, 129.9, 125.5, 124.7, 124.3, 122.7, 122.1, 118.9 (C^3-Py), 117.5, 114.1. HRMS (AP+) *m/z* = 732.1757 (M) calcd for $C_{36}H_{25}N_6Ir$ *m/z* = 732.1747. Mp ≥ 250 °C.

$[Ir(ppy)_2L^{15}]PF_6$

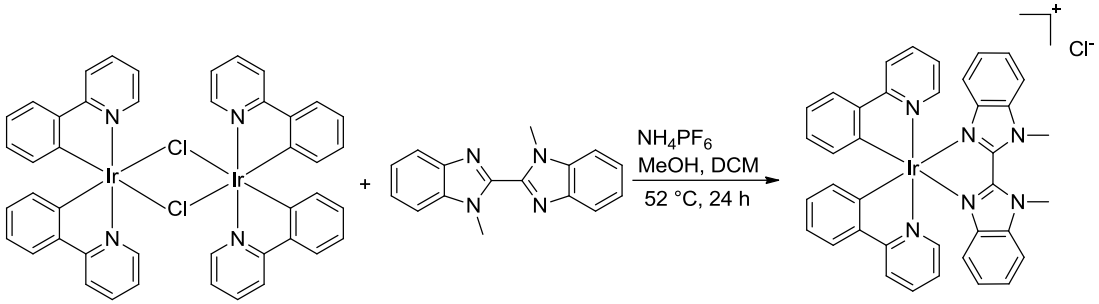

$[Ir(ppy)_2L^{15}]PF_6$ was prepared following **method B** from $[Ir(\mu\text{-}Cl)(ppy)_2]_2$ (50 mg, 0.046 mmol), and 1,1'-dimethyl-2,2'-bisbenzimidazole (25 mg, 0.103 mmol), giving a yellow powder (63 %). ^{1}H NMR (700 MHz, $CDCl_3$) δ = 8.04 (d, *J* = 5.6 Hz, 1H), 7.79 (d, *J* = 7.6 Hz, 1H), 7.69 – 7.61 (m, 2H), 7.57 (d, *J* = 8.3 Hz, 1H), 7.39 (t, *J* = 7.7 Hz, 1H), 7.07 (t, *J* = 7.4 Hz, 1H), 7.01 (dd, *J* = 16.2, 7.8 Hz, 2H), 6.93 (t, *J* = 7.5 Hz, 1H), 4.67 (s, 3H). $^{13}C\{^1H\}$ NMR (176 MHz, $CDCl_3$) δ = 150.5, 140.5, 137.4, 132.4, 130.1, 126.4, 125.6, 124.5, 123.5, 122.3, 118.9, 118.5, 37.6. HRMS (ES+) *m/z* = 761.2109 (M) calcd for $C_{36}H_{26}IrN_6$ *m/z* = 761.2138.

9. Experimental details for Chapter Five

$[Ir(ppy)_2(SPNPS)]$

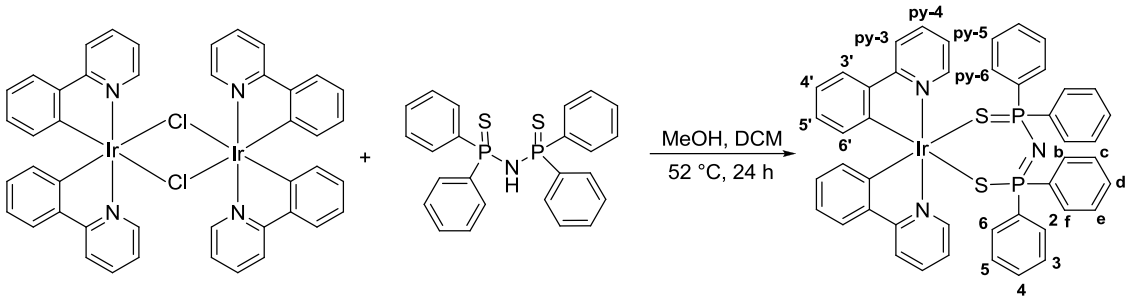

A suspension of $[Ir(\mu\text{-}Cl)(ppy)_2]_2$ (0.050 g, 0.046 mmol) and phosphinothioic amide (0.046 g, 0.10 mmol) in a mixture of MeOH (5 mL) and DCM (5 mL) was heated for 24 h at 52 °C. After cooling to room temperature, the solvent was removed and the crude residue was washed with Et_2O (3 × 10 mL). The product was dried under vacuum to give a yellow powder (0.057 g, 65 %). ^{1}H NMR (700 MHz, $CDCl_3$) δ = 9.27 (d, *J* = 7.7 Hz, 1 H, $H^{py\text{-}6}$), 7.97 (m, 2H, $H^{2,6}$), 7.69 (d, *J* = 8.0 Hz, 1 H, $H^{py\text{-}3}$), 7.62 (m, 2 H, $H^{b,f}$), 7.53 (d, *J* = 7.7 Hz, 1 H, $H^{6'}$), 7.39 (d, *J* = 8.0 Hz, 1 H, $H^{py\text{-}4}$), 7.35 (m, 3 H, $H^{3,4,5}$), 7.21 (t, *J* = 7.4 Hz, 1 H, H^4), 7.01 (m, 2

H, $H^{3,5}$), 6.84 – 6.79 (m, 1H, $H^{5'}$), 6.66 (t, *J* = 7.7 Hz, 1H, $H^{4'}$), 6.34 – 6.27 (m, 1 H, H^{py-5}), 5.99 (d, *J* = 7.7 Hz, 1 H, $H^{3'}$). $^{13}C\{^1H\}$ NMR (176 MHz, $CDCl_3$) δ = 167.9, 152.3, 151.0, 143.6, 141.2, 140.6, 140.0, 135.7, 131.0, 130.9, 130.2, 130.2, 130.0, 129.9, 129.8, 129.4, 128.2, 128.1, 128.0, 127.9, 123.7, 121.3, 121.1, 117.9. ^{31}P NMR (283 MHz, $CDCl_3$) δ = 29.20. HRMS (AP+) *m/z* = 948.1501 (M+) calcd for $C_{46}H_{37}IrN_3P_2S_2$ *m/z* = 948.1510.

[Pt(ppy)(SPNPS)]

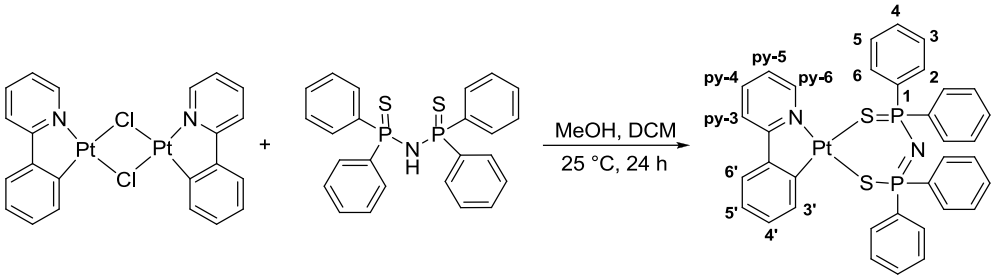

A suspension of $[Pt(ppy)(\mu\text{-}Cl)]_2$ (0.050 g, 0.065 mmol) and phosphinothioic amide (0.088 g, 0.19 mmol) in a mixture of MeOH (5 mL) and DCM (5 mL) was stirred for 24 h at 25 °C. After cooling to room temperature, the solvent was removed and the crude residue was washed with Et_2O (3 × 10 mL). The product was dried under vacuum to give a yellow powder (0.056 g, 54 %). ^1H NMR (700 MHz, $CDCl_3$) δ = 9.40 (d, *J* = 6.7 Hz, 1 H, H^{py-6}), 8.07 (d, *J* = 7.7 Hz, 1 H, $H^{3'}$), 8.00 – 7.85 (m, 8 H, $H^{2,6}$), 7.74 (t, *J* = 7.7 Hz, 1 H, H^{py-4}), 7.63 (d, *J* = 7.7 Hz, 1 H, H^{py-3}), 7.44 (d, *J* = 7.7, 1.2 Hz, 1 H, $H^{6'}$), 7.41 – 7.34 (m, 4 H, H^4), 7.34 – 7.26 (m, 8 H, $H^{3,5}$), 7.16 (t, *J* = 7.7 Hz, 1 H, $H^{4'}$), 7.08 (t, *J* = 7.7 Hz, 1.1 Hz, 1 H, $H^{5'}$), 7.01 (t, *J* = 6.7 Hz, 1 H, H^{py-5}). $^{13}C\{^1H\}$ NMR (176 MHz, $CDCl_3$) δ = 167.5, 148.1, 147.1, 145.0, 138.7, 138.6, 138.1, 138.0, 137.9, 137.5, 137.5, 136.9, 136.9, 132.2, 131.4, 131.4, 131.2, 131.1, 131.0, 131.0, 130.8, 130.8, 130.0, 128.2, 128.2, 128.1, 128.1, 123.8, 123.6, 121.9, 118.7. ^{31}P NMR (283 MHz, $CDCl_3$) δ = 36.68 (d, *J* = 4.6 Hz), 33.4 (d, *J* = 4.6 Hz). HRMS (AP+) *m/z* = 796.0790 (M) calcd for $C_{35}H_{28}N_2P_2PtS_2$ *m/z* = 796.0796.

[Pt(SPNPS)$_2$]

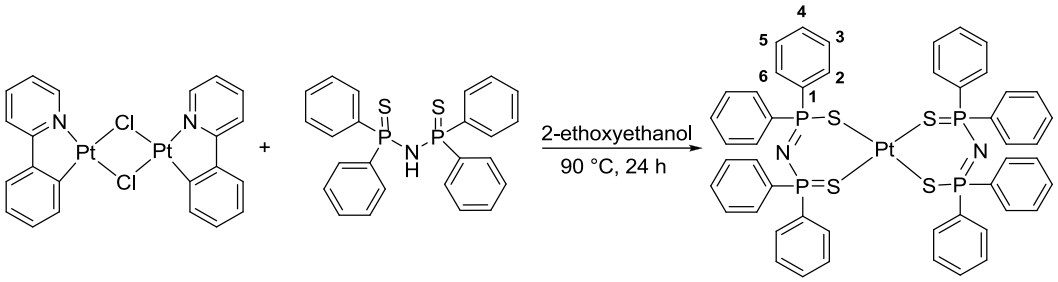

A suspension of [Pt(μ-Cl)(ppy)]$_2$ (0.050 g, 0.065 mmol) and phosphinothioic amide (0.088 g, 0.019 mmol) in 2-ethoxyethanol was heated for 24 h at 90 °C. After cooling to room temperature, the reaction was quenched with water and the precipitate was collected by centrifugation. The crude product was washed with EtOH (1 × 10 mL) and Et_2O (3 × 10 mL). The product was dried under vacuum to give a yellow powder. (0.065 g, 46 %). ^{1}H NMR (700 MHz, $CDCl_3$) δ = 7.89 – 7.83 (m, 16 H, $H^{2,6}$), 7.40 (t, J = 7.4 Hz, 8 H, H^4), 7.30 (m, 16 H, $H^{3,5}$). $^{13}C\{^1H\}$ NMR (176 MHz, $CDCl_3$) δ = 131.5, 131.4, 131.1 (C^4), 128.2, 128.1. ^{31}P NMR (283 MHz, $CDCl_3$) δ = 34.26. HRMS (AP+) *m/z* = 1090.0648 (M) calcd for $C_{48}H_{40}N_2P_4PtS_4$ *m/z* = 1090.0652.

10. References

[1] G. Huimin, M.-S. Maria, J. Shaomin, Z. Jianzhang, C. Felix, *Inorg Chem.*, 2010, **49**, 6802-6804.

[2] S. Muhammadi, S. Reimann, K. Wittler, P. Langer, *Eur. J. Org. Chem.*, 2011, **27**, 5261-5271.

[3] R. H. Mitchell, Y.-H. Lai, R. V. Williams, *J. Org. Chem.*, 1979, **44**, 4733-4735

[4] R. Debbas, P. K. Bharadwaj, *Inorg. Chem.*, 2008, **47**, 2252

[5] D. A. K. Vezzu, J. C. Deaton, J. S. Jones, L. Bartolotti, C. F. Harris, A. P. Marchetti, M. Kondakova, R. D. Pike, S. Huo, *Inorg. Chem.*, 2010, **49**, 5107-5119.

[6] K. Snégaroff, S. Komagawa , F. Chevallier, P. C. Gros, S. Golhen, T. Roisnel, M. Uchiyama, F. Mongin, *Chem. Eur. J.*, 2010, **16**, 8191-8201.

[7] W.-K. Huang, C.-W. Cheng, S.-M. Chang, Y.-P. Lee, D. E. Wei-Guang, *Chem. Comm.*, 2010, **46**, 8992-8994.

A1. Crystallographic Data

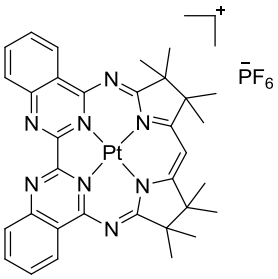

Crystal data and structure refinement for **[PtMabiq]PF_6**	
Empirical formula	$C_{33}H_{33}N_8Pt$ x PF_6 x CH_3CN
Formula weight	922.79
Temperature/K	100.0
Crystal system	triclinic
Space group	P-1
a/Å , b/Å, c/Å	9.9204(19), 11.790(2), 16.146(3)
α/°, β/°, γ/°	109.1410(19), 94.126(2), 104.617(2)
Volume/$Å^3$	1701.4(6)
Z	2
$\rho_{calc}mg/mm^3$	1.801
m/mm^{-1}	3.910
F(000)	912.0
Crystal size/mm^3	0.2 × 0.04 × 0.01
Radiation	synchrotron (λ = 0.68890 Å)
2Θ range for data collection	3.7 to 58°
Index ranges	$-8 \leq h \leq 12$, $-16 \leq k \leq 16$, $-22 \leq l \leq 22$
Reflections collected	19717
Independent reflections	9156 [R_{int} = 0.0242, R_{sigma} = 0.0333]
Data/restraints/parameters	9156/28/460
Goodness-of-fit on F^2	1.067
Final R indexes [I>=2σ (I)]	R_1 = 0.0286, wR_2 = 0.0731
Final R indexes [all data]	R_1 = 0.0317, wR_2 = 0.0749
Largest diff. peak/hole / e $Å^{-3}$	1.64/-1.88

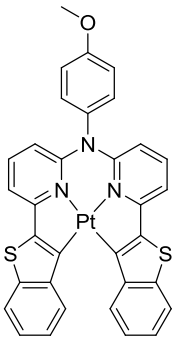

Crystal data and structure refinement for **PtL**[8]

Empirical formula	$C_{33}H_{21}N_3OPtS_2$ x CH_2Cl_2
Formula weight	819.66
Temperature/K	120
Crystal system	triclinic
Space group	P-1
a/Å, b/Å, c/Å	10.9257(3), 11.5129(3), 12.7088(3)
α/°, β/°, γ/°	81.4610(10), 69.8240(10), 72.7010(10)
Volume/Å^3	1430.75(6)
Z	2
ρ_{calc}mg/mm^3	1.903
m/mm^{-1}	5.272
F(000)	800.0
Crystal size/mm^3	0.28 × 0.06 × 0.03
2Θ range for data collection	3.72 to 58°
Index ranges	$-14 \leq h \leq 14$, $-15 \leq k \leq 15$, $-17 \leq l \leq 17$
Reflections collected	23429
Independent reflections	7609[R(int) = 0.0424]
Data/restraints/parameters	7609/0/389
Goodness-of-fit on F^2	1.082
Final R indexes [I>=2σ (I)]	R_1 = 0.0320, wR_2 = 0.0697
Final R indexes [all data]	R_1 = 0.0398, wR_2 = 0.0737
Largest diff. peak/hole / e Å^{-3}	4.26/-1.71

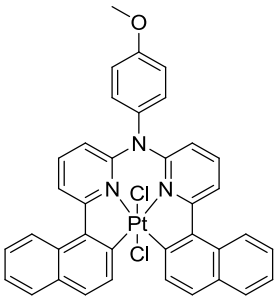

Crystal data and structure refinement for 180K **Pt L^3Cl_2**	
Empirical formula	$C_{37}H_{25}Cl_2N_3OPt \times CH_2Cl_2$
Formula weight	878.52
Temperature/K	180
Crystal system	triclinic
Space group	P-1
a/Å, b/Å, c/Å	11.1199(5), 12.6052(6), 12.6121(5)
α/°, β/°, γ/°	99.0680(10), 98.3320(10), 105.9410(10)
Volume/$Å^3$	1645.29(13)
Z	2
$\rho_{calc}mg/mm^3$	1.773
m/mm^{-1}	4.626
F(000)	860.0
Crystal size/mm^3	0.40 × 0.12 × 0.04
2Θ range for data collection	3.34 to 56°
Index ranges	$-14 \leq h \leq 14, -16 \leq k \leq 16, -16 \leq l \leq 16$
Reflections collected	17108
Independent reflections	7933[R(int) = 0.0418]
Data/restraints/parameters	7933/0/425
Goodness-of-fit on F^2	1.029
Final R indexes [I>=2σ (I)]	$R_1 = 0.0423$, $wR_2 = 0.1010$
Final R indexes [all data]	$R_1 = 0.0547$, $wR_2 = 0.1076$
Largest diff. peak/hole / e $Å^{-3}$	3.29/-2.14

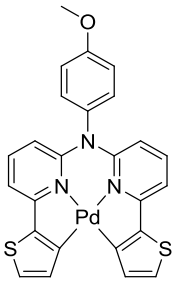

Crystal data and structure refinement for **PdL^7**	
Empirical formula	$C_{25}H_{17}N_3OS_2Pd$
Formula weight	545.94
Temperature/K	120
Crystal system	monoclinic
Space group	$P2_1/c$
a/Å, b/Å, c/Å	11.8429(5), 16.9154(8), 11.7698(5)
α/°, β/°, γ/°	90.00, 119.3810(10), 90.00
Volume/Å^3	2054.54(16)
Z	4
ρ_{calc}mg/mm^3	1.765
m/mm^{-1}	1.132
F(000)	1096.0
Crystal size/mm^3	0.42 × 0.06 × 0.05
2Θ range for data collection	3.94 to 57°
Index ranges	$-15 \leq h \leq 15$, $-22 \leq k \leq 22$, $-15 \leq l \leq 15$
Reflections collected	32335
Independent reflections	5190[R(int) = 0.0505]
Data/restraints/parameters	5190/0/357
Goodness-of-fit on F^2	1.106
Final R indexes [I>=2σ (I)]	R_1 = 0.0384, wR_2 = 0.0898
Final R indexes [all data]	R_1 = 0.0528, wR_2 = 0.1004
Largest diff. peak/hole / e Å^{-3}	1.77/-0.99

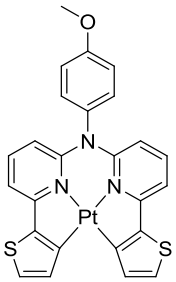

Crystal data and structure refinement for **PtL**[7]

Identification code	13srv293
Empirical formula	$C_{25}H_{17}N_3OPtS_2$
Formula weight	634.63
Temperature/K	120
Crystal system	monoclinic
Space group	$P2_1/c$
a/Å, b/Å, c/Å	11.8455(6), 16.9073(9), 11.7422(6)
α/°, β/°, γ/°	90.00, 119.0990(10), 90.00
Volume/Å^3	2054.85(18)
Z	4
ρ_{calc}mg/mm^3	2.051
m/mm^{-1}	7.057
F(000)	1224.0
Crystal size/mm^3	0.36 × 0.1 × 0.02
2Θ range for data collection	3.94 to 55°
Index ranges	$-15 \leq h \leq 15$, $-21 \leq k \leq 21$, $-15 \leq l \leq 15$
Reflections collected	29491
Independent reflections	4721 [R_{int} = 0.0522, R_{sigma} = 0.0360]
Data/restraints/parameters	4721/0/290
Goodness-of-fit on F^2	1.077
Final R indexes [I>=2σ (I)]	R_1 = 0.0250, wR_2 = 0.0556
Final R indexes [all data]	R_1 = 0.0368, wR_2 = 0.0610
Largest diff. peak/hole / e Å^{-3}	2.08/-1.74

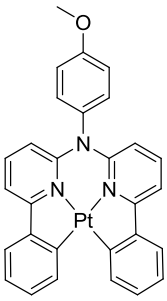

Crystal data and structure refinement for **PtL^1**	
Empirical formula	$C_{29}H_{21}N_3OPd$
Formula weight	533.89
Temperature/K	120.0
Crystal system	monoclinic
Space group	$P2_1/n$
a/Å, b/Å, c/Å	10.2400(2), 13.9674(3), 15.3870(3)
α/°, β/°, γ/°	90.00, 102.119(2), 90.00
Volume/Å^3	2151.72(8)
Z	4
ρ_{calc}mg/mm^3	1.648
m/mm^{-1}	0.892
F(000)	1080.0
Crystal size/mm^3	0.45 × 0.08 × 0.04
Radiation	MoKα (λ = 0.71073)
2Θ range for data collection	4.38 to 57.98°
Index ranges	$-13 \leq h \leq 13$, $-19 \leq k \leq 19$, $-20 \leq l \leq 20$
Reflections collected	39737
Independent reflections	5714 [R_{int} = 0.0725, R_{sigma} = 0.0466]
Data/restraints/parameters	5714/0/308
Goodness-of-fit on F^2	1.026
Final R indexes [I>=2σ (I)]	R_1 = 0.0322, wR_2 = 0.0684
Final R indexes [all data]	R_1 = 0.0476, wR_2 = 0.0750
Largest diff. peak/hole / e Å^{-3}	0.59/-0.62

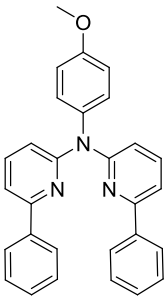

Table 1 Crystal data and structure refinement for $\mathbf{L^1H_2}$

Empirical formula	$C_{29}H_{23}N_3O$
Formula weight	429.50
Temperature/K	120.0
Crystal system	monoclinic
Space group	C2
a/Å, b/Å, c/Å	22.398(3), 5.5178(8), 17.919(3)
α/°, β/°; γ/°	90.00, 104.119(5), 90.00
Volume/Å^3	2147.6(5)
Z	4
ρ_{calc}mg/mm^3	1.328
m/mm^{-1}	0.082
F(000)	904.0
Crystal size/mm^3	0.27 × 0.18 × 0.13
Radiation	MoKα (λ = 0.71073)
2Θ range for data collection	4.68 to 60°
Index ranges	$-31 \le h \le 31$, $-7 \le k \le 7$, $-25 \le l \le 25$
Reflections collected	15073
Independent reflections	6161 [R_{int} = 0.0777, R_{sigma} = 0.1001]
Data/restraints/parameters	6161/1/390
Goodness-of-fit on F^2	1.002
Final R indexes [I>=2σ (I)]	R_1 = 0.0674, wR_2 = 0.1609
Final R indexes [all data]	R_1 = 0.0959, wR_2 = 0.1795
Largest diff. peak/hole / e Å^{-3}	0.35/-0.28

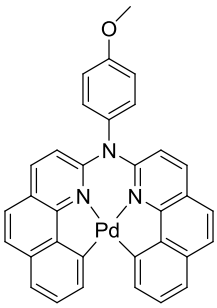

Crystal data and structure refinement for **PdL[9]**

Empirical formula	$C_{33}H_{21}N_3OPd$
Formula weight	581.93
Temperature/K	120.0
Crystal system	monoclinic
Space group	$P2_1/n$
a/Å , b/Å, c/Å	14.0765(8), 10.5865(6), 16.5111(10)
α/°, β/°, γ/°	90.00, 104.9793(17), 90.00
Volume/Å^3	2376.9(2)
Z	4
ρ_{calc}mg/mm^3	1.626
m/mm^{-1}	0.815
F(000)	1176.0
Crystal size/mm^3	0.41 × 0.24 × 0.14
Radiation	MoKα (λ = 0.71073)
2Θ range for data collection	4.62 to 58°
Index ranges	$-19 \leq h \leq 19$, $-14 \leq k \leq 14$, $-22 \leq l \leq 22$
Reflections collected	34079
Independent reflections	6324 [R_{int} = 0.0908, R_{sigma} = 0.0660]
Data/restraints/parameters	6324/0/344
Goodness-of-fit on F^2	1.027
Final R indexes [I>=2σ (I)]	R_1 = 0.0425, wR_2 = 0.0987
Final R indexes [all data]	R_1 = 0.0597, wR_2 = 0.1061
Largest diff. peak/hole / e Å^{-3}	0.94/-0.74

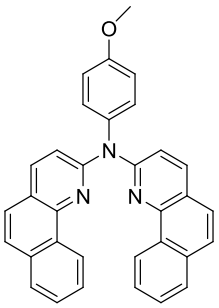

Crystal data and structure refinement for **L**[9]

Empirical formula	$C_{33}H_{23}N_3O$
Formula weight	477.54
Temperature/K	120
Crystal system	triclinic
Space group	P-1
a/Å, b/Å, c/Å	5.5915(3), 12.4353(7), 17.4649(8)
α/°, β/°, γ/°	90.294(4), 94.368(4), 100.667(4)
Volume/Å^3	1189.68(10)
Z	2
ρ_{calc}mg/mm^3	1.333
m/mm^{-1}	0.082
F(000)	500.0
Crystal size/mm^3	0.3007 × 0.1857 × 0.1608
Radiation	MoKα (λ = 0.71073)
2Θ range for data collection	5.8 to 60°
Index ranges	$-7 \leq h \leq 7$, $-17 \leq k \leq 17$, $-24 \leq l \leq 24$
Reflections collected	14103
Independent reflections	6930 [R_{int} = 0.0351, R_{sigma} = 0.0639]
Data/restraints/parameters	6930/0/426
Goodness-of-fit on F^2	1.041
Final R indexes [I>=2σ (I)]	R_1 = 0.0555, wR_2 = 0.1083
Final R indexes [all data]	R_1 = 0.0896, wR_2 = 0.1292
Largest diff. peak/hole / e Å^{-3}	0.31/-0.26

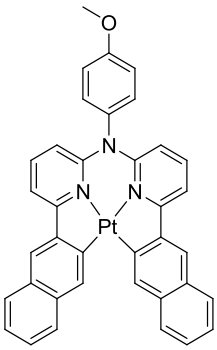

Crystal data and structure refinement for **PtL^4**

Empirical formula	$C_{37}H_{25}N_3OPt$
Formula weight	722.69
Temperature/K	120
Crystal system	triclinic
Space group	P-1
a/Å, b/Å, c/Å	8.6552(6), 9.9973(7), 15.9145(13)
α/°, β/°, γ/°	78.658(6), 84.855(6), 84.322(6)
Volume/Å^3	1340.05(17)
Z	2
ρ_{calc}mg/mm^3	1.791
m/mm^{-1}	5.273
F(000)	708.0
Crystal size/mm^3	0.2907 × 0.0779 × 0.0197
2Θ range for data collection	5.24 to 56°
Index ranges	$-8 \leq h \leq 11$, $-13 \leq k \leq 13$, $-21 \leq l \leq 20$
Reflections collected	13121
Independent reflections	6465[R(int) = 0.0685]
Data/restraints/parameters	6465/0/380
Goodness-of-fit on F^2	1.003
Final R indexes [I>=2σ (I)]	R_1 = 0.0514, wR_2 = 0.1033
Final R indexes [all data]	R_1 = 0.0702, wR_2 = 0.1133
Largest diff. peak/hole / e Å^{-3}	2.64/-1.77

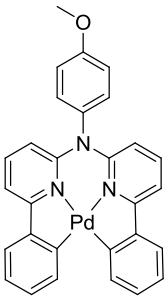

Crystal data and structure refinement for **PdL^1**

Empirical formula	$C_{29}H_{21}N_3OPd$
Formula weight	533.89
Temperature/K	120.0
Crystal system	monoclinic
Space group	$P2_1/n$
a/Å, b/Å, c/Å	10.2400(2), 13.9674(3), 15.3870(3)
α/°, β/°, γ/°	90.00, 102.119(2), 90.00
Volume/Å^3	2151.72(8)
Z	4
ρ_{calc}mg/mm^3	1.648
m/mm^{-1}	0.892
F(000)	1080.0
Crystal size/mm^3	0.45 × 0.08 × 0.04
Radiation	MoKα (λ = 0.71073)
2Θ range for data collection	4.38 to 57.98°
Index ranges	$-13 \leq h \leq 13$, $-19 \leq k \leq 19$, $-20 \leq l \leq 20$
Reflections collected	39737
Independent reflections	5714 [R_{int} = 0.0725, R_{sigma} = 0.0466]
Data/restraints/parameters	5714/0/308
Goodness-of-fit on F^2	1.026
Final R indexes [I>=2σ (I)]	R_1 = 0.0322, wR_2 = 0.0684
Final R indexes [all data]	R_1 = 0.0476, wR_2 = 0.0750
Largest diff. peak/hole / e Å^{-3}	0.59/-0.62

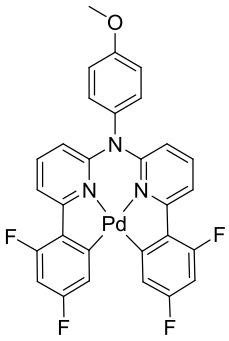

Crystal data and structure refinement for **PdL^{6}**

Empirical formula	$C_{29}H_{17}F_4N_3OPd$
Formula weight	605.86
Temperature/K	120.0
Crystal system	monoclinic
Space group	$P2_1/n$
a/Å, b/Å, c/Å	13.0656(12), 13.3619(12), 51.709(5)
α/°, β/°, γ/°	90.00, 94.561(2), 90.00
Volume/Å^3	8998.9(14)
Z	16
ρ_{calc}g/cm^3	1.789
μ/mm^{-1}	0.889
F(000)	4832.0
Crystal size/mm^3	0.242 × 0.233 × 0.079
Radiation	MoKα (λ = 0.71073)
2Θ range for data collection/°	4.36 to 56
Index ranges	$-17 \leq h \leq 17$, $-17 \leq k \leq 17$, $-68 \leq l \leq 68$
Reflections collected	135988
Independent reflections	21718 [R_{int} = 0.1023, R_{sigma} = 0.0673]
Data/restraints/parameters	21718/0/1373
Goodness-of-fit on F^2	1.122
Final R indexes [I>=2σ (I)]	R_1 = 0.0811, wR_2 = 0.1826
Final R indexes [all data]	R_1 = 0.0997, wR_2 = 0.1928
Largest diff. peak/hole / e Å^{-3}	2.32/-1.19

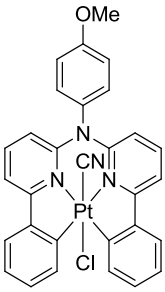

Crystal data and structure refinement for **PtL^1ClCN**

Empirical formula	$C_{30}H_{21}ClN_4OPt$
Formula weight	684.05
Temperature/K	120
Crystal system	triclinic
Space group	P-1
a/Å, b/Å, c/Å	8.8886(7), 11.8297(9), 12.3324(10)
α/°, β/°, γ/°	71.188(2), 74.189(2), 83.033(2)
Volume/Å^3	1180.24(16)
Z	2
ρ_{calc}mg/mm^3	1.925
m/mm^{-1}	6.091
F(000)	664.0
Crystal size/mm^3	0.197 × 0.077 × 0.06
Radiation	MoKα (λ = 0.71000)
2Θ range for data collection	5.2 to 60°
Index ranges	$-12 \leq h \leq 12$, $-16 \leq k \leq 16$, $-17 \leq l \leq 17$
Reflections collected	19246
Independent reflections	6863 [R_{int} = 0.0345, R_{sigma} = 0.0448]
Data/restraints/parameters	6863/6/336
Goodness-of-fit on F^2	1.096
Final R indexes [I>=2σ (I)]	R_1 = 0.0296, wR_2 = 0.0600
Final R indexes [all data]	R_1 = 0.0371, wR_2 = 0.0621
Largest diff. peak/hole / e Å^{-3}	3.01/-1.66

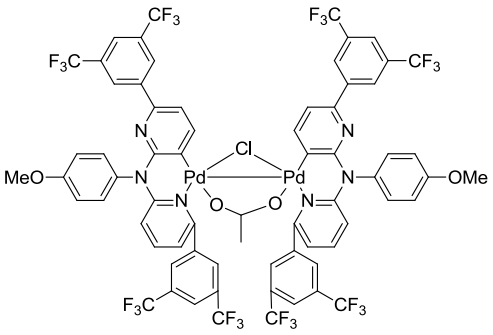

Crystal data and structure refinement for 14srv051	
Empirical formula	$C_{68}H_{37}Cl_1F_{24}N_6O_4Pd_2$ x 3 $CHCl_3$
Formula weight	2064.39
Temperature/K	120.0(2)
Crystal system	triclinic
Space group	P-1
a/Å, b/Å, c/Å	14.9235(6), 15.8217(7), 18.1312(7)
α/°, β/°, γ/°	97.389(3), 105.093(3), 107.245(4)
Volume/$Å^3$	3848.0(3)
Z	2
$\rho_{calc}mg/mm^3$	1.782
m/mm^{-1}	0.926
F(000)	2036.0
Crystal size/mm^3	0.2535 × 0.1186 × 0.027
Radiation	MoKα (λ = 0.71073)
2Θ range for data collection	3.88 to 56°
Index ranges	$-19 \leq h \leq 19$, $-20 \leq k \leq 20$, $-23 \leq l \leq 23$
Reflections collected	50243
Independent reflections	18554 [R_{int} = 0.0790, R_{sigma} = 0.1146]
Goodness-of-fit on F^2	1.023
Final R indexes [I>=2σ (I)]	R_1 = 0.0711, wR_2 = 0.1361
Final R indexes [all data]	R_1 = 0.1215, wR_2 = 0.1599
Largest diff. peak/hole / e $Å^{-3}$	2.08/-1.48

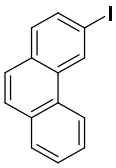

Crystal data and structure refinement for 13srv306

Identification code	13srv306
Empirical formula	$C_{13}H_8IN$
Formula weight	305.10
Temperature/K	120
Crystal system	triclinic
Space group	P-1
a/Å, b/Å, c/Å	7.4453(5), 7.5245(5), 9.8877(6)
α/°, β/°, γ/°	100.6280(10), 93.5190(10), 107.7040(10)
Volume/Å^3	514.55(6)
Z	2
ρ_{calc}mg/mm^3	1.969
m/mm^{-1}	3.072
F(000)	292.0
Crystal size/mm^3	0.3 × 0.18 × 0.11
Radiation	MoKα (λ = 0.71073)
2Θ range for data collection	4.22 to 58°
Index ranges	$-10 \leq h \leq 10$, $-10 \leq k \leq 10$, $-13 \leq l \leq 13$
Reflections collected	6347
Independent reflections	2730 [R_{int} = 0.0190, R_{sigma} = 0.0235]
Data/restraints/parameters	2730/0/168
Goodness-of-fit on F^2	1.079
Final R indexes [I>=2σ (I)]	R_1 = 0.0237, wR_2 = 0.0566
Final R indexes [all data]	R_1 = 0.0257, wR_2 = 0.0578
Largest diff. peak/hole / e Å^{-3}	1.89/-1.03

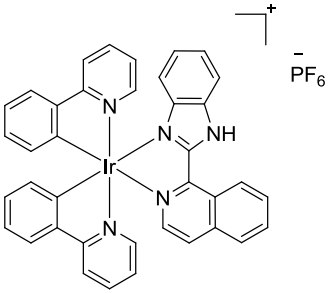

Crystal data and structure refinement for **[Ir(ppy)$_2$L^{12}H]PF$_6$**	
Empirical formula	$C_{38}H_{27}IrN_5$ x PF_6 x 2(C_3H_6O)
Formula weight	1006.97
Temperature/K	120
Crystal system	monoclinic
Space group	C2/c
a/Å, b/Å, c/Å	27.3787(14), 13.7434(7), 22.1437(11)
α/°, β/°, γ/°	90.00, 110.0600(10), 90.00
Volume/Å^3	7826.7(7)
Z	8
ρ_{calc}mg/mm^3	1.709
m/mm^{-1}	3.528
F(000)	4000.0
Crystal size/mm^3	0.51 × 0.22 × 0.04
Radiation	MoKα (λ = 0.71073)
2Θ range for data collection	3.16 to 55°
Index ranges	$-35 \leq h \leq 35$, $-17 \leq k \leq 17$, $-28 \leq l \leq 28$
Reflections collected	55912
Independent reflections	8983[R(int) = 0.0678]
Data/restraints/parameters	8983/5/533
Goodness-of-fit on F^2	1.036
Final R indexes [I>=2σ (I)]	R_1 = 0.0380, wR_2 = 0.0885
Final R indexes [all data]	R_1 = 0.0593, wR_2 = 0.1011
Largest diff. peak/hole / e Å^{-3}	1.71/-1.28

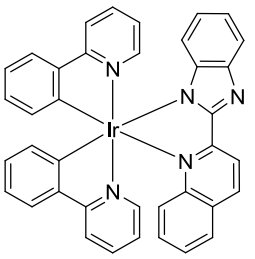

Crystal data and structure refinement for **Ir(ppy)$_2$L^{10}**	
Empirical formula	$C_{38}H_{26}N_5Ir$
Formula weight	744.84
Temperature/K	100
Crystal system	monoclinic
Space group	$P2_1/n$
a/Å, b/Å, c/Å	10.3173(3), 17.8089(6), 15.8935(5)
α/°, β/°, γ/°	90.00, 93.672(3), 90.00
Volume/Å^3	2914.27(16)
Z	4
ρ_{calc}mg/mm^3	1.698
m/mm^{-1}	4.217
F(000)	1464.0
Crystal size/mm^3	0.10 × 0.05 × 0.001
Radiation	Synchrotron (λ = 0.688900)
2Θ range for data collection	3.34 to 54°
Index ranges	$-13 \leq h \leq 13$, $-23 \leq k \leq 23$, $-20 \leq l \leq 17$
Reflections collected	27454
Independent reflections	6753[R(int) = 0.0556]
Data/restraints/parameters	6753/0/398
Goodness-of-fit on F^2	1.091
Final R indexes [I>=2σ (I)]	R_1 = 0.0310, wR_2 = 0.0743
Final R indexes [all data]	R_1 = 0.0383, wR_2 = 0.0795
Largest diff. peak/hole / e Å^{-3}	0.95/-1.14

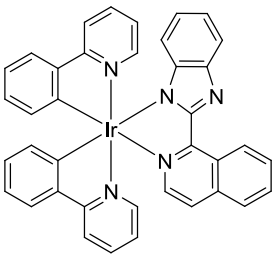

Crystal data and structure refinement for **Ir(ppy)$_2$L^{12}**	
Empirical formula	$C_{38}H_{26}IrN_5$ x C_3H_6O
Formula weight	802.92
Temperature/K	100.0
Crystal system	monoclinic
Space group	$P2_1/c$
a/Å, b/Å, c/Å	22.501(12), 8.487(5), 17.122(9)
α/°, β/°, γ/°	90.00, 102.036(5), 90.00
Volume/Å^3	3198(3)
Z	4
ρ_{calc}mg/mm^3	1.668
m/mm^{-1}	3.878
F(000)	1592.0
Crystal size/mm^3	0.1 × 0.05 × 0.01
Radiation	? (λ = 0.68890)
2Θ range for data collection	5.88 to 46°
Index ranges	$-25 \leq h \leq 23$, $-7 \leq k \leq 9$, $-12 \leq l \leq 18$
Reflections collected	7812
Independent reflections	4120 [R_{int} = 0.0537, R_{sigma} = 0.0743]
Data/restraints/parameters	4120/288/435
Goodness-of-fit on F^2	1.308
Final R indexes [I>=2σ (I)]	R_1 = 0.0956, wR_2 = 0.2093
Final R indexes [all data]	R_1 = 0.1134, wR_2 = 0.2176
Largest diff. peak/hole / e Å^{-3}	2.68/-2.92

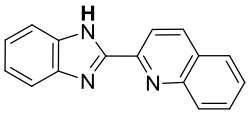

Crystal data and structure refinement for $\mathbf{L^{10}H}$	
Identification code	13srv246
Empirical formula	$C_{16}H_{11}N_3$ x H_2O
Formula weight	263.29
Temperature/K	120
Crystal system	monoclinic
Space group	Cc
a/Å, b/Å, c/Å	12.8724(8), 7.7651(5), 25.8262(15)
α/°, β/°, γ/°	90.00, 103.327(2), 90.00
Volume/Å^3	2512.0(3)
Z	8
ρ_{calc}mg/mm^3	1.392
m/mm^{-1}	0.090
F(000)	1104.0
Crystal size/mm^3	0.40 × 0.21 × 0.04
Radiation	MoKα (λ = 0.71073)
2Θ range for data collection	3.24 to 56°
Index ranges	$-16 \leq h \leq 16$, $-10 \leq k \leq 10$, $-34 \leq l \leq 34$
Reflections collected	18656
Independent reflections	6051[R(int) = 0.0699]
Data/restraints/parameters	6051/2/367
Goodness-of-fit on F^2	0.944
Final R indexes [I>=2σ (I)]	R_1 = 0.0679, wR_2 = 0.1603
Final R indexes [all data]	R_1 = 0.0960, wR_2 = 0.1781
Largest diff. peak/hole / e Å^{-3}	0.80/-0.29

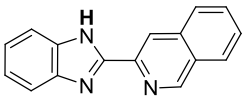

Crystal data and structure refinement for $\mathbf{L^{11}H}$	
Identification code	13srv247
Empirical formula	$C_{16}H_{11}N_3$ x $C_6H_8N_2$
Formula weight	353.42
Temperature/K	120
Crystal system	monoclinic
Space group	C2/c
a/Å, b/Å, c/Å	10.0514(9), 14.3896(13), 24.673(2)
α/°, β/°, γ/°	90.00, 99.011(2), 90.00
Volume/Å^3	3524.6(5)
Z	8
ρ_{calc}mg/mm^3	1.332
m/mm^{-1}	0.082
F(000)	1488.0
Crystal size/mm^3	0.34 × 0.18 × 0.12
Radiation	MoKα (λ = 0.71073)
2Θ range for data collection	3.34 to 58°
Index ranges	$-13 \leq h \leq 13$, $-19 \leq k \leq 19$, $-33 \leq l \leq 33$
Reflections collected	18462
Independent reflections	4677[R(int) = 0.0502]
Data/restraints/parameters	4677/0/320
Goodness-of-fit on F^2	1.006
Final R indexes [I>=2σ (I)]	R_1 = 0.0541, wR_2 = 0.1295
Final R indexes [all data]	R_1 = 0.0831, wR_2 = 0.1544
Largest diff. peak/hole / e Å^{-3}	0.34/-0.26

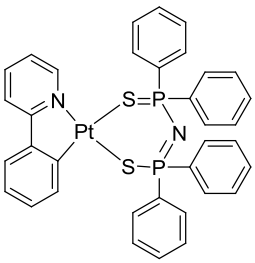

Crystal data and structure refinement for **[Pt(ppy)(SPNPS)]**	
Empirical formula	$C_{35}H_{28}N_2P_2PtS_2$
Formula weight	797.74
Temperature/K	120.0
Crystal system	monoclinic
Space group	$P2_1/n$
a/Å, b/Å, c/Å	9.5289(6), 13.6212(8), 22.9936(14)
α/°, β/°, γ/°	90.00, 96.765(2), 90.00
Volume/Å^3	2963.7(3)
Z	4
ρ_{calc}mg/mm^3	1.788
m/mm^{-1}	5.013
F(000)	1568.0
Crystal size/mm^3	0.351 × 0.196 × 0.115
Radiation	MoKα (λ = 0.71073)
2Θ range for data collection	4.46 to 60°
Index ranges	$-13 \leq h \leq 13$, $-19 \leq k \leq 19$, $-32 \leq l \leq 32$
Reflections collected	46564
Independent reflections	8660 [R_{int} = 0.0300, R_{sigma} = 0.0197]
Data/restraints/parameters	8660/0/379
Goodness-of-fit on F^2	1.067
Final R indexes [I>=2σ (I)]	R_1 = 0.0223, wR_2 = 0.0541
Final R indexes [all data]	R_1 = 0.0245, wR_2 = 0.0551
Largest diff. peak/hole / e Å^{-3}	1.44/-0.64

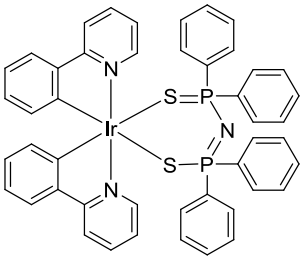

Crystal data and structure refinement for **[Ir(ppy)$_2$(SPNPS)]**	
Identification code	IrSPNPS
Empirical formula	$C_{47}H_{38}Cl_2IrN_3P_2S_2$ x CH_2Cl_2
Formula weight	1033.96
Temperature/K	120
Crystal system	orthorhombic
Space group	Pbca
a/Å, b/Å, c/Å	21.1512(17), 16.5056(13), 27.014(2)
α/°, β/°, γ/°	90.00, 90.00, 90.00
Volume/Å^3	9430.9(13)
Z	8
ρ_{calc}mg/mm^3	1.456
m/mm^{-1}	3.135
F(000)	4112.0
Crystal size/mm^3	0.05 × 0.1 × 0.46
Radiation	MoKα (λ = 0.71073)
2Θ range for data collection	1.5 to 62.08°
Index ranges	$-30 \leq h \leq 30$, $-23 \leq k \leq 23$, $-39 \leq l \leq 39$
Reflections collected	134186
Independent reflections	11380 [R_{int} = 0.1156, R_{sigma} = 0.0694]
Data/restraints/parameters	11380/6/512
Goodness-of-fit on F^2	1.082
Final R indexes [I>=2σ (I)]	R_1 = 0.0486, wR_2 = 0.1204
Final R indexes [all data]	R_1 = 0.0834, wR_2 = 0.1367
Largest diff. peak/hole / e Å^{-3}	2.45/-1.34

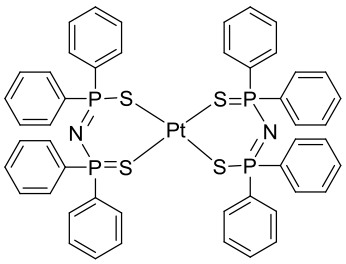

Crystal data and structure refinement for **$Pt(SPNPS)_2$**	
Identification code	13srv303
Empirical formula	$C_{48}H_{40}N_2P_4PtS_4$
Formula weight	1092.03
Temperature/K	120.0
Crystal system	triclinic
Space group	P-1
a/Å, b/Å, c/Å	9.5936(6), 12.9454(8), 13.4912(9)
α/°, β/°, γ/°	113.792(2), 94.410(2), 102.155(2)
Volume/$Å^3$	1474.02(16)
Z	1
$\rho_{calc}mg/mm^3$	1.230
m/mm^{-1}	2.658
F(000)	544.0
Crystal size/mm^3	0.22 × 0.2 × 0.04
Radiation	MoKα (λ = 0.71073)
2Θ range for data collection	4.88 to 58°
Index ranges	$-13 \leq h \leq 13$, $-18 \leq k \leq 18$, $-19 \leq l \leq 19$
Reflections collected	23585
Independent reflections	7787 [R_{int} = 0.0285, R_{sigma} = 0.0393]
Data/restraints/parameters	7787/0/268
Goodness-of-fit on F^2	1.096
Final R indexes [I>=2σ (I)]	R_1 = 0.0304, wR_2 = 0.0762
Final R indexes [all data]	R_1 = 0.0334, wR_2 = 0.0803
Largest diff. peak/hole / e $Å^{-3}$	2.42/-0.86

A.2 Relevant Publications

Aspects of the work presented in this thesis have been reported in the following publications:

B. Aranda, P. Aguirre, S. A. Moya, M. Bonneau, J. A. G. Williams, L. Toupet, M. Escadeillas, H. Le Bozec, V. Guerchais, "Luminescent *bis*-cyclometallated iridium(III) complexes containing phosphine-based ligands: Influence of the P^N bridge" *Polyhedron*, 2014, in press.

A.3 Attended Conferences

- RSC Photochemistry Early Career Researchers Meeting 2013, University of Ulster, Belfast Campus, Northern Ireland, UK, 15th and 16th May 2013.
  Poster presentation: "C–H bond activation/arylation of thienyl-based iridium (III) complexes with fluorophores"

- RSC Dalton 2014, University of Warwick, 15th until 17th April 2014.
  Poster presentation: "Luminescent iridium(III) complexes containing bis-benzimidazole and benzimidazol-(iso)quinolyl ligands"